Initial Exploration of 21-cm Cosmology with Imaging and Power Spectra from the Murchison Widefield Array

by

Christopher Leigh Williams

B.S., Stanford University (2005)

Submitted to the Department of Physics
in partial fulfillment of the requirements for the degree of

Doctor of Philosophy in Physics

at the

MASSACHUSETTS INSTITUTE OF TECHNOLOGY

June 2012

Author .....
Department of Physics
May 18, 2012

Certified by .....
Jacqueline N. Hewitt
Professor of Physics
Thesis Supervisor

Accepted by .....
Krishna Rajagopal
Professor of Physics
Associate Department Head for Education

Initial Exploration of 21-cm Cosmology with Imaging and Power Spectra from the Murchison Widefield Array

by

Christopher Leigh Williams

Submitted to the Department of Physics
on May 18, 2012, in partial fulfillment of the
requirements for the degree of
Doctor of Philosophy in Physics

Abstract

The Murchison Widefield Array (MWA) is a new low-frequency radio array under construction in Western Australia with a primary goal of measuring the power spectrum of the 21-cm signal from neutral hydrogen during the Epoch of Reionization (EoR). In this thesis, we detail efforts to characterize the MWA system, and present scientific results from a 32-element prototype interferometer deployed at the MWA site. We develop simulations and perform anechoic chamber measurements to verify the performance of the MWA antenna tiles. We develop a calibration and imaging pipeline for the MWA which uses w-projection widefield imaging techniques and direction-dependent point spread functions. Using data from an MWA expedition in March 2010, we produce confusion-limited maps covering ~ 2700 square degrees in a region of sky with low galactic temperature. We develop a blind source detection and extraction algorithm, and use it to perform a blind survey in these maps, and detect 655 sources at high significance with an additional 871 candidates. We compare these sources with existing low-frequency radio surveys in order to assess the MWA-32T system performance, and to identify new candidates for ultra-steep spectrum radio sources. In order to constrain the EoR, we apply two power spectrum estimation techniques to this dataset: a Fast Fourier Transform in order to rapidly compute power spectra, and a quadratic estimation method which uses inverse covariance weighting to produce an optimal estimate. We use a principal component analysis to identify and remove the foreground contaminants. In the resulting two-dimensional power spectra, we find the predicted "wedge" feature due to the chromaticity of the instrumental response, and identify a sensitive region free of strong contaminants which can be used for characterizing the EoR signal. We then use these data to produce new limits on the EoR power spectrum at $z = 9$.

Thesis Supervisor: Jacqueline N. Hewitt
Title: Professor of Physics

Acknowledgments

The work that I present here could not have been accomplished without the help and support of my mentors, colleagues, friends and family. I am deeply indebted to everyone who helped me along the way.

First and foremost, I would like to thank my advisor, Jackie Hewitt. Her guidance and encouragement have helped me immeasurably in my growth and development as a scientist. She has been a fantastic advisor and role model. I would also like to thank the rest of the MWA group at MIT, particularly Ed Morgan for his help with the MWA M&C system and all things computation related, as well as Al Levine for his extremely helpful editing and feedback on our first paper.

I thank my thesis committee for their support and guidance. Max Tegmark's incredible intuition, insight and optimistic attitude helped me to realize the potential of the MWA data, while Paul Schechter's advice kept me focused on what was most important.

My work has been done as part of the Murchison Widefield Array project, and would not have been possible without the efforts of the entire MWA team. It has been fantastic getting to know this diverse group of people from all over the world, and a real joy to work with them on the array. I want to acknowledge everyone that contributed to building the instrument and to making the project a reality.

Some of the most fun experiences I have had in graduate school were the MWA site expeditions, and it was a pleasure to work with everyone who participated in these trips. I would like to particularly acknowledge Dave Emrich, who made the MWA site expeditions a real pleasure (puns and all). I would also like to thank Frank Briggs for his advice and for imparting some of his encyclopedic radio astronomy knowledge to me.

I thank the Halleen family for their fantastic hospitality while staying and working at Boolardy station. Carolyn, Mark, Sarah, Ben and Edwina were incredibly welcoming, and their kindness (not to mention their fantastic cooking) helped to make my experiences at the MWA site even more enjoyable. I also acknowledge and thank the Wajarri Yamatji people, the traditional owners of the observatory site.

I also want to thank my fellow astrophysics grad students at MIT. There was an amazing sense of community and camaraderie as we progressed through our classes and general exams together. Adrian Liu was my "theoretical counterpart" and it was an absolute pleasure to work with him and to combine our areas of expertise to get some really exciting science out of the MWA data. I also want to thank some of my past and present office-mates, particularly Josh Carter and Leo Stein, who always made coming to work a lot of fun, as well as the other grad students who started and graduated with me, including Phil Zukin, Leslie Rogers, Sarah Vigeland and Nic Smith.

Last, but certainly not least, I want to thank my family. Their unflagging support and confidence, and knowing that they are proud of me helped me get through the inevitable ups and downs of graduate school. I thank Aubrey for putting up with my frequent long trips to the other side of the world, and bearing with me through it all.

THIS PAGE INTENTIONALLY LEFT BLANK

Contents

THIS PAGE INTENTIONALLY LEFT BLANK

List of Figures

List of Tables

THIS PAGE INTENTIONALLY LEFT BLANK

Chapter 1

Introduction

1.1 Cosmology and the Early Universe

Over the past several decades, humanity's understanding of the evolution and history of our Universe has undergone a revolution. Experiments such as the Wilkinson Microwave Anisotropy Probe (WMAP) and the Planck telescope have given us exquisitely detailed maps of the Cosmic Microwave Background (CMB) radiation, painting a detailed picture of our Universe a mere 380,000 years after the Big Bang, while galaxy surveys such as the Sloan Digital Sky Survey have mapped out the large scale structures that describe our Universe today. These observations have enabled us to construct a cosmological model which describes our observations throughout cosmic history with incredible accuracy. With powerful telescopes from the ground and in space, we have been able verify this model with observations of distant galaxies only 500 million years after the Big Bang. This has allowed us to form a near complete description of our Universe from its birth 13.7 billion years ago up to the present day.

There is, however, a conspicuous observational gap in our cosmic timeline. One of the great remaining unexplored periods in the history of universe falls between the epoch of the CMB and the oldest galaxies and quasars that we can observe. This era is called "Dark Ages," and represents a time before the formation of the first stars and galaxies. During this period, our Universe transitioned from an extremely smooth,

homogeneous, state with 1 part in 10^5 density fluctuations (determined from CMB observations), into the complex diversity of collapsed structures — clusters, galaxies and stars — that we observe today. Tracing the evolution of our Universe throughout this period of transition is extremely important for understanding the evolutionary history of our Universe, and will not only allow us to better understand how the first structures formed, but will enable us to probe the underlying density evolution and constrain fundamental cosmological parameters. This era has so far defied detailed study, and remains one of the frontiers of astrophysics and cosmology.

1.2 Probing the Epoch of Reionization

A particularly interesting time period comes at the end of the Dark Ages, and is known as the Epoch of Reionization (EoR). Throughout most of the Dark Ages, the hydrogen, which makes up $\sim$75% of the baryons in our Universe, is cool and neutral. However as this gas collapses gravitationally and stars and galaxies begin to form, the electromagnetic radiation emitted from these first objects interacts with the neutral hydrogen and ionizes the intergalactic medium (IGM). Ionized regions grow around these early objects and, over time, enough high energy (ultraviolet and X-ray) emission is produced to ionize nearly the entirety of the hydrogen in the IGM (Furlanetto et al., 2006). This represents a "cosmic dawn" of sorts, when high energy photons can stream throughout space without being absorbed, and the result of cosmic structure formation has been felt by nearly all of the baryons in the universe.

The EoR is a crucial period in the cosmological evolution of the universe and in the formation of astrophysical objects, and as such, has become an area of intense study. Observations of high redshift quasars (Fan, 2006) have placed limits on the ionization fraction in the early Universe, constraining the bulk of reionization to a redshift of $z \gtrsim 6$, while integral constraints on the optical depth to the CMB place reionization at a redshift of $z \approx 11$, under the assumption that reionization was instantaneous (Komatsu et al., 2011). Theoretical efforts have also focused on simulating the reionization process (see e.g. Gnedin & Shaver 2004; McQuinn et al.

2006; Lidz et al. 2008; Mesinger et al. 2011), however the details of the most important physical processes that contribute to reionization are still unconstrained. Direct measurements of the ionization state of hydrogen throughout this epoch are needed to inform these models and to give us a clear picture of the way in which these first objects formed and influenced their environments.

The redshifted 21-cm line from the hyperfine transition in neutral hydrogen has emerged as one of the most promising probes of the EoR. Although the Lyman-α transition of hydrogen has been useful in absorption studies of quasars, it suffers from saturation at relatively low neutral fractions ($x_{\rm HI} \sim 10^{-4}$, Fan 2006). The hyperfine transition, on the other hand, is a forbidden line with an extremely long mean lifetime ($\sim 3 \times 10^7$ years), and is therefore far from saturation and optically thin throughout the EoR (Furlanetto et al., 2006). As it is a spectral line with a well defined transition frequency of 1420 MHz, the cosmological redshift of the line can be used to trace out the full three-dimensional neutral hydrogen distribution. During the EoR, the 21-cm line is redshifted into the low-frequency radio regime, with a frequency in the $\sim 100 - 200$ MHz range.

The key observable of the 21-cm line is its strength relative to the CMB. The specific intensity of an object, I_ν, is often expressed as an effective "brightness temperature," T_b of a blackbody radiator, related by the Rayleigh-Jeans formula (the low-frequency limit of the Planck blackbody function):

$$T_b = I_\nu \frac{c^2}{2k_{\rm B}\nu^2}, \tag{1.1}$$

where c is the speed of light, $k_{\rm B}$ is Boltzmann's constant, and ν is the frequency. The strength of the 21-cm line can be calculated as a differential brightness temperature relative to the background radiation from the CMB at a particular redshift:

$$\Delta T_b(z) \approx 9 x_{\rm HI}(1+\delta)(1+z)^{1/2}\left(1 - \frac{T_\gamma(z)}{T_S(z)}\right) \ {\rm mK}, \tag{1.2}$$

where $x_{\rm HI}$ is the ionization fraction of the hydrogen, δ is the local over-density, $T_\gamma(z)$ is the temperature of the CMB at a particular redshift, and $T_S(z)$ is the spin temperature

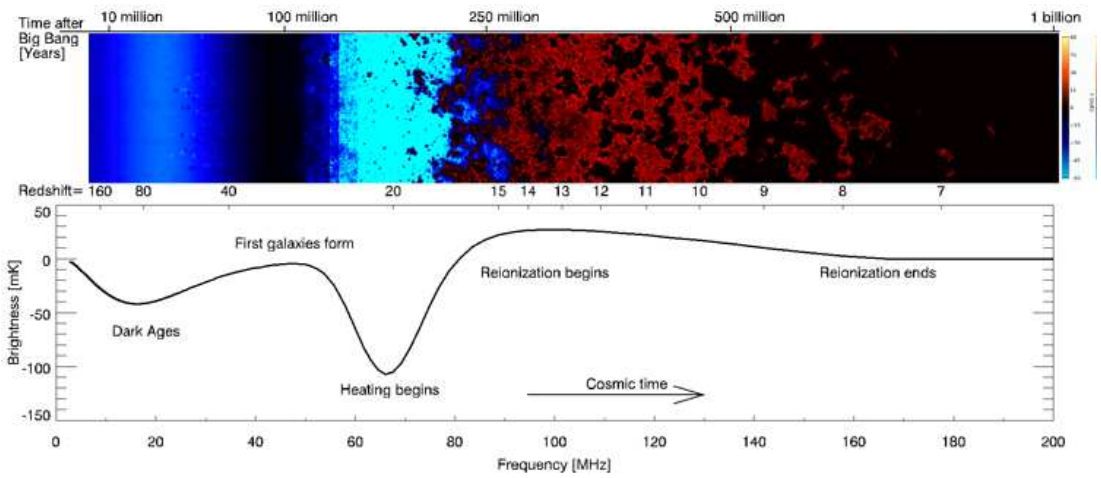

Figure 1-1: Illustration of the evolution of the 21-cm signal throughout cosmic history, taken from Pritchard & Loeb (2010). The bottom panel shows an evolution of the overall 21-cm brightness temperature relative to the CMB, while the top panel illustrates changes in the spatial properties of the 21-cm signal.

of the hydrogen (Furlanetto et al., 2006). The CMB temperature varies with redshift as $T_\gamma(z) = 2.73(1+z)$ K, while the spin temperature, T_S depends on the detailed processes which act to excite the HI hyperfine transition. These processes include the absorption of CMB photons, collisions with other atoms and scattering with UV photons (the Wouthuysen-Field effect, see e.g. Furlanetto et al. 2006). Depending on the relationship between T_S and T_γ, the 21-cm signal will either appear in emission or absorption relative to the background emission from the CMB. This expression ignores any peculiar velocity effects. An illustration of how the 21-cm signal evolves throughout cosmic history is shown in Figure 1-1.

Unfortunately, this leads to some observational challenges. Emission from the 21-cm line during the EoR is redshifted into the low-frequency radio regime, a region of the spectrum where terrestrial and satellite radio emitters are rife. Additionally, the expected signal is only on the order of ~ 10 mK, which is extremely faint relative to both the noise performance of typical radio telescopes (Taylor et al., 1999) and the expected low-frequency emission from astrophysical sources (see e.g. Shaver et al. 1999; de Oliveira-Costa et al. 2008; Pindor et al. 2011). It is likely that an array of the scale of a Square Kilometer Array will be necessary to directly image the

hydrogen at these redshifts (Furlanetto & Briggs, 2004). However, in principle, a wide field-of-view low-frequency radio array of modest collecting area may be able to make a *statistical* detection of the signal from neutral hydrogen during reionization by characterizing the power spectrum of 21-cm line (Morales & Hewitt, 2004; Zaldarriaga et al., 2004).

1.3 Low-Frequency, Wide-Field Radio Instrumentation

Given the challenges present in making a measurement of the 21-cm line during reionization, it is fortuitous that advances in technology have ushered in a new era of low-frequency, wide field-of-view radio astronomy. It has only recently become feasible to to build the large low-frequency arrays which have the potential to detect the 21-cm signal at high redshift. Advances in the speed of computers and digital electronics have made radio arrays with large numbers of elements, large fields of view and large bandwidths a reality. These types of instruments are well suited for making a power spectrum measurement during the EoR, as radio interferometric arrays directly probe Fourier modes of the sky (Morales & Hewitt, 2004).

The general operation of a radio interferometer relies on coherently detecting emission with multiple separate receptors, and combining them in a manner that allows a reconstruction of the true sky intensity. If we define the "visibility," $V_\nu(\mathbf{r}_1, \mathbf{r}_2)$ as the correlation between the electric field at two spatial points, $\mathbf{r}_1$ and $\mathbf{r}_2$ at frequency ν:

$$V_\nu(\mathbf{r}_1, \mathbf{r}_2) = \langle \mathbf{E}_\nu(\mathbf{r}_1)\mathbf{E}^*_\nu(\mathbf{r}_2)\rangle, \tag{1.3}$$

then the Van Cittert-Zernike theorem states:

$$V_\nu(u, v, w) = \int I_{\rm obs}(l, m) e^{-2\pi i[ul+vm+w(\sqrt{1-l^2-m^2}-1)]} \frac{dl\ dm}{\sqrt{1-l^2-m^2}}, \tag{1.4}$$

where the coordinate system is defined so that w is the separation in units of wavelength between $\mathbf{r}_1$ and $\mathbf{r}_2$ projected along the line-of-sight direction to an astrophysical source, and u and v are the separations in units of wavelength between $\mathbf{r}_1$ and $\mathbf{r}_2$ in the plane normal to w, projected in the West-East, and North-South directions respectively. l and m are the direction cosines, and $I_{\rm obs}(l,m)$ is the observed intensity on the sky. By measuring the visibility function at many different locations in the "uv" plane (i.e. many measurements with different antenna separations), Equation 1.4 can be inverted to recover $I_{\rm obs}(l,m)$. Furthermore, $I(l,m)$ is recovered with an angular resolution which scales as $1/\sqrt{u^2+v^2}$, effectively providing a similar maximum resolution to a single dish that is the size of the maximum extent of the array. This relationship is the cornerstone of "aperture synthesis" imaging in radio astronomy. For a further discussion, or more detailed review the reader is directed to Taylor et al. (1999) or Thompson et al. (2001).

There are several key challenges to the detection of the signal from the EoR with these arrays. The first challenge is one of sensitivity. Each visibility has a thermal noise level approximated by:

$$v_{\rm RMS} = \frac{2k_{\rm B}T_{\rm sys}}{A_{\rm eff}\sqrt{\Delta\nu\,\tau}}, \tag{1.5}$$

where $v_{\rm RMS}$ is the root-mean-square noise in a visibility measurement, $k_{\rm B}$ is Boltzmann's constant, $A_{\rm eff}$ is the effective area of an antenna, $\Delta\nu$ is the bandwidth over which the visibility is integrated, τ is the integration time, and $T_{\rm sys} = T_{\rm sky} + T_{\rm rec}$ is the system temperature, which consists of contributions from the sky noise, $T_{\rm sky}$ and the receiver, $T_{\rm rec}$ (see, e.g. Taylor et al. 1999 or Morales & Wyithe 2010 for a further discussion of sensitivity). In general at these wavelengths, the system temperature is dominated by $T_{\rm sky}$, which can be in the hundreds of Kelvin range or higher at frequencies relevant to the EoR. This noise in each visibility leads to an overall uncertainty in a resulting synthesis image of :

$$\Delta T = \frac{\lambda^2 T_{\rm sys}}{\Omega_{\rm PSF}A_{\rm eff}\sqrt{N(N-1)\Delta\nu\,\tau}}, \tag{1.6}$$

where ΔT is the root-mean-square sky noise in units of temperature, λ is the observation wavelength, $\Omega_{\rm PSF}$ is the angular size (in steradians) of the instrumental point spread function, N is the number of elements in the array, and $A_{\rm eff}$, $\Delta\nu$, τ, and $T_{\rm sys}$ are defined as above. Achieving the sensitivity necessary to measure a $\sim$ 10 mK signal, requires a large number of independent measurements (many antennas) and a long integration time over a wide field of view (there are more subtleties in the strategies used to maximizing array sensitivity, however they are out of the scope of the discussion here — see Morales & Wyithe 2010 for further discussion).

A second complication aries from the wide-field nature of these arrays. In the situation where the third term in the exponential of Equation 1.4 is negligible (i.e. $w(\sqrt{1-l^2-m^2}-1) \approx 0$), this equation reduces to a two-dimensional Fourier transform. This reduction can be performed if l^2+m^2 is small — the so called"narrow-field" limit. Radio astronomy imaging is typically performed in this regime, so that the Fast Fourier Transform (FFT) algorithm can be leveraged in order to avoid the large computation cost associated with directly inverting Equation 1.4. For a wide field of view instrument, this assumption can no longer be made. Traditionally, wide-field images have been computed by stitching together a large number of smaller images, where each image is made over a field of view small enough to assume the narrow-field limit. However, this procedure is extremely computationally intensive (Cornwell et al., 2008).

Recently, new methods have been developed which use techniques to warp images to correct for this effect (see, e.g. Ord et al. 2010). This technique requires that the array be coplanar (it is important to note that this is not the same as requiring $w \equiv 0$). In this regime, Equation 1.4 can be re-parameterized using (Ord et al., 2010):

$$w = au + bv, \tag{1.7}$$

which allows Equation 1.4 to be expressed as:

$$V_\nu(u,v) = \int I_{\rm obs}(l,m) e^{-2\pi i(ul'+vm')} \frac{dl\ dm}{\sqrt{1-l^2-m^2}}, \tag{1.8}$$

with

$$l' = l + a(\sqrt{1 - l^2 - m^2} - 1), \tag{1.9}$$

$$m' = m + b(\sqrt{1 - l^2 - m^2} - 1), \tag{1.10}$$

and

$$dl\ dm = \left(1 - \frac{al + bm}{\sqrt{1 - l^2 - m^2}}\right) dl'\ dm'. \tag{1.11}$$

This expression can be inverted efficiently with a two-dimensional FFT. Using this re-parameterization is effectively a coordinate system distortion ($l \rightarrow l',\ m \rightarrow m'$), which can be corrected with a suitable "re-gridding" in the image plane.

Another promising method (of which this thesis makes extensive use) is the w-projection algorithm of Cornwell et al. (2008). In this method, Equation 1.4 is rearranged:

$$V_\nu(u, v, w) = \int I_{\rm obs}(l, m) G(l, m, w) e^{-2\pi i(ul+vm)} \frac{dl\ dm}{\sqrt{1 - l^2 - m^2}}, \tag{1.12}$$

with

$$G(l, m, w) = e^{2\pi i w(\sqrt{1-l^2-m^2}-1)}. \tag{1.13}$$

Using the convolution theorem, we can then re-express this as:

$$V_\nu(u, v, w) = \tilde{G}(u, v, w) * V(u, v, w \equiv 0), \tag{1.14}$$

where $\tilde{G}(u, v, w)$ is the two-dimensional Fourier transform of $G(l, m, w)$, and represents a w-dependent convolution kernel. Using $\tilde{G}$ as a gridding kernel, we can then project each visibility on to a uv plane with $w \equiv 0$. This allows us to efficiently form a map of the sky using only a two-dimensional FFT. The gridding kernels can be pre-computed and re-used, which improves the efficiency of this method. An advantage of this technique is that it does not require the array be co-planar. The development of these imaging methods, along with the Moore's law increase in computational power has enabled a new generation of wide field radio observatories.

Another complication arises from the ionosphere. At low radio frequencies, time and position variability of the electron content in the ionosphere can lead to variable propagation delays of radio waves. These manifest themselves as variable phase errors in a radio interferometric measurement (Baldwin et al., 1985; Kassim et al., 2007; Parsons et al., 2010). This acts like a variable refractive screen, which distorts the sky coordinate system and needs to be calibrated in order to produce astrometrically correct maps. However, the techniques for doing this in a high fidelity, computationally efficient manner are still in development (see, e.g. Mitchell et al. 2008).

1.4 Towards Measuring the EoR Power Spectrum

In spite of these difficulties, a first generation of pathfinder telescopes is under construction which aims to measure the 21-cm power spectrum, and will serve as a testbed for developing future generations of these arrays. Experiments such as the Precision Array to Probe the Epoch of Reionization (PAPER, Parsons et al. 2010), the LOw Frequency ARray (LOFAR, Rottgering et al. 2006), the Giant Metrewave Radio Telescope EoR experiment (GMRT, Paciga et al. 2011) and others are all seeking to measure the power spectrum from highly redshifted 21-cm emission. Each of these arrays is focusing on slightly different techniques and optimizations to explore how best to make an EoR detection.

This thesis focuses on another of these pathfinder experiments, the Murchison Widefield Array (MWA), which is a new low-frequency radio interferometer currently under construction at a radio quiet site in Western Australia. This work is divided into four main sections. In Chaper 2, the MWA instrument is introduced. We discuss the architecture of the array, and the design and performance of the subsystems. The MWA is an unconventional instrument in many ways, and understanding the unique nature of its design is crucial for leveraging its scientific capabilities. The data used in this thesis was obtained from the MWA 32-Tile prototype system, which served as an engineering and scientific test-bed for the full MWA system. The MWA is being developed by a large collaboration, including research groups from MIT, the MIT

Haystack Observatory, the Harvard-Smithsonian Center for Astrophysics, the Australian National University, the University of Sydney, the University of Melbourne, the International Centre for Radio Astronomy Research at Curtin University, the University of Western Australia, the Swinburne University of Technology, the Raman Research Institute, the Australian Commonwealth Scientific and Industrial Research Organisation, the University of Washington, Arizona State University and the University of Wisconsin-Milwaukee, as well as industry partners.

In Chapter 3, we document efforts to understand the performance of the MWA antenna tiles. A detailed model of the MWA collecting elements is necessary for verifying the performance of the instrument as well as interpreting the results. We undertook a campaign of anechoic chamber measurements at the MIT Lincoln Lab to measure the performance of an MWA tile in a controlled laboratory setting. We compare the results of these tests to analytic models and numerical simulations of the MWA dipoles and antenna tiles. The content of this chapter is partially based on an MWA antenna memorandum (Williams et al., 2007), and relied on the generous assistance of the MIT Lincoln Lab staff.

In Chapter 4, we present the results of a first MWA survey of point sources using observations of a candidate field for the MWA EoR experiment. It serves as a first quantitative scientific verification of MWA imaging performance, as well as a characterization of the population of foreground astrophysical sources for an MWA EoR experiment. It gives a new picture of this region of the southern sky at low frequencies, identifying a significant number of new source candidates. The data for this chapter were obtained during MWA site expedition 13 in March 2010. The content of this chapter is based on the paper by Williams et al. (2012), and has contributions from several MWA collaborators.

In Chapter 5, we use data from the MWA 32-Tile prototype to produce power spectra in an effort to characterize emission from the Epoch of Reionization. Although the sensitivity of the prototype array is not sufficient to detect the predicted EoR signal, this chapter serves as an important first effort towards developing the tools and techniques needed for a full-scale EoR experiment with the MWA. We

explore techniques for producing power spectra, and culminate with a limit on the power spectrum during reionization. The work in this chapter represents a collaborative effort, with Adrian Liu. The inverse-variance weighted optimal estimator power spectra were produced by him, and the data analysis was a joint effort. The results of this chapter are being prepared for publication in a scientific journal.

Taken together, this thesis chronicles an effort to develop a new array which pushes the boundaries of low-frequency radio astronomy in order to investigate one of the remaining unexplored epochs in the history of our Universe. As these techniques are further developed, and our observational capabilities are expanded, we will eventually open a new window into this era of cosmic history, and will be able to study the rich astrophysics and cosmology that it contains.

THIS PAGE INTENTIONALLY LEFT BLANK

Chapter 2

The Murchison Widefield Array 32-Tile Prototype

2.1 Overview

The Murchison Widefield Array (MWA) is a new low-frequency array being constructed with the goal of measuring emission from neutral hydrogen during the Epoch of Reionization (EoR) of the Universe. The MWA will consist of a 128-element interferometer operating in the 80 MHz to 300 MHz frequency band, located at the radio-quiet Murchison Radio-astronomy Observatory (MRO) near Boolardy Station in Western Australia[1]. In addition to the study of the EoR, other key science goals of the MWA include the study of radio transients, the study of the heliosphere and ionosphere, and low-frequency Galactic and extragalactic studies. These four goals and potentially others are addressed by an array made of a large number of small antenna elements that simultaneously give a large collecting area and a large field of view. This is a departure in many ways from a traditional radio array design, with phased arrays of dipoles constituting the fundamental antenna elements, digitization early in the data stream, and full correlation of a large number of baselines. This design promises large improvements with regard to wide-field surveys and detection of the EoR, but, at the same time, it poses new challenges, especially with regard

[1]We acknowledge the Wajarri Yamatji people as the traditional owners of the Observatory site.

to calibration and imaging of the large field of view and compensation for the effects of the ionosphere. The location, instrumental attributes and design of the MWA system have led to the MWA being designated as an official Square Kilometre Array precursor. Further details of the MWA are described in Lonsdale et al. (2009) and Tingay et al. (in prep.).

As a first step in demonstrating the new technologies required for the full MWA array, a 32-element (32T) prototype was built at the MRO. This prototype system was operated for four years, from its initial deployment in November 2007 until decommissioning in February 2012. The 32T system was deployed and operated in campaign mode with a series of site expeditions, each consisting of typically 4-6 people over a duration of 1-2 weeks. A total of 16 expeditions, labeled "X1" through "X16", were conducted during the 32T effort, with the early expeditions focusing on deploying the 32T hardware, and the later expeditions focusing on engineering development and initial science observations.

The 32T prototype follows the general architecture of the full MWA system. It consists of 32 antenna tiles serviced by 4 digital receiver nodes, a hardware correlator, and data capture and control computers. The full 32T hardware system is detailed in the remainder of this chapter.

2.2 Antenna Tiles & Beamformers

The individual collecting elements of the MWA consist of 16-element "tiles" of dipole antennas. These antennas use a vertical bowtie design which has low horizon gain (for RFI mitigation) and good wideband performance. They are optimized for low cost manufacturability. Each antenna has two independent orthogonal arms, sensitive to the North-South and East-West linear polarizations. An integrated low-noise amplifier (LNA) functions as a balun, and is located at the center of each dipole arm, inside a PVC hub. The antennas are manufactured out of extruded "U"-shaped aluminum channels which are 5/8 in wide and 9/16 in tall. The dipole arms are 74 cm wide, and 40 cm tall, and are positioned so that the center of the arms is 27.4 cm above the

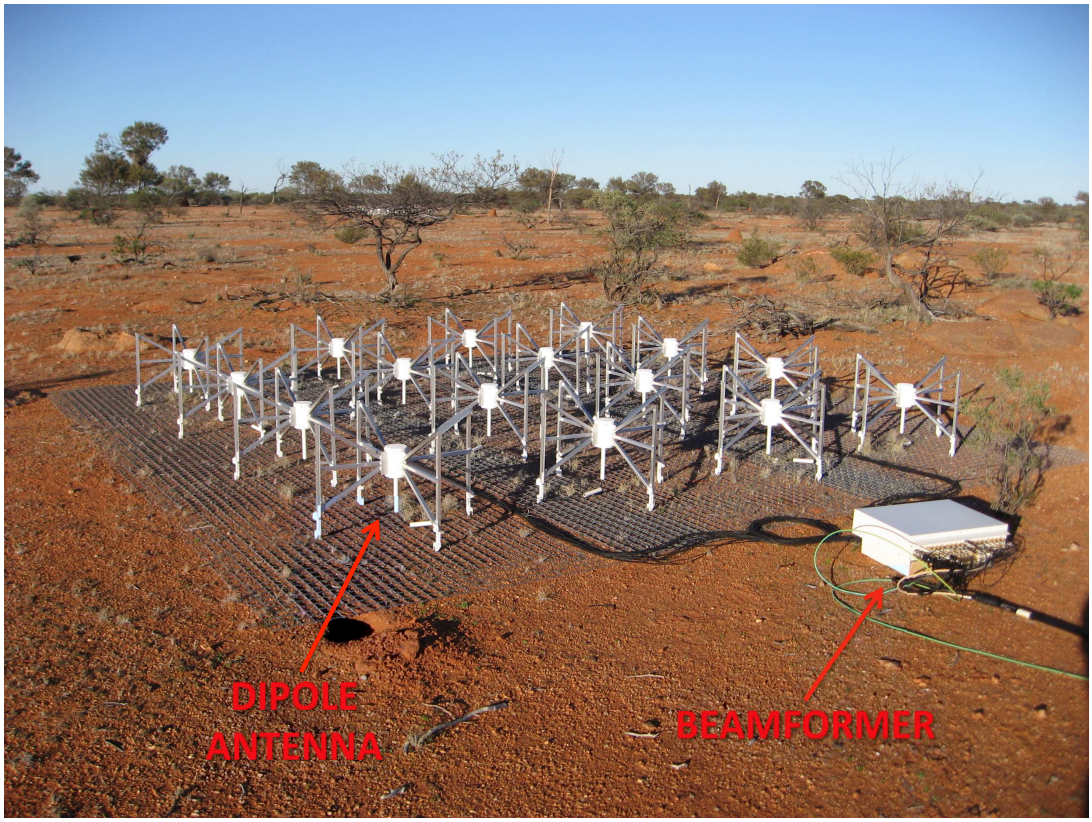

Figure 2-1: MWA Antenna Tile and Beamformer deployed at the MWA Site.

ground. A detailed discussion of the properties of the MWA antennas can be found in Chapter 3.

Groups of 16 antennas are laid out over a metal ground screen to form a tile. The ground screen is 5m $\times$ 5m, made of steel wire mesh with a 10 cm spacing. The dipoles are placed in a 4×4 grid, with a 1.1 m center-to-center distance. The signals from each polarization of each antenna on a single tile are fed over 32 coaxial cables into an analog beamformer located adjacent to the tile. In the beamformer, each incoming signal is first amplified and then passed through a set of analog delay lines. Each set of analog delay lines consists of five PCB traces, which differ by a factor of two in length. The shortest trace introduces a nominal time delay to the signal of 435 ps, up to a maximum delay of 13.5 ns (using all 5 delay lines in series). A set of digital switches is used to select whether a signal is passed through a particular delay

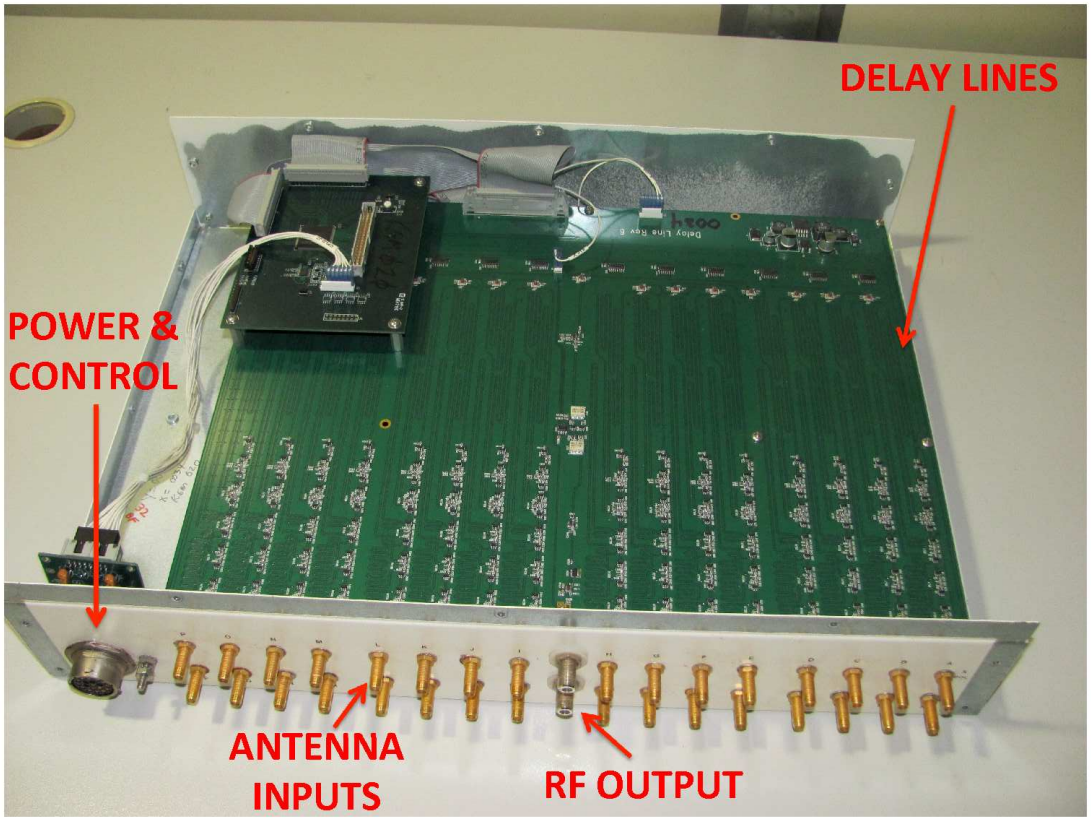

Figure 2-2: MWA Beamformer with cover removed. This beamformer is an "old style" beamformer which uses a twisted pair cable for power, and control functionality (seen on the left of the image). The new "DOC" interface combines this communication with the RF signal on the RG-6 cables. The 32 inputs (16 antennas, each with two polarizations), and 32 sets of delay lines are also visible and indicated in the figure. Photo Credit: David Emrich

line, or whether that delay line is bypassed (in this case the signal passes through an attenuator to mimic the added attenuation of the delay line). This combination of delays allows the antenna tile beam to be steered in $\sim 7^\circ$ increments down to a lower elevation limit of $\sim 20^\circ$. Steering to low elevations, or with finer beam centroid positioning is possible at the expense of a degraded beam shape. The signals from all antennas are summed separately for each polarization in a series of mixers, and output over a pair of RG-6 coaxial cables.

In the initial MWA-32T deployment, command and control communications for the MWA beamformer used a bundled twisted-pair cable which communicates with the MWA receiver module. However, midway through the MWA-32T campaign, excessive RF feedback was observed in the antenna tile system. This issue was traced to the Soriau connector used for this twisted-pair communications link. The beamformer design was modified to remove the twisted-pair communications link by implementing a Data-Over-Coax (DOC) communications scheme whereby the beamformer communications data is sent directly over the same RG-6 cables as the RF data stream. During the 32T campaign, 8 beamformers were replaced with the updated DOC design.

The MWA antenna tiles are arranged in a low-redundancy circular configuration, designed for good snapshot imaging performance, with an instantaneously filled uv-plane. The array layout uses a mixture of baseline lengths, with a minimum baseline of $\sim$ 6.5 m (corresponding to the antenna tiles nearly touching) and a maximum baseline of $\sim$ 350 m. This results in a point spread function size (full width at half maximum) of $18'$ at 150 MHz. The location of the antenna tiles relative to the fiducial array center is displayed in Figure 2-3.

2.3 Digital Receivers

The output RF spectrum from each antenna tile is digitized at a "receiver node". Each MWA receiver node services 8 tiles, using 16 parallel, independent data channels (8 tiles with two polarizations each). The receiver node performs three separate functions: analog signal conditioning, digitization and spectral filtering. The first stage is performed in the Analog Signal Conditioning (ASC) module. The ASC contains two sets of attenuators which are used to adjust the amplitude of the incoming signal. Each attenuator set allows up to 31 dB of attenuation, providing a total of up to 62 dB of attenuation. These levels can be adjusted separately for each channel in $\sim$1 dB increments. The ASC also contains a band-limiting filter, which removes

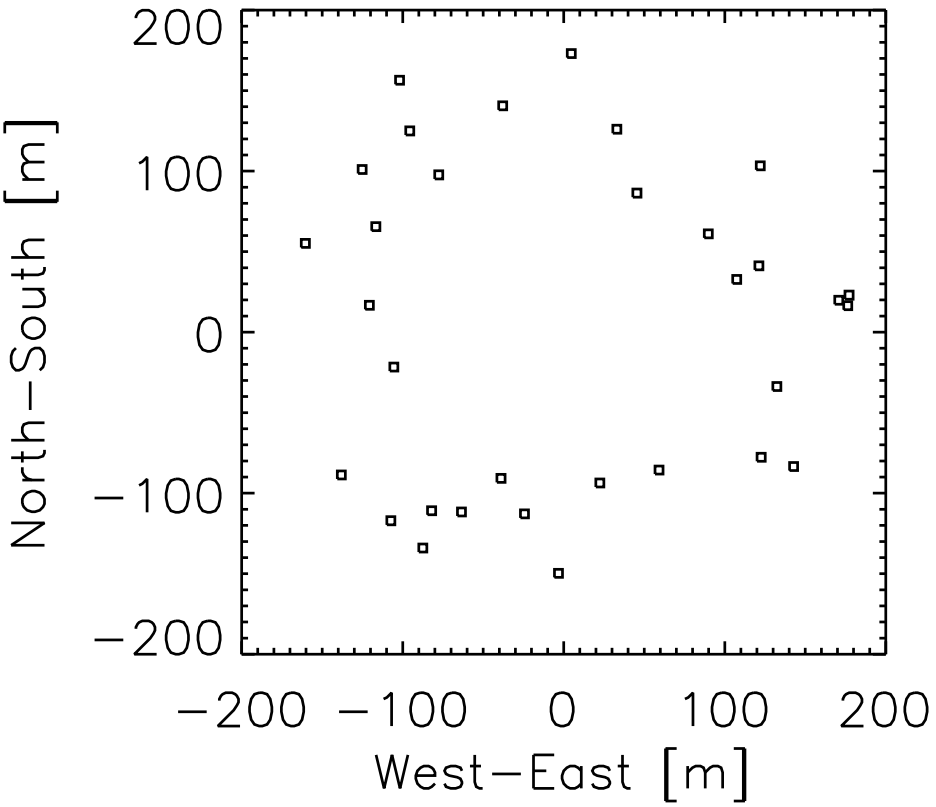

Figure 2-3: MWA 32T prototype antenna tile layout. The tiles are drawn to scale as 5×5 meter squares.

components outside of the MWA band in order to prevent aliasing when the signal is digitized.

The conditioned data are fed from the ASC into the Analog/Digital Filter Boards (ADFBs). Each ADFB processes signals from 4 antenna tiles. The ADFB boards each contain four dual 8-bit analog-to-digital converter (ADC) chips, operating at 655.36 MHz, which are used to digitize the incoming data streams at baseband. The resulting digital data stream contains frequency components between 0 MHz (DC) and 327.68 MHz, corresponding to sampling the 1st Nyquist zone. The data stream from each ADC is fed to a digital polyphase filterbank (PFB), implemented on a pair of Xilinx Virtex-4 Field Programmable Gate Arrays (FPGAs). The data are accumulated, and a weighted Fourier transform is performed to produce 256 "coarse" frequency channels, each 1.28 MHz wide. The effect of this coarse channelization can be seen in Figure 2-5. Due to data rate constraints, 24 of these coarse frequency channels are selected for further processing (a total bandwidth of 30.72 MHz). The values in each coarse channel are multiplied by an integer digital gain factor in order to normalize the levels across the channels.

The resulting set of 24 coarse channels are fed to the Aggregating, Formatting and Transmission (AgFo) module. Using a Xilinx Virtex-5 FPGA, the 24 coarse channels are split into three groups, each containing the data from 8 coarse channels for all antenna tiles and polarizations. Each group of data is then truncated to 5-bit words, packetized, and serialized using the RocketIO^{TM} multi-gigabit transceiver on the FPGA. The three groups of 8 coarse channels are transmitted via three separate optical fibers for further processing. The output data rate for each fiber is approximately 1.6 Gb per second (not including the encoding and packetization overhead).

The receiver nodes used in the MWA-32T array served as prototypes for the receivers that will be used in the full MWA array. The first 4 receivers, labeled Node 1 through Node 4, were designed to be mounted in an electronics rack in a climate controlled environment. This is distinct from the final MWA design, where the receivers are intended to be self-contained units deployed in the ambient environment. The initial receiver design also included a twisted-pair interface for communicating with

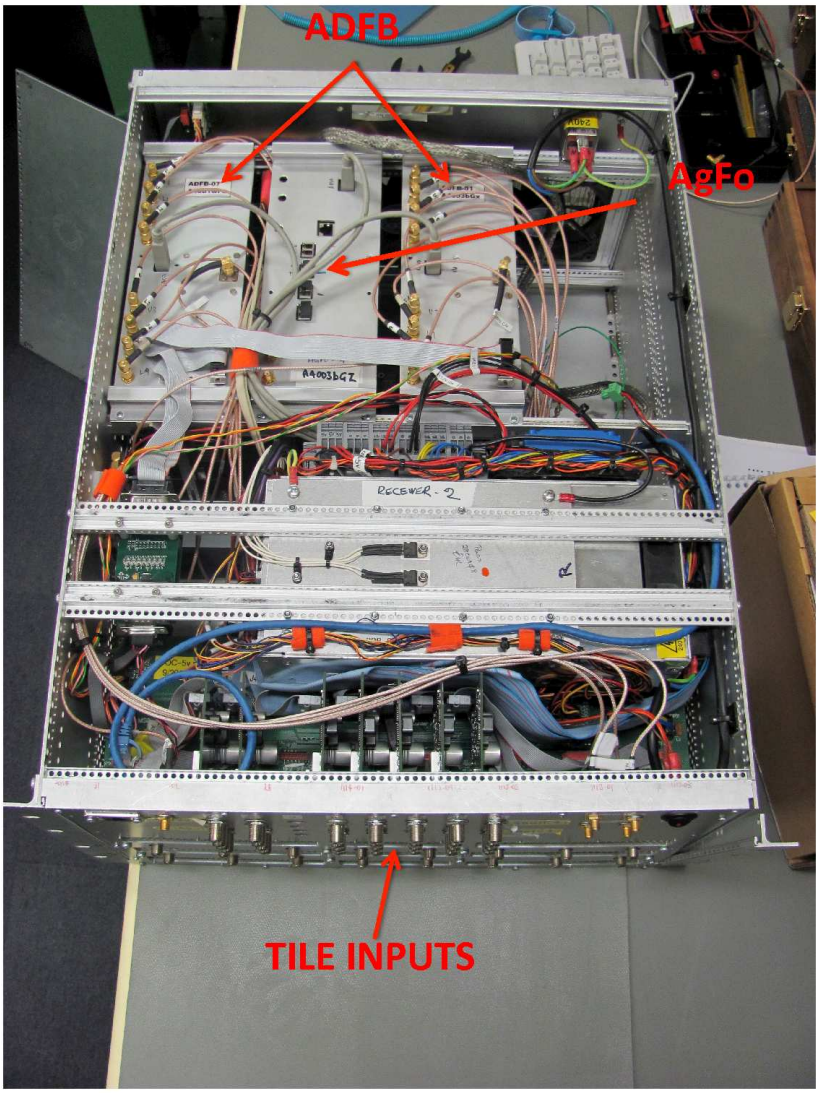

Figure 2-4: MWA Receiver (Node 2) with lid removed. This receiver is one of the 32T rack mounted receiver prototypes that has been converted to the DOC interface. The ADFB and AgFo modules are indicated on the diagram. The ASC and single board computer module are not visible. The fiber optic and VSIB outputs are on the rear of the unit, and are also not visible. Photo Credit: David Emrich

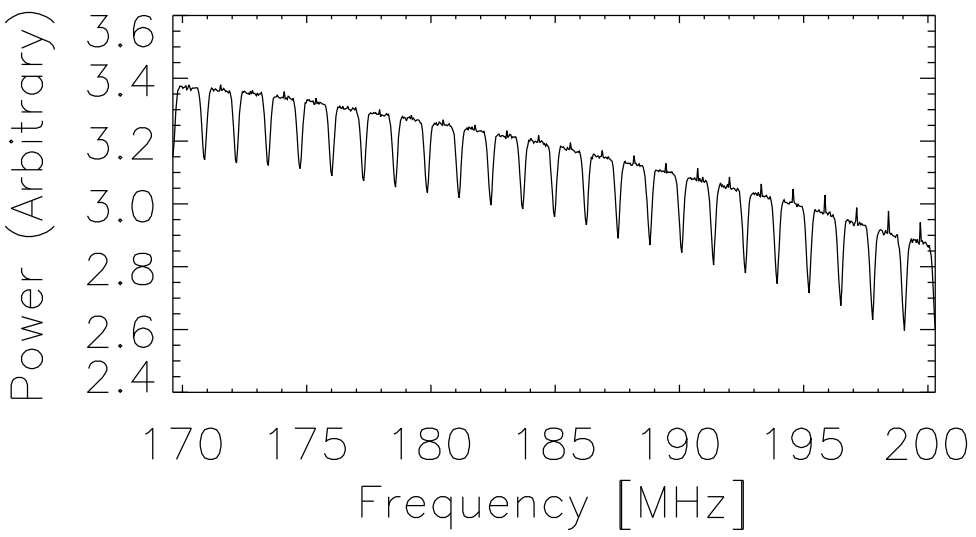

Figure 2-5: Raw autocorrelation spectrum from MWA Tile 1, captured from the output of the MWA correlator during an observation of Centaurus A on April 19th, 2011, with a central frequency of 186 MHz. The spectrum is plotted in arbitrary units of power on a linear scale. No correction for the MWA passband or gain has been applied. The modulation of the spectrum introduced by the 1.28 MHz wide coarse polyphase filter bank is evident in the overall spectral shape, as is a small "DC spike" at the center of each coarse channel due to a rounding issue in the MWA receivers.

the beamformers (as described in 2.2). Midway through the 32T campaign, Node 2 was retrofitted with the DOC interface in order to verify the updated design. These first 4 receivers also included a separate twisted-pair data (VSIB) interface which allowed data from a single coarse channel from each receiver to be transmitted to a data capture computer. A fifth receiver (labeled Node 10) was used as a prototype for the production version of the MWA receiver. This receiver revision had an environmentally controlled enclosure, so that it could be deployed outside, and used the DOC interface.

2.4 Correlator

The function of the correlator is to compute the cross-multiplication products of all input signals. The MWA-32T correlator uses an "FX" design in which the incoming

data stream is first filtered into fine spectral channels (F) before being cross-multiplied (X). The MWA correlator does not perform any phase or delay tracking (the correlator phase center is always at the zenith), however the integration time and frequency bandwidth of each sample is sufficiently small so that decorrelation away from the phase center is minimal.

The MWA-32T correlator design was based on an FPGA architecture using Xilinx Virtex-4 chips. The input data from the twelve optical fibers (three fibers from each of the four receivers) is first transmitted to the "fine" polyphase filterbank. The fine PFB performs an additional filtering on the incoming 24 coarse channels, which increases the frequency resolution to 10 kHz and produces 3072 output channels. The data are then transmitted over an ATCA backplane to a second set of FPGAs which perform the correlation. Each of the 64 input signals (32 tiles, 2 polarizations each) is cross multiplied with every other input, as well as itself, producing a total of 2016 cross-correlation and 64 auto-correlation products for each of the 10 kHz frequency channels.

Due to data rate constraints in the 32T system, groups of four 10 kHz channels are averaged together, reducing the output frequency resolution to 40 kHz, and are then integrated for 100 ms. Additionally, as a result of resource limitations in the correlator board, the system was operated at a 50% time duty cycle, discarding every other incoming sample. The data are packetized and output over four 1 Gb ethernet lines. In the 32T system, each of these 1 Gb data streams is captured by a separate Data Acquisition and Storage (DAS) computer, integrated for 1 s and then written to disk. The output data rate to disk is $\sim$ 700 MB per minute.

2.5 Monitor & Control

The numerous hardware components described in this chapter have a myriad of configurations and settings, which need to function in concert for the MWA system to produce useful scientific results. To accomplish this task, we have developed a Monitor and Control (M&C) system which manages the state of all of the MWA subsystems.

The M&C system is based around a PostgreSQL database, which stores the settings of each MWA component, so that the current and full historical state of every piece of hardware can be constructed. Observations are scheduled by entering a desired system state into the database for a future time. A system of daemons then change hardware settings based on discrepancies between the desired system state and the reported system state. This system allows for relatively autonomous operation of the MWA system. A web-based interface is used for an observer to monitor the system operations.

2.6 Summary

The architecture of the MWA represents a shift from traditional radio telescope design, with a large number of elements and early digitization. This represents an evolution in the techniques of low-frequency radio astronomy, leveraging the advances in technology and computation that have arisen in the past several years. The wide bandwidth, large number of elements and digital processing will enable the new capabilities which make high fidelity measurements of the EoR a realizable possibility.

THIS PAGE INTENTIONALLY LEFT BLANK

Chapter 3

The MWA Primary Beam

3.1 Introduction

The "primary beam" of a radio interferometer, such as the MWA, defines the sensitivity of the telescope as a function of direction on the sky, effectively setting the field of view that can be imaged. The shape of the primary beam comes from the power pattern of the collecting elements of the array, namely the antenna tiles for the case of the MWA. For a wide field-of-view instrument, such as the MWA, an accurate characterization of the primary beam of the instrument is crucial for its scientific performance. An inaccurate beam model can introduce errors during the calibration of complex fields, and will lead to position dependent flux scale biases in the resultant maps. In order to assess the primary beam performance of the MWA we undertook a campaign of numerical simulation and laboratory measurements in order to characterize the MWA antenna tiles.

3.2 Anechoic Chamber Measurements

3.2.1 MIT Lincoln Lab Anechoic Chamber

Prior to the first field deployment of the MWA-32T prototype, we conducted laboratory measurements of MWA antennas for performance verification purposes. The

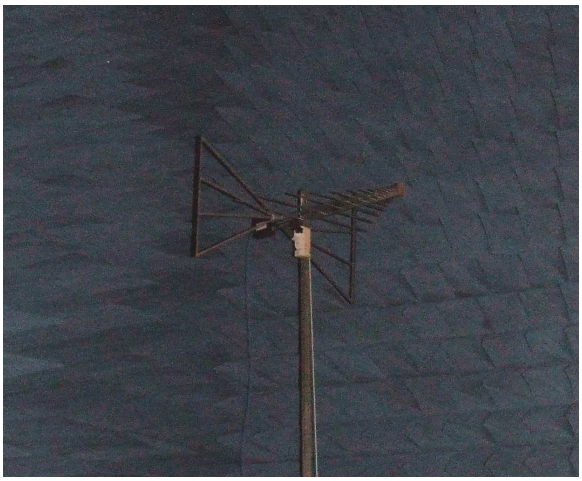

Figure 3-1: Photograph of the yagi-bowtie type transmitting antenna used in the Lincoln Lab System Test Chamber

tests were performed at the MIT Lincoln Lab System Test Chamber. This chamber is a 60 foot long by 40 foot wide by 30 foot tall EMI shielded anechoic chamber. The specified operating range is between 150 MHz and 20 GHz, although Lincoln Lab personnel report the chamber has been successfully operated down to 90 MHz. The internal surfaces of the chamber are covered with 48-inch pyramidal absorber made of polyurethane foam (Cuming Microwave CRAM-SFC), with an estimated reflectivity of -28 dB at 120 MHz and -30 dB at 300 MHz for normal incidence radiation. The reflectivity rises to roughly -13 dB and -25 dB respectively for an incident angle of 45 degrees from normal and to -5.6 dB and -13 dB respectively for an incident angle of 70 degrees from normal.

An antenna "positioner" located in the test chamber allowed an antenna mounted on it to be rotated about a vertical axis. A yagi-bowtie type transmitting antenna (see Figure 3-1) was located on a height-adjustable pole in the opposite corner of the chamber from the positioner, and was used in the testing. The height of the transmitter was set to be aligned with the center of an MWA antenna tile mounted vertically on the positioner, corresponding to a height of 4.0 ± 0.1 m ($\sim$ 13 feet). The distance from the pole supporting the transmitter antenna to the antenna positioner was 10.0 ± 0.2 m ($\sim$ 39 feet).

3.2.2 The RF Test System

The RF measurements in the chamber were conducted with a Hewlett-Packard 85301 Antenna Measurement System (with a Hewlett-Packard 8530 receiver). This system included all the components necessary to control the test system, including a controller and encoder for the antenna positioner. This allowed accurate rotation of the antenna tile as well as an RF source, local oscillator, mixer and receiver. These components were combined into an integrated system controlled by a computer.

3.2.3 The Antenna Tile Layout and Mounting

In order to test the properties of a complete MWA antenna tile in the anechoic chamber, a duplicate set of dipoles and electronics as used in the initial MWA 32T deployment effort was procured for use in the Boston area. Since it was not feasible to assemble an additional prototype beamformer, one of the three beamformers used in the field for the MWA early Deployment effort was returned to MIT for use in the tests.

Because the test system required a vertical mounting of the antenna tile, a wooden frame was constructed to provide structural support for the antenna tile. The frame was constructed out of 2 X 4 lumber in a square 16' 6" (5.029 m) on a side. The frame was covered with 16 4-foot by 4-foot, 1/8-inch thick aluminum panels, leaving 6 inches of the frame uncovered on the top and left edge (see Figure 3-2). To ensure the conductivity of the ground plane, the joints between the panels were covered with electrically-conductive copper tape.

In order to mount the dipoles on this solid ground screen, holes were drilled through the aluminum panels, allowing the use of cable ties to secure the feet of the dipoles, and allowing the coaxial cables from each dipole to pass through to the rear of the ground screen. Holes were drilled at the geometric center of the screen for the characterization of a single, isolated antenna, and at the 16 antenna positions constituting a full MWA tile. These were calculated from the center of the tile using

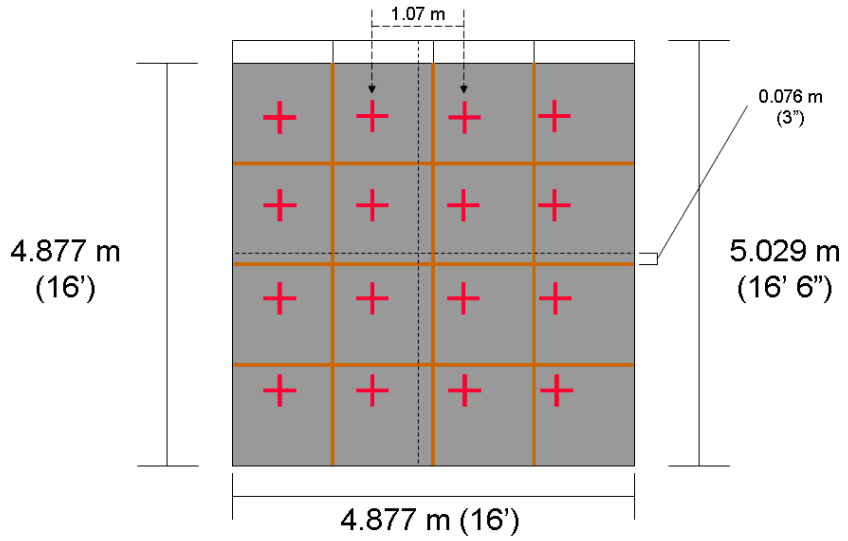

Figure 3-2: Diagram of the ground screen used for the Lincoln Lab tests. The red crosses represent the locations of the 16 dipoles in the full tile. Note that the center of this layout is offset from the actual center of the tile

a 1.07 meter spacing (note that a spacing of 1.10 meters was used in the tiles deployed in the field).

Due to logistical difficulties encountered while moving the ground screen into the anechoic chamber, a 6-inch section on the side of the wooden frame not covered by aluminum panels was removed. In addition, another 6-inch section un-paneled section of the wooden frame was left uncovered so that the tile could be more easily suspended from the crane in the anechoic chamber. These changes resulted in final dimensions for the ground screen of 16 feet by 16 feet (4.877 meters by 4.877 meters) with the layout of the antenna tile offset from the center of the groundscreen by 3 inches (0.076 meters). The final layout of the tile is illustrated in Figure 3-2.

The tile was hung vertically from a crane on the ceiling of the chamber, with the bottom edge of the tile attached to the antenna positioner. The positioner was calibrated (approximately) so that 0° azimuth corresponded to the transmitter being at an effective zenith angle of 0°, or in other words, so that the normal to the ground screen was pointing toward the transmitter. The azimuth was typically scanned from

-90° to $+90^\circ$, with clockwise rotation of the tile corresponding to an increase in azimuth.

3.2.4 Test Setup

The general methodology of the antenna tests was to measure different slices through the antenna or tile beam at multiple frequencies. In order to do this, the test system was configured to scan the positioner from -90° to $+90^\circ$. During this scan the transmitting antenna and receiver were configured to transmit and receive, switching frequency from 80 MHz to 300 MHz in 5 MHz increments, for a total of 45 separate frequencies. The test system was set up so that the antenna positioner rotated continuously, and within each 1° of rotation each of the 45 frequencies were measured. The rotation angle of the positioner at the time of each frequency sample was determined by an encoder. Each measurement consisted of an average of 64 samples. This technique allowed the measurements to be conducted quickly, as it did not require repeated stopping and starting of the positioner.

This setup allowed the characterization of two different cuts through the antenna patterns. Attaching the receiver to the bowtie arms oriented vertically (parallel to the axis of the positioner rotation) provided a cut through the H-plane of the vertical dipole arms, perpendicular to their electrical axes. Measuring the horizontally aligned bowtie arms provided a cut through the E-plane of the arms. The transmitting antenna was on a mount that allowed it to rotate 90°, effectively changing the polarization of the transmitted wave. Measurements were made in both transmitter configurations so that both the co-polarization and cross-polarization response of each cut were recorded.

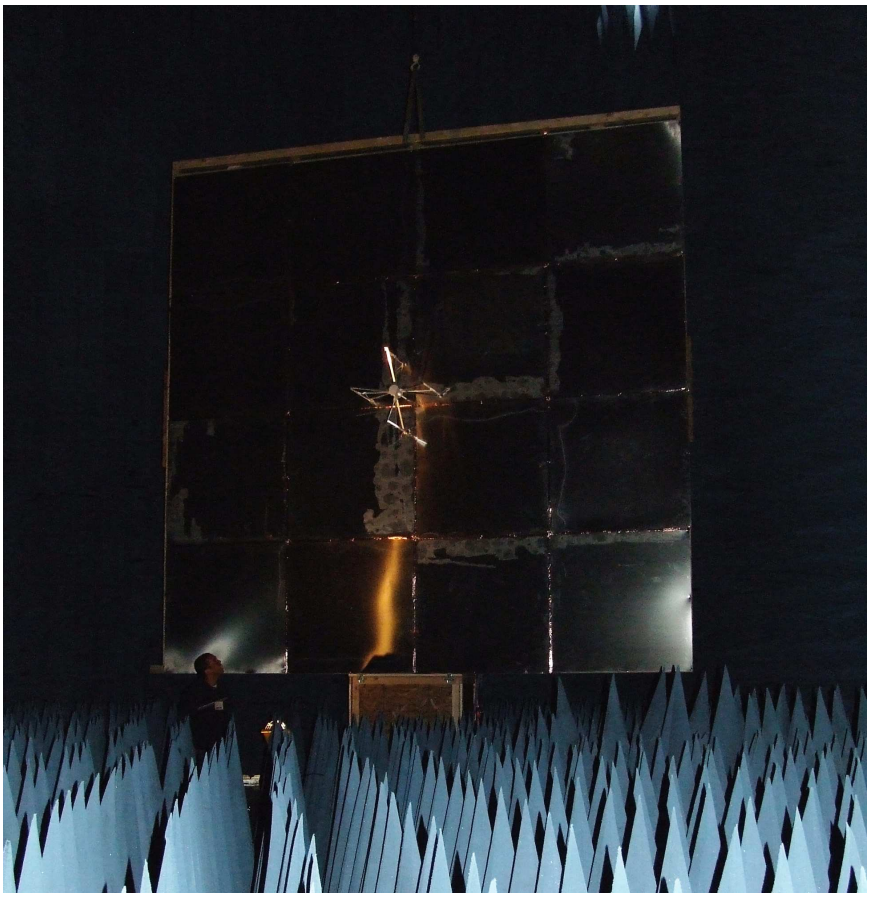

Figure 3-3: Photo of a single dipole mounted at the center of the ground screen.

3.3 Single Dipole Characterization

3.3.1 Single Dipole at Center of Ground Screen

In order to characterize the performance of the individual dipole antennas, a single dipole was attached to the ground screen at the position of the pre-marked center (NOTE: this position differs from the exact geometric center of the final ground screen; see Section 3.2.3 for a description of the precise layout of the tile). Dipole #14 was chosen for this first test. Several beam pattern measurements were initially taken to confirm the functionality of the system. At this point it was noticed that the reciever system was saturating at high transmitter powers (see Section 3.5.2 for a further discussion of the saturation issues encountered). The transmitter power was reduced to a level where this saturation effect was no longer present.

Scans were taken of each polarization of the receiving antenna; then the transmitter was rotated by 90 degrees and and the scans of each polarization were repeated. This correspond to measurements of both co-polarization and cross-polarization response in the E-plane and H-plane of the dipole pattern.

3.3.2 Single Dipole Rotations at Center of Ground Screen

A fiberglass loop was attached to the base of Dipole #13 so that the dipole could be rotated to an arbitrary angle, allowing cuts to be taken through the dipole beam pattern at angles intermediate to the E and H planes. This dipole was then secured at the center position (as noted before, this is not the exact geometric center) of the ground screen, and measurements were taken of the standard E and H plane cuts to confirm consistency with the previous mesurements taken with Dipole # 14 and to gain some understanding of the intrinsic variations between the different antennas. The dipole was then rotated in 15 degree increments and cuts were taken of the beam pattern.

Due to time constraints, full cuts were not taken at each of the intermediate angles, and instead the antenna was rotated only from -90° to 0° and the frequency resolution was decreased to make a measurement every 10 MHz instead of 5 MHz for the previous cuts. Furthermore these measurements were only taken with the transmitter in the horizontal polarization configuration, though both receiving polarizations were measured. This compressed set of measurements would provide the necessary information needed to characterize the intermediate angle cuts through the dipole beam pattern by exploiting the assumed symmetry of the dipole pattern.

3.3.3 Single Dipoles in the Full Tile Configuration

Following the previous single dipole measurements the tile was populated with the full 16 dipoles in their positions as described in Section 3.2.3. Each individually numbered dipole was placed at its respective position as shown in Figure 3-5. The cables from each of the antennas were connected to the Early Deployment type beamformer

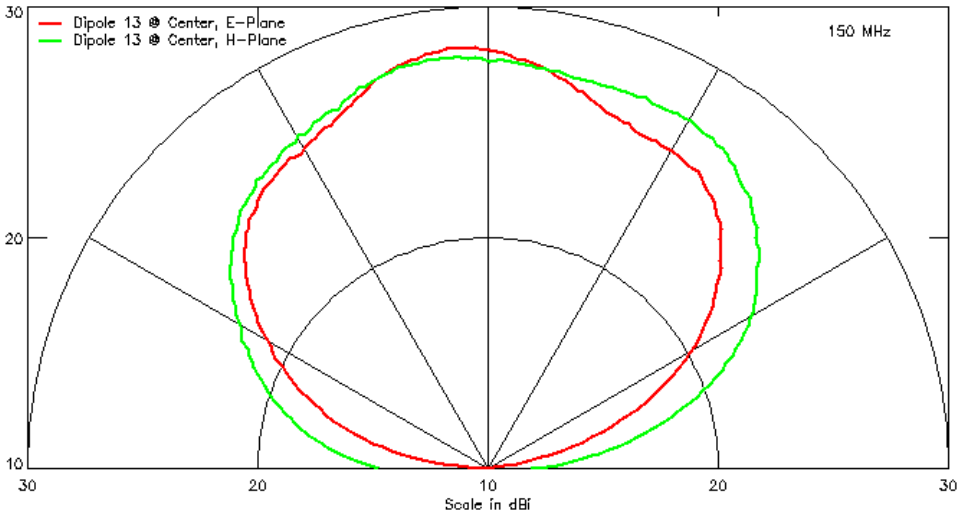

(a)

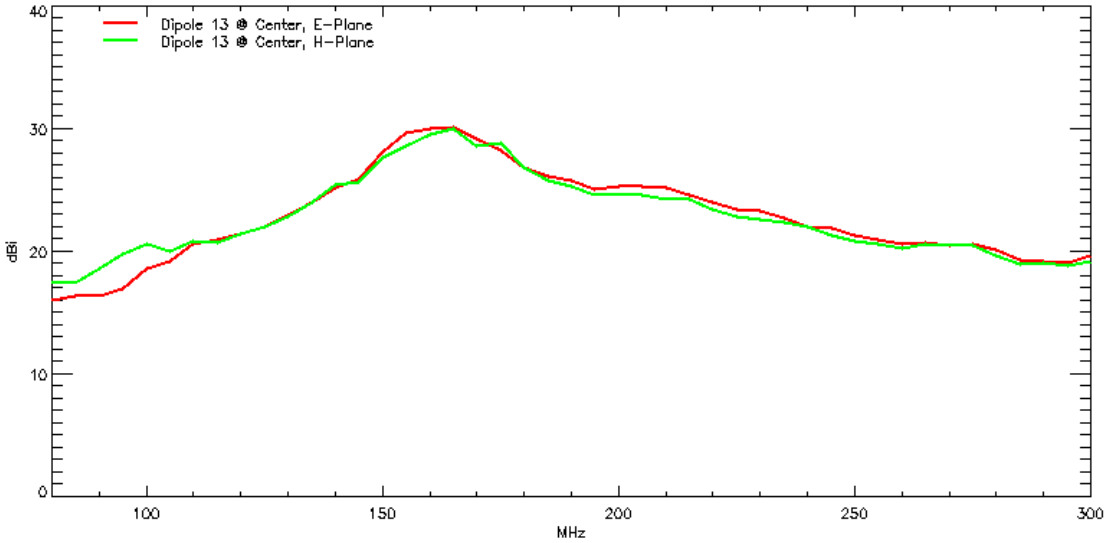

(b)

Figure 3-4: Example beam patterns from a single dipole - Dipole #13 mounted at the center of the tile showing the E-plane and H-plane co-polarization (a) power response for all zenith angles at 150 MHz and (b) bandpass at zenith.

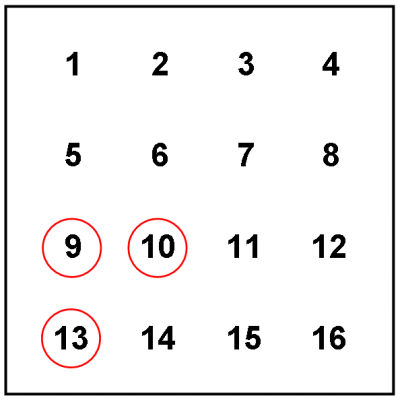

Figure 3-5: Schematic of the tile numbering scheme. The point of view is facing towards the front of the tile. The dipoles are numbered in ascending order starting at the top left corner. The three unique dipole positions that were measured are circled.

mounted in a box beneath the antenna tile. Although each of the dipoles was individually tested for properly soldered LNAs and for the correct marking of which coaxial cable corresponded to which polarization prior to mounting, the dipoles were again tested individually to insure their proper orientation and functionality before combining their signals to get the full tile response. This test was conducted by using the beamformer to disable all dipoles except for the desired dipole and then taking a single measurement with the tile at an angle of 0° (normal incidence), essentially giving a bandpass of each individual dipole. This was done for each transmitter and receiver polarization combination.

The antenna tile layout contains three unique antenna locations (assuming the basic symmetries of the layout hold), one of the central dipoles, one of the corner dipoles and one of the middle dipoles on the edge. Theoretically, by measuring the radiation patterns of each of these unique dipoles and applying the necessary reflections the different radiation patterns of each individual dipole in the tile can be modeled. Three dipoles were selected, #9, #10, and #13 and a full cut from $-90°$ to $+90°$ in 5 MHz increments was taken of each of these antennas. In addition, several scans were taken of Diploe #8 for a consistency check.

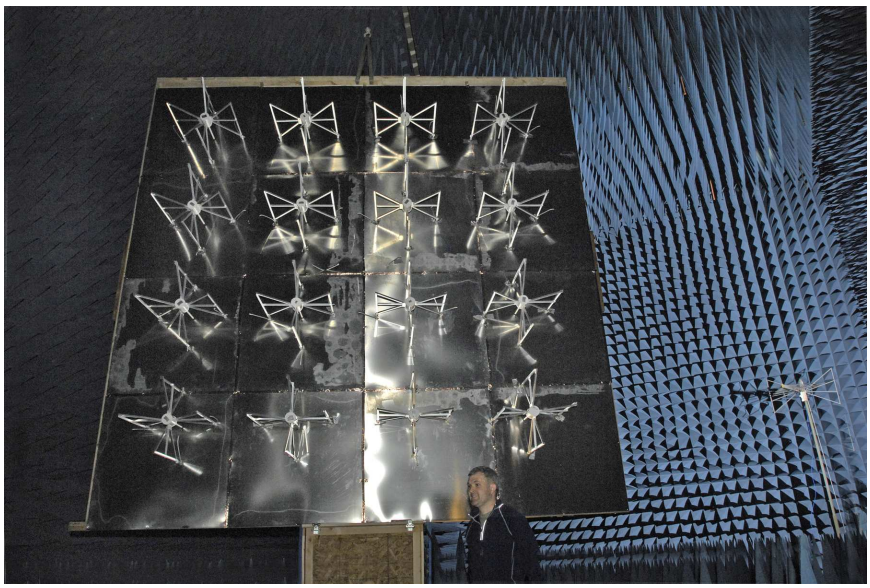

Figure 3-6: Photo of the full 16 dipoles mounted on the ground screen. The transmitting antenna can also be seen at the right of the image.

3.4 MWA Tile Characterization

3.4.1 Full Tile Phased to Zenith

After completion of the single tile antenna tests, all of the antennas were connected and enabled through the beamformer. For these tests, the cables from the dipoles were fed behind the ground screen through through holes drilled in the aluminum panels. The beamformer control program was then used to set the dipoles to be phased towards the zenith (i.e. directly away from the ground screen). It was noted that these full tile measurements were even more strongly affected by the saturation effects noted in Section 3.5.2. Consequently a 20 dB attenuator was inserted into the signal path between the beamformer and the Lincoln Lab receiver. This was deemed preferrable to simply decreasing the transmitter power, as the beam patterns were much noisier when the transmitter power was low enough for the output to be below the threshold for the nolinearity to be present. Several cuts of both the E and H planes were taken with the tile phased towards the zenith.

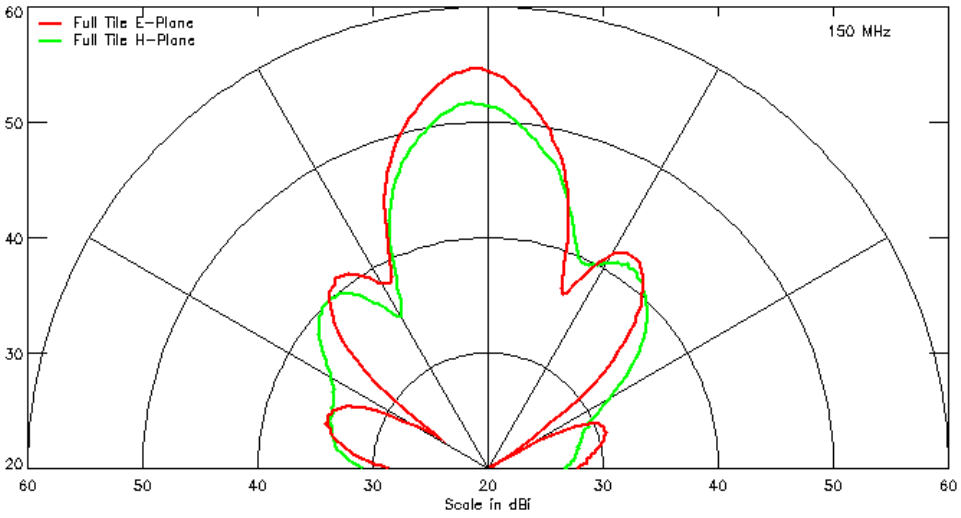

(a)

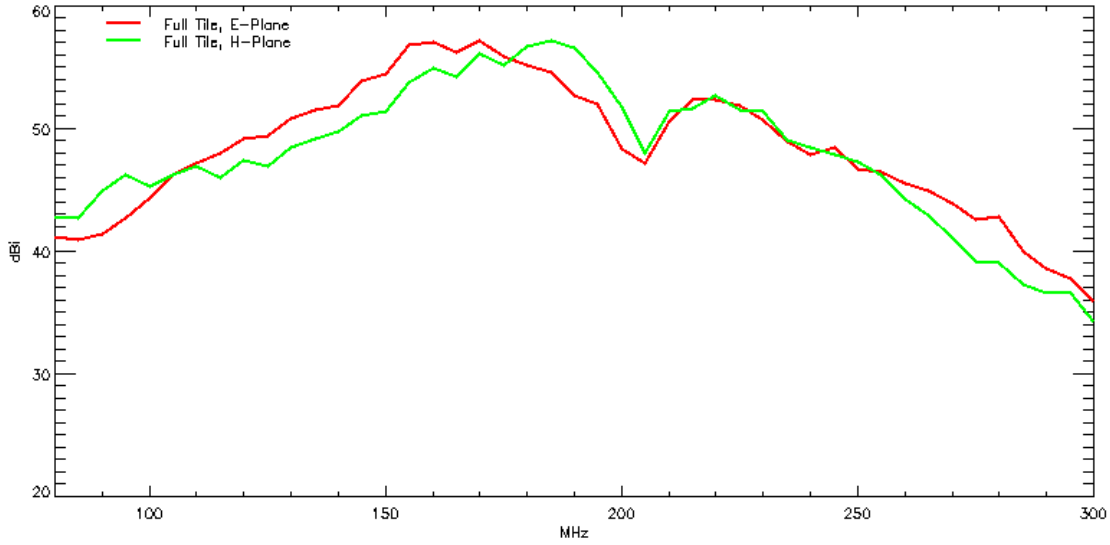

(b)

Figure 3-7: Example beam patterns from the full antenna tile showing both the E-pland and H-plane co-polarization (a) power response for all zenith angles at 150 MHz and (b) bandpass at zenith. A notch in the full tile bandpass is evident at $\sim$ 205 MHz.

3.4.2 Full Tile Phased Off Zenith

The beamformer was used to electronically steer the tile beam to several locations to characterize the dipole beam off zenith. The beamformer was used to steer the tile beam to zenith angles of 20° and 45°. The azimuth control of the beamformer was then used to steer to azimuths of 0° and 270° corresponding to off axis in the plane of rotation of the tile (in the direction "ahead" of the tile rotation) and perpendicular to the plane of rotation of the tile (towards the ceiling of the anechoic chamber).

3.4.3 Cables In Front of Ground Screen

In order to estimate the effects of running the cables above the ground screen (rather than below the ground screen in the ideal case), the coaxial cables from the dipoles were fed back through to the front of the tile and roughly secured to the front of the ground screen with duct tape. Measurements were then repeated in this configuration with the tile phased to zenith as well as the various steered configurations. Due to time constraints a full set of measurements at all polarizations was only conducted with the tile phased to zenith.

3.4.4 Calibration of the RF System

Following the completion of the MWA antenna tile tests, the Lincoln Laboratory personnel performed an absolute calibration of the RF system using a receiving antenna of known response. Since the chamber and the RF system were known to exhibit little time-variability in the their properties (as was confirmed by repeating some of our measurements on different days), this calibration is assumed to be valid for the duration of the tests. Calibration measurements were taken with the normal test setup and also with the same 20 dB attenuator inserted into the signal path that was used in the full tile measurements. This calibration was applied to the data and all results shown in this report.

An additional effect that needs to be considered in the analysis of these data is that the polarization purity of the transmitting antenna is not known. Combined with

any inherent imprecision in the vertical alignment of the transmitter and the dipoles on the tile, this introduces a potentially large uncertainty into the interpretation of the cross-polarization measurements.

3.5 Results

3.5.1 Asymmetry of the Beam Patterns

Many of the observed beam patterns which should theoretically be symmetric about a zenith angle of 0° (for example, a single dipole at the center of the ground screen) instead appear asymmetrical. This asymmetry may airse from several factors. A careful alignment of the antenna tile was not done, so a 0° reading from the positioner may not exactly correspond to the transmitter being at the antenna tile zenith. In addition, the potential offset of the dipoles on the ground screen (described in Section 3.2.3) may introduce an asymmetry to the beam shape (preliminary simulation results do show asymmetry introduced by an offset from the center of the ground screen, but not to the degree seen in the data). A final possible cause of this asymmetry is the anechoic chamber. The chamber and its absorber are not rated down to these frequencies, and it is possible that reflections or other effects can impact the recorded patterns. These potential sources of error need to be considered during the analysis of this data.

3.5.2 Saturation of the RF System

During the course of the testing, it was noticed that when a high power signal was received, the receiving electronics system saturated and entered a regime of non-linearity. This effect was especially worrisome because it artificially enhanced the observed received power, leading to artificially narrow beam patterns without giving any warning or indication of a malfunction in the system. An example of this effect is shown in Figure 3-8. To detect and eliminate this saturation the power level of the transmitting antenna was varied until changing the transmitter power had no effect

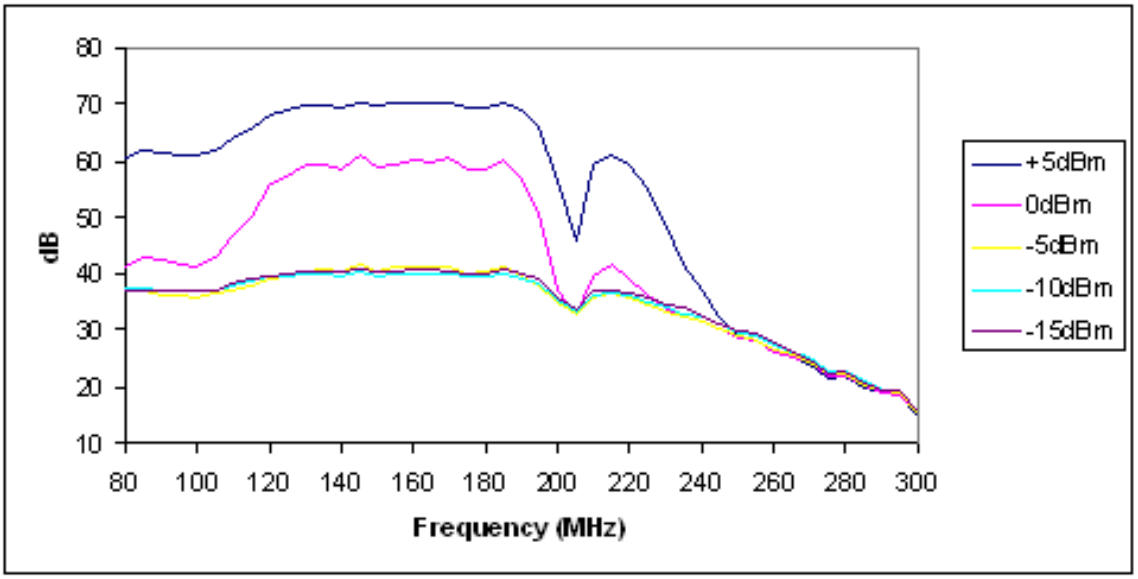

Figure 3-8: Plot of several bandpasses taken at varying levels of transmitter power illustrating the nonlinearity caused by saturation. At transmitter powers of -5 dBm and lower the bandpasses are identical. When the power is raised above -5 dBm the receiver gives artificially large power values.

on the beam pattern shape (this is expected because the beam pattern measurement is a measure of input power divided by received power, so one expects this to stay constant independent of input power). This test was performed with the tile pointed at zenith (and hence receiving the maximal amount of power) to ensure that the power received during a scan would always remain in the saturation free regime. In addition, several beam patterns were recorded at varying transmitter power levels so that if it becomes evident that this saturation effect is present in the data it will be possible to derive corrections for this nonlinearity.

During the testing of the full tile with the beamformer present in the signal path, the extra amplification again caused the system to go into the nonlinear regime even at very low transmitter power levels to the point that further decreasing the transmitter power markedly increased the noise present in the beam patterns. As discussed in Section 3.4.1, a 20 dB attenuator was added between the output of the beamformer and the input to the receiver to prevent the system from entering the nonlinear regime

while still maintaining a high enough transmitter power to prevent excess noise in the beam pattern.

3.5.3 Bandbass Notch

One of the most striking features of the MWA tile bandshape is the "notch" at approximately 205 MHz. This can be clearly seen in Figure 3-7. Rogers (2007) identified this feature as resulting from interactions between the vertical elements of the bowtie dipoles. This was confirmed with numerical modeling (see Section 3.6). This bandshape notch results in decreased zenith gain, and increased gain towards the horizon at these frequencies. This undesirable, as it adds a relatively sharp spectral feature to the instrumental response in a frequency range that is important for EoR science. The sharpness of this feature can lead to difficulties in calibration and the corresponding increase in horizon gain will increase the susceptibility to terrestrial RFI. As a result of the identification of this feature, the MWA antennas were redesigned, resulting in the "short-wide" design described in Chapter 2. In this redesign, the height of the dipoles was reduced and the width of the dipoles was increased. This decreased the strength of the resonance and moved it to a higher frequency, ~ 240 MHz, where RFI from satellites precludes observing.

3.6 Beam Modeling and Simulation

3.6.1 Introduction

The anechoic chamber measurements serve as a useful test of the MWA tiles, and identified important deficiencies in the design. However, the measurements were limited to several one-dimensional slices through the antenna and tile beam patterns, and contained several systematic effects (discussed above). In order to use the primary beam measurements during analysis of MWA data, a full spatial and spectral description of the patterns is necessary. In order to accomplish this, we developed

a suite of models which describe the MWA primary beam. The MWA Lincoln Lab results described above serve as an important verification of these models.

3.6.2 Analytic Short Dipole

As a simple analytic model, we first approximate the MWA bowtie antennas as electrically short dipole antennas. Electrically short dipoles have a simple analytic form for their response pattern:

$$V(\alpha, \beta) \propto \sin(\alpha), \tag{3.1}$$

where α is the angle from the axis of the dipole, β is the toroidal angle around the axis of the dipole, and $V(\alpha, \beta)$ is the complex voltage response of the antenna to an incoming electromagnetic wave (this analysis ignores any overall gain factors, and only determines the relative angular response). For the case of the MWA antennas, the antenna orientation is such that the dipole axis is parallel to the ground, and perpendicular to the zenith direction. Transforming to a more convenient astronomical coordinate system where θ is the zenith angle and ϕ is the azimuth, the voltage pattern becomes:

$$V(\theta, \phi) \propto \sqrt{1 - \sin^2(\theta)\cos^2(\phi)}, \tag{3.2}$$

for a dipole which has its electrical axis aligned at an azimuth of zero, and perpendicular to the zenith. The MWA dipoles are situated above a conductive ground screen, which, for this analytic model, we approximate as an infinite conducting sheet. This modifies the angular response of the voltage pattern:

$$V(\theta, \phi) \propto \sqrt{1 - \sin^2(\theta)\cos^2(\phi)}(1 - e^{4\pi i h \cos(\theta)/\lambda}), \tag{3.3}$$

where h is the height of the dipole antenna above the ground, and λ is the wavelength of the radiation. This serves as a basic analytic model for an MWA antenna. As it is only valid when the antenna is electrically short, it should be a better approximation at low frequencies.

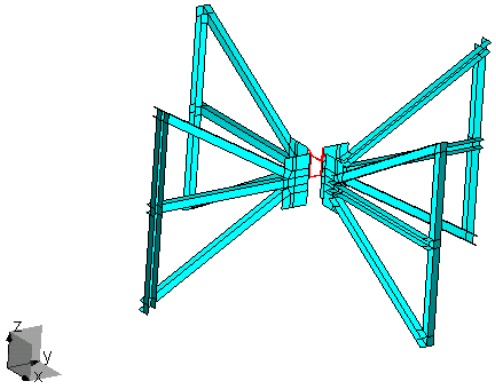

Figure 3-9: WIPL-D model of a MWA "short-wide" dipole antenna

3.6.3 Numerical Models

Numerical models of the MWA antennas were also constructed using the WIPL-D Pro v4.1 electromagnetic modeling software[1]. This software uses the "Method of Moments" (MOM, see, e.g. Harrington 1993) to compute the far-field radiation patterns of the antennas. This method involves solving a boundary value problem for Maxwell's equations given a set of excitations and metal wire and plate elements. We constructed a model for the "old style" dipoles to compare with the Lincoln Lab test results as well as a new "short-wide" dipole to model the performance of the deployed antennas. An example WIPL-D model of the "short-wide" antenna is shown in Figure 3-9. These models were evaluated both in isolation as well as in a tile configuration with zero additional delay between the elements. Rogers & Williams (2008) additionally ran simulations of MWA antennas using the Numerical Electromagnetics Code (NEC, Burke & Poggio 1981). They found that the simulated results from WIPL-D and NEC (version 2 and version 4) had a maximum difference of -26 dB, implying strong consistency between the numerical modeling packages for the case of the MWA antennas.

In addition to the single dipole WIPL-D models, we also constructed a WIPL-D model of a full tile phased to the zenith. This model included sixteen dipoles, located

[1]http://www.wilp-d.com

above a finite 5 meter by 5 meter ground plane. The dipoles were simulated with zero delay between the elements to replicate the a zenith observation. These models were used for the verification of the tile performance, however, due to the running time of these simulations, the analytic prescription for the beamformer described in section 3.6.4 was used for generating patterns for arbitrary beam pointings.

3.6.4 Tile and Beamformer Model

In order to combine MWA single element patterns to form a tile beam pattern, a model of the tile and beamformer system is also needed. The relative locations of the antennas introduce a direction-dependent time delay for each of the antennas, and the beamformer can additionally add further delays to individual signal paths. We developed software to model this process. The nominal MWA antenna tile positions are first used to calculate the phase offset for each dipole in the tile. The settings of the beamformer are then used to apply additional gain and delay corrections to each signal. Measurements of the properties of the individual beamformer delay lines (Kratzenberg 2010, private communication) are used to derive an amplitude change and time delay for each delay line which is used for a particular beamformer setting. These complex gains are then multiplied by a single element pattern before being combined to form a full tile pattern. This code is used to form models for tiles using analytic short dipoles as well as for tiles with single dipole patterns derived from the WIPL-D simulations. This model also has the capability of using different single element patterns for different dipoles in the tile. This allows mutual coupling effects between the elements to be accounted for.

3.6.5 Comparison to Lincoln Lab Data

Comparisons of the analytic short dipole, WIPL-D simulations and Lincoln Lab measurements for a single dipole in both the E and H planes are shown in Figure 3-10. These plots have all been set to the same normalization by fitting a scale factor to minimize the variance in the 45° diameter region near the zenith. These comparisons

Table 3.1. Single Dipole Comparison

Frequency	Plane	Short Dipole		Numerical WIPL-D	
		$\Delta_{22.5^\circ}$	Δ_{45°	$\Delta_{22.5^\circ}$	Δ_{45°
100 MHz	E	0.59	0.63	0.66	0.90
100 MHz	H	0.24	1.57	0.15	0.67
140 MHz	E	0.56	3.11	0.54	3.31
140 MHz	H	0.43	0.96	0.36	0.65
180 MHz	E	0.70	1.79	0.62	1.07
180 MHz	H	0.24	1.03	0.21	0.97

Note. — Δ_n is defined as the maximum gain deviation in decibels within n degrees of the zenith between the Lincoln Lab measurements and the specified model

were performed at 100 MHz, 140 MHz and 180 MHz in order to assess the agreement in a regime that is particularly important for EoR science. Deviations between the Lincoln Lab measurement and the models within several regions are quantified in Table 3.1. The overall agreement between the models is quite good, with maximal power deviations within 22.5° of the zenith of less than 10%. The analytic short dipole and WIPL-D model appear to have comparable agreement, with the WIPL-D model having slightly better agreement in the H plane. However it is important to note that the Lincoln Lab measurements may include systematic errors and offsets which will distort the quantitative assessment of these comparisons.

Similarly, comparisons for the full tile patterns are shown in Figure 3-11, and quantified in Table 3.2. These plots have been scaled to minimize the deviation between the Lincoln Lab measurements and the models within a 15° radius of the zenith. The agreement between both models and the Lincoln Lab measurements is better than 17% within this 15° zenith radius. However, it does appear that the measured Lincoln Lab patterns are systematically narrower than either of the simulations. Additionally, there seems to be a large variation between the Lincoln Lab measurements and the models in both the depth of the sidelobes and the nulls.

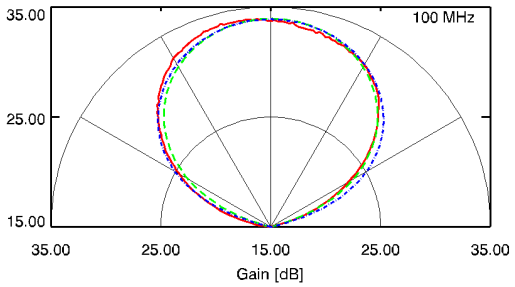

(a) 100 MHz, E-plane

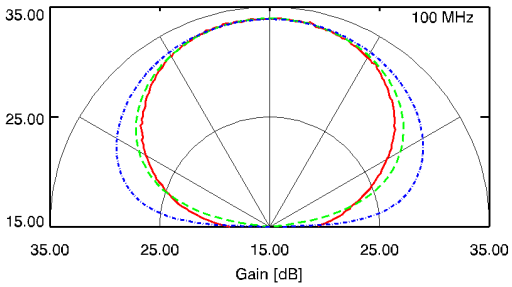

(b) 100 MHz, H-plane

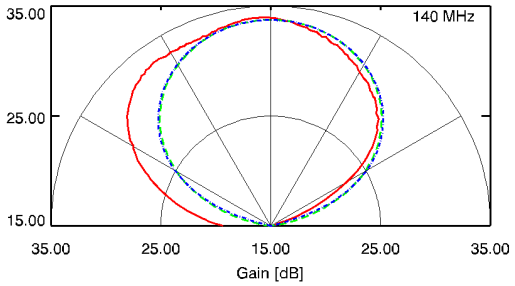

(c) 140 MHz, E-plane

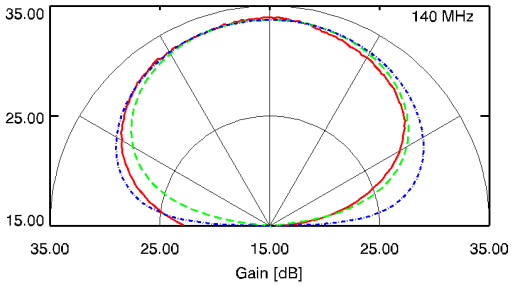

(d) 140 MHz, H-plane

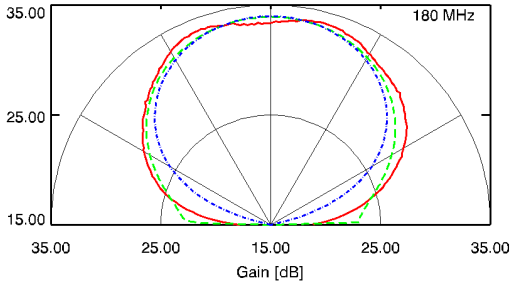

(e) 180 MHz, E-plane

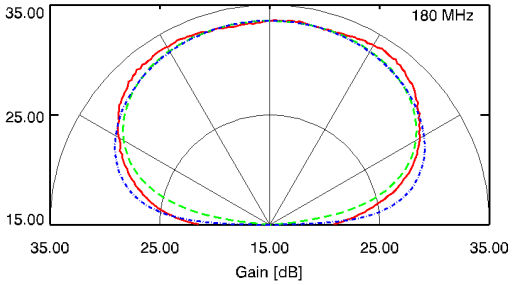

(f) 180 MHz, H-plane

Figure 3-10: Comparison of numerical (green, dashed line), analytic (blue, dot-dashed line) and measured (red, solid line) antenna patterns for a single MWA bowtie dipole. The numerical estimates are from the WIPL-D electromagnetic modeling package, the analytic estimate is an electrically short dipole over a ground screen, and the measured pattern is from the Lincoln Lab test chamber measurement (see Section 3.2.1 for a discussion of the systematics in the measurement of these beam patterns). The plots show the antenna gain on an arbitrary logarithmic scale in decibel units of power for several frequencies and for both the E and H plane.

Table 3.2. Full Tile Model Comparison

Frequency	Plane	Short Dipole Δ_{15°	Numerical WIPL-D Δ_{15°
100 MHz	E	0.43	0.31
100 MHz	H	0.74	1.05
140 MHz	E	1.34	1.32
140 MHz	H	0.52	0.63
180 MHz	E	1.09	1.14
180 MHz	H	1.09	1.21

Note. — Δ_n is defined as the maximum gain deviation in decibels within n degrees of the zenith between the Lincoln Lab measurements and the specified model

The null depth discrepancy is not unexpected, as any imperfections in the laboratory setup of the dipoles will make the nulls shallower, however the Lincoln Lab sidelobes seem to be sysematically larger than expected from the models.

3.6.6 Conclusions

The agreement between the Lincoln Lab test measurements and numerical and analytic models builds confidence in our ability to simulate the performance of the MWA antennas and tiles. The agreement between the laboratory measurements and the models of better than 10% in the region near zenith gives us confidence that we can accurately describe the radiation pattern of single MWA antennas. Although there appears to be larger deviations with the full tile patterns, the overall level of agreement is still reasonable given the systematic uncertainties in the Lincoln Lab test setup. Additionally, the antenna tiles deployed in the field will have many further sources of uncertainty. Variation in the gains of the individual antennas in a tile, as well as errors in their positioning and alignment will affect the tile patterns, as will the finite extent of the ground screen, and the moisture content and composition of

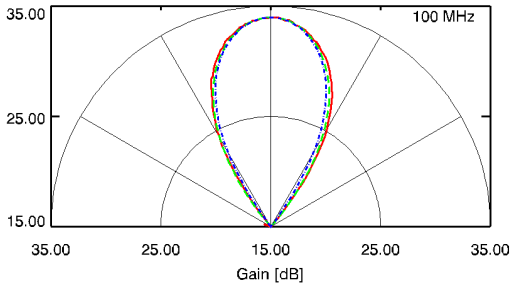

(a) 100 MHz, E-plane

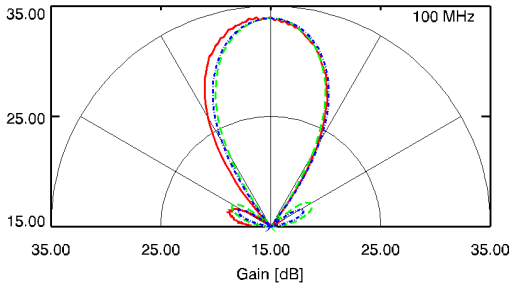

(b) 100 MHz, H-plane

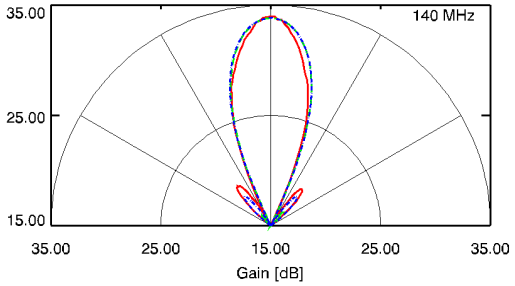

(c) 140 MHz, E-plane

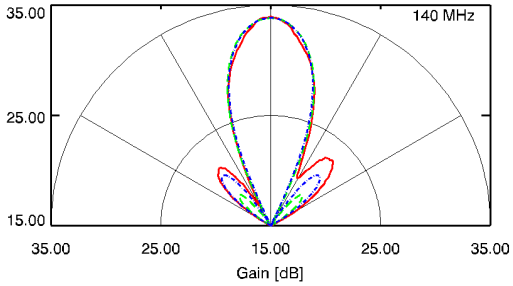

(d) 140 MHz, H-plane

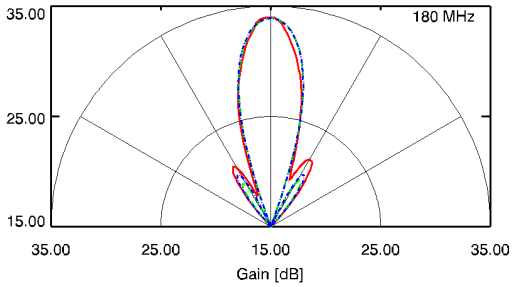

(e) 180 MHz, E-plane

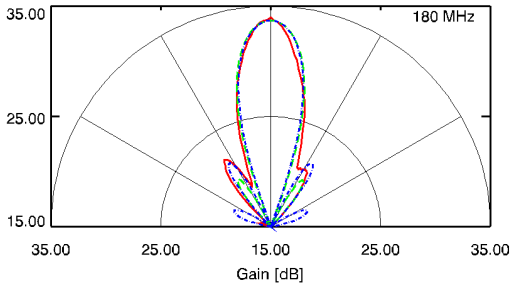

(f) 180 MHz, H-plane

Figure 3-11: Comparison of numerical (green, dashed line), analytic (blue, dot-dashed line) and measured (red, solid line) antenna patterns for an MWA antenna tile, phased to the zenith. The numerical estimates are from the WIPL-D electromagnetic modeling package, using a model of the full tile over a finite ground screen. The analytic estimate is for an electrically short dipole over a ground screen, combined analytically to simulate an antenna tile and the measured pattern is from the Lincoln Lab test chamber measurement (see Section 3.2.1 for a discussion of the systematics in the measurement of these beam patterns). The plots show the antenna gain on an arbitrary logarithmic scale in decibel units of power for several frequencies and for both the E and H plane.

the surrounding soil. Nearby antenna tiles may also be affected by mutual coupling. Additionally, the exact properties of the production beamformers may add perturbations to the formed tile beam. Accurate assessment of the MWA tile performance in the field will require *in-situ* gain measurements with the production level hardware[2].

With the confidence derived from this analysis, we have constructed simulations using the improved "short-wide" design, which will serve as a good initial model for a deployed MWA tile. We have developed software for the MWA collaboration which uses simulations of single MWA dipole antennas, and an analytic approximation of the functionality of an MWA beamformer. This simulation package can be used to produce directional response models for the MWA tiles at any frequency within the MWA band. These models are necessary in order to correct for the primary beam response across the MWA field of view so that accurate flux measurements can be made. As further observations are analyzed and quantitatively assessed, these models can be further refined to provide a more accurate estimate of the MWA element response.

Acknowledgements

We would like to extend our deep appreciation to Ed LaFave, Alan Fenn, David Bruno, John Glover, and Jeffrey Herd at Lincoln Laboratory for their extensive support of the anechoic chamber tests. Without their assistance these measurements would not have been possible.

[2]The MWA Real Time System (Mitchell et al., 2008) is designed to produce real-time measurements of the beam pattern for each tile as a part of its calibration loop.

THIS PAGE INTENTIONALLY LEFT BLANK

Chapter 4

MWA-32T Low-Frequency Imaging[1]

4.1 Introduction

The study of the origin and evolution of the Universe draws upon observations of phenomena at a large range of distances and look-back times, connecting the initial conditions probed by the cosmic microwave background to present-day conditions dominated by galaxies and clusters of galaxies. A major chapter of this history has yet to be examined — the chapter that corresponds to redshifts from $z = 1000$ to $z = 6$ and comprises the Dark Ages and the Epoch of Reionization (EoR) of the Universe. The EoR, in particular, marks a major milestone when the first stars and galaxies formed and reionized the intergalactic medium. It was recognized some time ago that studies of the redshifted 21-cm radio emission from neutral hydrogen would be a promising probe of the EoR (Hogan & Rees, 1979; Scott & Rees, 1990; Madau et al., 1997). Indeed, the possible existence of extensive regions containing significantly large amounts of neutral hydrogen at redshifts of $z = 15$ to $z = 8$ motivates an interest in developing highly sensitive low-frequency radio telescopes in order to detect the redshifted 21-cm signal. Not long ago it was recognized that a statistical detection of the patchy neutral hydrogen distribution during the EoR

[1]This chapter is adapted from Williams et al. (2012)

should be possible with an array with a modest collecting area and a large field of view (Morales & Hewitt, 2004). In the past decade considerable efforts have been made towards this goal, through advances in theoretical modeling of the EoR signature (see e.g. Pritchard & Loeb 2011, Morales & Wyithe 2010, and Furlanetto et al. 2006 for recent reviews), as well as through the development of new instrumental approaches to measure the redshifted 21-cm signal (see e.g. Bowman & Rogers 2010, Chippendale 2009, Lonsdale et al. 2009, Tingay et al. in prep., Parsons et al. 2010, Rottgering et al. 2006, and Paciga et al. 2011).

One particularly daunting challenge for these experiments is emission from foreground astrophysical sources, which is at least two to three orders of magnitude brighter than the redshifted 21-cm signal (in the total intensity as well as in the magnitude of the spatial fluctuations, see e.g. Shaver et al. 1999; Bernardi et al. 2009; Pen et al. 2009; de Oliveira-Costa et al. 2008). The foreground emission arises mainly from synchrotron and free-free processes, and therefore is highly likely to have an intrinsically smooth radio spectrum. The 21-cm signal, however, is likely to be produced under conditions that vary rapidly with redshift, and, if this is the case, will appear to have rather sharp spectral features. Techniques have been developed to exploit this differing spectral behavior in order to separate and remove the foreground contamination (Furlanetto & Briggs, 2004; McQuinn et al., 2006; Bowman et al., 2009; Harker et al., 2009; Liu et al., 2009; Liu & Tegmark, 2011). However, any calibration imperfection or instrumental defect has the potential to introduce distortions into measured spectra, and thereby to mix the extremely bright foreground emission with the signal from the redshifted 21-cm signal in ways that are difficult to disentangle (Datta et al., 2010). Thus, an equally daunting challenge is to learn how to calibrate any new instrumentation that is being developed for these observations with extremely high fidelity.

The Murchison Widefield Array (MWA, Lonsdale et al. 2009; Tingay et al. in prep.) is a new array being constructed to characterize the 21-cm signal during the EoR[2].

[2]Additionally, the MWA has been designated an official precursor instrument for the Square Kilometre Array (SKA).

In addition to the study of the EoR, other key science goals of the MWA include the study of radio transients, the study of the heliosphere and ionosphere, and low-frequency Galactic and extragalactic studies. These four goals and potentially others are addressed by an array made of a large number of small antenna elements that simultaneously give a large collecting area and a large field of view. This is a departure in many ways from a traditional radio array design, with phased arrays of dipoles constituting the fundamental antenna elements, digitization early in the data stream, and full correlation of a large number of baselines. This design promises large improvements with regard to wide-field surveys and detection of the EoR, but, at the same time, it poses new challenges, especially with regard to calibration and imaging of the large field of view and compensation for the effects of the ionosphere. The instrument is currently under construction; work on a 128-element array commenced in early 2012 at the radio-quiet Murchison Radio-astronomy Observatory (MRO) in Western Australia. As a first step in demonstrating the new technologies required for the MWA, a 32-element prototype was built at the MRO site prior to the build-out to 128 elements. This prototype system was operated for two years in campaign mode, and underwent a cycle of equipment installation, testing, and redesign as necessary. Beginning in March 2010, the prototype was used for initial science observations, and has already yielded several results. Oberoi et al. (2011) present findings from an investigation of solar radio emission, and Ord et al. (2010) present wide-field images using a prototype real-time imaging and calibration pipeline. Herein, we also report results based on data obtained during this initial science run.

The goals of the measurements and analysis presented here are to verify the performance of the MWA subsystems and the 32-element prototype array, to explore techniques for future EoR experiments, and to deepen our understanding of the astronomical foregrounds. We observed two overlapping fields at high Galactic latitude, each 50° across. One field was identified for possible EoR studies in the future, and the other was chosen to have a very bright radio source at its center to facilitate calibration. The observations are deep in the sense that they combine data from a large range of hour angles and multiple snapshot images to improve sensitivity and

image fidelity; developing such techniques for deep observations is critical for the success of future EoR experiments and other scientific investigations with the MWA. We have developed a data reduction pipeline that implements wide-field calibration and imaging algorithms, compensates for the direction-dependent and changing primary beam as different snapshots are combined, and automatically extracts sources from the images. We compare our results directly to the results from other sensitive low-frequency radio surveys in the southern hemisphere, and we compare them statistically to the results from surveys carried out in the northern hemisphere. We use these comparisons to assess the performance of the MWA prototype and the wide-field imaging and calibration algorithms. We assess the completeness and reliability of our point source catalog through comparison to these surveys. We make a number of simplifying assumptions in this first phase of analysis; future work will refine the techniques and algorithms until the stringent calibration requirements of EoR experiments with the full MWA can be met. The content of this

4.2 Low-Frequency Radio Surveys

In this work we make extensive use of the results of previous sensitive low-frequency radio surveys to verify the performance of the MWA and to provide external data for calibration. We summarize here the properties of the surveys used in our comparisons.

The Molonglo Reference Catalog (MRC; Large et al. 1981) is the product of a blind survey at 408 MHz that covered nearly all of the southern sky to moderate depth. The catalog covers all right ascensions in the declination range from $-85.0°$ to $+18.5°$, excluding the area within $3°$ of the Galactic plane. The observations were conducted with the Molonglo Radio Telescope in a 2.5 MHz wide band with a synthesized beam of $2.62' \times 2.86' \sec(\delta + 35.5°)$ in width. The MRC has a stated completeness limit of 1 Jy, although it contains sources down to a flux of $\sim$0.7 Jy.

At frequencies below 408 MHz, there have been many targeted observations of known sources in the southern sky. The Culgoora Circular Array (Slee, 1995) was used to observe Galactic and extragalactic sources selected from existing higher fre-

quency surveys. The observations were made at frequencies of 80 MHz and 160 MHz. The beam size was $3.70' \times 3.70' \sec(\delta + 30.3^\circ)$ at 80 MHz, and $1.85' \times 1.85' \sec(\delta + 30.3^\circ)$ at 160 MHz. The limiting flux density was 4 Jy at 80 MHz, and 2 Jy at 160 MHz. However, only a small patch of sky around each selected source was imaged. Although flux density uncertainties are not directly reported in this list, Slee (1977) note that the standard deviation in the flux density for sources measured with the Culgoora array is $\sim 13\%$ for the brightest sources, and $\sim 39\%$ for the faintest sources, with a potential systematic flux scale depression of $\sim 10\%$. Similarly, Jacobs et al. (2011) present results from PAPER, an array of east-west polarized dipoles, that were obtained over the 110 MHz to 180 MHz band. The results were derived from multi-frequency synthesis maps of the entire sky south of a declination of 10° having a resolution of $26'$. A sample of 480 sources with fluxes greater than 4 Jy in the MRC were identifed and measured in these PAPER maps. Jacobs et al. (2011) find a 50% standard deviation in their fluxes relative to values obtained from the MRC and Culgoora source lists. They quote a flux limit of 10 Jy for the sources in their catalog.

There are several ongoing efforts to perform low-frequency blind surveys. Pandey (2006) presents results from a survey that used the Mauritius Radio Telescope (MRT) to image $\sim$1 steradian of the sky at 151 MHz and to thereby produce a catalog of 2782 sources[3]. The deconvolved images achieve an angular resolution of $4' \times 4.6' \sec(\delta + 20^\circ 14')$ and a root-mean-square (RMS) noise level of approximately 300 mJy beam^{-1} (Nayak et al., 2010). The TIFR GMRT Sky Survey (TGSS, Sirothia et al. 2011) is producing a 150 MHz survey of the sky at declinations above -30°. Each pointing covers ~ 7 square degrees and yields a map that reaches an RMS noise of ~ 8 mJy beam^{-1} at an angular resolution of $\sim 20''$. The flux density scales of the maps are limited by systematic errors and have relative errors of 25%. As of 2012 January, the TGSS website[4] reports results from images of approximately 2600 square degrees of the southern sky.

[3]Electronic catalogs are available at `http://www.rri.res.in/surveys/MRT`

[4]`http://tgss.ncra.tifr.res.in/150MHz/tgss.html`

Surveys which primarily cover the northern sky have also been carried out at low frequencies. The most extensive wide-field uniform survey near our observing frequency of 150 MHz is the 6C survey (Baldwin et al., 1985; Hales et al., 1988, 1990, 1991, 1993b,a). The 6C survey covered the northern sky above declination 30° with a sensitivity of 200 mJy; the angular resolution was $4.2' \times 4.2' \csc \delta$. The 7C survey (Hales et al., 2007) covers 1.7 sr of the northern sky to a greater depth and at higher resolution than the 6C survey. We have chosen to use the 6C survey for comparison to our results in this paper because it covers a somewhat larger sky area, and has served as the basis for other investigations of EoR foregrounds (in particular, Di Matteo et al. 2002). At lower frequencies, Cohen et al. (2007) have used the VLA 74 MHz system to perform a survey of the sky north of declination $\delta = -30°$. This survey, known as the VLA Low-Frequency Sky Survey (VLSS), produces maps with an $80''$ angular resolution which achieve a typical RMS noise level of 100 mJy beam^{-1}. Each VLSS image is $14° \times 14°$ across in order to fully image the VLA primary beam, which has a FWHM diameter of 11.9° degrees. Cohen et al. (2007) perform a blind source extraction on the VLSS maps and produce a source catalog of 68,311 radio sources above a significance level of 5σ. They quote a 50% point source detection limit of 0.7 Jy beam^{-1}.

For completeness we note that additional low-frequency surveys include the Sydney University Molonglo Sky Survey (843 MHz, Bock et al. 1999), the Miyun survey (232 MHz, Zhang et al. 1997), and the Levedev Physical Institute Survey (102.5 MHz, Dagkesamanskiĭ et al. 2000). We have not extensively compared our results to results from these surveys.

Low frequency surveys have also been used to study the distribution of spectral indices of radio sources. De Breuck et al. (2000) used results from the MRC and from the Parkes-MIT-NRAO 4.85 GHz survey (PMN, Wright et al. 1994; Griffith & Wright 1993; Griffith et al. 1994; Condon et al. 1993; Tasker et al. 1994; Griffith et al. 1995; Wright et al. 1996) to study the distribution of spectral indices of sources in the southern sky. They also carried out similar comparisons of the results from the Westerbork Northern Sky Survey (325 MHz; Rengelink et al. 1997) and the Texas Survey

(365 MHz; Douglas et al. 1996) with results from the NRAO VLA Sky Survey (1.4 GHz; Condon et al. 1998) in the northern hemisphere. The spectral index distributions showed significant differences between samples selected at low frequencies and samples selected at high frequencies. The combined MRC-PMN source list was also used to generate a sample of ultra-steep spectrum sources.

In Chapter 4.7.1, we carry out source-by-source comparisons of our survey results to those of the MRC, the Culgoora flux density measurements, the PAPER flux density measurements, and the TGSS. There is no overlap at present between our survey and the Mauritius survey, but comparisons should become possible when the analysis of the Mauritius data is completed. We also carry out statistical comparisons of our survey results to those of the 6C survey by comparing source counts, and to the De Breuck et al. (2000) spectral index catalogs by comparing spectral index distributions.

4.3 The MWA-32T Instrument

The Murchison Widefield Array 32-Tile prototype (MWA-32T) was built and operated for the purpose of verifying the performance of MWA subsystems in preparation for building a larger, more capable array. As noted above, construction of a 128-tile array has commenced and is expected to be complete later this year (2012). We summarize the design here; the reader is referred to Lonsdale et al. (2009), Tingay et al. (in prep.), and Chapter 2 for more detailed descriptions.

The MWA-32T was designed to cover a frequency range from 80 MHz to 300 MHz, with an instantaneous bandwidth of 30.72 MHz at a spectral resolution of 40 kHz. The array consisted of 32 antenna tiles, which served as the primary collecting elements of the array. The tiles are designed to have an effective collecting area larger than 10 m^2 in the MWA frequency band, and to provide a steerable beam which can be pointed up to 60° from zenith while maintaining a system temperature which is dominated by sky noise within the MWA band. The primary beam of the tiles is frequency and position dependent, with a FWHM size at zenith of roughly $25°/(\nu/150$ MHz). Each

tile consists of 16 dual-polarization, active dipole antennas laid out over a metal mesh ground screen in a 4×4 grid with a 1.1 meter center-to-center spacing. Each dipole antenna consists of vertical bowtie elements that feed a pair of integrated low-noise amplifiers (LNAs) located within a tube at the juncture of the orthogonal arms of the dipole. The antennas are designed to have low horizon gain to reduce terrestrial RFI contamination, and to have a low manufacturing cost.

The signals for the two polarizations are processed in parallel. For each polarization, the signals from the 16 dipoles on each tile are carried over coaxial cable to an analog beamformer, where they are coherently summed to form a single tile beam. A system of switchable analog delay lines is used to apply an independent time delay to each of the dipole signals, allowing the tile beam to be steered on the sky. The delay lines employ a series of 5 switchable traces, each differing by a factor of two in length, with the shortest trace introducing a nominal delay of 435 ps. This allows for 32 discrete delay settings for each of the input signals. The discretization of the delays implies that the primary beam can only be steered in discrete steps, and so can only coarsely track a sky field. The summed signal is amplified and sent over coaxial cables to the MWA digital receiver for digitization.

Each MWA digital receiver node services 8 tiles. The 16 received signals are first subjected to additional filtering and signal conditioning for low-frequency rejection, anti-aliasing, and level adjustment. The signals are then digitized at baseband by eight dual 8-bit analog-to-digital converter (ADC) chips operating at a sampling rate of 655.36 MHz. The data stream from each ADC is fed to a digital polyphase filterbank (PFB) implemented in FPGA hardware which produces 256 frequency channels, each 1.28 MHz wide. A sub-selection of 24 of these channels (a bandwidth of 30.72 MHz) are transmitted via optical fiber to the correlator.

At the correlator, the data streams from each receiver are processed by a second stage PFB to obtain a frequency resolution of 10 kHz. The signals are then cross-multiplied to produce a 3072 channel complex spectrum for each of the 2080 correlation products. These comprise the four polarization products for all pairs of tiles as well as the autocorrelations. The visibilities are averaged into 40 kHz wide

channels and integrated for 50 ms due to output data rate constraints. During the 32T observing campaign described in this work, the correlator was operating at a 50% time duty cycle due to hardware limitations. The visibilities are captured and averaged into 1 second integrations before being written to disk.

4.4 Observations

Observations were conducted with the MWA-32T in March 2010 during a two-week campaign (X13) when personnel were present on-site to operate the instrument. Data were taken in three 30.72 MHz sub-bands centered at 123.52 MHz, 154.24 MHz, and 184.96 MHz in order to give (nearly) continuous frequency coverage between ∼110 MHz and ∼200 MHz. During the observations, the beamformers were used to steer the beam in steps as the fields crossed the sky. This stepped steering is a consequence of the discretization of the analog delay lines in the beamformer. The typical sequence was to steer the beam to a new position, observe at a particular frequency for five minutes (without tracking), and then steer the beam again. Thus, the measurements can be considered to be a series of short drift scans.

The observing time was divided between two fields. One field was centered on the bright extragalactic source Hydra A at RA(J2000) = $9^{\rm h}\ 18^{\rm m}\ 6^{\rm s}$, Dec.(J2000) = $-12^\circ\ 5'\ 45''$ to facilitate calibration. The other covered the EoR2 field, centered at RA(J2000) = $10^{\rm h}\ 20^{\rm m}\ 0^{\rm s}$, Dec.(J2000) = $-10^\circ\ 0'\ 0''$. The EoR2 field is one of two fields at high Galactic latitude that have been identified by the MWA collaboration as targets for future EoR experiments. The locations of these fields are shown in Figure 4-1, along with an additional calibration field centered on Pictor A. The EoR2 field had the advantage of being above the horizon at night during the observing campaign. Although the centers of the Hydra A and EoR2 fields are separated by 15.3°, there is considerable overlap between them since the half power beam width of the primary beam is $\sim 25^\circ$ at 150 MHz. A total of 61 ∼5 minute scans of the Hydra A field and 248 scans of the EoR2 field were obtained in interleaved sequences over the course of the observing sessions. Table 4.1 gives a journal of the observations.

Table 4.1. Journal of Observations

Field	Frequency (MHz)	Date	Number of Scans	Observation[a] Time (minutes)
EoR2	123.52	2010/03/24	35	208
		2010/03/28	26	154
	154.24	2010/03/22	35	208
		2010/03/26	18	107
		2010/03/28	10	59
	184.96	2010/03/21	35	208
		2010/03/25	35	208
		2010/03/26	18	106
		2010/03/29	36	214
Hydra A	123.52	2010/03/24	8	39
		2010/03/28	7	34
	154.24	2010/03/22	8	39
		2010/03/26	5	24
		2010/03/28	3	15
	184.96	2010/03/21	8	39
		2010/03/25	8	39
		2010/03/26	5	24
		2010/03/29	9	44

[a]The effective integration time is less than half of this observation time due to the 50% duty cycle of the correlator and additional flagging.

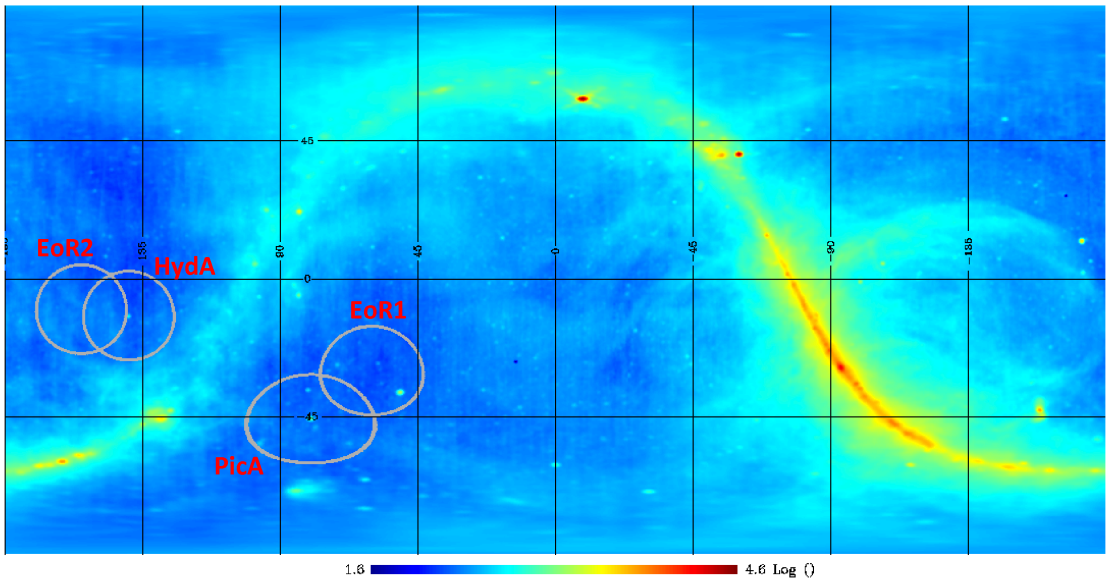

Figure 4-1: Location of the MWA Epoch of Reionization fields, and Hydra A / Pictor A calibration fields plotted on the global sky model of de Oliveira-Costa et al. (2008) at 150 MHz. The color scale of the image is logarithmic in units of temperature (Kelvin). The EoR fields were selected for their low brightness temperature.

4.5 Data Reduction Strategy

4.5.1 Instrumental Gain Calibration

The MWA antenna tile architecture poses several nontraditional calibration issues due to both the nature of the primary beam and the wide field-of-view. The primary beam is formed by the summation of beamformer-delayed zenith-centered dipole responses. The beamformer delays are periodically changed to track a field across the sky. Although this moves the center of the primary beam as intended, the overall shape of the beam changes as well. For a given set of beamformer delays, the beam is fixed relative to the tile, and therefore moves relative to the sky as the Earth rotates. As a further complication, the time and direction dependence of the primary beam response is different for the two polarizations of the crossed dipoles in the array. This leads to apparent polarization in inherently unpolarized sources due to the different responses in the two orthogonal dipole polarizations unless the appropriate corrections are applied in the analysis procedure.

Methods for measuring and calibrating the primary beam have been developed for the full MWA system by Mitchell et al. (2008), who plan to use a real-time system (RTS) to calibrate and image MWA data. Their method performs a calibration of the instrument in real time, solving for direction- and frequency-dependent gains for each antenna based on the simultaneous measurement of multiple known bright sources across the field of view. This method was developed for use in a 512-tile array, where the instantaneous sensitivity and uv-plane coverage enable the measurement of several hundred sources in each 8-second iteration (Mitchell et al., 2008). Ord et al. (2010) have successfully demonstrated the use of a modified version of the RTS in order to calibrate and image data from the MWA-32T. However, the reduced sensitivity of the MWA-32T array makes this full calibration challenging. For the MWA-32T system, the data rate is sufficiently low that real-time calibration and imaging are not necessary, and the raw visibility data can be captured and stored. We have chosen to pursue an alternative data reduction pipeline based on more traditional calibration and imaging software which allows us to use the full visibility data set in order to perform a detailed investigation of the calibration and imaging performance of the MWA-32T instrument.

Without the ability to directly measure the primary beam for each tile, we instead assume a model and use it to account for the instrumental-gain direction dependences. Knowledge of the primary beams is also needed for an optimized weighting of the maps when combining them to obtain deeper maps (see Chapter 4.6.4). It is likely that precise characterization of individual tile beams will be necessary to achieve dynamic range sufficient for accurate foreground subtraction and EoR detection, but this is not attempted in the work described herein.

For present purposes, we assume the polarized primary beam patterns are identical across all tiles, and can be modeled by simply summing together the direction-dependent complex gains of the individual dipoles in the tile, i.e., mutual coupling between elements and tile-to-tile differences are ignored. We model the complex beam patterns of an isolated individual dipole for both the north-south (Y) and east-west

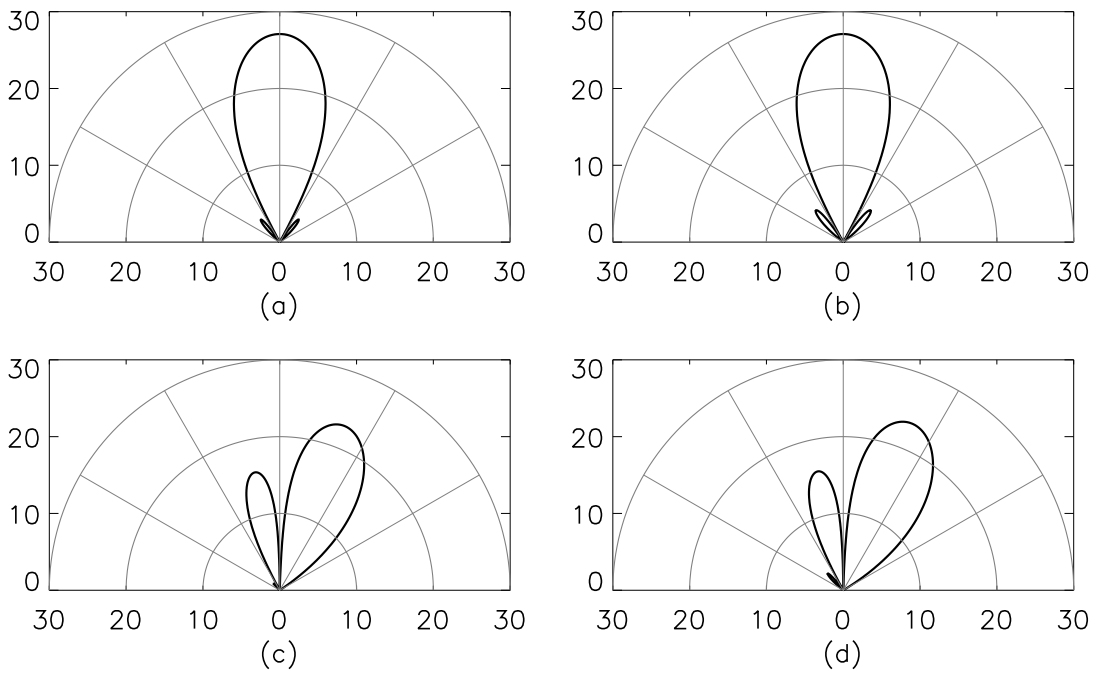

Figure 4-2: West-east cuts through simulated MWA antenna tile patterns for a zenith (a,b) and a 28° easterly pointing (c,d) at 150 MHz. Panels (a) and (c) show the X polarization dipole power response pattern, while panels (b) and (d) show the Y polarization power response pattern. The scale is logarithmic, with arbitrarily normalized decibel units. The polarization-dependent gain structure is clearly visible in the sidelobes.

(X) electric field polarizations using the `WIPL-D Pro`[5] electromagnetic modeling software package. A tile beam pattern is then computed by summing the 16 dipole responses with the dipoles assumed to be at their nominal locations in a tile and with the individual responses modified by the nominal amplitudes and phases introduced by the beamformer for the given delay settings. Figure 4-2 shows cuts through power patterns (square modulus of the complex beam) at zenith and at a pointing direction 28° east of zenith for both the X and Y polarizations. Model beam patterns were calculated at frequency intervals of 2 MHz, since they vary significantly across the MWA frequency band.

We assume that this model fully describes the direction dependence of each tile. We do, however, allow for a different overall, i.e., direction-independent, complex gain

[5]http://www.wipl-d.com

for each tile. We follow the Jones matrix formalism as presented by Hamaker et al. (1996). The instrumental model then takes the following form for a single tile at a single frequency:

$$\mathbf{v}_\mathrm{A} = \mathbf{G}_\mathrm{A}\mathbf{B}\mathbf{e}_\mathrm{A}, \tag{4.1}$$

where

$$\mathbf{e}_\mathrm{A} = \begin{pmatrix} e_\mathrm{x} \\ e_\mathrm{y} \end{pmatrix}, \tag{4.2}$$

is the incident electric field at tile A, decomposed into linear E-W and N-S polarizations,

$$\mathbf{v}_\mathrm{A} = \begin{pmatrix} v_\mathrm{x} \\ v_\mathrm{y} \end{pmatrix}, \tag{4.3}$$

is the vector of measured antenna voltages,

$$\mathbf{G}_\mathrm{A} = \begin{pmatrix} g_\mathrm{A,x} & 0 \\ 0 & g_\mathrm{A,y} \end{pmatrix}, \tag{4.4}$$

is the matrix of direction-independent complex gains for an antenna, and

$$\mathbf{B} = \begin{pmatrix} b_\mathrm{x}(\theta,\phi) & 0 \\ 0 & b_\mathrm{y}(\theta,\phi) \end{pmatrix}, \tag{4.5}$$

is the matrix of direction- and frequency-dependent but tile-independent gains due to the primary beam shape (we represent spatial coordinates with θ and ϕ). We neglect the feed-error "D" matrix of Hamaker et al. (1996); in other words we assume that the sensitivity of the X-polarization response of a dipole to Y-polarization radiation (the cross-polarization) is zero, and vice versa. This is likely to be a good approximation since ideal dipoles have zero cross-polarization by definition. In reality, various effects, such as the finite thickness of our dipole elements, interactions between structures in neighboring dipoles, or projection effects may produce a nonzero cross-polarization response. In this paper we restrict our imaging and analysis to these two senses of linear polarization and their combination as total intensity. Errors caused by

neglecting cross-polarization effects are second order in the small off-diagonal elements of the D-matrix.

The strategy we adopt for the data reduction is first to analyze short snapshots wherein the settings in the analog beamformer were static so that the primary beam pattern can be taken as constant over the duration of each snapshot, and any gain changes due to the sidereal motion of the sky relative to the beam can be neglected. In this regime, the direction-dependent gain can be factored out of the response and corrected in the image plane in the resulting map. Under this approximation, we are able to use standard tools for radio astronomical data analysis for much of the processing. Finally, the frequency dependences of the overall antenna complex gains are in principle determined by modeling the summed spectra of the bright sources in the field used in the calibration.

Standard calibration procedures rely on being able to observe a field containing a strong source with easily modeled structure that substantially dominates the visibilities. For the two fields presented in this work, Hydra A is the strongest source in the field. Lane et al. (2004) present low-frequency images that show that while it is quite extended at the VLA's resolution, most of the flux is contained within a region that is a few arcminutes in radius. Since this extent is smaller than the angular resolution of the MWA-32T, we were able to treat Hydra A as a point source in our calibration analysis. One might expect that for a large field-of-view instrument such as the MWA, we would also need to include several or even many additional strong sources in the calibration model with known direction-dependent gains. We therefore experimented with calibration models that included several point sources in addition to Hydra A, but we found that the complex tile gain solutions were not significantly changed. We therefore simply used Hydra A as the only calibration source in subsequent analysis. It should be noted that this is a potential source of error.

4.5.2 Ionosphere

At the low radio frequencies of the MWA, position- and time-dependent variations in the electron density of the ionosphere cause variations in propagation times, which

appear in the visibility data as frequency- and time-dependent phase shifts. For the short baselines of the MWA-32T, these variations are, except at times of extreme ionosphere disturbance, refractive in effect, i.e., they simply cause apparent changes in the positions of point sources on the sky. These positions shifts may be different in different directions, especially over a wide field such as that of the MWA, and consequently may lead to distortions in the derived images.

Ionospheric effects have been quantified by studies with other low-frequency interferometers. Baldwin et al. (1985), using the Cambridge Low-Frequency Synthesis Telescope at 150 MHz, found that the ionosphere typically caused 5° (RMS) phase variations on 1 km baselines on sub-day timescales, which were uncorrelated from day to day. They also remarked that ionospheric irregularities on large spatial scales, most likely related to the day-night cycle and strongly correlated from one day to the next, could induce apparent position shifts of sources of up to 20′. Kassim et al. (2007) found, with the VLA operating at 74 MHz, that during times of moderate ionospheric disturbance relative position variations on short timescales across a 25° field of view were at most 2′. Similarly, Parsons et al. (2010), using observations of bright sources with the PAPER array at 150 MHz, found short-term small (typically less than 1′) position offsets that were not correlated from day to day, and long-term large (up to 15′) position offsets which were correlated from day to day, and were mainly in the zenith direction.

In our analysis, we average snapshots taken with the center of the field within several hours of the local meridian over a period of eight days. The results in the papers cited above suggest that uncorrelated short-term variations in source directions will be significantly smaller than our beam size of $\sim 15'$ and, furthermore, that they will tend to average out when images derived from individual snapshots are combined. We therefore neglect them. Long-term correlated variations in source directions may be comparable to our beam size, and may not average to zero as we combine snapshot images. However, our calibration strategy, described in Chapter 4.5.1, will tend to remove any ionospheric offset at the position of Hydra A through the phase terms in the direction-independent gain solutions. It is possible, depending on the behavior of

the ionosphere during the present observations, that long-term differential position shifts of several arc minutes might be present in our final images. We investigate this possibility through comparisons of the positions of our extracted sources with source positions listed in published catalogues.

Our neglect of short-term ionospheric effects is justified only because of the small baselines (<350 m) of the MWA-32T array. For the longer baselines (∼3 km) of the full MWA, we believe that these effects will need to be corrected to achieve the dynamic range required for many of the science goals.

4.6 Reduction Pipeline

4.6.1 Initial Processing and Editing

We developed a calibration and imaging pipeline based on the NRAO Common Astronomical Software Applications[6] (CASA) package and additional tools that we developed in Python and IDL. The pipeline uses a series of short observations to generate "snapshot" images which are weighted, combined, and jointly deconvolved to produce final integrated maps.

In the first stage of the pipeline, the visibilities were averaged over 4-s intervals and converted from the MWA instrumental format into UVFITS files. The MWA-32T correlator does not perform fringe-stopping (the correlation phase center is always at zenith), so phase rotations were applied to the visibilities to track the desired phase center. As a part of this process, data corrupted by RFI were flagged for later exclusion from the analysis. The data were then imported into CASA. Additional editing was done to flag data affected by known instrumental problems or RFI. Approximately 25% of the data were flagged at this stage, mainly because a problem in the data capture software corrupted 480 of the 2080 correlation products.

[6] `http://casa.nrao.edu`

4.6.2 Calibration of Antenna Gains

Calibration was performed separately for each snapshot with CASA, using Hydra A as the gain and phase reference (as discussed in Chapter 4.5.1). Although Hydra A was not at the center of the primary beam during observations of the EoR2 field, it was still strong enough to substantially dominate the visibilities. Model visibilities were calculated using a point source model for Hydra A, assuming an unpolarized flux of unity. The overall frequency-dependent flux scale of the data was set at a later point, along with a correction for the direction-dependent gain. Time-independent channel-by-channel gain factors were calculated for each tile using the task `bandpass`. After this was done and the visibilities corrected for the gain factors, time-dependent overall tile gain factors were calculated on a 32 second cadence using the task `gaincal`. The factors determined in the two tasks give the frequency- and time-dependent $g_{\mathrm{A,x}}$ and $g_{\mathrm{A,y}}$ terms of Equation 4.4.

The $g_{\mathrm{A,x}}$ and $g_{\mathrm{A,y}}$ terms were examined for temporal stability and spectral smoothness; regions where deviations were apparent were flagged. Such deviations were rare, and an important outcome of this analysis is the recognition that the MWA antenna gains are quite stable over frequency and time. In fact, the gains even tended to be stable from one day to the next. However, some complicated variations in gain as a function of frequency were identified. These were associated with damaged cables and connectors that have since been replaced or repaired.

4.6.3 Snapshot Imaging

The data from each snapshot were subdivided into 7.68 MHz wide frequency bands, and multifrequency synthesis imaging was performed for each snapshot using the `CASA` task `clean`. Images were made with a $3'$ cell size over a $\sim 51^\circ \times \sim 51^\circ$ patch of sky in order to cover the majority of the main lobe of the primary beam. The "XX" and "YY" polarizations were imaged separately. Conversion to the standard Stokes parameters was not performed at this stage, since, as discussed in Chapter 4.5.1, the gains for the two polarizations have different direction dependence. The "w-

projection" algorithm (Cornwell et al., 2008) was used to correct for wide field-of-view effects, and to produce an image with an approximately invariant point spread function in each of the snapshot images. The images were deconvolved using the Cotton-Schwab `CLEAN` algorithm (see Schwab 1984) down to a threshold of 1% of the peak flux in the image.

A position-dependent "noise" map was also computed for each of the 7.68 MHz wide snapshot images by selecting a 64-pixel by 64-pixel window around each pixel in the image and fitting a Gaussian to the central 80% of a histogram of the pixel values. This procedure was employed because of the high point-source density in these maps. Throughout much of the area of these maps, it was impossible to identify a source free region from which to estimate the background noise fluctuations, and the presence of sources artificially skewed the noise estimates calculated strictly as the root-mean-square (RMS) of the pixel values. We found that this clipped histogram fitting procedure provided a more robust estimate of the RMS of the background noise. These noise maps were smoothed on a 1° scale to remove local anomalies introduced by extended or clustered sources. However, despite these procedures, some areas, particularly in especially crowded regions, still had anomalously high noise estimates.

As discussed above, each snapshot was only $\sim$5 minutes in duration, and was obtained while the delay line settings in the analog beamformers were fixed. This allowed us to model the primary beam pattern of each tile as fixed relative to the sky for the duration of the snapshot. Our calculated model beams for each polarization formed the frequency-dependent $b_x(\theta, \phi)$ and $b_y(\theta, \phi)$ terms of Equation 4.5. These terms are time-dependent only in that they are different for each snapshot.

4.6.4 Snapshot Combination and Joint Deconvolution

Deeper images were obtained by combining snapshot maps from a particular 7.68 MHz wide band according to:

$$I_{\rm dirty}(\theta, \phi) = \frac{\sum_i \frac{D_i(\theta,\phi) B_i(\theta,\phi)}{\sigma_i^2(\theta,\phi)}}{\sum_i \frac{B_i^2(\theta,\phi)}{\sigma_i^2(\theta,\phi)}}, \tag{4.6}$$

where $I_{\rm dirty}$ is the integrated, primary-beam corrected, dirty map, the snapshots are distinguished by index i, D_i is a snapshot dirty map, B_i is the primary beam calculated for that snapshot, and σ_i is the fitted rms noise obtained from the noise map for snapshot i. This combination optimizes the signal to noise ratio of the final image. Beam patterns are calculated independently for each 7.68 MHz channel. The same weighting scheme was used to combine the "clean components" and residual maps of the individual snapshots.

A variant of the Högbom CLEAN algorithm (Högbom, 1974) was used to further deconvolve the integrated residual maps, using a position-dependent point spread function calculated using the same weighting scheme:

$$P_{{\rm int},j}(\theta,\phi) = \sum_i \frac{B_i(\theta,\phi)B_i(\theta_j,\phi_j)P_i(\theta-\theta_j,\phi-\phi_j)}{\sigma_i^2(\theta,\phi)}, \tag{4.7}$$

where $P_{{\rm int},j}$ is the point spread function for a source at position (θ_j,ϕ_j), B_i is the primary beam pattern for the ith snapshot with a PSF given by P_i, and the peak of the function is normalized to unity. CLEAN components were selected by choosing the pixel in the residual map with the largest signal-to-noise ratio (SNR, determined by dividing the residual map by its noise map). The PSF was scaled to a peak of 10% of the flux of the pixel. The images were restored with a Gaussian beam determined by a fit to the weighted average of the individual snapshot point spread functions at the field center.

4.6.5 Averaging

In order to increase the signal to noise ratio and image fidelity for source detection and characterization, the individual 7.68 MHz maps, after deconvolution and restoration, were averaged together. An approximate flux scale for the maps was first set by scaling the surface brightness of the maximum pixel at the location of Hydra A to a value of $296 \times (\nu/150\ {\rm MHz})^{-0.91}$ Jy beam^{-1} (this model was derived from fitting a power law to other low-frequency measurements). For each field, 30.72 MHz bandwidth maps centered at 123.52 MHz, 154.24 MHz, and 184.96 MHz were each made from

four 7.68-MHz maps. Before averaging, the 7.68-MHz map fluxes were scaled to the averaged map frequency using an assumed spectral index of $\alpha = -0.8$ (where $S \propto \nu^{\alpha}$). The averages were computed in a weighted sense using the integrated primary beam weights from each map. A full-band (92.16 MHz bandwidth) weighted average map was made from the three 30.72-MHz bandwidth maps after scaling them to a common reference frequency of 154.24 MHz, again using a spectral index of $\alpha = -0.8$. The portion of each field within 25° of the field center was used for the subsequent analysis.

4.6.6 Source Extraction

Sources were identified in each full-band, i.e., 92.16 MHz wide, averaged map using an automated source extraction pipeline. The first step of this pipeline was the calculation of a position-dependent noise map using the method described in Chapter 4.6.4. The full-band map was then divided by the noise map to produce a SNR map. An iterative process then was initiated by identifying contiguous regions of pixels above a certain SNR detection threshold and, for each such region, defining a fitting region that extended beyond the set of connected pixels by several synthesized beamwidths. A two-dimensional Gaussian fit was performed on the corresponding region in the full-band map. The parameters determined in each fit included the background level, peak position, peak amplitude, major axis width, minor axis width, and position angle. If the fit converged to a Gaussian centered within the fitting region, then the source was subtracted from the map, and the extracted source parameters were recorded. After fitting all regions identified for a certain SNR level, the detection threshold was reduced and the process was repeated. Regions above the detection threshold for which a fit failed to converge are refit in subsequent iterations at lower detection thresholds (where the fitting regions are typically larger in size). For completeness, sources were extracted down to a detection SNR threshold of 3. It should be noted that in this fitting procedure, each region that is fit by a single two-dimensional Gaussian is taken to correspond to a separate source. Sources that are too close together to be resolved into separate components will be fit with a single component and erroneously taken to be a single source that is a "blend" of the two components.

Sources that were identified in the full-band average map were then extracted from each of the 30.72-MHz bandwidth maps. The sources were sorted by their detection signal-to-noise level and, for each of the three maps, were fitted in descending order. For each source, the position and shape (axial ratio and position angle) parameters of the Gaussian fitting function were held fixed to the values determined in the full-band map extraction, while the peak value, background level, and a scaling factor for the widths of both the major and minor axes of the Gaussian were allowed to vary. This procedure was performed for all sources. When the fit successfully converged, the best-fit model was subtracted from the sub-band map. A total of 908 sources were extracted in the Hydra A field and 1100 sources were extracted from the EoR2 field.

4.6.7 Astrometric Corrections & Flux Calibration

We compared the positions and relative fluxes of the sources identified in the full-band maps with the positions and fluxes of possible counterparts in other catalogs. These comparisons formed the basis for astrometric corrections, and for the determination of the overall MWA flux scale. Counterparts to MWA-32T sources were identified at 408 MHz by locating sources in the MRC which were within $15'$ of an MWA source. Although we expect our astrometric accuracy to be much better than $15'$, this value was chosen to be comparable to the size of the MWA-32T synthesized beam major axis full width at half maximum response, viz., $13'$ for the Hydra A field and $14'$ for the EoR2 field, and to allow for some degree of systematic error in the MWA source positions. To avoid possible blending issues, we only considered an identification to be secure when there was precisely one source in the MRC within $30'$ of the (pre-adjustment) MWA source position. A total of 419 sources were matched uniquely to the MRC in the Hydra A field and 520 sources were matched in the EoR2 field.

An astrometric correction was then calculated by allowing for a linear transformation of the MWA source coordinates in order to minimize the positional differences between corresponding MWA and MRC sources. The transformation permits offsets in both right ascension and declination as well as rotation and shear with respect to the field center. Optimal transformation parameters were determined by performing

weighted least-squares fits. The results from initial fits indicated that there were errors in the (Earth-referenced) coordinates of the MWA tiles and in the conversion of coordinates in the maps from the epoch of observation frame to the J2000 frame. These errors were then corrected. The final fits were found to be consistent solely with offsets of the MWA source coordinates, with no shear or rotational effects. We therefore applied offsets of $\Delta\alpha = -0.6'$ and $\Delta\delta = 1.6'$ to the positions of the sources in the Hydra A field, and of $\Delta\alpha = 2.2'$ and $\Delta\delta = 1.9'$ to those in the EoR2 field. We believe the coordinate offsets are likely due to a combination of the effects of structure in Hydra A and to ionospheric refraction. Figure 4-3 shows the post-offset-correction differences in position between corresponding MWA and MRC sources in the EoR2 field. Histograms of residual positional differences from both the Hydra A and EoR2 fields are plotted in Figure 4-4. For this figure the difference for each source is normalized by the expected error based on the signal to noise ratio for the intensity and the 32T synthesized beamwidth (with the assumption of a circular source, see Condon 1997). The residual position differences are generally consistent with those expected, even though there are a small number of large position differences.

A final flux scale was set for each map using the MWA sources which had counterparts in both the MRC and Culgoora source lists. Only sources in the MWA catalog above a detection SNR threshold of 5 were used. Hydra A was excluded for reasons discussed in Chapter 4.7.1. A prediction for each source was obtained by fitting a power law spectrum to the 408 MHz MRC flux and the 80 MHz and 160 MHz Culgoora fluxes. Under these criteria, measurements in all 3 bands were found for a total of 64 uniquely matching sources in the Hydra A field and 81 uniquely matching sources in the EoR2 field. Using these flux predictions, a flux scale correction was calculated of the form:

$$S_{\text{calibrated}} = C_\nu \times S_{\text{uncalibrated}}. \tag{4.8}$$

These calibration terms were calculated independently for each of the three sub-band maps as well as for each averaged map for each field. For the Hydra A field, the calculation yeilded $C_\nu = 1.26$ for the full-band average map, 1.17 for the 123.52 MHz

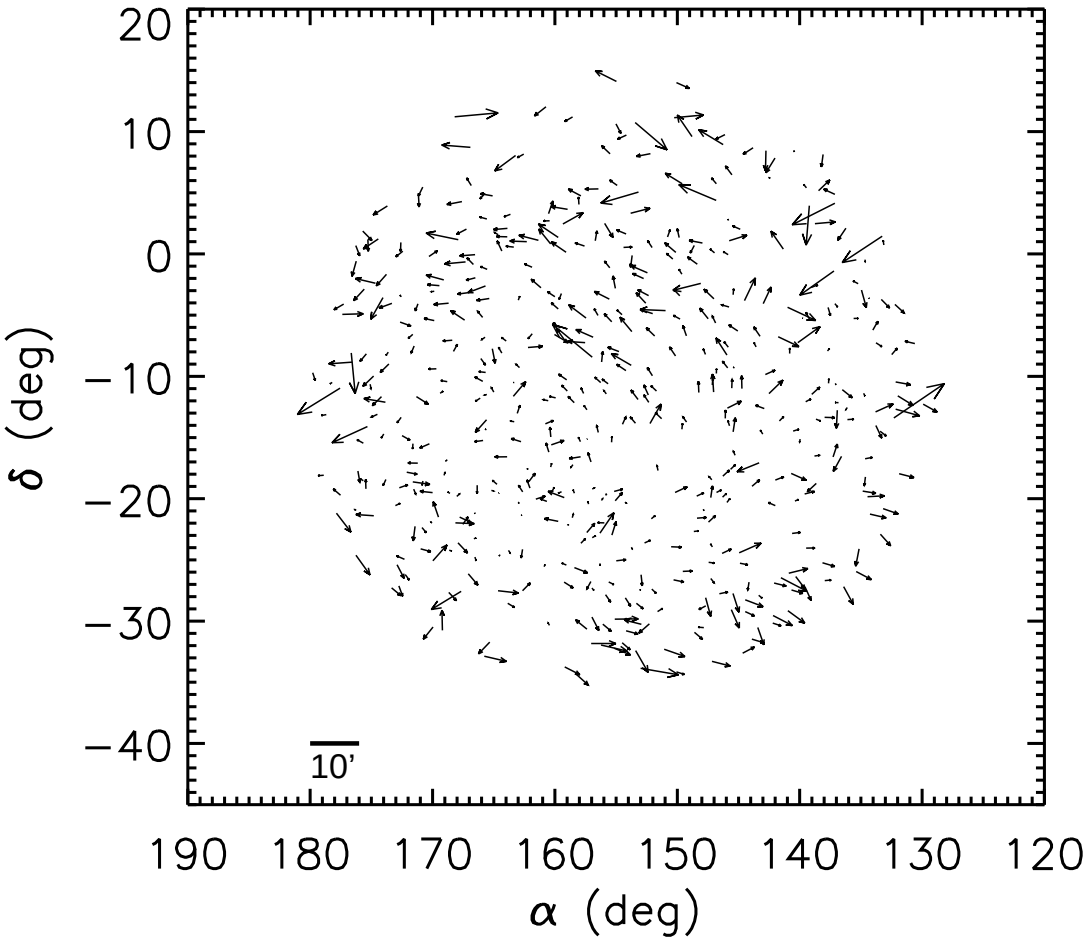

Figure 4-3: Spatial offsets between the positions of MWA sources in the EoR2 field and matched sources in the Molonglo Reference Catalog (Large et al., 1981). An overall coordinate system shift has been removed.

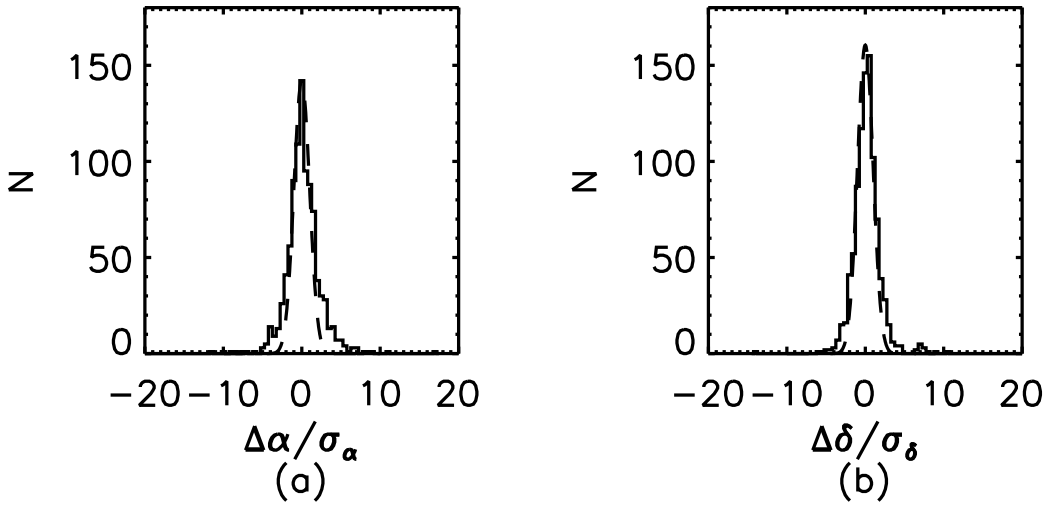

Figure 4-4: Histograms of the normalized right ascension, α, (a) and declination, δ, (b) errors for the extracted MWA sources relative to matched sources in the Molonglo Reference Catalog (Large et al., 1981). The standard deviations, σ_α, and σ_δ, are calculated following Condon (1997) with the simplifying assumption of circular source geometry Assuming Gaussian error properties, the residual distribution should approximate a standard normal distribution, which is over-plotted with a dashed line. Hydra A is omitted from the histograms.

map, 1.20 for the 154.24 MHz map and 1.18 for the 184.96 MHz map, and for the EoR2 field, the calculation yielded $C_\nu = 1.24$ for the full-band average map, 1.19 for the 123.52 MHz map, 1.23 for the 154.24 MHz map and 1.17 for the 184.96 MHz map. The residuals after applying these flux scale corrections were analyzed to determine if additional biases were present as a function of position in the image (biases would potentially be seen, e.g., if the assumed primary beam model was incorrect). An example of these plots is shown in Figure 4-5, which shows no evidence for a radially increasing flux bias.

The magnitude of the post-correction residual differences between the MWA measurements and the predicted fluxes for calibration sources are still larger on average than expected under the assumption that the uncertainty in each MWA-32T flux measurement is due to the RMS map noise at the source location, and that the uncertainty in the predicted flux of each source is propagated for the power-law fitting procedure. This excess in the differences could be due to errors in the spectral model

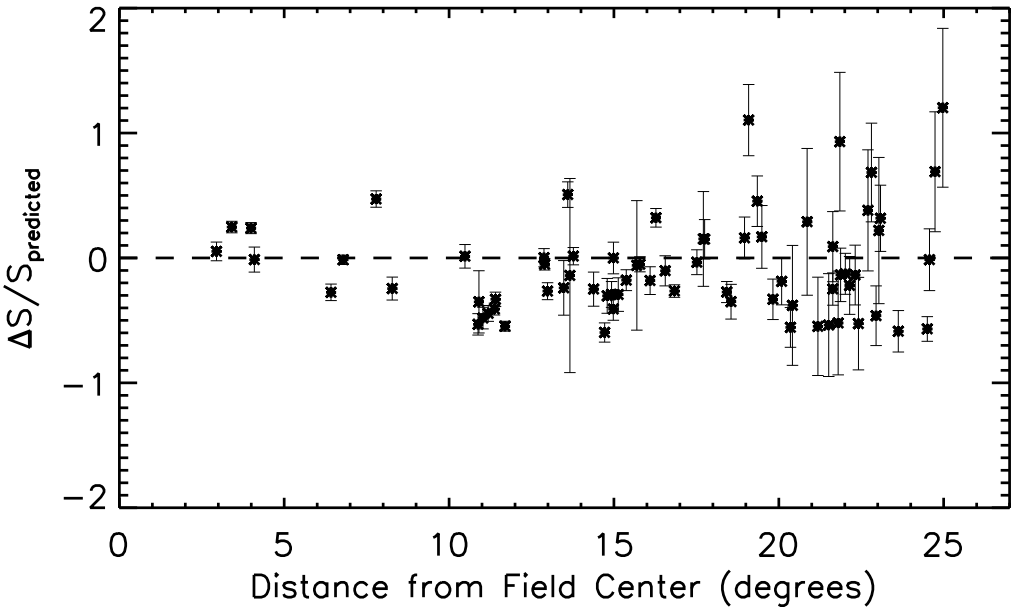

Figure 4-5: The fractional differences between predicted and measured fluxes for the EoR2 field at 154.24 MHz (described in Chapter 4.6.7), where ΔS is defined as the MWA-32T measured flux minus the flux predicted from fitting MRC and Culgoora measurements. The error bars are derived from combining the RMS noise in the MWA map at the source position in quadrature with the flux prediction uncertainty. The differences are displayed as a function of distance from the field center, in order to assess the presence of any radial biases in the MWA flux measurements. No significant bias was found out to large distances from the field center.

for the calibration sources, temporal variability of the sources, or to as yet unidentified errors. Since this is the first work based on MWA-32T data to report the fluxes of a large number of sources, we make the conservative assumption that these excessively large residuals are due solely to errors in the MWA-32T flux measurements. We assume the flux uncertainties follow a Gaussian distribution which includes the effects of the RMS map noise added in quadrature with an additional component proportional to the measured flux of the source:

$$\sigma^2_{\rm MWA} = \beta^2 S^2_{\rm MWA} + \sigma^2_{\rm Map}, \tag{4.9}$$

where $\sigma_{\rm MWA}$ is the 1σ flux uncertainty for a particular source, β is the fractional flux uncertainty, $S_{\rm MWA}$ is the measured source flux, and $\sigma_{\rm Map}$ is the RMS map noise at the position of the source. We evaluated the standard deviation, σ_D, of the fractional flux difference, D, where D is calculated as:

$$D = \frac{S_{\rm MWA} - S_{\rm Predicted}}{S_{\rm Predicted}}. \tag{4.10}$$

We then solved for the fractional uncertainty in the MWA measurements which would be needed to account for the magnitude of the measured value of σ_D:

$$\beta^2 = \sigma^2_D \left(\frac{S_{\rm Predicted}}{S_{\rm MWA}}\right)^2 - \left(\frac{\sigma_{\rm Predicted}}{S_{\rm Predicted}}\right)^2 - \left(\frac{\sigma_{\rm Map}}{S_{\rm MWA}}\right)^2. \tag{4.11}$$

We calculated the average value of β separately for each field. For the higher-frequency maps, we found that the values of β were much larger far from the field center where the primary beam approaches the first null; for these maps the sources were separated into inner and outer region sets using a cutoff of 18°, and β was calculated separately for each region. Using these results, we assign fractional flux uncertainties of 30% for all sources in the full-band average maps, 35% for all sources in the 123.52 MHz maps, 35% for sources in the inner region of the 154.24 MHz maps, 60% for sources in the outer region of the 154.24 MHz maps, 35% for sources in the inner region of the 184.96 MHz maps and 80% for sources in the outer region of the

184.96 MHz maps. These fractional uncertainty values are applied to all sources in the catalog by adding them in quadrature to the map RMS values as described in Equation 4.9.

4.7 Results

4.7.1 Radio Maps and Source Catalog

The full band average maps of the Hydra A and EoR2 fields are displayed in Figure 4-6 and Figure 4-7. These images overlap partially. Together, they cover ∼2700 square degrees. The synthesized beam for the Hydra A field has a major-axis width of 19′ in the 124.52 MHz map, 14′ in the 154.24 MHz map, 12′ in the 184.96 MHz map, and 13′ in the full band average map. For the EoR2 field, the major-axis beam widths are 18′ in the 124.52 MHz map, 16′ in the 154.24 MHz map, 13′ in the 184.96 MHz map, and 14′ in the full band average map.

The bright radio galaxy Hydra A is the dominant source in these maps. The flux of the source is measured to be 710 ± 210 Jy in the full band average map of the Hydra A field, and 550 ± 170 Jy in the full band average map of the EoR2 field. These measurements of Hydra A are significantly brighter than expected based on previous measurements: the Culgoora 160 MHz measurements give a flux of 243 Jy, and a prediction based off of the Culgoora and MRC measurements (as described in Chapter 4.6.7) gives a flux of 284 Jy. Although Hydra A is slightly extended in the MWA-32T maps, the structures seen in the previous low frequency maps of Hydra A presented by Lane et al. (2004) are below the scale of the MWA synthesized beam. We note that the MWA-32T array has a significantly more compact *uv* distribution than the VLA, Molonglo or Culgoora telescopes. A flux from Hydra A above what is expected from the Culgoora measurements is also noted in measurements with the PAPER array (Jacobs 2011, private communication), which has a similar baseline distribution to that of the MWA-32T. Consequently we did not include Hydra A in the final flux scale calibration procedure described in Chapter 4.6.7.

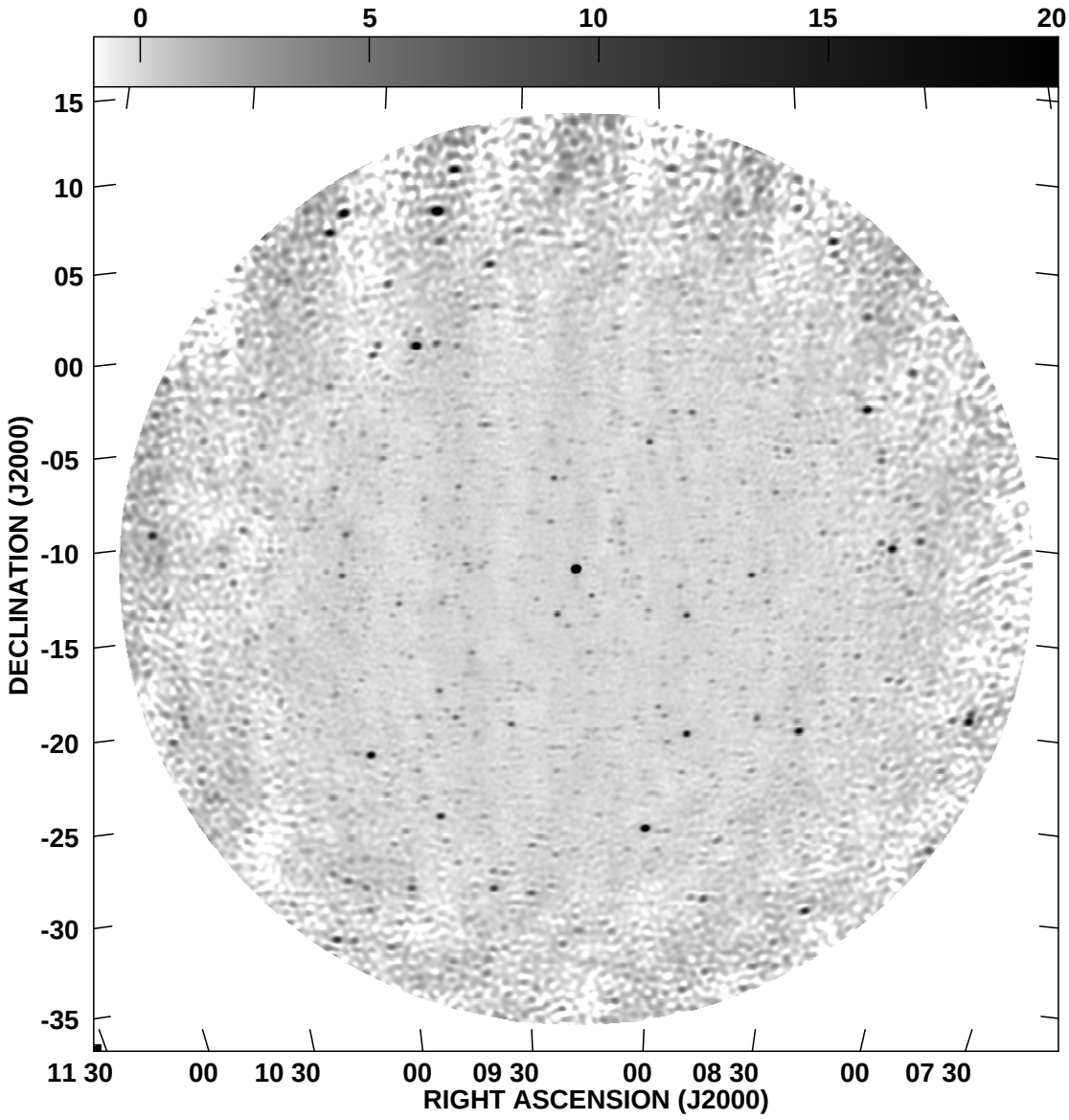

Figure 4-6: Full bandwidth synthesis map of the Hydra A field, with a 50° diameter. This map was produced using the pipeline described in Chapter 4.6, and served as a basis for source identification in this field.

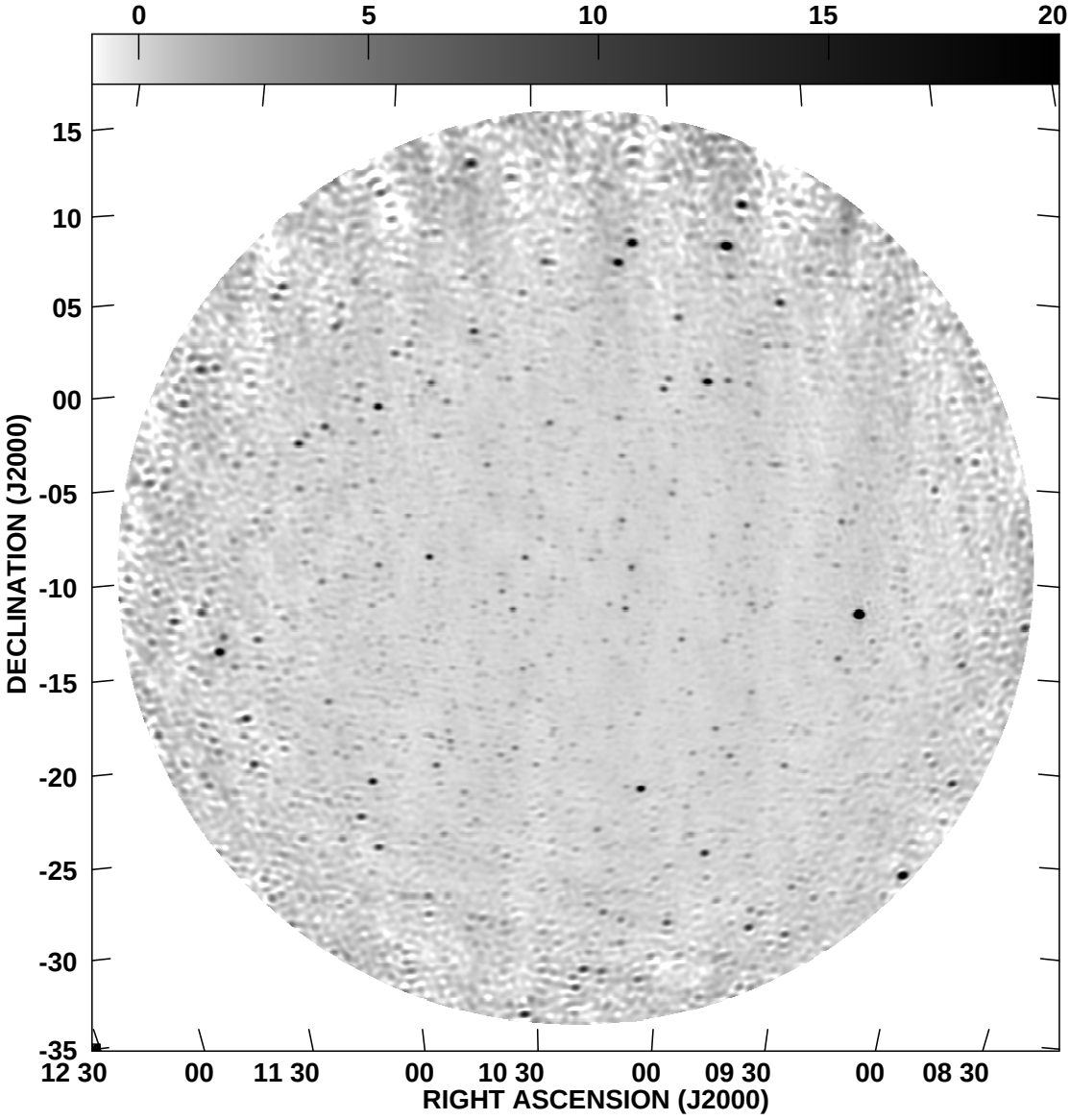

Figure 4-7: Full bandwidth synthesis maps of the EoR2 field, with a 50° diameter. This map was produced using the pipeline described in Chapter 4.6, and served as a basis for source identification in this field.

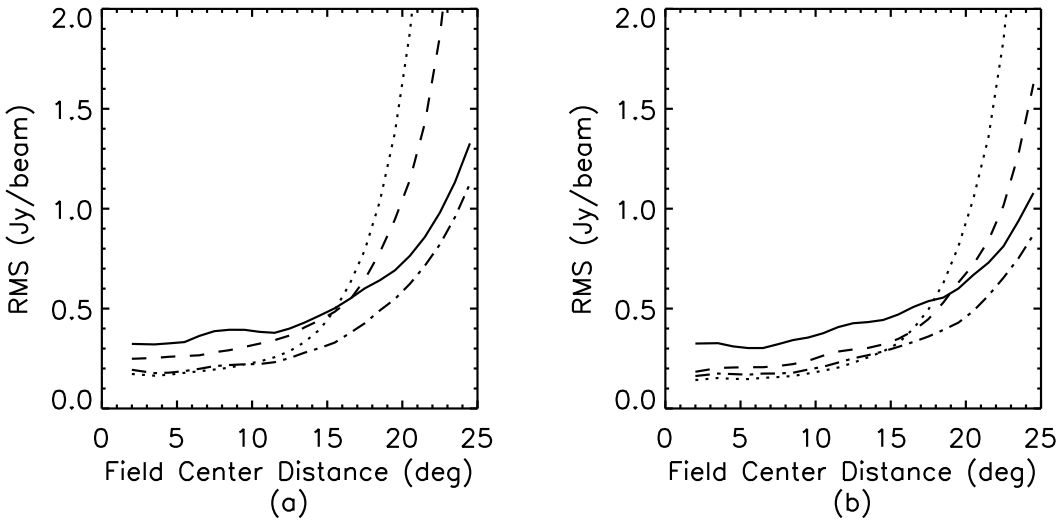

Figure 4-8: Radial dependence of the calculated RMS noise in the Hydra A (a) and EoR2 (b) field images. The RMS is plotted for the three sub-band maps, with central frequencies of 123.52 MHz (solid lines), 154.24 MHz (dashed lines), and 184.96 MHz (dotted line) as well as for the full-band averaged maps (dot-dashed lines). The values shown are the medians of 1° wide radial annuli. The points are connected with lines for clarity. The frequency dependent primary beam shape is evident from the increasing RMS at large distance from the field center, and the confusion limited nature of the maps is illustrated by the flat RMS profile near the center of the field. The minimum RMS approaches a value of ∼130 mJy/beam.

The behavior of the fitted RMS noise in these images is illustrated in Figure 4-8, which shows annular averages as a function of distance from the field center. We can estimate a lower limit to the RMS noise in each map by calculating the classical source confusion limit. Note that this differs from the sidelobe confusion limit; see, e.g. Condon 1974 for a rigorous discussion of classical source confusion in radio telescopes. Di Matteo et al. (2002) present a model of the radio source counts derived from the 6C (Hales et al., 1988) catalog at 150 MHz. Their expression takes the form of a broken power law[7]:

$$\frac{dn}{dS} = \begin{cases} 4000\ (\frac{S}{1\ \mathrm{Jy}})^{-2.51}\ \mathrm{sources\ Jy^{-1}\ sr^{-1}}, & S > S_0 \\ 4000\ (\frac{S_0}{1\ \mathrm{Jy}})^{-0.76}\ (\frac{S}{1\ \mathrm{Jy}})^{-1.75}\ \mathrm{sources\ Jy^{-1}\ sr^{-1}}, & S < S_0 \end{cases} \tag{4.12}$$

where $S_0 = 0.88$ Jy. Integration of this expression gives the source density in each beam above a minimum flux value, S_{min}:

$$\rho_S = \frac{\pi\theta^2}{4\ln 2}\int_{S_{\mathrm{min}}}^{\infty}\frac{dn}{dS}dS\ \mathrm{sources\ beam^{-1}}, \tag{4.13}$$

where ρ_S is the source density in units of sources per beam, and θ is the FWHM synthesized beam size. The source confusion limit then corresponds to the flux, S_{min}, for which the source density approaches one source per synthesized beam area (typically maps are considered to be source confusion limited when they have a source density of greater than 1 source per 10 synthesized beams). The average RMS noise (Figure 4-8) reaches a minimum value of ∼160 mJy for the full band average map of the EoR2 field. Using the corresponding flux threshold for an unresolved source of $S_{\mathrm{min}} = 160$ mJy in combination with the EoR2 full band map synthesized beam area gives $\rho_S \sim 0.30$ sources per synthesized beam, or, in other words, one source of at least 160 mJy in roughly every three synthesized beams. Estimates for the other average and sub-band maps give expected source densities of one source per every 3

[7]The notation of Di Matteo et al. (2002) is ambiguous, and is interpreted differently by several authors. We note that Lidz et al. (2008) quote a modified form of the expression, which affects the normalization of the power law. Although the Lidz et al. (2008) expression fits the 6C source counts slightly better at high flux values, the formulation presented in this paper fits the data better throughout the entire flux range. The expression from Di Matteo et al. (2002) has been corrected with an additional minus sign to make it continuous across the transition at $S = S_0$.

to 6 synthesized beams . Thus, source confusion is likely the limiting source of noise in the central region of these maps. This explains the relatively flat nature of the central noise floor seen in Figure 4-8. Near the edges of the images, not far from the first null of the primary beam, we expect the noise to be dominated by receiver noise, and to scale with the inverse of the primary beam power pattern. This is also seen in Figure 4-8 (the frequency dependence of the noise curves illustrates the frequency dependence of the primary beam).

A catalog was constructed from the 2008 detections at a detection SNR threshold ≥ 3 of potential sources in the EoR2 and Hydra A fields. In the cases where there were detections at corresponding celestial positions in the two fields, the measurement where the source was closer to the observation field center was retained, resulting in a list of 1526 unique source detections. The quality of this source list is assessed in Chapter 4.7.2 and Chapter 4.7.3 as a function of the detection SNR level. The 655 sources detected at an SNR level $\geq$5 in the detection images are reported in Table 4.2. The 871 sources with 3$\leq$SNR$<$5 are considered to be less reliable detections. A list of these candidate detections can be obtained by contacting the authors.

4.7.2 Reliability of the Source List

The reliability of the identified sources was evaluated through comparison with the flux limited sample from the MRC, the VLSS, and maps from the TGSS. The MRC source list has a well-defined completeness flux limit and covers our entire field; however it gives fluxes at a different frequency (408 MHz) and does not go quite as deep as our survey. The VLSS covers a portion of our fields at a lower frequency than the MWA (74 MHz), and provides a useful complementary assessment. The TGSS maps are at the same frequency as the MWA observations (150 MHz), but the maps which have been released to date only cover a small fraction of our fields and are based on a significantly different sampling of the visibility function due to the different array baselines.

In order to assess the MWA-32T catalog reliability, we first evaluate the detectability of an MWA source in the external comparison survey. The MWA full band average

Table 4.2. Detected sources in the the Hydra A and EOR 2 fields

Name	RA	DEC	$S_{\rm avg}$	$S_{123.52}$	$S_{154.24}$	$S_{184.96}$	Field	$r_{\rm FC}$	Detection SNR Level
J0747−1854	07h47m05s	−18°54′12″	8.8±2.8	10.1±3.7	9.2±6.0	8.9±8.5	HydA	22.9°	8.6
J0747−1919	07h47m27s	−19°19′33″	22.2±6.7	25.2±8.9	23.8±14.5	15.1±13.0	HydA	23.0°	22.4
J0751−1919	07h51m20s	−19°19′30″	7.1±2.2	8.1±3.0	8.5±5.3	4.7±5.1	HydA	22.1°	8.7
J0752−2204	07h52m30s	−22°04′38″	4.4±1.5	4.7±1.8	7.1±4.5	14.4±12.1	HydA	22.7°	5.6
J0752−2627	07h52m30s	−26°27′43″	8.4±2.7	9.8±3.7	3.6±3.1	···	HydA	24.7°	7.0
J0757−1137	07h57m10s	−11°37′10″	3.9±1.3	4.7±1.8	5.1±3.3	2.5±2.5	HydA	19.8°	6.0
J0802−0915	08h02m18s	−09°15′32″	3.4±1.2	5.8±2.2	2.1±1.5	1.9±1.8	HydA	18.8°	5.0
J0802−0958	08h02m34s	−09°58′55″	8.9±2.8	12.4±4.4	6.0±3.7	9.1±7.3	HydA	18.6°	12.6
J0803−0804	08h03m60s	−08°04′48″	4.5±1.4	6.5±2.4	2.4±1.6	6.7±5.4	HydA	18.7°	7.0
J0804−1244	08h04m17s	−12°44′32″	4.6±1.5	4.8±1.8	5.2±3.2	4.5±3.7	HydA	18.0°	9.3
J0804−1726	08h04m42s	−17°26′41″	4.9±1.5	5.8±2.1	4.5±2.8	3.1±2.6	HydA	18.5°	9.1
J0804−1502	08h04m53s	−15°02′54″	2.8±0.9	2.2±1.0	4.6±2.9	1.0±1.1	HydA	18.0°	6.4
J0805−0100	08h05m30s	−01°00′12″	9.4±2.9	10.8±3.9	8.3±5.2	6.4±5.4	HydA	21.1°	10.4
J0805−0739	08h05m40s	−07°39′22″	3.5±1.2	4.4±1.7	3.7±2.4	1.9±1.9	HydA	18.4°	5.5
J0806−2204	08h06m26s	−22°04′43″	3.7±1.2	4.2±1.6	3.8±2.4	3.6±3.1	HydA	19.8°	6.2

Note. — Table 4.2 is published in its entirety in Appendix A. A sample is shown here to illustrate its content.

Note. — The flux of each source detected in the MWA full-band averaged maps is presented along with the flux measured in each 30.72 MHz sub-band. Duplicate sources in the region of overlap of the two fields are not listed. Missing data indicates that the automatic source measurement algorithm failed to converge in a flux fit for that source in the sub-band map. The field from which each source measurement comes from is listed, along with the distance of the source from the center of the field ($r_{\rm FC}$). We expect systematic errors to be larger for sources far from the field center. The "Detection SNR Level" indicates the signal-to-noise ratio at which the source was detected in the full-band averaged map. Chapter 4.7.2 discusses the reliability of the catalog at different detection SNR levels. This list includes sources identified above a detection SNR threshold of 5. The full source list of all sources above a detection SNR threshold of 3 is also presented in Appendix A, however we view this list to be less reliable

flux is extrapolated to the relevant frequency using a spectral index of $\alpha = -0.8$, and the extrapolated value is then compared to the parameters of the comparison map or catalog to evaluate whether it meets the detection criteria for that survey. If the source is deemed detectable, then we search for a companion source in that catalog or map to see if the source was actually detected by the other survey. Under the assumption that the other surveys are complete, this allows us to assess how many spurious sources are present in the MWA catalog. We define the reliability as:

$$R = \frac{N_{\rm detected}/N_{\rm detectable} - f}{1 - f}, \tag{4.14}$$

where R is the fraction of MWA sources we believe to be reliable, $N_{\rm detectable}$ is the number of MWA sources which we believe should have been detectable in the comparison survey, $N_{\rm detected}$ is the number of detectable MWA sources for which we found counterparts in the other survey, and f is the false source coincidence fraction. We determine f by calculating the source density of the comparison survey in the MWA fields, and use our counterpart matching criteria to estimate the probability that a randomly chosen sky location will lead to an association with a source in the comparison survey. This analysis was performed for different MWA source detection thresholds.

For the reliability comparison with the MRC, we used the completeness limit of 1 Jy (Large et al., 1981) to assess the detectability of the extrapolated MWA source fluxes. An MRC counterpart is associated with the MWA source if it is within $10'$ of the MWA source position. Based on the counterpart search radius and source densities in the MRC field, we estimate a false coincidence chance of 4%. A fixed flux completeness limit is not given for the VLSS, however Cohen et al. (2007) note that for a typical VLSS RMS of 0.1 Jy beam^{-1}, the 50% point source detection limit is approximately 0.7 Jy. We then assume the VLSS is complete down to a flux level of 1 Jy, and we again use a $10'$ source association radius in the reliability calculation. At the present time, the VLSS catalog does not cover the entire combined EoR2 and Hydra A region that we have surveyed. To ensure we are only including sources in the

VLSS survey area, we only analyzed MWA sources above a declination of $\delta = -25°$. We estimate a false coincidence chance of 18% for the VLSS matching.

The cumulative and differential catalog reliabilities are listed as functions of the MWA detection level in Table 4.3 and Table 4.4. We view these reliability estimates as lower limits, particularly at the lower flux levels, because our assessments of comparison survey detectability do not take into account errors in the source flux extrapolation or source time variability. MWA sources which are erroneously calculated as detectable will not, in general, lead to detections of counterparts in the comparison catalog, whereas sources erroneously calculated as undetectable will be omitted from the analysis and, therefore, will not be included in the calculation of the reliability ratio. These catalog comparisons imply a reliability of $\gtrsim 99\%$ for sources detected above a detection SNR of 5.

For the reliability comparison using the TGSS, we used the maps from TGSS Data Release 2 available at the time of our analysis. Although the baseline distribution of the GMRT is substantially different from that of the MWA-32T, the GMRT has a compact central array consisting of fourteen antennas within an area of radius 500 meters (Swarup et al., 1991) that leads to substantial overlap with the MWA-32T regarding the region of the uv plane that was sampled. Twenty-seven TGSS fields overlapped the EoR2 field; none overlapped the Hydra A field. We modeled the effects of source blending by the large MWA beam by convolving the CLEANed and restored TGSS maps to a Gaussian full width at half maximum resolution of $12'$. Care was taken in the convolution to preserve the flux density scale. The resulting convolved images have typical RMS surface brightness fluctuations of $\sim$0.4 Jy/beam in regions free of sources. Sources in these maps were identified by taking all pixels above 4σ and associating a source with each island of bright pixels. The resulting TGSS source catalog was compared to those sources in the MWA list with flux density greater than the 4σ level in the TGSS field, and thus expected to be detected in the TGSS field. Pairs of sources in the two catalogs coincident within $10'$ were recorded as sources detected in both surveys. MWA sources without a TGSS counterpart were counted as non-detections. Reliability values are presented in Tables 4.3 and 4.4. These values

Table 4.3. Cumulative Source Reliability

Detection SNR Threshold	MRC Reliability $N_{\rm detected}/N_{\rm detectable}$	R	VLSS Reliability $N_{\rm detected}/N_{\rm detectable}$	R	TGSS Reliability $N_{\rm detected}/N_{\rm detectable}$	R
> 3	488/589	82%	1215/1312	91%	183/197	93%
> 4	421/444	95%	826/839	98%	132/133	99%
> 5	349/357	98%	575/579	99%	85/85	100%
> 7	257/259	99%	325/326	100%	49/49	100%
> 10	167/167	100%	173/173	100%	26/26	100%

Note. — The reliability is assessed by comparing the MWA source list with the MRC catalog, VLSS catalog, and convolved TGSS maps as descriged in Chapter 4.7.2. The MRC and VLSS comparisons are made by extrapolating the MWA source flux to 408 MHz and 74 MHz respectively, assuming a spectral index of $\alpha = -0.8$, to assess the detectability of the MWA source in the catalogs. The TGSS results are based on using sources in convolved TGSS maps above 4σ significance. The reliability percentages, R, have been corrected for false positives.

are ratios for each MWA detection SNR bin of the number of TGSS detections to the number of MWA sources expected to be detected in the TGSS field, and are, of course, a function of the threshold chosen in the TGSS maps. As an example of the TGSS comparison we present Figure 4-9, which plots the positions of MWA and MRC sources on a grey scale image of a convolved TGSS field. It is important to note that these reliability estimates solely test for the presence of a source coincident with the reported position, and do not speak to the fidelity of the fluxes of these sources or whether the MWA sources are due to single objects or blends of multiple fainter objects.

4.7.3 Completeness of the Source Catalog

We used the Culgoora source list to assess the completeness of the MWA catalog presented in this paper. We chose the Culgoora list because it includes observations done at 160 MHz, a frequency not far from the midpoint of the MWA band and because its synthesized beam is similar in size to that of the MWA-32T. For each Culgoora source within a field observed by the MWA we used the position-dependent RMS noise in the MWA full-band averaged maps to evaluate its detectability in the MWA map. Culgoora sources which should be detectable above a specified SNR level in the MWA images were then checked for a matching source within $10'$ in the

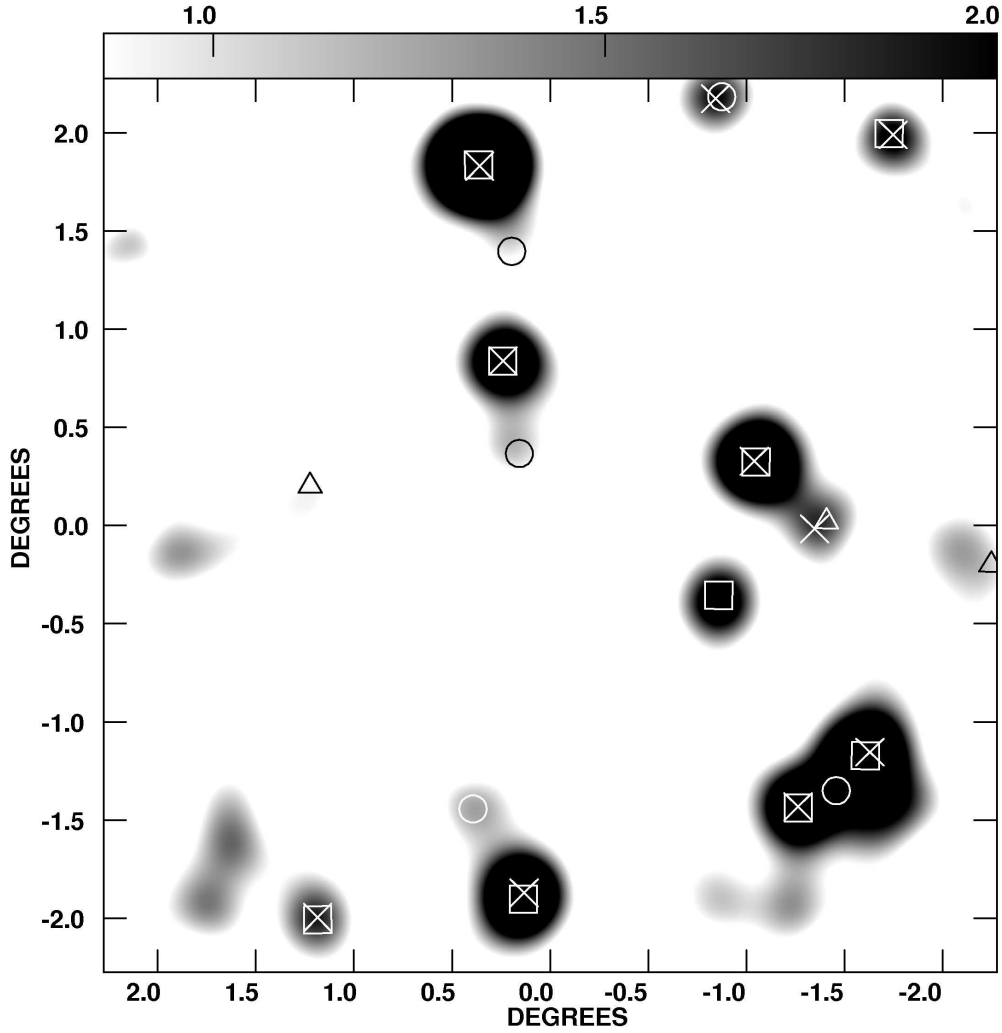

Figure 4-9: Grey scale image of a TGSS field (field R33D18), with positions of MWA and MRC sources overlaid. Only pixels with SNR > 4 are plotted, and the mapping of pixels to grey scale is shown by the scale in Jy beam^{-1} at the top of the image. Positions of MWA sources with Detection Threshold > 5 are plotted with a square, of MWA sources with $4 <$ Detection Threshold ≤ 5 are plotted with a circle, of MWA source with $3 <$ Detection Threshold ≤ 4 with a triangle, and of MRC sources with an X. All MWA and MRC sources in this field have a counterpart in the TGSS image. There are five sources in the field that are detected in the MWA and TGSS surveys, but not in the MRC.

Table 4.4. Differential Source Reliability

Detection SNR Threshold (DT)	MRC Diff. Reliability $N_{\rm detected}/N_{\rm detectable}$	R	VLSS Diff. Reliability $N_{\rm detected}/N_{\rm detectable}$	R	TGSS Diff. Reliability $N_{\rm detected}/N_{\rm detectable}$	R
$3 < \mathrm{DT} \leq 4$	67/145	44%	389/473	78%	51/64	80%
$4 < \mathrm{DT} \leq 5$	72/87	82%	251/260	96%	47/48	98%
$5 < \mathrm{DT} \leq 6$	43/48	89%	142/144	98%	20/20	100%
$6 < \mathrm{DT} \leq 7$	49/50	98%	108/109	99%	16/16	100%
$7 < \mathrm{DT} \leq 8$	33/34	97%	68/69	98%	15/15	100%
$8 < \mathrm{DT} \leq 9$	31/32	97%	44/44	100%	7/7	100%
$9 < \mathrm{DT} \leq 10$	26/26	100%	40/40	100%	1/1	100%

Note. — The reliability is assessed by comparing the MWA source list with the MRC catalog, VLSS catalog, and convolved TGSS maps for various ranges of detection SNR threshold (DT) as discussed in Chapter 4.7.2. The MRC and VLSS comparisons are made by extrapolating the MWA source flux to 408 MHz and 74 MHz respectively, assuming a spectral index of $\alpha = -0.8$, to assess the detectability of the MWA source in the catalogs. The TGSS results are based on using sources in convolved TGSS maps above 4σ significance. The reliability percentages, R, have been corrected for false positives.

MWA catalog. Since we used the Culgoora source list to assess the completeness, the results are only valid down to a level comparable to the lowest Culgoora fluxes of ~ 1.2 Jy. The completeness ratio was calculated similarly to the reliability described in Chapter 4.7.2:

$$C = \frac{N_{\rm detected}/N_{\rm detectable} - f}{1 - f}, \tag{4.15}$$

where C is the completeness percentage, $N_{\rm detectable}$ is the number of Culgoora sources which we believe should have been detectable in the MWA source list , $N_{\rm detected}$ is the number of detectable Culgoora sources for which we found counterparts in the MWA list, and f is the false source coincidence fraction calculated from the MWA catalog source density using the $10'$ source matching criteria. The results are presented in Table 4.5.

The completeness was analyzed separately for sources within inner and outer regions separated by a circle of radius $r = 18^\circ$ around the field center. All Culgoora sources within the inner region which did not have a corresponding detection in the MWA source list were inspected and found to coincide with a local maximum in the map, implying the completeness is limited by the robustness of the source extraction algorithm and the flux calibration rather than the intrinsic map quality.

Table 4.5. Source List Completeness

Field Name	$r < 18^\circ$ $N_{\rm detected}/N_{\rm detectable}$	Completeness	$r > 18^\circ$ $N_{\rm detected}/N_{\rm detectable}$	Completeness
Detection SNR Level ≥ 5				
Hydra A	56/63	89%	36/44	82%
EoR2	72/77	93%	49/58	84%
Detection SNR Level ≥ 3				
Hydra A	62/63	98%	52/67	77%
EoR2	75/77	97%	61/66	92%

Note. — The completeness as assessed by a comparison with the Culgoora source list (Slee, 1995), as described in Chapter 4.7.3. The minimum source flux in the Culgoora list is ∼1.2 Jy, so these results are only valid for sources brighter than this level. We view these completeness estimates as a lower limit on the catalog completeness – source variability or flux errors in the Culgoora measurement will decrease the calculated completeness ratio. Due to the varying sensitivity across the MWA field, the completeness is calculated relative to the local noise in the MWA source detection map, rather than an absolute flux level. The completeness percentages have been corrected for false positives as described in Chapter 4.7.3. Analyzing the source counts in the field (see Chapter 4.7.4) indicates that the source list is complete above ∼2 Jy.

It is important to note that because the MWA maps have a sensitivity that varies strongly across the field, this completeness value does not specify a flux limit to the catalog, but rather assesses the efficacy of the source extraction. As with the above reliability estimate, variability and incompleteness act to make this a lower limit on the true completeness.

4.7.4 Source Counts and Correlation Function

Radio source counts provide another useful diagnostic test to assess the quality of the catalog and consistency with previous works. As discussed in Chapter 4.7.1, Di Matteo et al. (2002) fit the 151 MHz 6C survey results of Hales et al. (1988) to

obtain a power law model for radio source counts. The fit is valid up to $\sim$ 10 Jy, but the actual 6C counts fall somewhat below the fit at the high end of the range. Using the MWA-32T catalog generated from the EoR2 field, we calculate the differential source counts, using the noise map of the field to correct for the effects of sensitivity variations on the effective survey area for different flux values (i.e., bright sources can be detected over a larger area than faint sources). No Eddington bias correction is applied (to correct for the artificial enhancement of faint sources due to noise in the map) and the error bars are calculated from the square root of the number of counts in each bin. These source counts are shown in Figure 4-10, along with the expected source counts from integrating the Di Matteo et al. (2002) model. We note that more sophisticated models of 150 MHz source counts models have been described by, e.g., Wilman et al. (2008) and Jackson (2005). These models have different behavior at the sub-Jansky flux levels that have been probed by high resolution, deep, narrower field-of-view studies such as those described in Intema et al. (2011) and Ishwara-Chandra et al. (2010). We compare our results with the Di Matteo et al. (2002) source counts model because it is commonly used as a basis for studies of EoR foregrounds and sensitivities.

The results from the catalog presented in this work agree with the Di Matteo et al. (2002) model above flux levels of $\sim$2 Jy. Below this level, the MWA-32T source counts diverge from the model, likely because of the incompleteness of the MWA source extraction for low flux sources. A power law fit to the EoR2 field source counts above 2 Jy yields $dn/dS = (3500 \pm 500)(S/1\text{ Jy})^{-2.59\pm0.09}$ sources Jy^{-1} sr^{-1} for sources with a detection SNR greater than 5. Fitting for a power law to the full list of sources in the field down to a detection SNR of 3 yields $dn/dS = (5700 \pm 700)(S/1\text{ Jy})^{-2.76\pm0.08}$ sources Jy^{-1} sr^{-1}.

As an additional test for systematic effects, we have constructed the angular two-point correlation function, $w(\theta)$, of the sources in our catalog. This correlation function can show systematic effects that manifest themselves on characteristic angular scales in the catalog – see, e.g. Blake & Wall (2002). We measure $w(\theta)$ using the

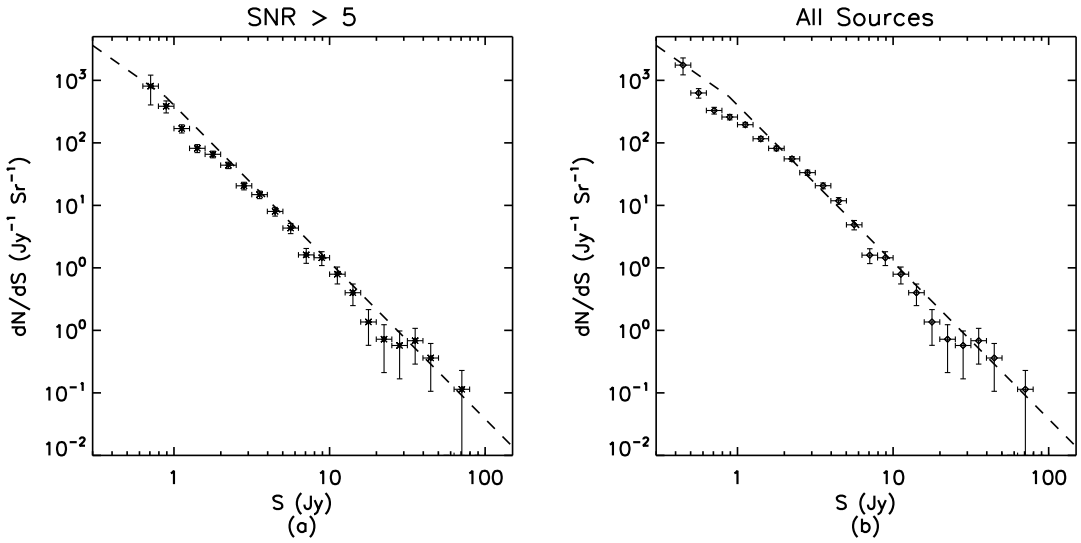

Figure 4-10: Differential source counts histograms from the MWA EoR2 field, calculated using both the high reliability catalog (a) and the full list of source candidates (b). The noise maps were used to correct for the effective area surveyed in each bin. Poisson error bars are assigned based on the number of counts in each bin. No Eddington bias correction is applied. The source counts model from Di Matteo et al. (2002) is shown for reference with a dashed line. We believe the deviations from the Di Matteo et al. (2002) model below $S \sim 3$ Jy are not due to an intrinsic change in the source counts distribution at this scale, but are instead due to incompleteness of the source catalog in this flux range.

estimator defined by Hamilton (1993):

$$w(\theta) = \frac{DD(\theta)RR(\theta)}{DR(\theta)} - 1, \tag{4.16}$$

where $DD(\theta)$ is the measured angular autocorrelation function from the MWA source catalog, $RR(\theta)$ is the autocorrelation function calculated using a simulated "mock" catalog, and $DR(\theta)$ is the cross-correlation between the MWA and the mock catalog. We generate an ensemble of 100 mock catalogs and evaluate the correlation function with each one separately in order to produce a set of normally distributed estimates of $w(\theta)$. Each mock catalog is produced using an approach developed to simulate point sources at CMB and FIR frequencies (Argüeso et al., 2003; González-Nuevo et al., 2005), but tailored specifically for the MWA experiment (de Oliveira-Costa et al., in prep.), i.e., we drew sources from the observed MWA-32T source counts distribution described above in accordance with the expected low-frequency source clustering statistics (de Oliveira-Costa & Capodilupo, 2010; de Oliveira-Costa & Lazio, 2010). On the angular scales probed by this survey, no observable clustering is expected. By constructing the mock catalogs in this manner, and correlating them with the observed distribution, the resulting estimate of $w(\theta)$ identifies any unexpected correlation which may be due to systematic errors in our survey or in our catalog construction procedure. Figure 4-11 shows our measurement of $w(\theta)$ above a flux limit of $S \approx 3$ Jy (black squares). Distances between the observed and/or simulated sources are measured in bins of $\sim 1^\circ$, which is substantially above the MWA resolution. The mean value of $w(\theta)$ is shown, along with uncertainties derived from calculating the covariance between $w(\theta)$ bins in the mock catalogs. As expected, $w(\theta)$ is consistent with zero, implying that there is no excess correlation in our catalog.

4.7.5 Comparison with PAPER Results

Comparing the present results from the MWA with results from PAPER (Parsons et al., 2010) is a particularly useful exercise, as both arrays are new, broadband, wide field-of-view instruments with similar uv coverage, and both are intended to be used to

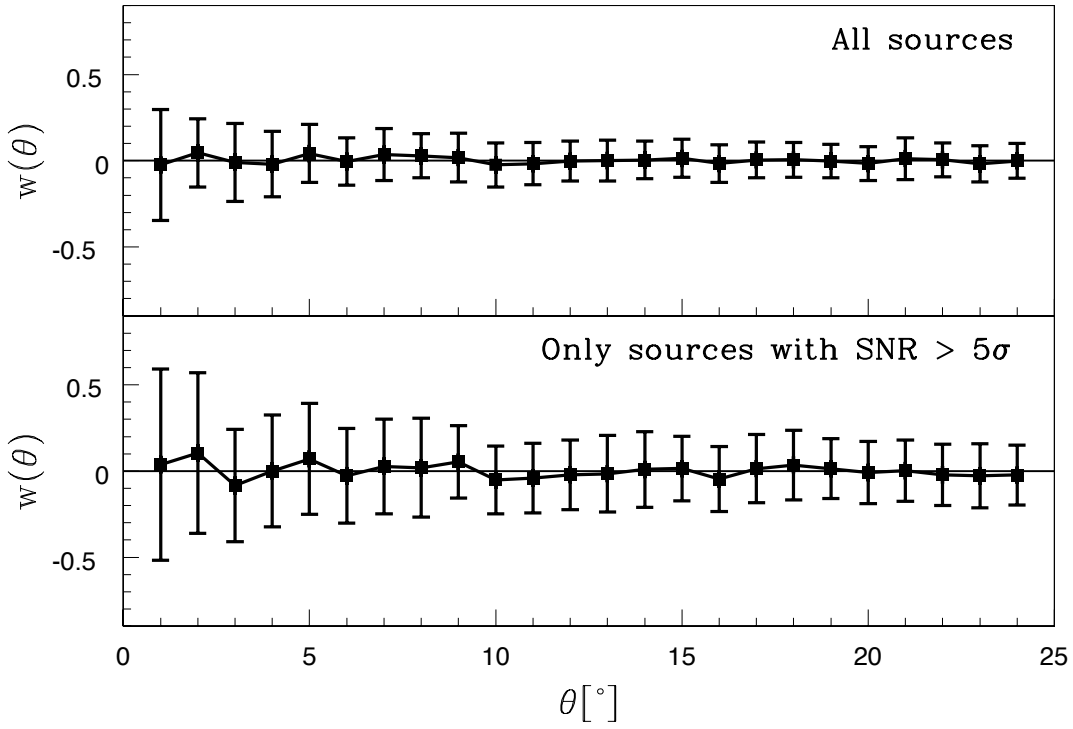

Figure 4-11: Measured angular correlation function, $w(\theta)$, of the full MWA catalog. The angular correlations are calculated using sources with fluxes above $S \sim 3$ Jy. The top panel shows $w(\theta)$ calculated from all sources in our final catalog, while the bottom panel shows $w(\theta)$ calculated only from sources detected above a detection SNR threshold of 5. As expected, the results are consistent with zero correlation.

make EoR power spectrum measurements. We find that 43 of the sources found in the survey (described in Chapter 4.2) of Jacobs et al. (2011) are located in our survey region. A search in our MWA-32T catalog reveals unique counterparts within $30'$ (the PAPER beam size used by Jacobs et al. 2011 for source association) of the PAPER locations for 31 out of these 43 sources, multiple counterparts in 11 cases, and no counterpart in one case.

The one source with no MWA counterpart is 24° from the center of the MWA Hydra A field, and corresponds to a local maximum in the MWA image; however it was not detected by the automatic source finding algorithm. For each of the 10 sources with multiple MWA counterparts, an estimate of the blended flux was obtained by summing the flux of all MWA sources within the PAPER beam. Other than Hydra A, all 41 PAPER fluxes are consistent with the MWA blended fluxes (the Hydra A flux reported in the PAPER catalog was corrupted by the filtering used in the PAPER analysis, Jacobs 2011, private communication). A weighted average of the ratios of the MWA and PAPER source fluxes yields the average ratio $< S_{\rm MWA}/S_{\rm PAPER} > = 1.17 \pm 0.10$. However, we note that the PAPER flux scale was set using measurements of two calibration sources from the Culgoora source list, whereas the MWA-32T flux scale was set using a fit to an ensemble of Culgoora and MRC measurements. Slee (1977) note that the Culgoora flux scale may be depressed by 10%, with additional flux uncertainties of between 13% and 39% for individual source measurements. If these Culgoora flux uncertainties are taken into account as potential errors on the PAPER flux scale, then the significance of the difference between the MWA and PAPER flux scales is decreased.

The standard deviation of the MWA to PAPER flux ratios after correcting for the different flux scales is $\sim$25%. This is smaller than our estimate of the MWA flux uncertainties based on flux predictions from the MRC and Culgoora measurements. This indicates that the flux comparison with the MRC and Culgoora lists may be affected to a considerable extent by radio source variability or other systematic effects.

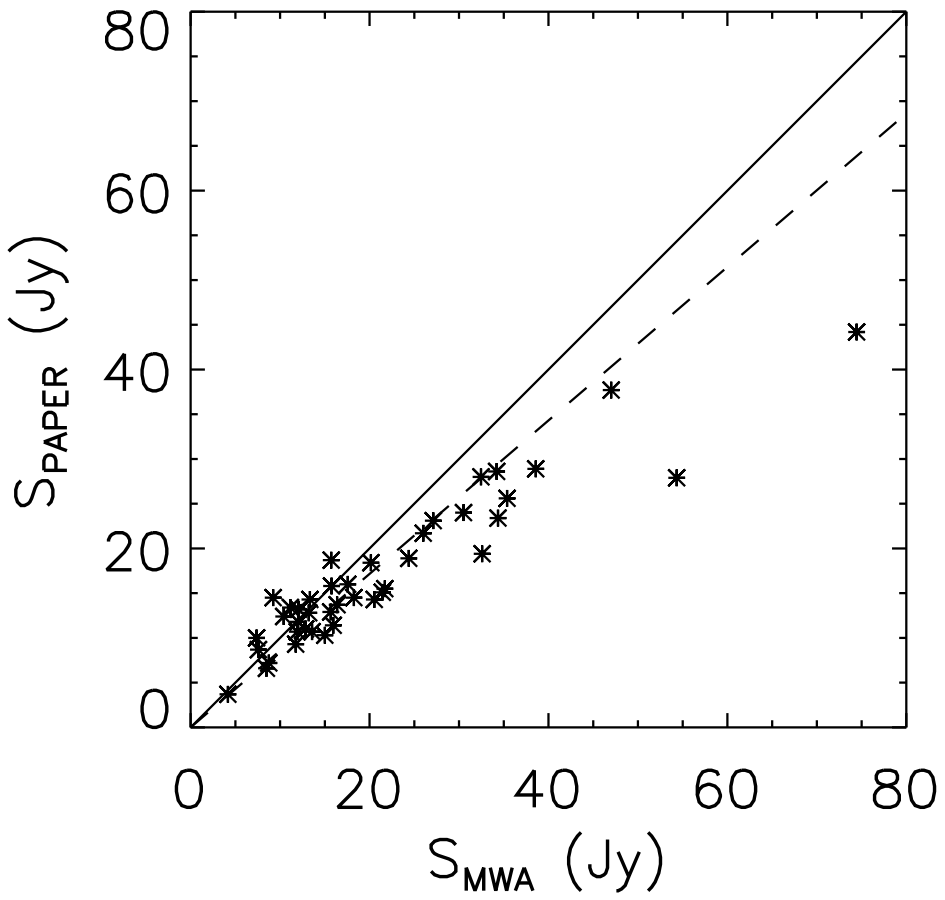

Figure 4-12: Comparison of the fluxes presented in this work with those from the 145 MHz PAPER source list presented in Jacobs et al. (2011). Error bars have been omitted from the plot for clarity. A total of 43 sources from the PAPER list are within the MWA field. MWA sources, which are within 30′ of a PAPER source are matched. A total of 31 of the PAPER sources had unique counterparts, while 11 PAPER sources matched with multiple MWA sources and 1 PAPER source did not have a detected MWA counterpart (although there is a local maximum in the MWA map at the location of the PAPER source). The MWA fluxes are calculated by summing the flux of all MWA sources which match with a PAPER source, and scaling the flux to a frequency of 145 MHz assuming a spectral index of $\alpha = -0.8$ ($S \propto \nu^{-\alpha}$). The solid line shows the unity flux-ratio locus; the MWA sources are on average 17% brighter than the PAPER sources. This fitted flux ratio locus is plotted as a dashed line.

4.7.6 Candidate Ultra Steep Spectrum Sources

"Ultra Steep Spectrum" (USS) radio sources form a compelling class of candidate high redshift radio sources (De Breuck et al., 2000; Di Matteo et al., 2004; De Breuck et al., 2002; Broderick et al., 2007). Low frequency radio observations are particularly sensitive to these objects (see, e.g. Pedani 2003). We have conducted an analysis of the sources detected in the MWA fields in an attempt to identify additional USS radio sources. A table of candidates is presented in Table 4.6. We calculated spectral indices by using the PMN 4.85 GHz survey (Griffith & Wright, 1993) together with the MWA full-band average flux measurements. We associated MWA sources with PMN counterparts if their positions were coincident within $5'$. To avoid source confusion and blending issues, we excluded any MWA sources with more than one PMN counterpart within a $30'$ radius. A total of 331 sources were identified for which we could unambiguously identify a counterpart and extract a spectral index. A histogram of the spectral indices are shown in Figure 4-13. This histogram appears consistent with the low-frequency selected spectral index distributions obtained by De Breuck et al. (2000), and plotted in their Figure 7 (however, the De Breuck et al. 2000 analysis used slightly different frequencies). Using a low-frequency selected distribution results in a sample which is significantly more sensitive to the USS sources.

We choose a spectral index cutoff of $\alpha \leq -1.2$ for USS source candidates, and find 3 sources which match the criteria. All three sources have counterparts in the MRC, and the source MWA J1032-3421 has a counterpart in both the PAPER and Culgoora source lists (although the other two USS candidates do not). A further 33 sources are identified which have no counterpart in the PMN catalog within 1°. Using the PMN catalog limiting flux of 50 mJy (Griffith & Wright, 1993) for these sources, we find that 25 of these 33 sources have an inferred spectral index of $\alpha \leq -1.2$. Of these 25 sources, 11 have unique counterparts in the MRC (one additional source has multiple counterparts), 9 have counterparts in the Culgoora source list, and none have counterparts in the PAPER source list.

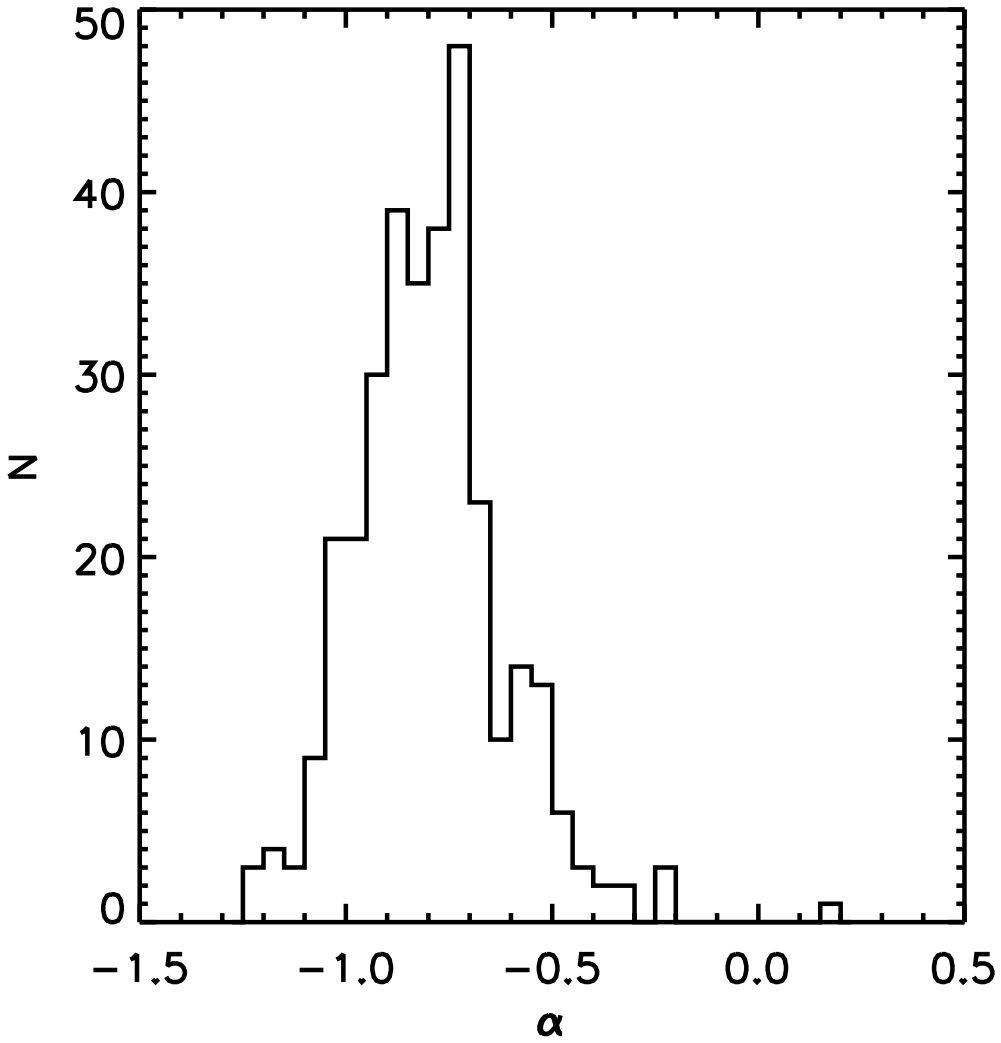

Figure 4-13: Distribution of spectral indices ($S_\nu \propto \nu^\alpha$) between 154.25 MHz and 4.85 GHz for sources identified in this paper, based on a comparison with the Parkes-MIT-NRAO catalog (Griffith & Wright, 1993). To avoid issues of source confusion and blending, only sources which could be unambiguously associated with single PMN counterparts are included in the histogram.

Table 4.6. Ultra-Steep Spectrum Source Candidates

Name	RA	DEC	$S_{\rm MWA,avg}$	$S_{\rm PMN}$	$\alpha_{\rm PMN}$	$S_{\rm MRC}$	$\alpha_{\rm MRC}$	Detection SNR Level
J1009−1207	10h09m19s	−12°07′46″	10.69±3.21	0.17±0.01	-1.20±0.09	3.23±0.11	-1.23±0.31	52.5
J1032−3421	10h32m60s	−34°21′19″	17.38±5.31	0.27±0.02	-1.21±0.09	5.59±0.25	-1.17±0.32	15.5
J1042+1201	10h42m56s	+12°01′30″	15.55±4.80	···	<-1.66±0.09	8.90±0.37	-0.57±0.32	15.1
J1034+1111	10h34m13s	+11°11′23″	5.89±1.92	···	<-1.38±0.09	3.80±0.16	-0.45±0.34	8.3
J1000+1400	10h00m16s	+14°00′17″	7.54±2.51	···	<-1.45±0.10	3.06±0.10	-0.93±0.34	6.3
J0831−2922	08h31m24s	−29°22′26″	3.65±1.24	···	<-1.24±0.10	1.51±0.06	-0.91±0.35	5.7
J1007+1246	10h07m28s	+12°46′50″	7.46±2.52	···	<-1.45±0.10	···	···	5.6
J0855+0552	08h55m18s	+05°52′50″	4.11±1.40	0.06±0.01	-1.23±0.12	1.62±0.07	-0.96±0.35	5.4
J0834−3443	08h34m29s	−34°43′22″	6.14±2.12	···	<-1.40±0.10	···	···	5.0
J0828−3201	08h28m14s	−32°01′26″	4.68±1.66	···	<-1.32±0.10	···	···	4.8
J1001+1108	10h01m01s	+11°08′19″	3.98±1.37	···	<-1.27±0.10	1.57±0.06	-0.96±0.36	4.6
J0832−3326	08h32m38s	−33°26′00″	5.14±1.84	···	<-1.34±0.10	2.30±0.09	-0.83±0.37	4.4
J1008+1201	10h08m11s	+12°01′07″	4.48±1.65	···	<-1.30±0.11	···	···	4.2
J1028+1158	10h28m32s	+11°58′58″	3.56±1.30	···	<-1.24±0.11	···	···	4.1
J1112+1112	11h12m45s	+11°12′45″	4.88±1.92	···	<-1.33±0.11	1.45±0.07	-1.25±0.41	3.8
J1021+1303	10h21m34s	+13°03′55″	3.76±1.47	···	<-1.25±0.11	···	···	3.7
J1034+1428	10h34m18s	+14°28′48″	4.68±1.85	···	<-1.32±0.11	···	···	3.5
J1104+1103	11h04m21s	+11°03′31″	5.35±2.01	···	<-1.36±0.11	···	···	3.4
J0827−3322	08h27m30s	−33°22′43″	3.61±1.47	···	<-1.24±0.12	···	···	3.4
J0918+1226	09h18m48s	+12°26′31″	5.67±2.34	···	<-1.37±0.12	2.02±0.09	-1.06±0.43	3.3
J1027+1347	10h27m10s	+13°47′25″	3.94±1.52	···	<-1.27±0.11	···	···	3.3
J1114+1048	11h14m39s	+10°48′59″	4.28±1.71	···	<-1.29±0.12	···	···	3.2
J0843+1115	08h43m31s	+11°15′20″	6.34±2.43	···	<-1.40±0.11	1.34±0.07	-1.60±0.40	3.2
J1015+1141	10h15m39s	+11°41′05″	3.16±1.31	···	<-1.20±0.12	···	···	3.2
J0929+1133	09h29m20s	+11°33′39″	5.71±2.13	···	<-1.37±0.11	1.69±0.08	-1.25±0.39	3.1
J1019+1405	10h19m53s	+14°05′41″	3.69±1.46	···	<-1.25±0.11	0.87±0.06	-1.49±0.41	3.1
J1026+1431	10h26m53s	+14°31′09″	3.96±1.67	···	<-1.27±0.12	···	···	3.0
J0918+1114	09h18m34s	+11°14′45″	5.40±2.24	···	<-1.36±0.12	···	···	3.0

Note. — This USS sample is created by matching sources in the MWA-32T catalog with uniquely corresponding sources in the 4.85 GHz PMN catalog. Sources which have spectral indices of $\alpha < -1.2$ ($S \propto \nu^{\alpha}$) are identified as ultra-steep candidates. The sources are sorted in order of decreasing detection SNR level. MWA sources which are within 5′ of a PMN source, and have no other PMN counterparts within 30′ are matched as counterparts and used to calculate the spectral index. Additionally, for MWA sources with no PMN source within 1°, a spectral index limit is calculated using the PMN flux limit of 50 mJy. For comparison, the ultra-steep candidates are matched with MRC candidates within 15′ (sources with multiple matches within 30′ are excluded), and an additional spectral index is calculated.

A comparison between the USS source list of De Breuck et al. (2000) and the source list identified in this work finds only 1 source from their list which matches a MWA USS candidate within 15′: MWA J1032-3421. They select this source from an analysis of the MRC and PMN samples, and find a spectral index of -1.23 ± 0.04, which is consistent with the MWA-32T measurements. There are an additional 21 sources from the De Breuck et al. (2000) sample which match MWA sources, however only three of these MWA sources matched uniquely with a PMN counterpart: MWA J1133-2717, MWA J0941-1627, and MWA J0937-2243. These three sources were identified as USS sources in the "TN" sample of De Breuck et al. (2000), which used measurements at 365 MHz and 1.4 GHz, but they did not meet the USS criteria in the MWA-PMN comparison. The flatter MWA-PMN spectra may indicate a high-frequency turnover in the source spectrum, similar to that noted for J0008-421 in Jacobs et al. (2011). This interpretation is supported by 74 MHz VLSS measurements of these sources (Cohen et al., 2007), which imply a spectral flattening at low frequencies, although further follow-up will be important to definitively establish this behavior.

It is important to note that these MWA sources are only candidates, and should not be treated as definitive ultra-steep spectrum sources. Flux calibration and measurement errors as well as blending issues due to the low MWA resolution and time variability may result in a reclassification of these sources upon more detailed investigation. Additionally any time variability or errors introduced by the different catalog resolutions and fitting algorithms will add to errors in this candidate list. The MWA instrument is under continued development, and the fidelity of these studies will improve as the systematics are better understood. However, this candidate list serves as a good basis for more detailed follow-up and investigation.

4.8 Conclusions and Future Work

The goals of this work were to verify the performance of the MWA subsystems and the MWA-32T system, to explore techniques for future EoR experiments, and to

deepen our understanding of the radio sky at these frequencies. The analysis and results presented in this paper served to help commission MWA-32T and represent an assessment of its performance. Specifically, our ability to successfully solve for antenna gains in spite of the wide field of view and direction-dependent primary beam increases our confidence in our ability to calibrate the full 128-tile MWA array. The high level of agreement of our position measurements with existing source position measurements provides further verification of our understanding of the geometry of the array and the calibration procedures as well as our expectations for ionospheric effects on scales relevant to the MWA-32T array. In short, the high fidelity, wide-field images produced in this analysis helps to build confidence that the MWA will be able to achieve its design goals. The measured fluxes in the maps agree with expectations from previous catalogs with a scatter of about 30%. The magnitude of these flux residuals is similar to what is reported from other pathfinder low-frequency arrays, however it is significantly larger than expected based on the noise in the maps. Further work is needed to understand the effects that cause these flux discrepancies.

Future EoR experiments with the MWA will require long integrations, which will require the combination of data from many pointings. We have shown in this work that these data can be corrected for primary beam effects and weighted averages can be formed to increase the sensitivity and fidelity of the resulting maps. In this initial exploration we made certain simplifying assumptions that allowed us to do this analysis in the image domain. Future, deeper, investigations will require more sophisticated techniques that account for differences between individual antenna elements. Developing and verifying these techniques should also be a priority.

A distinguishing feature of the images presented in this paper is the degree to which they are confusion-limited. The effects of source confusion are not expected to be an issue for EoR experiments. Simulations indicate, though it remains to be shown in practice, that subtracting the brightest sources, and treating the fainter sources as smooth contributors to each pixel will allow an adequate separation of foregrounds from the EoR signal (see, e.g. Liu & Tegmark 2011). For other science goals, however, it is quite clear that for the low-frequency arrays planned for the near

future, the confusion limit of continuum images will be reached in relatively short integration times. Thus, much of the science will have to contend with the difficulties of measurements in crowded fields. We have presented the results of an automatic source extraction algorithm. While the results are quite good, with reliability over 90%, further development of algorithms that extract more accurate source models from crowded fields (such as the algorithm presented in Hancock et al. 2012) should be a priority.

The source list presented in this paper serves as the deepest catalog of radio sources generated from a blind search in this region of the southern sky in this frequency band and is the first MWA characterization of the EoR point source foreground in the MWA EoR field. Further refinement of statistical descriptions of this component of the foreground should be possible, and represent a promising avenue for future work. The production of this large, high quality survey with only $\sim$25 hours of data highlights the survey power of this instrument. The techniques used to survey these two fields can be extended to complete an MWA all-sky survey. It is important to note that because this survey was carried out near the source confusion limit, many of the fainter sources in the sample are likely blends of multiple sources. The USS candidates identified in this work, although likely affected by this blending, serve as a set of candidates for high-redshift radio sources, and are good targets for follow-up with higher resolution low-frequency instruments.

The MWA is in the process of a buildout to a 128-tile (128T) interferometer. The 128T array will have four times the number of collecting elements as the 32T array, and the maximum baseline length will be increased to $\sim$3 km. The higher resolution of the 128T array will yield maps with a lower source confusion limit, and will enable a deeper survey of this sky field with a reduced number of blended sources. With the added sensitivity, the 128T array will still be able to rapidly produce source confusion limited maps. The techniques developed as part of the work described herein will allow evaluation of the 128T instrument as it is commissioned. As the quality of the sky model at these frequencies improves, the increased calibration accuracy and ability to

subtract foregrounds from the data will move us closer towards the goal of detecting the 21-cm signal during reionization.

THIS PAGE INTENTIONALLY LEFT BLANK

Chapter 5

Power Spectrum Estimation[1]

5.1 Introduction

The 21-cm hyperfine line of neutral hydrogen has the potential to serve as an extremely powerful probe of the high redshift universe (see e.g. Furlanetto et al. 2006 and Morales & Wyithe 2010 for recent reviews). Precision measurements of the redshifted 21-cm signal during the Epoch of Reionization (EoR) will enable the detailed study of structure formation and the properties of the IGM (Hogan & Rees, 1979; Scott & Rees, 1990; Kumar et al., 1995; Madau et al., 1997), and will allow us to improve our constraints on the fundamental cosmological parameters of the Universe (Mao et al., 2008). Several experiments are currently underway which seek to make these measurements, including the MWA (Lonsdale et al., 2009; Tingay et al., in prep.), PAPER (Parsons et al., 2010), LOFAR (Rottgering et al., 2006), and the GMRT (Paciga et al., 2011). Although this first generation of experiments is unlikely to have the sensitivity necessary to make high signal-to-noise images of the 21-cm emission at these redshifts, a statistical detection of the power spectrum of the 21-cm emission may be possible(Morales & Hewitt, 2004; Barkana & Loeb, 2005; McQuinn et al., 2006)).

Although no detection of the 21-cm power spectrum has yet been made, several upper limits have been produced which are close to being able to constrain physical

[1]The work presented in this chapter was done in close collaboration with Adrian Liu

models of reionization. Parsons et al. (2010), using the 8 stations of the PAPER instrument placed a limit of ~ 5 K on the angular power spectrum at frequencies between 149 MHz and 173 MHz, which is 2-3 orders of magnitude above their fiducial EoR power spectrum model. They report a thermal noise limit of 310 mK from subtracting adjacent time samples in their data and conclude that this limit is dominated by foreground sources. Paciga et al. (2011) present an upper limit on the spherically averaged EoR power spectrum using 50 h of observation with the GMRT at a frequency of 150 MHz, with a bandwidth of 16.7 MHz. They perform a cross-correlation power spectrum estimation procedure directly from the visibility data using only short baselines, and perform a median filtering to remove spectrally smooth foreground components. They present a limit of ~ 70 mK on the power spectrum, and use this limit to rule out a cold bubble model of the IGM.

Although previous limits have produced spherically averaged power spectra, it is often useful to analyze the two-dimensional cylindrical power spectrum, $P(k_\perp, k_\parallel)$, where the Fourier modes have been averaged only in annuli perpendicular to the line of sight (Barkana & Loeb, 2005; McQuinn et al., 2006; Bowman et al., 2009), with $k_\parallel$ representing the line-of-sight modes, and $k_\perp$ representing the modes perpendicular to the line of sight. Although the cosmological signal from the 21-cm line is expected to be intrinsically isotropic, observational effects will influence the line of sight modes differently from the angular modes. Because the line of sight distance is inferred from the redshift of the 21-cm line, the line of sight modes will be affected by redshift space distortions, as well as the Alcock-Paczyński effect (Nusser, 2005; Barkana, 2006).

In addition to the anisotropy of spatial distortions, contaminating effects from foregrounds also enter the line of sight modes in a different manner than for the transverse modes. Foreground sources are expected to be spectrally smooth (Furlanetto & Briggs, 2004; Santos et al., 2005; Wang et al., 2006), contributing most of their power at small values of $k_\parallel$. The diffuse galactic foreground emission, which has relatively large spatial structure, will be confined to small values of $k_\perp$, while discrete point sources will contribute on all $k_\perp$ scales. Additionally, the imperfect uv sampling of the array can lead to bright point sources causing "ripples" in the $k_\parallel$ direction (Bowman et al., 2009;

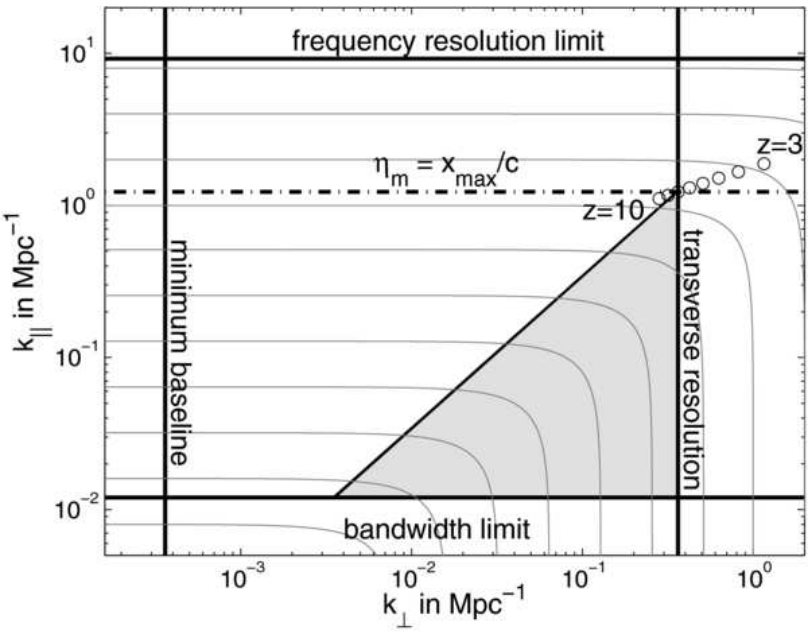

Figure 5-1: Illustration of the "wedge" contamination and EoR window, reproduced from Vedantham et al. (2011), their Figure 4. The grey area represents the region contaminated by the instrumental point spread function.

Liu et al., 2009). An additional "wedge" feature arises in the cylindrical power spectrum as a result of the instrumental point spread function (Datta et al., 2010). This wedge feature has been explained by (Vedantham et al., 2011) and (Morales et al., 2012), and is interpreted as resulting from the chromatic nature of the sidelobes of the point spread function.

The localization of contaminants in the $k_\perp$-$k_\parallel$ plane provides a useful way to understand how to extract a measurement of the EoR signal in the presence of this contamination. As has been suggested by Liu & Tegmark (2011); Vedantham et al. (2011); Morales et al. (2012), an "EoR Window" exists which is relatively free from foreground and instrumental effects. A schematic of this from Vedantham et al. (2011) is displayed in Figure 5-1, which illustrates the boundaries of the EoR window set by the array geometry, frequency bandwidth/resolution and the "wedge" component due to PSF contamination. In addition to the limits shown in this figure, spectrally smooth foreground sources may contaminate modes at low $k_\parallel$.

To date, this EoR window has only been identified and characterized theoretically. In this chapter we use data from the Murchison Widefield Array 32-Tile array to produce cylindrical power spectra and provide the first experimental verification of the presence of this EoR window. The identification of a suitable uncontaminated region of the $k_\perp$-$k_\parallel$ plane is a key validation of MWA EoR science performance, and represents a significant step towards characterizing the EoR with the MWA. We then produce a spherically binned power spectrum in order to place limits on the 21-cm emission during the EoR.

5.2 Data Reduction

The first step in our power spectrum estimation was to produce integrated image cubes of the dataset from X13, described in Chapter 4. These data are from approximately 15 hours of integration on the MWA "EoR2" field, split among three 30.72 MHz wide bands observed for 5 h each, covering the 110 MHz to 200 MHz frequency range. We used a reduction procedure similar to that described in Chapter 4.5 for the initial flagging and calibration of the data, however we developed a modified imaging pipeline which is more suitable for power spectrum estimation purposes.

In order to remove the contaminating effects of the bright source Hydra A (it is the dominating bright source in the images – see Chaper 4.7.1), a point-source model for Hydra A was first subtracted from the *uv* data set. As Hydra A was also used for gain and phase calibration, this is akin to the "peeling" source removal procedure (Noordam, 2004; van der Tol et al., 2007; Mitchell et al., 2008; Intema et al., 2009) on a single source. Although further bright point source removal is likely necessary for the highest fidelity measurement of the EoR power spectrum (see, e.g., Bowman et al. 2009; Morales & Wyithe 2010; Bernardi et al. 2011; Pindor et al. 2011), we choose not to perform any additional bright source subtraction at this time so that we can assess the effect of these remaining sources in the resulting power spectrum.

The subtracted data are imaged using the CASA task `clean`. Image cubes were created which maintain the full 40 kHz spectral resolution of the data (no multi-

frequency synthesis is performed), at a spatial resolution of $3''$ over a 25° field of view. The *uv* data were gridded using w-projection kernels (Cornwell et al., 2008) with natural (inverse-variance) weighting. The resulting cubes contained ~ 200 million voxels, with 512 elements along each spatial dimension and 768 elements in the frequency domain. It is important to note that the pre-flagging performed on the data results in the flagging of entire frequency bands (i.e. there are gaps in the data cubes). Cubes were generated for each 5 minute snapshot image; a total of $\sim$60 snapshot cubes are generated for each 30.72 MHz frequency band.

The individual snapshot data cubes were combined using the primary beam inverse-variance weighting method described in Chapter 4.6.4, Equation 4.6. The weighting and primary beams are simulated separately for each 40 kHz frequency channel in each 5 minute snapshot. The combined maps and weights are saved, along with the effective point spread function at the center of the field. An additional flux scale calibration of the integrated cubes was performed using three bright point sources: MRC 1002-215, PG 1048-090, and PKS 1028-09 to set the flux scale on a channel-by-channel basis. A two dimensional Gaussian fitting procedure is used to fit the peak flux of each of these sources in each 40 kHz channel of the data cube. Predictions for each source are derived by fitting a power law to source measurements from the 4.85 GHz Parkes-MIT-NRAO survey (Griffith et al., 1995), the 408 MHz Molonglo Reference Catalog (Large et al., 1981), the 365 MHz Texas Survey (Douglas et al., 1996), the 160 MHz and 80 MHz Culgoora Source List (Slee, 1995) and the 74 MHz VLA Low-frequency Sky Survey (Cohen et al., 2007). A weighted least-squares fit was then performed to calculate and apply a frequency-dependent flux scaling for the cube to minimize the square deviations of the source measurements from the power law models.

An additional flagging of spectral channels was performed based on the root-mean-square (RMS) noise in each spectral channel of the cube. A smooth noise model was determined by median filtering the RMS channel noise as a function of frequency (bins of 16 channels were used in the filtering). Any channel with 5σ or larger deviations from the smoothed noise model was flagged. Upon inspection, these

additional flagged channels were observed to be primarily located at the edges of the coarse digital filterbank channels. The maps of these channels were strongly affected by artifacts, and often did not show the presence of the expected calibrator point sources, implying that these channels have poor calibration. After this procedure, approximately one third of the spectral channels were found to have been flagged.

For each cube, the comoving transverse and line-of-sight coordinates of each voxel were computed at the corresponding redshift of the 21 cm line, according to the formulae given by Hogg (1999):

$$D_{\rm C} = \frac{c}{H_0} \int_0^z \frac{dz'}{\sqrt{\Omega_{\rm M}(1+z')^3 + \Omega_k(1+z')^2 + \Omega_\Lambda}}, \tag{5.1}$$

and,

$$D_{\rm M} = D_{\rm C} \text{ (for } \Omega_k = 0). \tag{5.2}$$

The comoving line of sight distance from the observer is directly given by $D_{\rm C}$, and the transverse distance from a fiducial point is given by $D_{\rm M}\delta\theta$ where δ_θ is the angular separation on the sky. For this conversion, we used the WMAP-7 derived cosmological parameters, with $\Omega_{\rm M} = 0.266$, $\Omega_\Lambda = 0.734$, $H_0 = 71$ km s^{-1} Mpc^{-1}, and $\Omega_k \equiv 0$ (Komatsu et al., 2011). These cubes serve as the reduced data product from which the power spectra are computed.

5.3 Power Spectrum Computation

5.3.1 Fast Fourier Transform Method

Power spectra were computed using two methods. The first method uses the Fast Fourier Transform (FFT). The favorable computational complexity of the FFT operation enables the rapid computation of power spectra over a large range in "k space" (see e.g. Press et al. 1992). This allows power spectrum computation using the entire input data cube, allowing investigation of the full range of available modes in k-space. Furthermore, the speed of the FFT power spectrum computation enables the inves-

tigation of multiple different frequency bands (corresponding to different redshifts of HI), as well as multiple different analysis techniques to emphasize particular features of the power spectrum.

We estimate the power spectrum, $P(k)$, by explicitly evaluating the Fourier transform of our measured sky temperature maps:

$$\tilde{T}(\vec{k}) = \frac{1}{V} \int T(\vec{x}) e^{-i\vec{k}\cdot\vec{x}} d^3x, \tag{5.3}$$

where $T(\vec{x})$ is the temperature for a voxel in our cube, $\tilde{T}(\vec{k})$ is the Fourier dual of the temperature and V is the survey volume. However, in the limit of a discrete data cube, we perform the integral instead as a sum over voxels:

$$\tilde{T}(\vec{k}) = \frac{1}{N} \sum_{i}^{N} T(\vec{x_i}) e^{-i\vec{k}\cdot\vec{x_i}/N}, \tag{5.4}$$

where N is the number of voxels in our cube, and $\vec{x}_i$ is the location of the i^{th} voxel. This sum is computed efficiently using an FFT. Note that we first zero-pad the input data cube, increasing each dimension by a factor of 3 before the computation. We then compute the power spectrum as:

$$P(\vec{k}) = |\tilde{T}(\vec{k})|^2. \tag{5.5}$$

The power spectrum is commonly expressed in terms of the variance of the temperature per logarithmic k interval (see e.g. Peacock 1999; Bharadwaj & Ali 2004; McQuinn et al. 2006):

$$\Delta^2(\vec{k}) = \frac{V}{(2\pi)^3} 4\pi k_\perp^2 k_\parallel P(\vec{k}). \tag{5.6}$$

This power spectrum is then binned in annuli of constant $k_\perp$ in order to form the cylindrical power spectrum.

We also use this formalism to evaluate the cross-power spectrum between two different data intervals. The advantage of the cross-power spectrum is that thermal noise should be uncorrelated between the two time intervals, and consequently the bias

due to the noise will be removed (see e.g. Hinshaw et al. 2003). To accomplish this, the individual snapshots are divided into two groups by separating the even numbered and odd numbered scans. Each of these data sets is then analyzed independently, and the power spectrum is calculated as:

$$P_{\rm Cross}(\vec{k}) = \tilde{T}_{\rm Even}(\vec{k})\tilde{T}^*_{\rm Odd}(\vec{k}). \tag{5.7}$$

The data are then binned and nondimensionalized as before.

We also performed a foreground subtraction procedure on the data prior to the power spectrum estimation in order to remove the spectrally smooth foreground emission component (as well as any potential spectrally smooth instrumental contamination). Following the suggestion of Liu & Tegmark (2012), we perform principal component analysis (Karhunen-Loève transform) along the line of sight direction to identify the spectral principal components ("eigenforeground modes"). We use a 30.72 MHz bandwidth to calculate the principal components, even though our power spectrum is computed from a reduced bandwidth of 7.68 MHz. We identify the dominant spectral principal components and subtract any contribution along those components separately from each line of sight.

As a final step in the pipeline, we remove the effect of the synthesized beam from the power spectrum. The synthesized beam pattern defines a window function with which our maps have been convolved (Hinshaw et al., 2003), and can be removed by dividing the power spectrum by the Fourier transform of the synthesized beam. This can be seen explicitly by noting that that Equation 5.3 should be corrected to reflect this beam convolution:

$$T(\vec{x}) \rightarrow (T * P)(\vec{x}), \tag{5.8}$$

where $P(\vec{x})$ is the instrumental point spread function (which we assume to be translation invariant). This modifies the right hand side of Equation 5.3, giving:

$$\frac{1}{V}\int (T * P)(\vec{x}) e^{-i\vec{k}\cdot\vec{x}} d^3x, \tag{5.9}$$

which reduces to:

$$\frac{\tilde{P}(\vec{k})}{V} \int T(\vec{x}) e^{-i\vec{k}\cdot\vec{x}} d^3x, \tag{5.10}$$

by the convolution theorem, where $\tilde{P}(\vec{k})$ is the Fourier transform of the point spread function (or, in other words, the uv distribution of the array). We can see that we recover $\tilde{T}(\vec{k})$ by dividing out the extra factor of $\tilde{P}(\vec{k})$. As the subsequent pipeline operations are distributive, we can leave this division to the last step, and produce "dirty" power spectra which we can then correct by dividing through by the appropriate transformation of the instrumental response.

Although we can model the spatial effect of the instrument on the true sky as a convolution with the point spread function, this convolution does not extend to the spectral dimension. We approximate the response function of the instrument in the spectral dimension as a delta function (i.e. the instrument does not add any excess correlation between spectral channels). This assumption is warranted because the MWA uses a sharp polyphase filter (see Chapter 2.3), which has low levels of aliasing between channels. Consequently, we take $\tilde{P}(\vec{k}) \approx \tilde{P}(k_\perp)$, independent of $k_\parallel$. We calculate $\tilde{P}(k_\perp)$ by taking the two-dimensional spatial Fourier transform of the synthesized beam at the center frequency of each band, and binning in an identical manner to the dirty power spectrum.

It is important to note that several key assumptions are necessary in order to calculate the power spectra using this FFT framework. The first assumption is that of fully sampled, regularly gridded data. This assumption is broken in several ways for the data cubes that are generated by the procedure in 5.2. Firstly, although the data are drawn from a regularly gridded data cube, the coordinate system of this cube is instrumental in nature. The spatial axes of the cube are regularly gridded in sine projections of the sky, while the spectral axis is regularly gridded in frequency. The mapping of the angular sine projection into comoving transverse coordinates results in an uneven transverse sampling, as does the comoving line-of-sight coordinate transform performed over the frequency axis. Although this breaks the uniform input grid assumptions of the FFT, the problem is less severe over a relatively small field of

view or over a narrow frequency range. Additionally, our point spread function is only approximately translation invariant, which will introduce errors into our synthesized beam correction procedure.

An additional issue arises due to spectral gaps in the data. Instrumental artifacts in the digital receivers, poor performance at the edges of filter bands, and RFI lead to the excision of all data from particular frequency channels. Approximately 1/3 of the frequency channels in the dataset have been removed, primarily at the coarse channel boundaries, which also results in a periodicity of the gaps in the data (see Figure 2-5). These gaps will have implications for the sensitivity to particular k-modes in the final analysis, and the methods we use to fill in these gaps with synthetic data have implications for the interpretation of these results.

5.3.2 Direct Quadratic Estimator

An alternative method to the FFT is the direct quadratic estimator of Liu & Tegmark (2011). This method adapts the techniques of Tegmark (1997) and Tegmark et al. (1998) for estimating the 21-cm power spectrum in the presences of foreground contaminants, and results in an unbiased, optimal estimate of the band powers in the $k_\perp$-$k_\parallel$ plane. This technique is derived in detail in Liu & Tegmark (2011), and we summarize the key results necessary for our power spectrum estimation below.

Central to this technique is the estimator, p_α, defined by Liu & Tegmark (2011) in their equation 2:

$$\widehat{p}_\alpha = (\mathbf{x} - \mathbf{m})^t \mathbf{E}^\alpha (\mathbf{x} - \mathbf{m}) - b_\alpha, \tag{5.11}$$

where $\widehat{p}_\alpha$ is the estimator of the power spectrum at a particular location of the $k_\parallel$-$k_\perp$ plane denoted by α, $\mathbf{x}$ is the vector of observed data values, $\mathbf{m}$ is the expectation value of $\mathbf{x}$, b_α is the bias for a particular bin, and $\mathbf{E}^\alpha$ is a matrix which performs the Fourier transform, binning, weighting and foreground subtraction. If no foreground subtraction is performed, the $\mathbf{E}^\alpha$ matrix reduces to the direct Fourier transform and binning detailed in equation 3 of Liu & Tegmark (2011). As the Liu & Tegmark (2011) method uses a direct Fourier transform rather than the FFT described in

section 5.3.1, it does not suffer from the constraint of needing a uniformly sampled regular grid of input data. Additionally, this formalism explicitly produces "window functions" and temperature uncertainties for each power estimate in the $k_\perp$-$k_\parallel$ plane.

By including the full covariance of the data in the $\mathbf{E}^\alpha$ matrix, Liu & Tegmark (2011) are able to form an optimal estimator with uncertainties which reach the Cramer-Rao lower bound. For this estimator, they choose (their equation 15):

$$\mathbf{E}^\alpha = \frac{1}{2\mathbf{F}_{\alpha\alpha}}\mathbf{C}^{-1}\mathbf{C}_{,\alpha}\mathbf{C}^{-1}, \tag{5.12}$$

where $\mathbf{C}$ is the covariance matrix of the input data vector, $\mathbf{C}_{,\alpha}$ is the Fourier transformation and binning matrix, and $\mathbf{F}$ is the Fisher information matrix given by:

$$\mathbf{F}_{\alpha\beta} = \frac{1}{2}\mathrm{tr}\left[\mathbf{C}_{,\alpha}\mathbf{C}^{-1}\mathbf{C}_{,\beta}\mathbf{C}^{-1}\right]. \tag{5.13}$$

In our analysis pipeline, we modified the normalization of Equation 5.12 following Tegmark et al. (2004) so that the each row of the resultant window functions sum to unity. We also modify the Liu & Tegmark (2011) method to calculate a cross-power spectrum.

One complication is the need to form a covariance matrix which accurately reflects the data. We used two different techniques to estimate this matrix. For the first estimate of $\mathbf{C}$, we used an instrumental model. We form the covariance as:

$$\mathbf{C} = \mathbf{C}_{\mathrm{LOS}} + \mathbf{C}_{\mathrm{Spatial}}, \tag{5.14}$$

where we form $\mathbf{C}_{\mathrm{LOS}}$ by averaging over the spatial dimension and calculating a solely spectral covariance (after the inverse-covariance weighting, this has a similar net result to performing the spectral PCA subtraction described in section 5.3.1), and we use the instrumental point spread function to form $\mathbf{C}_{\mathrm{Spatial}}$ by calculating:

$$\mathbf{C}_\nu^{ij} = \sum_{\mathrm{x}} \sigma^2(x) P_i(x) P_j(x), \tag{5.15}$$

where $\mathbf{C}_\nu$ is the spatial covariance at frequency ν, the summation is computed over all map pixels, x, i and j are pixel indices in a map at a particular frequency, P_i and P_j are the instrumental point spread functions centered at spatial pixels i and j, and σ is the instrumental noise at a particular pixel in the map. The map noise is computed by differencing two maps from adjacent time slices. We form the full $\mathbf{C}_{\text{Spatial}}$ by forming a block-diagonal matrix of the $\mathbf{C}_\nu$ matrices from each frequency.

The Liu & Tegmark (2011) method has some tremendous advantages over the FFT method, in that it properly accounts for the data geomtry, and produces well quantified, optimal error estimates. However, this method has some large computational challenges. The covariance matrix C needs to be computed for every pair of voxels in the input data cube, and then inverted, leading to a computational complexity of $\mathcal{O}(N^3)$, where N is the number of input voxels, as opposed to $\mathcal{O}(N \log N)$ for the FFT method. Methods for computing this estimator more efficiently in the narrow field regime are being developed (Dillon et al., in prep.), but due to computational limitations of the existing implementation, this method has only been used on a subset of the data.

5.4 Results

5.4.1 FFT Power Spectra

As a first step in calculating FFT power spectra described in Section 5.3.1 , we divided the data into 12 sets, each with a bandwidth of 7.68 MHz, covering the frequency range from ∼110 to ∼ 200 MHz. Each 7.68 MHz band corresponds to $\Delta z \approx 0.5$, which is roughly the range over which we expect to be able to ignore cosmological evolution of the 21-cm signal (Bowman et al., 2007). The bands are centered at 111.925 MHz, 119.605 MHz, 127.285 MHz, 134.965 MHz, 142.645 MHz, 150.325 MHz, 158.005 MHz, 165.685 MHz, 173.365 MHz, 181.045 MHz, 188.725 MHz, and 196.405 MHz, which correspond to redshifts of $z = 11.69$, $z = 10.88$, $z = 10.16$, $z = 9.52$, $z = 8.96$, $z = 8.45$, $z = 7.99$, $z = 7.57$, $z = 7.19$, $z = 6.85$, $z = 6.53$, and $z = 6.23$.

Point Source Response

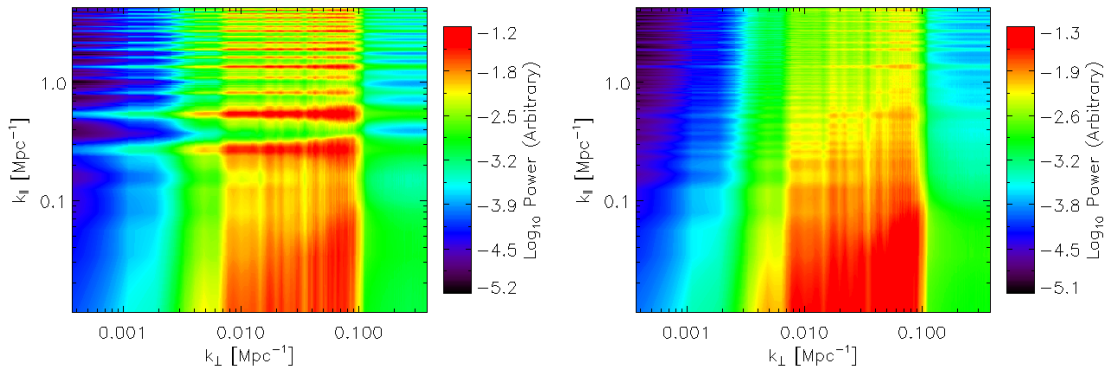

Figure 5-2: FFT power spectrum of the synthesized beam of the 142.645 MHz data cube, where the flagged channels have been (a) zeroed or (b) interpolated over in the spectral dimension. This simulates the power spectrum of a unit-flux flat-spectrum point source, and illustrates the effect of treating flagged channels in different manners.

We first calculated the Fourier-space response of the synthesized beam pattern using the FFT estimation procedure. This simulates the power spectrum of a flat-spectrum point source at the center of the field. In order to use the FFT, we first need to fill in the flagged channels to restore a uniformly spaced grid. In these data, typically $\sim 30\%$ of the channels are flagged due to the MWA coarse polyphase filter. In Figure 5-2(a), we show an example for a particular band where we have set the values of all flagged channels to zero. In Figure 5-2(b), we have used a smooth polynomial interpolation along the frequency axis of each pixel to fill in the flagged channels. As can be seen in the difference between the figures, using zeros for the flagged channels has the effect of adding strong "stripes" at particular values of $k_\parallel$, which not present in the spectrum produced after the interpolation procedure. It is important to note, however that this smooth interpolation does add unphysical power to the low $k_\parallel$ modes.

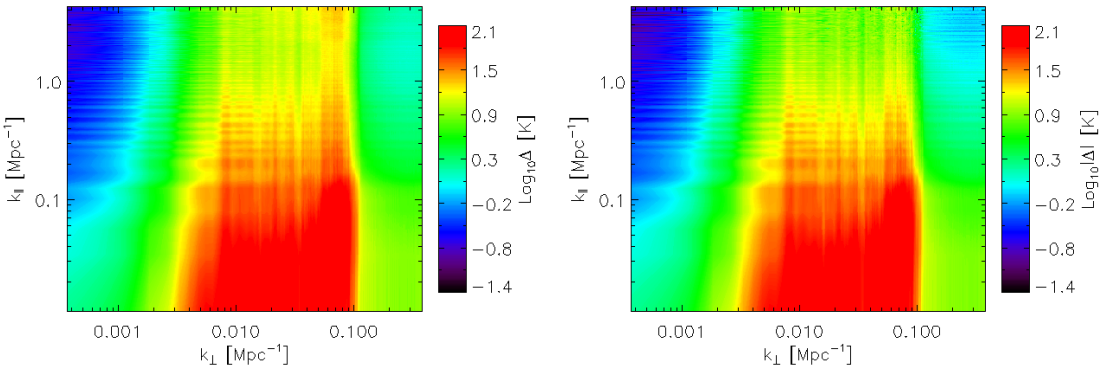

(a) (b)

Figure 5-3: Auto- (a) and cross-correlation(b) raw power spectra produced from the FFT power spectrum estimation pipeline from data at 142.645 MHz.

"Dirty" Power Spectra

After performing the spectral interpolation described above, we then produce "dirty" power spectra, which have not had the effects of the instrumental synthesized beam removed. An example of this is shown in Figure 5-3. The auto-power spectrum is shown in panel (a), and the cross-power spectrum is shown in panel (b). The effect of the cross-power spectrum is to remove the bias due to thermal noise. This effect can most easily be seen by comparing the high $k_\parallel$ regions.

The thermal noise component of the auto-power spectrum can be further assessed by forming a "noise cube" which contains only the thermal noise component of the input data. This can be generated by taking the difference of data from two separate time intervals. Although the noise between these cubes is uncorrelated and will remain after the subtraction, any true signal will be common between the two maps, and will be removed when the difference is taken. The expectation for the noise power spectrum is that any structure in $k_\perp$ will be due to the uv sampling of the MWA baselines, while the $k_\parallel$ structure will be due to frequency variations of the noise performance. The computed spectrum, shown in Figure 5-4 supports this interpretation.

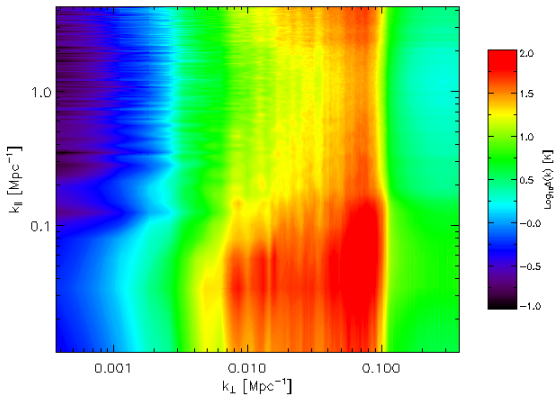

Figure 5-4: FFT power spectrum of thermal noise produced by differencing from separate time intervals at 142.645 MHz.

Foreground Subtraction

In order to remove any spectrally smooth contaminants from the data, we performed a principal component analysis along the line-of-sight direction. We use a 30.72 MHz bandwidth (768 channels) in order to compute the components. The eigenvalues of the PCA are displayed in Figure 5-5, along with plots of the first few eigenmodes. The steep drop in the eigenvalues indicates that the spectra are dominated by relatively few modes. We use a fiducial foreground model where we ascribe the largest 50 eigenmodes to foreground components and/or smooth instrumental contamination. We subtract these modes from each line of sight of the input data cube, and re-perform the FFT power spectrum estimation. An example foreground-subtracted power spectrum is displayed in Figure 5-6.

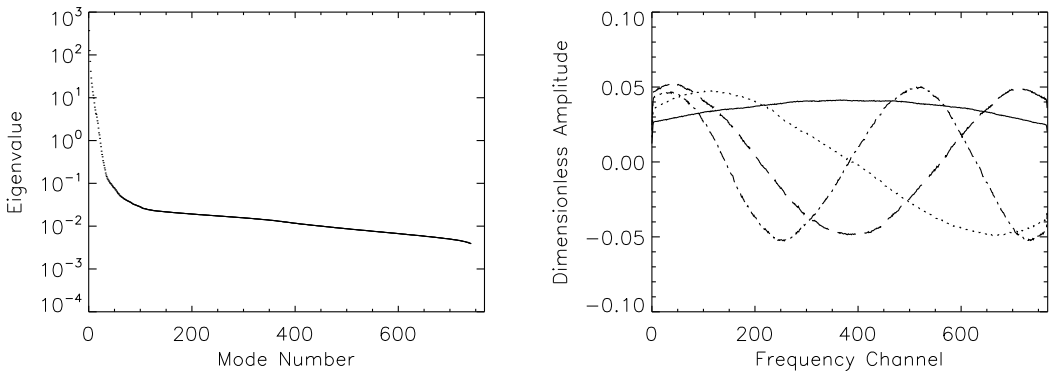

(a) (b)

Figure 5-5: Results of the spectral principal component analysis. The left panel shows the eigenvalues of the different modes, plotted with a logarithmic vertical axis. The steep drop in eigenvalue with mode number indicates that the power in the spectrum is dominated by the first few modes. The right panel shows the first four eigenmodes, with the solid line being the lowest mode, followed by the dotted line, then the dashed line, then the dot-dashed line. This panel is an observed analog of Figure 3 of Liu & Tegmark (2012).

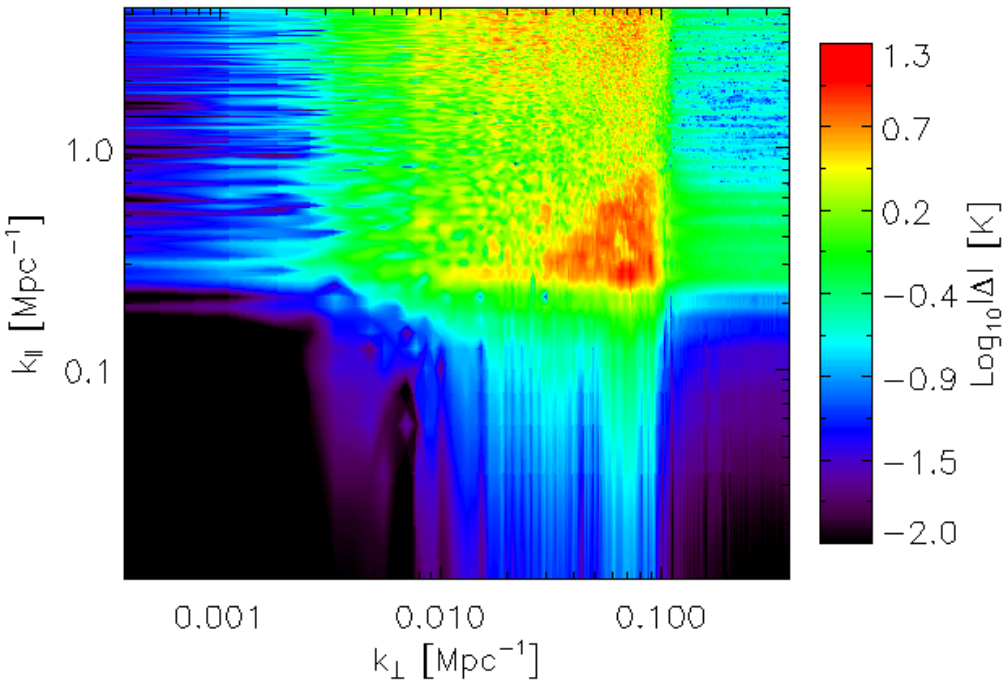

Figure 5-6: Cross-power spectra produced from the FFT power spectrum estimation pipeline from data at 142.645 MHz, which have had a smooth foreground components subtracted by removing the strongest principal component modes.

Deconvolved Power Spectra

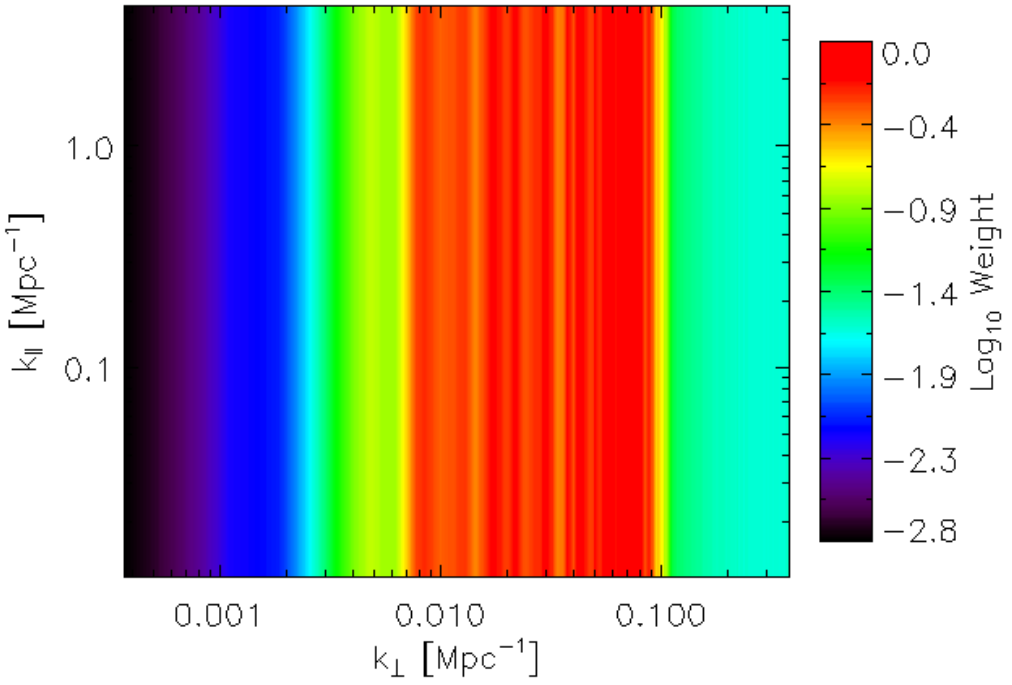

Figure 5-7: Power spectrum of the instrumental response ($\tilde{P}(k_\perp, k_\parallel)$, calculated at 142.645 MHz, under the assumption that the instrumental response acts solely as a spatial convolution to the data. This assumption leads to $\tilde{P}$ being independent of $k_\parallel$. The power spectrum is formed by taking the two-dimensional Fourier transform of the instrumental point spread function at the mid-frequency of the band, and binning the result to determine the structure in $k_\perp$.

An example instrumental response power spectrum, $\tilde{P}(k_\perp, k_\parallel)$, is shown in Figure 5-7. The dirty power spectra are divided by this function, effectively deconvolving the instrumental response from the power spectra. In Figure 5-8, we show the result of dividing the power spectrum from Figure 5-6 by $\tilde{P}$ from Figure 5-7. The resulting power spectrum shows the edges of the instrumental sensitivity in the $k_\perp$ dimension which result from the array layout, and resulting sampling of the uv plane.

The "EoR Window"

An annotated version of Figure 5-8 is shown in Figure 5-9. Several features are emphasized in this presentation. In the $k_\perp$ direction the edges of the baseline sampling

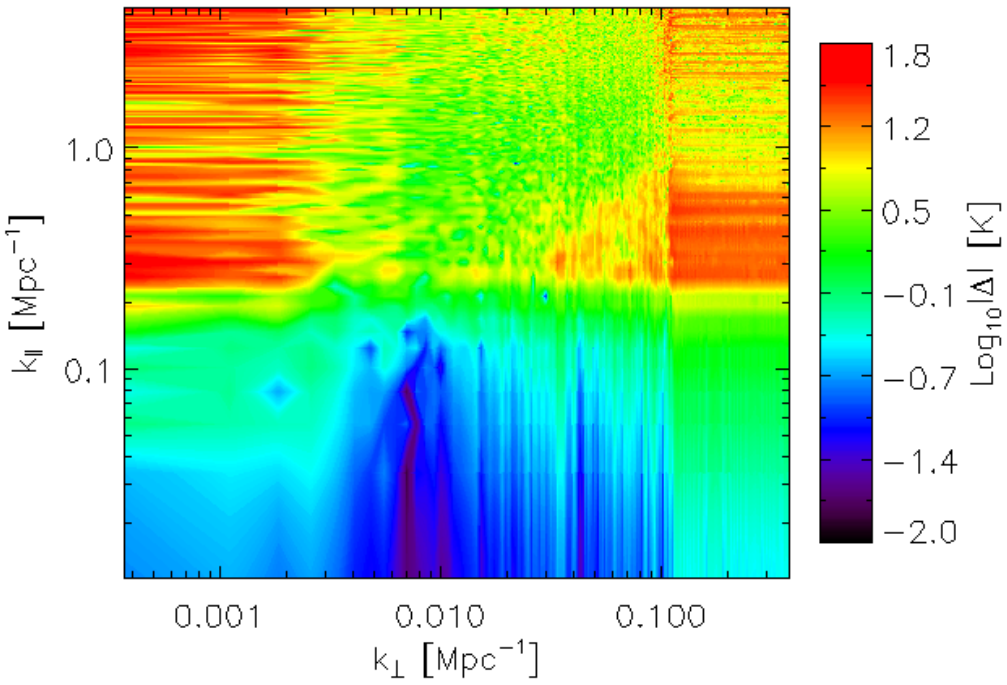

Figure 5-8: Cross-power spectra produced from the FFT power spectrum estimation pipeline from data at 142.645 MHz, which have had a smooth foreground components subtracted using a principal component analysis, and have had the instrumental response removed.

can be seen. The minimum baseline of the 32T array included in this analysis had a length of $\sim$ 16 m (there were several shorter baselines in the array, but they were flagged due to RF feedback issues), and the longest baseline had a length of $\sim$ 343 m. The vertical lines correspond to the values of $k_\perp$ probed by these baselines. The solid horizontal lines correspond to the minimum $k_\parallel$ value, which is defined by the total bandwidth (7.24 MHz, after accounting for the flagging of edge channels), and the maximum value of $k_\parallel$ is set by the frequency resolution of 40 kHz. The two additional dashed lines correspond to limits on contaminants. The horizontal dashed line corresponds approximately to the limit of where modes are entirely removed due to the foreground subtraction. The diagonal "wedge" is also illustrated. The wedge of contamination can clearly be seen in the power spectrum, and has the shape observed in simulations by Datta et al. (2010) and explained by Vedantham et al. (2011) and

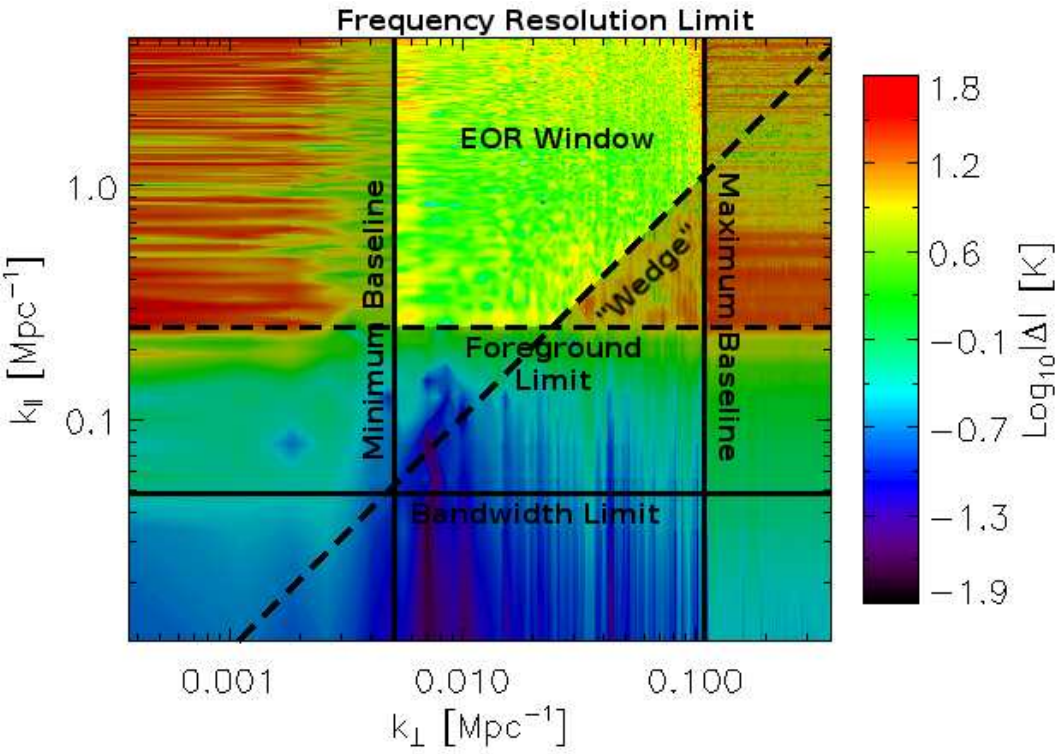

Figure 5-9: Beam-corrected FFT cross-power spectrum in the 142.645 MHz frequency band. Boundaries are drawn and annotated indicating the range accessible for EoR power spectrum measurements. The solid lines indicate fundamental limits governed by the geometry of the array and the frequency bandwidth and resolution. The dotted lines indicate approximate boundaries on various contaminants. The horizontal line indicates the approximate cutoff of the foreground principal component subtraction, while the "wedge" indicates the region bounded by a $k_\perp \propto k_\parallel$ line formed by point spread function contamination. This figure serves as an observed analog to and confirmation of the predictions from (Vedantham et al., 2011) reproduced in Figure 5-1.

Morales et al. (2012), with $k_\perp \propto k_\parallel$. These boundaries define a window within which an EoR power spectrum measurement can be made.

Multi-redshift Power Spectra

As mentioned above, the data from X13 cover 12 frequency bands, ranging in frequency from 110 MHz to 200 MHz, or in terms of the redshifted 21-cm line, from $z = 6.23$ to $z = 11.69$. The results of FFT power spectra in each of these bands is displayed in Figure 5-9. An important feature in the power spectra is the presence of the EoR window in these maps. Although these power spectra are significantly brighter than the predicted EoR signal (which is expected to be $\lesssim 10$ mK in most models, see e.g. McQuinn et al. 2006), that this EoR window does not appear to be contaminated by any large instrumental or foreground effects across the MWA EoR frequency band is an important result, and a crucial assessment of the performance of the array for EoR science. As the MWA array is expanded and operated for a long integrations, we expect to be able to obtain higher fidelity measurements within this region.

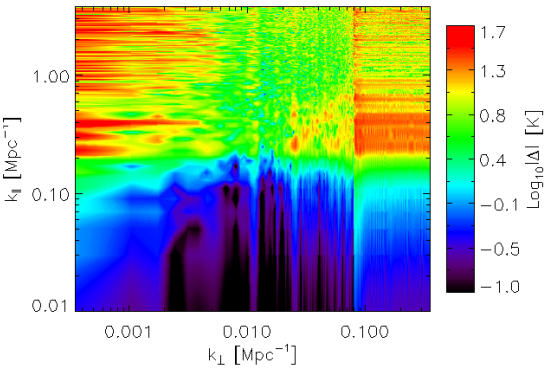

(a) 111.925 MHz ($z = 11.69$)

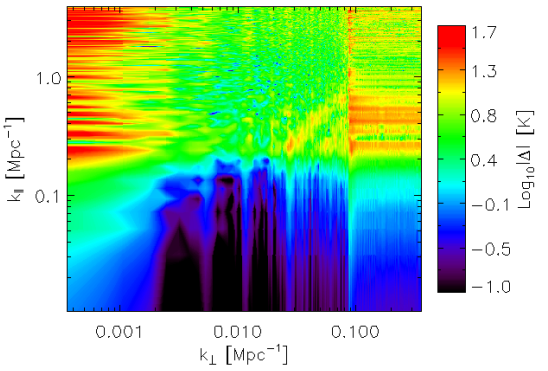

(b) 119.605 MHz ($z = 10.88$)

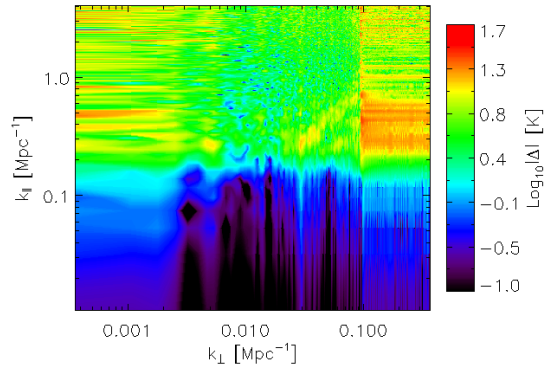

(c) 127.285 MHz ($z = 10.16$)

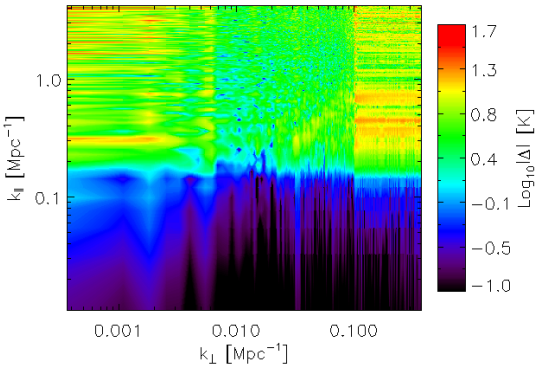

(d) 134.965 MHz ($z = 9.52$)

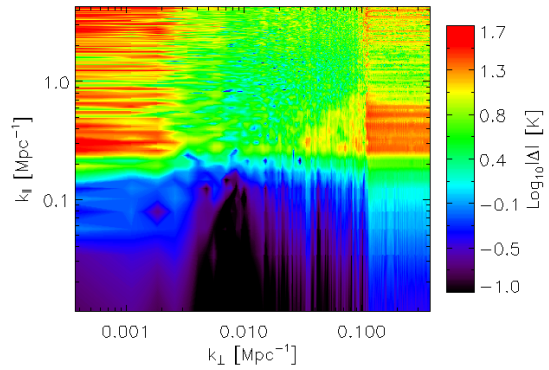

(e) 142.645 MHz ($z = 8.96$)

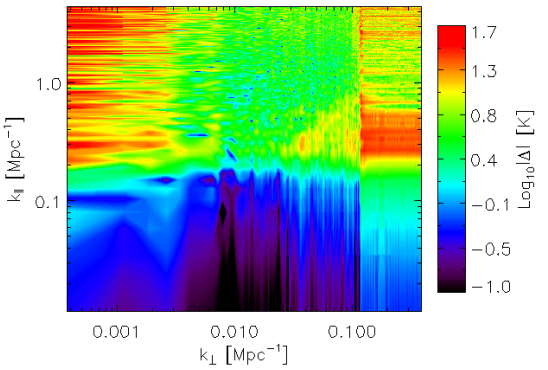

(f) 150.325 MHz ($z = 8.45$)

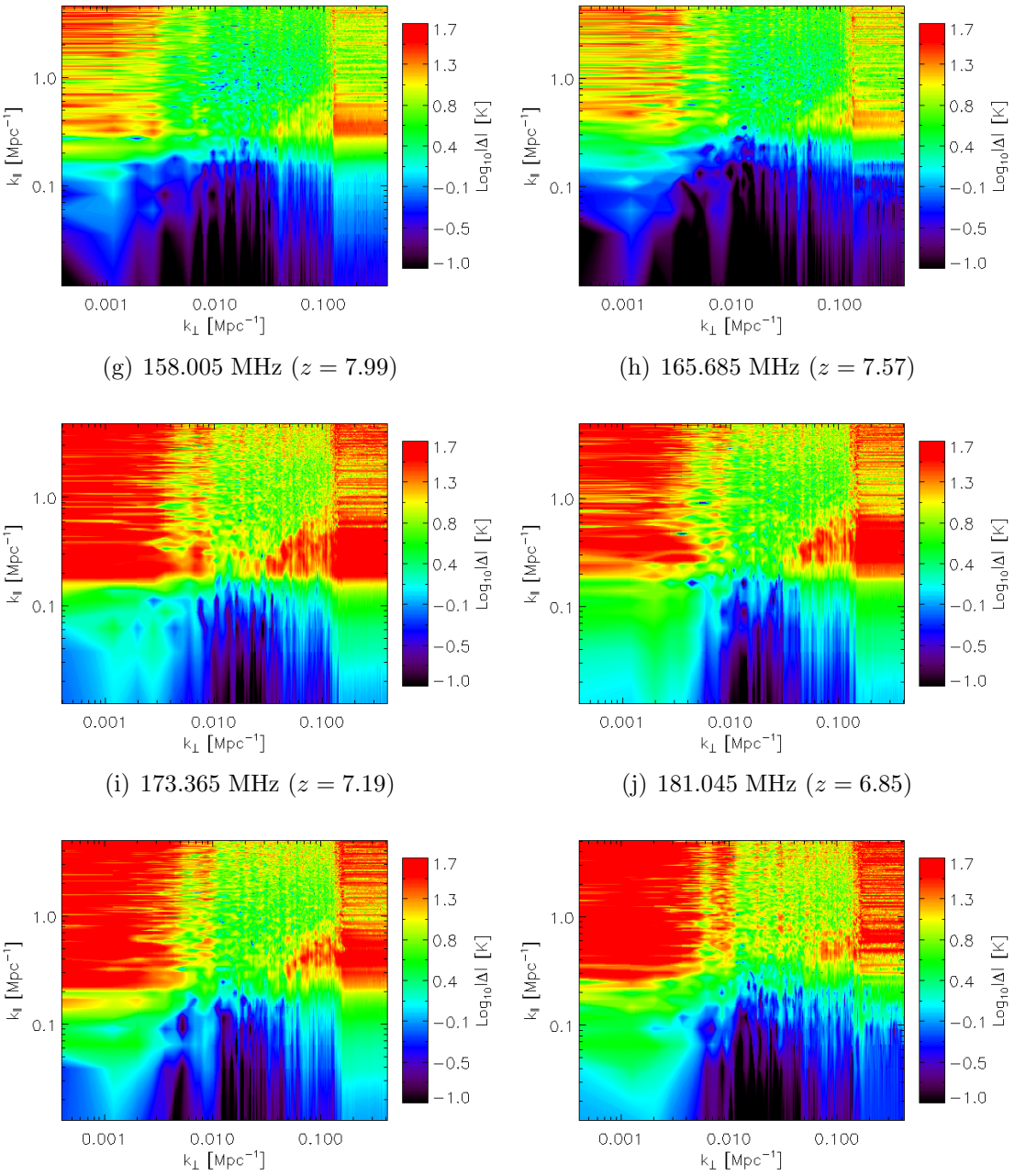

(g) 158.005 MHz ($z = 7.99$)

(h) 165.685 MHz ($z = 7.57$)

(i) 173.365 MHz ($z = 7.19$)

(j) 181.045 MHz ($z = 6.85$)

(k) 188.725 MHz ($z = 6.53$)

(l) 196.405 MHz ($z = 6.23$)

Figure 5-9: FFT power spectra covering the full range of frequencies observed in the MWA X13 EoR campaign. These power spectra have had a foreground model subtracted (see text) and have had the effect of the point spread function response removed. The EoR observing window is visible in each of the power spectra, with the edges of the window defined by the foreground subtraction limit, the limits of the *uv* sampling of the array, and the "wedge" feature due to point-spread function contamination.

5.4.2 Quadratic Estimator Power Spectra

The FFT power spectra presented in Section 5.4.1 served a diagnostic of our data set, and a verification of our techniques and predictions for the qualitative attributes of the power spectra produced with the 32T array. We have used the quadratic estimator formalism described in Section 5.3.2 to determine an optimal estimate of the power spectrum at $z \sim 9$ in order to place a limit on the 21-cm power spectrum during reionization. Due to computational limitations, we used a reduced data set, covering a frequency range from 139.82 MHz to 140.67 MHz, and a reduced spatial extent, so that the input image cube contained only 12000 voxels. We tuned the spatial extent of the cube to probe the EoR window identified in Section 5.4.1.

Cylindrical Power Spectra

As a verification of the quadratic estimator pipeline, we produced a cylindrical power spectrum, which is displayed in Figure 5-10. This power spectrum has not been corrected for the effects of the synthesized beam, however the inverse-covariance weighting effectively suppresses the foreground contaminants. This figure is analogous to the power spectrum produced by the FFT pipeline that is displayed in Figure 5-6. The same qualitative features are evident in the results from both pipelines - in particular the "wedge" of PSF contamination at low $k_{\parallel}$ and high $k_{\perp}$.

With the inverse covariance weighting technique, we also obtain an estimate of the uncertainties in the power spectrum from the diagonal components of the Fisher information matrix. The uncertainties in the power spectrum from Figure 5-10 are displayed in Figure 5-11. The structure in the uncertainty is qualitatively similar to the power spectrum of the noise presented in Figure 5-4, implying that thermal noise is the dominant source of uncertainty in these estimates. In Figure 5-12, the signal-to-noise ratio of the cylindrical power spectrum is displayed, showing that there is a significant detection of power in "wedge" region, likely corresponding to contaminating emission from foreground sources.

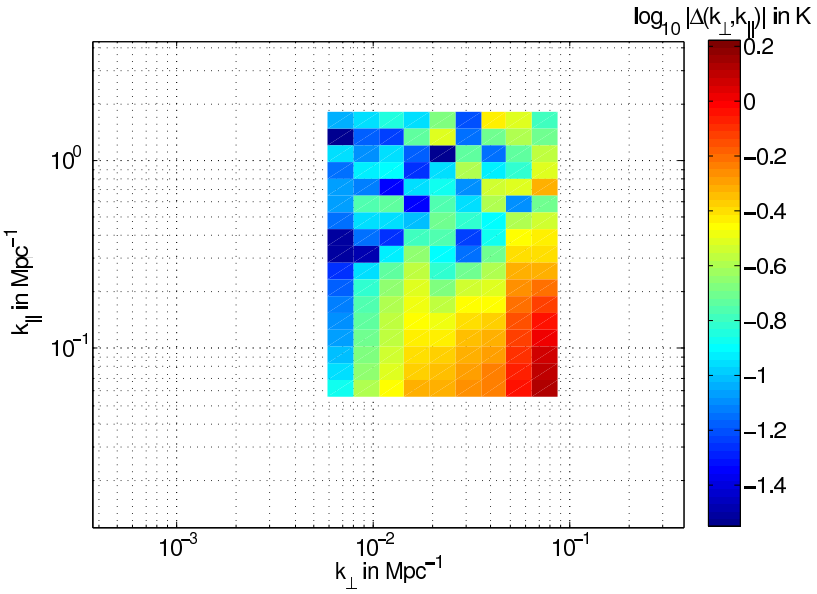

Figure 5-10: Cylindrical cross-power spectrum produced using the optimal quadratic estimator at redshift $z = 9.16$. This power spectrum has not had any beam correction applied, and is an optimally estimated version of the power spectrum presented in Figure 5-6. The power spectra are plotted on approximately the same scale, and appear consistent in their major features.

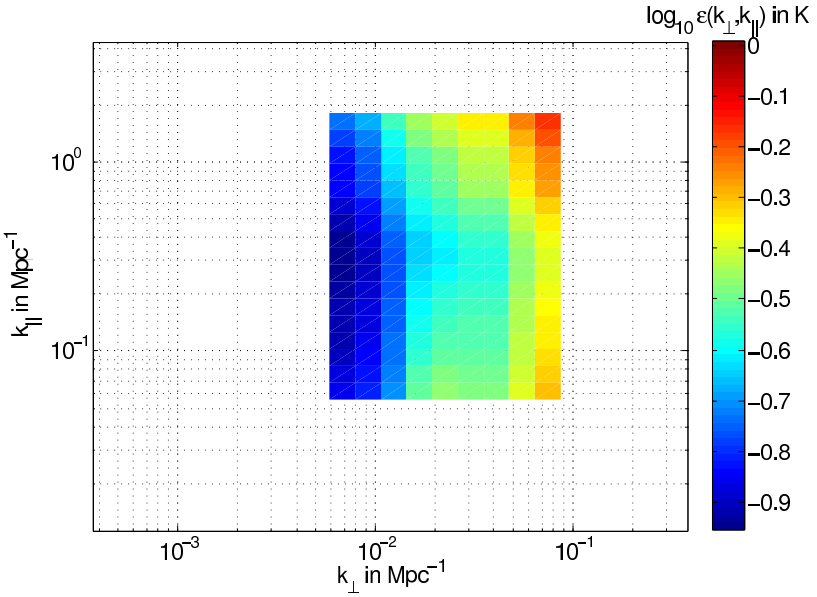

Figure 5-11: Uncertainties in the optimally estimated cross-power spectrum presented in Figure 5-10. These uncertainties have been calculated using the Fisher information derived from the covariance matrix used in the optimal estimation procedure.

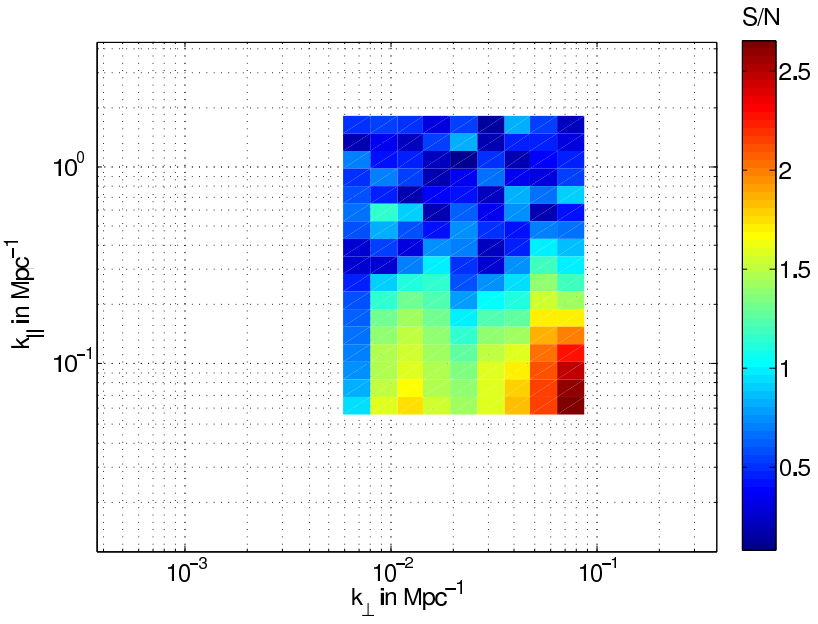

Figure 5-12: Signal to noise ratio in the power spectrum plotted in Figure 5-10.

Spherical Power Spectrum

The cylindrical power spectra presented in this section are an important diagnostic for assessing systematics and contaminants in the sky, instrument, and power spectrum estimation procedure. However, the ultimate goal of the experiment is to constrain the power spectrum from reionization. As this signal is expected to be isotropic, the highest signal-to-noise measurement is obtained by forming a fully spherically averaged power spectrum. We computed this spherical power spectrum using the optimal quadratic estimator formulation by excising the "wedge" region from the cylindrical power spectrum shown in Figure 5-10, and then averaging in annuli of constant k, with an inverse-variance weighting determined by the uncertainty shown in Figure 5-12. A correction for the synthesized beam was applied to the resulting power spectrum by dividing by the Fourier transform of the instrumental point spread function at the central frequency of the band.

The resulting band powers were found to be smaller than twice the uncertainties derived from the estimation procedure. Consequently, we take our measurements as 2σ upper limits on the 21-cm power spectrum, where σ is the derived uncertainty in our measurements. These limits are displayed in Figure 5-13, along with exper-

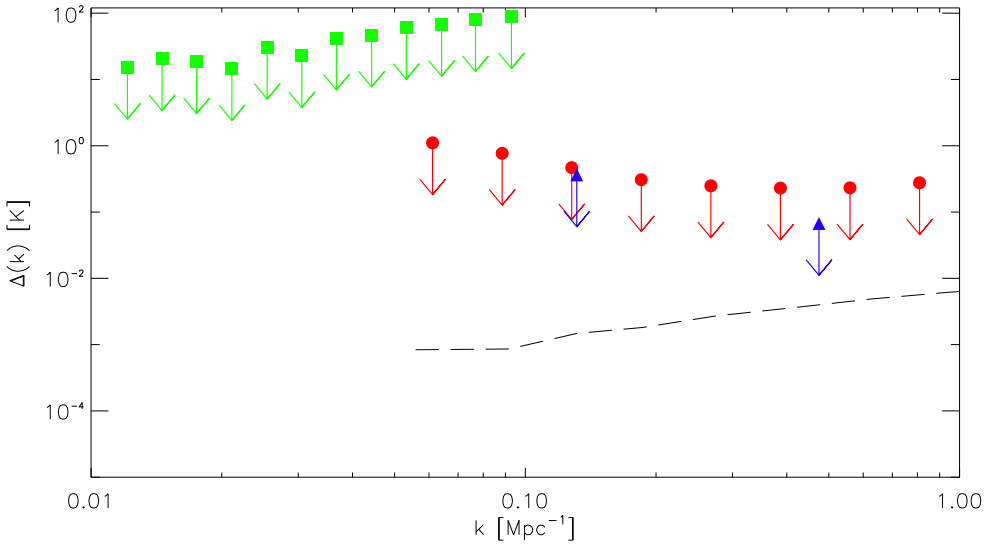

Figure 5-13: Current limits on the EoR power spectrum. The red circles show 2σ upper limits calculated using the optimal quadratic estimator technique at redshift $z = 9.2$ ($\nu = 139.8$ MHz), while the blue triangles show 2σ upper limits from Paciga et al. (2011) at a redshift of $z = 8.5$ ($\nu = 150$ MHz), and the green squares show measured values for the foreground power spectrum from Parsons et al. (2010) at $z = 8.7$ ($\nu = 146.9$ MHz), which serve as an upper limit to the EoR power spectrum. A model power spectrum at $z = 9$ (with a neutral fraction of 0.86) from Mesinger et al. (2011) is shown with a dashed line.

imental limits from the PAPER array (Parsons et al., 2010) and from the GMRT EoR experiment (Paciga et al., 2011) for comparison, as well as a theoretical limit at $z = 9$ from Mesinger et al. (2011). The MWA power spectrum is comparable to the results from the GMRT EoR experiment, both of which are ∼2 orders of magnitude above the expected EoR signal. In most realistic theoretical models, the peak of the power spectrum is below a value of $\Delta \lesssim 10$ mK during reionization (see, e.g. McQuinn et al. 2006; Lidz et al. 2008; Iliev et al. 2008). This measurement should be taken as an upper limit.

5.5 Conclusions

The power spectra presented in this section serve as the one of the first efforts to produce a power spectrum of the 21-cm signal during reionization from the Murchi-

son Widefield Array. Although the power spectrum limits that we have produced are several orders of magnitude larger than the expected theoretical signal, this serves as a useful assessment of instrumental contamination, and provides a competitive constraint relative to other first generation experiments (Parsons et al., 2010; Paciga et al., 2011).

The cylindrical power spectra presented in this chapter serve as the first observational measurements of the $k_\perp$-$k_\parallel$ plane. Simulations and theoretical efforts have provided a strong motivation for specific features in the $k_\perp$-$k_\parallel$ plane (Datta et al., 2010; Vedantham et al., 2011; Morales et al., 2012), however these features have not been confirmed observationally until now. We have confirmed the "wedge" due to point spread function contamination, and find that it has the expected shape and location in the $k_\perp$-$k_\parallel$ plane. The presence of an "EoR window" that appears to be relatively free from contamination is an important verification that the measurements are not dominated by any unexpected instrumental systematics or other foregrounds. This analysis has highlighted the effects of the gaps between channels in the MWA polyphase filterbank. This may motivate a future update to the filterbank firmware to improve the filter shape, and the resulting power spectrum estimates which can be produced from the data.

As the MWA is expanded to a 128 tile instrument, the increased uv coverage and collecting area will provide a large increase in EoR sensitivity. The analysis techniques developed and incorporated as part of this effort will serve as a prototype for the reduction and power spectrum estimation which will be used with the full MWA array. The application of the optimal quadratic estimator technique of Liu & Tegmark (2011) to MWA data is an important verification of this method with observed data, and verifies that it can be successfully applied in spite of the potential computational constraints and non-ideal features of the instrument. We plan to continue to improve our model of the covariance and to apply the optimal quadratic estimator to the full X13 data set to determine the best possible MWA constraints across a wide range of redshifts.

THIS PAGE INTENTIONALLY LEFT BLANK

Chapter 6

Conclusion

This thesis has chronicled an ongoing effort to place some of the first observational constraints on the Epoch of Reionization using redshifted emission from the 21-cm hydrogen line. In Chapter 1, we began by introducing the Epoch of Reionization, and motivated why it is an extremely important period in the history of the universe that has inspired several new observational efforts. In Chapter 2, we described the MWA, one of the new instruments under development which promises to make significant advances towards observing the 21-cm line during the EoR. However, as these instruments are complicated and need to be characterized to a high degree of accuracy, we devoted Chapter 3 to describing an effort to model and verify the performance of the MWA's primary collecting elements. In Chapter 4, we described some of the first observations with the MWA 32-Tile prototype which study the population of astrophysical sources which represent one of the most daunting challenges to successfully making an EoR measurement. Finally, in Chapter 5, we have produced some of the first MWA power spectra aimed at characterizing the EoR, and have used them to verify theoretical predictions for the shapes of confusing foregrounds and finally to place an upper limit on the power spectrum of 21-cm emission. The survey of point sources and EoR power spectra presented as part of this thesis represent the first reionization science results with the MWA.

The future is bright for the MWA. Construction is currently in progress which will expand the instrument to a 128-Tile interferometer, incorporating many improve-

ments which were developed over the course of the 32-Tile campaign (Tingay et al., in prep.). As a part of this expansion, the array will include a dense core optimized for sensitivity in an eventual EoR measurement. The expanded array also includes longer baselines (1.5 km) which will increase the calibration fidelity, give a lower source confusion limit, and will allow the array to perform a deep survey of the low-frequency sky. The increased instantaneous sensitivity and more complete *uv* coverage will also allow the MWA Real Time System (RTS) to operate as intended, providing *in situ* measurements of the MWA primary beam, and corrections for the varying direction-dependent response of the tiles. With a planned 1000 hour integration (Beardsley et al., 2012), this 128T should be able to place constraints on realistic models of reionization. The techniques developed and employed in this thesis will serve as a prototype for this effort.

However, several outstanding issues remain along the path towards an EoR measurement with the MWA. A more complete characterization of the instrumental response and systematics remains an open issue. Although the simulations of the MWA primary beam presented in Chapter 3 represent a good first step in modeling the MWA instrumental response, a more systematic study of the accuracy of these beam patterns based off of observed data is necessary. The relatively large flux uncertainties between the MWA and other low-frequency surveys described in Chapter 4 suggests that there is still considerable work to be done in understanding both the low frequency sky as well as the details of calibration and measurement. The polarization properties of both the MWA and the radio sky at these frequencies also remains a large outstanding issue. The leakage of polarized galactic emission into the total intensity measurements have the potential to contaminate the EoR power spectrum signature (Geil et al., 2011), and they have yet to be investigated in detail. Resolving these issues should remain a high priority.

The broader effort towards 21-cm science effort has promising prospects. In addition to the MWA buildout to a 128-tile instrument, the PAPER collaboration is also in the process of scaling up to a $\gtrsim$ 100 element array, and experimenting with using redundant k-mode sampling to improve EoR sensitivity (Parsons et al.,

2011), while the GMRT and LOFAR experiments continue to expand in scope. As these first-generation experiments reach their design sensitivities over the next several years, the limits on the reionization power spectrum will continue to improve, and eventually culminate in a detection. In addition to efforts in the radio band, new optical and infrared measurements with the Hubble Space Telescope as well as the James Webb Space Telescope and ground-based instrumentation are identifying galaxies and quasars at ever increasing redshift. New galaxy candidates at redshifts of $z \gtrsim 9$ (Yan et al., 2010; Bouwens et al., 2011; Zheng et al., 2012) provide a tantalizing glimpse at some of the early sources which ionized our Universe, and when combined with eventual 21-cm observations and constraints, will help to develop a unified picture of this epoch.

The march of technology will lead to further improvements in the capabilities of low-frequency radio arrays. Affordable high performance digital electronics will lead to the feasibility of telescopes with larger numbers of elements and higher bandwidths. The Hydrogen Epoch of Reionization Array (HERA)[1] plan describes a roadmap for the future development of radio instrumentation for 21-cm science, and has received a strong endorsement from 2010 Decadal Survey (National Research Council, 2010). HERA describes a unified architecture for combining the advances in technologies and techniques of the first generation of EoR experiments, and moving towards a larger instrument with a $100,000$ m^2 collecting area which will be able to go beyond the first detection of the reionization power spectrum, and move into the regime of performing a detailed characterization of the signal. Further in the future, a Square Kilometer Array[2] class instrument will allow direct imaging of the neutral hydrogen in reionization and the dark ages.

All of these efforts, when viewed together, are aimed at the common goal of exploring one of the most compelling frontiers of cosmology. This thesis represents one small part of the process of developing new instruments and techniques which will open a new window on our Universe. Just as the Epoch of Reionization represents a

[1] http://reionization.org/
[2] http://www.skatelescope.org

cosmic dawn of sorts for the first stars and galaxies, the MWA and other instruments like it represent a new dawn of exciting low-frequency radio capabilities which promise new and exciting discoveries in the years to come.

Appendix A

Detected Radio Sources in the EoR2 and HydraA Fields

Table A.1: Sources Detected Above SNR 5

Name	RA	DEC	S_{avg}	$S_{123.52}$	$S_{154.24}$	$S_{184.96}$	Field	r_{FC}	SNR
J0747−1854	07h47m05s	−18°54′12″	8.8±2.8	10.1±3.7	9.2±6.0	8.9±8.5	HydA	22.9°	8.6
J0747−1919	07h47m27s	−19°19′33″	22.2±6.7	25.2±8.9	23.8±14.5	15.1±13.0	HydA	23.0°	22.4
J0751−1919	07h51m20s	−19°19′30″	7.1±2.2	8.1±3.0	8.5±5.3	4.7±5.1	HydA	22.1°	8.7
J0752−2204	07h52m30s	−22°04′38″	4.4±1.5	4.7±1.8	7.1±4.5	14.4±12.1	HydA	22.7°	5.6
J0752−2627	07h52m30s	−26°27′43″	8.4±2.7	9.8±3.7	3.6±3.1	···	HydA	24.7°	7.0
J0757−1137	07h57m10s	−11°37′10″	3.9±1.3	4.7±1.8	5.1±3.3	2.5±2.5	HydA	19.8°	6.0
J0802−0915	08h02m18s	−09°15′32″	3.4±1.2	5.8±2.2	2.1±1.5	1.9±1.8	HydA	18.8°	5.0
J0802−0958	08h02m34s	−09°58′55″	8.9±2.8	12.4±4.4	6.0±3.7	9.1±7.3	HydA	18.6°	12.6
J0803−0804	08h03m60s	−08°04′48″	4.5±1.4	6.5±2.4	2.4±1.6	6.7±5.4	HydA	18.7°	7.0
J0804−1244	08h04m17s	−12°44′32″	4.6±1.5	4.8±1.8	5.2±3.2	4.5±3.7	HydA	18.0°	9.3
J0804−1726	08h04m42s	−17°26′41″	4.9±1.5	5.8±2.1	4.5±2.8	3.1±2.6	HydA	18.5°	9.1
J0804−1502	08h04m53s	−15°02′54″	2.8±0.9	2.2±1.0	4.6±2.9	1.0±1.1	HydA	18.0°	6.4
J0805−0100	08h05m30s	−01°00′12″	9.4±2.9	10.8±3.9	8.3±5.2	6.4±5.4	HydA	21.1°	10.4
J0805−0739	08h05m40s	−07°39′22″	3.5±1.2	4.4±1.7	3.7±2.4	1.9±1.9	HydA	18.4°	5.5
J0806−2204	08h06m26s	−22°04′43″	3.7±1.2	4.2±1.6	3.8±2.4	3.6±3.1	HydA	19.8°	6.2
J0807−1724	08h07m30s	−17°24′59″	6.8±2.1	7.7±2.8	6.1±2.2	7.2±2.6	HydA	17.9°	14.2
J0808−0749	08h08m18s	−07°49′14″	3.3±1.1	3.9±1.5	2.4±1.1	4.2±1.7	HydA	17.7°	5.2
J0808−2314	08h08m37s	−23°14′50″	3.4±1.1	4.0±1.5	3.2±2.1	1.9±2.0	HydA	19.9°	7.0
J0808−1028	08h08m51s	−10°28′13″	25.8±7.8	33.2±11.7	21.5±7.6	15.1±5.3	HydA	17.1°	24.7
J0810−1834	08h10m49s	−18°34′31″	2.6±0.9	3.0±1.2	2.6±1.0	3.0±1.2	HydA	17.5°	6.1
J0811−1011	08h11m24s	−10°11′44″	6.9±2.3	7.2±2.7	7.2±2.6	6.8±2.5	HydA	16.5°	7.1
J0811−0227	08h11m49s	−02°27′47″	4.0±1.4	4.4±1.8	5.0±3.2	3.5±3.0	HydA	19.0°	5.0

Continued on Next Page...

Table A.1 – Continued

Name	RA	DEC	$S_{\rm avg}$	$S_{123.52}$	$S_{154.24}$	$S_{184.96}$	Field	$r_{\rm FC}$	SNR
J0812−0519	08h12m00s	−05°19′32″	4.5±1.4	6.3±2.3	6.0±2.2	3.5±1.4	HydA	17.7°	8.6
J0812−0550	08h12m06s	−05°50′28″	6.8±2.1	7.6±2.7	6.8±2.5	7.2±2.6	HydA	17.4°	13.8
J0814−2520	08h14m17s	−25°20′50″	2.9±1.0	3.6±1.5	2.5±1.7	2.6±2.5	HydA	20.1°	5.1
J0814−1835	08h14m55s	−18°35′50″	3.7±1.1	4.4±1.6	3.5±1.3	3.1±1.2	HydA	16.6°	10.1
J0815−1616	08h15m08s	−16°16′10″	4.8±1.5	5.7±2.1	4.1±1.5	4.6±1.7	HydA	15.8°	13.0
J0815−0308	08h15m29s	−03°08′48″	29.1±8.8	35.2±12.4	25.5±9.0	18.9±6.7	HydA	17.9°	49.9
J0815+0152	08h15m31s	+01°52′41″	8.8±2.8	9.3±3.5	11.3±6.9	13.0±10.5	HydA	20.9°	9.3
J0815−1140	08h15m52s	−11°40′30″	2.9±0.9	3.5±1.4	3.0±1.2	2.5±1.0	HydA	15.2°	6.5
J0817−1520	08h17m46s	−15°20′59″	1.8±0.6	2.1±0.9	2.0±0.8	1.4±0.6	HydA	15.0°	5.4
J0818−1959	08h18m09s	−19°59′19″	2.5±0.8	2.9±1.1	2.3±0.9	2.6±1.0	HydA	16.4°	6.9
J0819−1056	08h19m09s	−10°56′48″	2.4±0.8	1.2±0.7	3.4±1.3	2.7±1.0	HydA	14.5°	6.3
J0820−1348	08h20m06s	−13°48′60″	1.6±0.5	1.7±0.7	1.5±0.6	1.7±0.7	HydA	14.2°	7.4
J0820−1259	08h20m55s	−12°59′05″	1.7±0.6	1.7±0.8	2.1±0.8	1.9±0.8	HydA	14.0°	7.3
J0820−1526	08h20m58s	−15°26′50″	2.1±0.7	2.6±1.0	1.7±0.7	2.2±0.8	HydA	14.3°	6.2
J0821−1938	08h21m08s	−19°38′01″	2.1±0.7	2.5±1.0	1.9±0.8	2.1±0.8	HydA	15.6°	5.4
J0821−3012	08h21m16s	−30°12′52″	15.0±4.6	17.2±6.1	14.9±9.1	15.6±12.8	HydA	22.4°	20.0
J0822−1850	08h22m27s	−18°50′51″	2.4±0.8	2.9±1.1	2.2±0.8	2.5±0.9	HydA	15.0°	6.7
J0822+0514	08h22m30s	+05°14′18″	6.5±2.1	6.8±2.6	10.9±6.8	7.7±6.6	HydA	22.2°	7.9
J0822−1452	08h22m35s	−14°52′08″	1.6±0.5	1.9±0.8	1.6±0.7	1.5±0.6	HydA	13.8°	6.4
J0822−0456	08h22m38s	−04°56′26″	3.3±1.1	···	5.0±1.8	4.0±1.5	HydA	15.5°	9.3
J0822+0556	08h22m45s	+05°56′28″	16.7±5.1	19.0±6.7	17.6±10.7	14.0±11.6	HydA	22.7°	17.9
J0823−1650	08h23m04s	−16°50′46″	2.7±0.9	4.1±1.5	···	2.2±0.8	HydA	14.1°	6.7
J0823−1203	08h23m16s	−12°03′13″	1.4±0.5	1.7±0.7	1.0±0.5	1.3±0.6	HydA	13.4°	5.1
J0823−0745	08h23m46s	−07°45′43″	2.2±0.7	2.0±0.9	2.2±0.9	2.4±0.9	HydA	14.1°	6.7
J0823−1529	08h23m49s	−15°29′35″	2.5±0.8	2.8±1.1	2.0±0.8	2.5±0.9	HydA	13.6°	8.4
J0824−1252	08h24m18s	−12°52′10″	1.8±0.6	1.5±0.6	2.1±0.8	1.8±0.7	HydA	13.2°	7.4
J0824−0949	08h24m25s	−09°49′42″	4.2±1.3	4.8±1.7	4.1±1.5	3.6±1.3	HydA	13.4°	13.4
J0824−2454	08h24m33s	−24°54′35″	3.0±1.0	2.9±1.2	3.4±2.1	2.3±2.0	HydA	18.0°	6.5
J0825−0500	08h25m58s	−05°00′31″	2.3±0.8	1.2±0.7	2.3±1.0	3.5±1.3	HydA	14.7°	7.0
J0826−2315	08h26m35s	−23°15′24″	2.6±0.9	2.3±1.0	2.7±1.1	3.4±1.3	HydA	16.6°	5.5
J0826−1530	08h26m55s	−15°30′26″	1.4±0.5	1.6±0.7	1.1±0.5	1.8±0.7	HydA	12.9°	5.1
J0827−0614	08h27m04s	−06°14′15″	2.6±0.8	3.2±1.3	2.5±1.0	2.9±1.1	HydA	13.9°	8.4
J0827−2026	08h27m13s	−20°26′29″	23.2±7.0	27.5±9.6	22.2±7.8	16.2±5.7	HydA	14.8°	75.7
J0827−1953	08h27m51s	−19°53′55″	2.9±0.9	4.4±1.6	2.1±0.9	3.0±1.1	HydA	14.4°	9.6
J0828+0114	08h28m04s	+01°14′34″	3.4±1.2	4.1±1.6	3.3±2.1	3.2±2.7	HydA	18.2°	5.8
J0828−2214	08h28m08s	−22°14′38″	2.5±0.8	1.4±0.7	3.2±1.2	3.4±1.3	HydA	15.7°	6.8
J0829−1810	08h29m21s	−18°10′45″	1.7±0.6	1.9±1.1	1.5±0.6	1.6±0.6	HydA	13.2°	6.5
J0830+0744	08h30m25s	+07°44′00″	8.7±2.9	10.1±3.8	7.0±4.9	8.8±7.8	HydA	23.1°	6.4
J0830−1914	08h30m27s	−19°14′51″	1.9±0.6	2.0±1.0	1.9±0.8	2.0±0.8	HydA	13.5°	6.8
J0830−0337	08h30m44s	−03°37′58″	3.7±1.1	5.2±1.9	2.7±1.1	4.0±1.5	HydA	14.4°	11.9
J0830−1632	08h30m59s	−16°32′51″	1.6±0.6	1.8±0.8	1.6±0.6	1.3±0.5	HydA	12.3°	5.6

Continued on Next Page...

Table A.1 – Continued

Name	RA	DEC	$S_{\rm avg}$	$S_{123.52}$	$S_{154.24}$	$S_{184.96}$	Field	$r_{\rm FC}$	SNR
J0831−2922	08h31m24s	−29°22′26″	3.6±1.2	4.2±1.7	3.7±2.4	4.1±3.6	HydA	20.4°	5.7
J0832−1159	08h32m25s	−11°59′20″	1.4±0.5	···	1.4±0.6	1.7±0.6	HydA	11.2°	6.0
J0832−0532	08h32m39s	−05°32′20″	5.2±1.6	6.0±2.2	4.2±1.5	4.6±1.6	HydA	13.0°	17.2
J0833−1418	08h33m05s	−14°18′21″	1.2±0.4	2.3±0.9	1.1±0.5	1.1±0.5	HydA	11.2°	5.6
J0834−3443	08h34m29s	−34°43′22″	6.1±2.1	6.9±2.7	7.5±5.3	···	HydA	24.7°	5.0
J0834−0553	08h34m43s	−05°53′35″	2.6±0.8	2.7±1.1	2.9±1.1	1.9±0.7	HydA	12.4°	8.5
J0835−1620	08h35m00s	−16°20′46″	1.9±0.6	2.7±1.1	1.7±0.7	1.5±0.6	HydA	11.3°	7.5
J0835−0746	08h35m06s	−07°46′42″	4.8±1.5	5.1±1.9	4.7±1.7	4.1±1.5	HydA	11.4°	18.8
J0835−0527	08h35m11s	−05°27′25″	2.9±0.9	2.0±0.9	2.6±1.0	3.1±1.1	HydA	12.5°	9.5
J0835−0148	08h35m40s	−01°48′54″	3.6±1.1	4.2±1.6	3.4±1.3	2.8±1.1	HydA	14.7°	8.9
J0835−1539	08h35m43s	−15°39′48″	1.6±0.5	0.5±0.5	1.3±0.5	2.1±0.8	HydA	10.9°	7.1
J0836−1335	08h36m05s	−13°35′56″	3.8±1.1	3.5±1.3	3.7±1.3	3.4±1.2	HydA	10.4°	16.5
J0836−1714	08h36m06s	−17°14′59″	1.3±0.4	1.8±0.7	1.1±0.5	1.1±0.4	HydA	11.4°	6.0
J0836−0041	08h36m18s	−00°41′06″	2.6±0.9	3.1±1.2	2.3±0.9	2.0±0.9	HydA	15.4°	5.5
J0836−2017	08h36m32s	−20°17′10″	1.6±0.5	1.5±0.7	1.8±0.7	2.1±0.8	HydA	12.9°	5.8
J0836−1156	08h36m58s	−11°56′15″	2.2±0.7	···	···	1.9±0.7	HydA	10.1°	9.6
J0837−1936	08h37m03s	−19°36′04″	0.8±0.3	···	1.5±0.6	2.2±0.8	HydA	12.4°	5.1
J0837−1949	08h37m05s	−19°49′04″	6.2±1.9	6.4±2.3	5.9±2.1	6.3±2.2	HydA	12.5°	29.3
J0837−2239	08h37m32s	−22°39′01″	3.5±1.1	3.9±1.4	3.2±1.2	3.3±1.2	HydA	14.3°	11.2
J0838−0040	08h38m50s	−00°40′30″	2.6±0.9	3.2±1.3	2.3±0.9	1.5±0.7	HydA	15.0°	6.1
J0838−0135	08h38m53s	−01°35′15″	2.2±0.8	···	2.3±0.9	2.0±0.8	HydA	14.3°	5.4
J0839−1213	08h39m50s	−12°13′35″	13.4±4.0	15.8±5.5	12.9±4.5	10.4±3.7	HydA	9.4°	61.0
J0840−2148	08h40m17s	−21°48′09″	1.4±0.5	1.6±0.7	1.3±0.5	1.2±0.5	HydA	13.3°	5.6
J0840−1816	08h40m41s	−18°16′45″	2.4±0.7	3.5±1.2	2.6±0.9	2.0±0.7	HydA	10.9°	13.0
J0841−2527	08h41m31s	−25°27′41″	2.6±0.9	2.7±1.2	3.0±1.1	1.6±0.7	HydA	15.9°	5.9
J0841−1939	08h41m52s	−19°39′47″	1.2±0.4	1.5±0.6	0.8±0.4	1.4±0.5	HydA	11.5°	5.9
J0842−0717	08h42m16s	−07°17′54″	2.5±0.8	3.6±1.3	2.3±0.9	1.8±0.7	HydA	10.0°	11.2
J0842−1514	08h42m51s	−15°14′43″	1.9±0.6	2.8±1.0	1.5±0.6	1.4±0.5	HydA	9.1°	10.6
J0842−0641	08h42m53s	−06°41′25″	1.2±0.4	0.5±0.5	1.3±0.5	1.6±0.6	HydA	10.2°	5.0
J0843−0857	08h43m12s	−08°57′14″	2.3±0.7	2.3±0.9	2.1±0.8	2.1±0.8	HydA	9.1°	9.0
J0844−1310	08h44m14s	−13°10′54″	1.6±0.5	2.0±0.8	1.3±0.5	1.5±0.5	HydA	8.3°	8.1
J0844−1813	08h44m20s	−18°13′50″	1.0±0.3	1.6±0.6	1.1±0.4	0.9±0.4	HydA	10.2°	5.0
J0844−2629	08h44m26s	−26°29′44″	4.9±1.5	5.7±2.1	4.5±1.6	3.7±1.4	HydA	16.4°	10.6
J0844−3350	08h44m53s	−33°50′46″	5.8±2.0	6.6±2.6	5.9±4.1	5.8±7.5	HydA	23.0°	5.5
J0845−1401	08h45m11s	−14°01′06″	1.6±0.5	1.7±0.7	1.1±0.5	1.5±0.5	HydA	8.2°	8.0
J0845−1135	08h45m14s	−11°35′26″	1.9±0.6	2.0±0.8	1.7±0.6	1.6±0.6	HydA	8.1°	10.1
J0845−2333	08h45m37s	−23°33′36″	2.0±0.7	1.6±0.7	1.9±0.8	2.8±1.0	HydA	13.8°	6.4
J0846−2257	08h46m36s	−22°57′51″	2.2±0.7	3.0±1.1	1.9±0.8	1.9±0.7	HydA	13.2°	7.9
J0846−2945	08h46m49s	−29°45′35″	8.1±2.5	9.4±3.4	7.9±4.8	7.4±6.1	HydA	19.1°	16.3
J0847−2057	08h47m04s	−20°57′50″	0.9±0.3	2.0±0.8	0.6±0.3	1.0±0.4	HydA	11.6°	5.2
J0847−1755	08h47m38s	−17°55′37″	2.5±0.8	1.5±0.6	2.7±1.0	2.3±0.8	HydA	9.4°	15.9

Continued on Next Page...

Table A.1 – Continued

Name	RA	DEC	$S_{\rm avg}$	$S_{123.52}$	$S_{154.24}$	$S_{184.96}$	Field	$r_{\rm FC}$	SNR
J0848−1133	08h48m10s	−11°33′15″	1.7±0.5	2.9±1.1	···	1.5±0.5	HydA	7.3°	8.4
J0848−2230	08h48m15s	−22°30′16″	1.4±0.5	···	1.3±0.6	1.6±0.6	HydA	12.6°	5.5
J0848−1626	08h48m17s	−16°26′47″	1.6±0.5	···	···	1.4±0.5	HydA	8.4°	9.6
J0848−1026	08h48m50s	−10°26′17″	1.4±0.5	2.5±1.0	1.5±0.6	1.1±0.4	HydA	7.4°	5.8
J0848+0554	08h48m51s	+05°54′25″	5.4±1.8	6.5±2.5	4.9±3.3	5.5±4.8	HydA	19.4°	7.6
J0848−1238	08h48m57s	−12°38′41″	2.6±0.8	3.0±1.1	2.3±0.9	2.4±0.8	HydA	7.1°	13.5
J0849−0404	08h49m02s	−04°04′58″	1.9±0.6	1.6±0.7	1.5±0.6	1.9±0.7	HydA	10.7°	7.4
J0849−1905	08h49m10s	−19°05′48″	0.9±0.3	0.7±0.4	0.8±0.3	1.0±0.4	HydA	9.9°	5.2
J0849−0531	08h49m33s	−05°31′05″	1.7±0.6	2.0±0.8	1.9±0.7	1.3±0.5	HydA	9.6°	6.3
J0849−1327	08h49m43s	−13°27′15″	1.4±0.5	1.6±0.7	1.1±0.5	1.2±0.5	HydA	7.1°	6.7
J0849−0814	08h49m57s	−08°14′39″	1.7±0.6	0.8±0.5	1.2±0.5	1.9±0.7	HydA	7.9°	7.2
J0849−2942	08h49m57s	−29°42′07″	3.5±1.1	3.9±1.5	3.5±2.2	3.9±3.4	HydA	18.8°	6.6
J0850−3454	08h50m28s	−34°54′55″	6.0±2.0	6.9±2.6	5.7±4.2	···	HydA	23.7°	6.2
J0850−0911	08h50m37s	−09°11′16″	1.7±0.6	2.7±1.0	···	1.5±0.6	HydA	7.3°	6.9
J0850−1028	08h50m48s	−10°28′40″	2.8±0.9	2.7±1.0	2.9±1.0	2.3±0.8	HydA	6.9°	14.3
J0852+0043	08h52m32s	+00°43′13″	3.0±1.0	3.4±1.4	3.2±1.3	2.4±1.0	HydA	14.3°	7.1
J0852−2046	08h52m56s	−20°46′60″	20.4±6.1	20.9±7.3	19.6±6.9	17.5±6.1	HydA	10.6°	99.7
J0853−0340	08h53m25s	−03°40′02″	7.0±2.1	7.7±2.7	7.2±2.6	6.1±2.2	HydA	10.4°	29.5
J0853−1642	08h53m40s	−16°42′40″	1.6±0.5	2.9±1.1	···	1.2±0.5	HydA	7.5°	9.8
J0853−2250	08h53m42s	−22°50′47″	3.4±1.1	3.9±1.4	3.4±1.2	2.9±1.0	HydA	12.2°	12.8
J0853−1426	08h53m49s	−14°26′46″	13.4±4.0	12.4±4.3	12.9±4.5	11.0±3.8	HydA	6.4°	60.2
J0854−1153	08h54m19s	−11°53′01″	1.1±0.4	···	···	1.4±0.5	HydA	5.8°	5.6
J0855−0713	08h55m08s	−07°13′33″	3.3±1.0	4.3±1.6	3.0±1.1	2.8±1.0	HydA	7.5°	16.1
J0855+0552	08h55m18s	+05°52′50″	4.1±1.4	4.7±1.8	4.3±2.8	2.6±2.6	HydA	18.8°	5.4
J0855−1255	08h55m26s	−12°55′27″	3.7±1.1	5.8±2.1	4.4±1.6	2.5±0.9	HydA	5.6°	18.1
J0856−0611	08h56m12s	−06°11′04″	1.4±0.5	2.2±0.9	1.7±0.6	0.8±0.4	HydA	8.0°	5.4
J0856−1123	08h56m50s	−11°23′43″	0.9±0.3	1.6±0.7	1.3±0.5	0.6±0.3	HydA	5.2°	5.3
J0856−2603	08h56m56s	−26°03′01″	2.6±0.8	3.0±1.2	2.4±0.9	2.7±1.0	HydA	14.8°	9.7
J0857−2114	08h57m16s	−21°14′29″	3.4±1.0	2.6±1.0	2.9±1.1	3.4±1.2	HydA	10.4°	16.8
J0857−0338	08h57m16s	−03°38′33″	4.2±1.3	3.9±1.4	4.8±1.7	3.4±1.2	HydA	9.9°	17.9
J0857+0946	08h57m33s	+09°46′50″	9.1±2.9	10.3±3.8	10.4±6.9	25.0±23.2	HydA	22.4°	7.0
J0858−1949	08h58m04s	−19°49′23″	3.3±1.0	3.6±1.3	3.4±1.2	2.7±1.0	HydA	9.1°	17.1
J0858−1810	08h58m25s	−18°10′48″	1.5±0.5	2.8±1.0	1.5±0.6	1.1±0.4	HydA	7.7°	9.7
J0858−2706	08h58m43s	−27°06′40″	2.4±0.8	2.8±1.1	2.4±0.9	2.6±1.1	HydA	15.7°	8.6
J0858−1643	08h58m46s	−16°43′31″	1.6±0.5	2.7±1.0	0.9±0.4	1.6±0.6	HydA	6.6°	8.6
J0858−0026	08h58m49s	−00°26′57″	2.7±0.9	···	···	3.2±1.2	HydA	12.6°	6.3
J0859−1122	08h59m07s	−11°22′10″	1.3±0.4	1.4±0.6	1.4±0.5	1.0±0.4	HydA	4.7°	6.8
J0859−1921	08h59m34s	−19°21′41″	4.7±1.4	5.7±2.0	5.1±1.8	3.6±1.3	HydA	8.5°	28.0
J0859−0740	08h59m48s	−07°40′37″	0.9±0.3	···	0.8±0.4	···	HydA	6.3°	5.2
J0900−2401	09h00m23s	−24°01′18″	1.5±0.5	2.9±1.2	2.3±0.8	1.6±0.6	HydA	12.7°	6.4
J0900−0225	09h00m52s	−02°25′10″	2.1±0.7	···	1.8±0.7	2.3±0.8	HydA	10.6°	6.9

Continued on Next Page...

Table A.1 – Continued

Name	RA	DEC	$S_{\rm avg}$	$S_{123.52}$	$S_{154.24}$	$S_{184.96}$	Field	$r_{\rm FC}$	SNR
J0901−2555	09h01m42s	−25°55′32″	50.7±15.2	55.6±19.5	49.9±17.5	43.4±15.2	HydA	14.4°	164.7
J0901−0551	09h01m51s	−05°51′51″	1.5±0.5	1.6±0.7	1.6±0.6	···	HydA	7.4°	5.9
J0902−1414	09h02m16s	−14°14′08″	3.5±1.1	4.0±1.4	2.5±0.9	3.5±1.2	HydA	4.4°	21.5
J0902−0515	09h02m26s	−05°15′42″	10.1±3.0	10.1±3.6	10.9±3.8	8.2±2.9	HydA	7.8°	37.3
J0902−1439	09h02m29s	−14°39′21″	0.9±0.3	2.0±0.8	1.4±0.6	0.8±0.3	HydA	4.6°	6.0
J0903−2014	09h03m14s	−20°14′23″	1.2±0.4	1.2±0.6	0.9±0.4	1.2±0.4	HydA	8.9°	6.0
J0903−1929	09h03m52s	−19°29′19″	0.9±0.3	2.0±0.8	1.0±0.4	0.7±0.3	HydA	8.2°	5.2
J0904−1331	09h04m29s	−13°31′20″	2.1±0.6	···	1.7±0.6	1.8±0.6	HydA	3.6°	10.5
J0904−1231	09h04m36s	−12°31′07″	1.9±0.6	2.8±1.1	1.6±0.6	1.6±0.6	HydA	3.3°	10.8
J0904−1957	09h04m37s	−19°57′08″	2.2±0.7	3.8±1.4	2.1±0.8	2.0±0.7	HydA	8.5°	12.3
J0905−0421	09h05m18s	−04°21′03″	2.4±0.8	···	2.0±0.8	2.2±0.8	HydA	8.3°	6.8
J0905−2706	09h05m46s	−27°06′55″	2.0±0.7	0.9±0.6	2.7±1.0	4.0±1.5	HydA	15.3°	7.7
J0906−1630	09h06m15s	−16°30′38″	1.0±0.3	1.4±0.6	0.7±0.3	0.9±0.4	HydA	5.3°	5.3
J0907−1208	09h07m13s	−12°08′27″	1.8±0.6	2.8±1.1	2.3±0.8	1.3±0.5	HydA	2.7°	9.2
J0907−1243	09h07m44s	−12°43′53″	1.2±0.4	2.1±0.8	1.1±0.4	0.9±0.4	HydA	2.6°	6.4
J0907−3537	09h07m49s	−35°37′24″	6.1±2.0	6.8±2.6	8.2±6.2	17.4±14.3	HydA	23.7°	5.3
J0908−1042	09h08m03s	−10°42′05″	2.7±0.9	6.7±2.4	2.3±0.8	1.8±0.7	HydA	2.8°	6.8
J0908−1111	09h08m05s	−11°11′56″	1.6±0.5	0.4±0.5	1.4±0.5	1.3±0.5	HydA	2.6°	7.0
J0908+0412	09h08m20s	+04°12′60″	3.7±1.2	3.3±1.4	3.9±1.6	···	HydA	16.5°	5.5
J0908−2419	09h08m33s	−24°19′19″	1.3±0.4	2.6±1.0	0.8±0.4	2.1±0.8	HydA	12.5°	5.9
J0908−0119	09h08m38s	−01°19′41″	1.7±0.6	2.5±1.0	1.4±0.6	1.8±0.7	HydA	11.0°	5.5
J0908−2033	09h08m39s	−20°33′02″	1.7±0.5	1.9±0.8	1.3±0.5	1.6±0.6	HydA	8.8°	7.8
J0909−3140	09h09m11s	−31°40′30″	3.8±1.2	4.8±1.8	1.7±1.3	···	HydA	19.7°	6.7
J0909−1635	09h09m13s	−16°35′06″	1.4±0.4	1.8±0.8	1.7±0.6	0.9±0.4	HydA	5.0°	6.7
J0909−1551	09h09m20s	−15°51′53″	0.9±0.3	1.4±0.7	1.0±0.4	0.7±0.3	HydA	4.3°	5.4
J0909+0053	09h09m37s	+00°53′07″	3.4±1.1	3.9±1.4	3.5±1.4	3.0±1.2	HydA	13.1°	8.0
J0909−0341	09h09m57s	−03°41′13″	1.6±0.6	1.1±0.7	2.4±0.9	1.3±0.6	HydA	8.6°	5.4
J0910−2231	09h10m09s	−22°31′06″	1.4±0.5	1.6±0.7	1.3±0.5	1.1±0.4	HydA	10.6°	6.3
J0910−0419	09h10m40s	−04°19′19″	1.6±0.5	1.6±0.8	1.3±0.6	1.4±0.6	HydA	8.0°	5.4
J0910−1033	09h10m41s	−10°33′19″	2.9±0.9	···	2.7±1.0	2.3±0.9	HydA	2.4°	7.6
J0910−0754	09h10m58s	−07°54′29″	2.5±0.8	···	2.6±1.0	2.0±0.8	HydA	4.5°	8.2
J0911−3112	09h11m16s	−31°12′25″	2.7±0.9	3.1±1.2	2.6±1.8	3.9±3.8	HydA	19.2°	5.1
J0911−0706	09h11m59s	−07°06′27″	1.5±0.5	···	2.0±0.7	1.2±0.5	HydA	5.2°	5.3
J0912−2512	09h12m44s	−25°12′36″	2.3±0.7	2.6±1.0	2.1±0.8	2.3±0.8	HydA	13.2°	9.4
J0913−1431	09h13m40s	−14°31′18″	1.8±0.6	1.7±0.7	1.7±0.6	1.6±0.6	HydA	2.7°	9.8
J0913−2040	09h13m46s	−20°40′18″	1.6±0.5	2.1±0.8	1.5±0.6	1.3±0.5	HydA	8.7°	6.6
J0913−1717	09h13m51s	−17°17′07″	1.1±0.4	0.6±0.5	0.9±0.4	1.0±0.4	HydA	5.3°	5.8
J0914−1839	09h14m30s	−18°39′41″	1.3±0.4	···	1.8±0.7	1.1±0.4	HydA	6.6°	7.6
J0914−1328	09h14m42s	−13°28′17″	7.9±2.4	8.0±3.1	7.3±2.6	6.3±2.2	HydA	1.6°	33.2
J0914−1737	09h14m58s	−17°37′35″	1.3±0.4	···	1.7±0.6	1.1±0.4	HydA	5.6°	6.4
J0915−1629	09h15m13s	−16°29′04″	3.4±1.0	2.1±0.9	2.8±1.0	3.0±1.1	HydA	4.5°	17.3

Continued on Next Page...

Table A.1 – Continued

Name	RA	DEC	$S_{\rm avg}$	$S_{123.52}$	$S_{154.24}$	$S_{184.96}$	Field	$r_{\rm FC}$	SNR
J0915−2101	09h15m39s	−21°01′03″	1.3±0.5	···	2.2±0.8	1.7±0.6	HydA	9.0°	5.8
J0916−1128	09h16m10s	−11°28′00″	2.0±0.6	···	1.4±0.6	1.7±0.6	HydA	0.8°	6.8
J0916−0242	09h16m21s	−02°42′59″	2.0±0.7	4.7±1.7	···	1.7±0.7	HydA	9.4°	8.1
J0916+0357	09h16m35s	+03°57′16″	2.9±1.0	3.1±1.3	2.8±1.2	3.5±1.5	HydA	16.0°	6.1
J0916−0521	09h16m46s	−05°21′36″	1.5±0.5	···	···	1.2±0.5	HydA	6.7°	6.7
J0916−1717	09h16m58s	−17°17′23″	0.8±0.3	···	···	1.0±0.4	HydA	5.2°	5.2
J0917−3137	09h17m18s	−31°37′45″	3.5±1.2	3.3±1.3	···	13.1±10.8	HydA	19.6°	6.9
J0917+0523	09h17m45s	+05°23′17″	4.7±1.6	5.5±2.1	4.3±1.8	5.2±2.3	HydA	17.5°	6.8
J0917−2401	09h17m57s	−24°01′52″	1.7±0.6	···	1.8±0.7	1.8±0.7	HydA	12.0°	7.0
J0918−1204	09h18m05s	−12°04′09″	713.9±214.2	705.0±246.9	652.6±228.4	553.6±193.8	HydA	0.0°	2575.3
J0918−2204	09h18m19s	−22°04′45″	1.4±0.5	0.7±0.5	1.5±0.6	1.4±0.5	HydA	10.0°	6.4
J0918−2709	09h18m27s	−27°09′30″	2.1±0.7	2.2±0.9	2.9±1.1	2.5±1.0	HydA	15.1°	6.0
J0918−1936	09h18m28s	−19°36′29″	1.3±0.4	1.3±0.5	1.2±0.5	1.2±0.5	HydA	7.5°	7.4
J0919−0512	09h19m15s	−05°12′47″	1.7±0.5	···	···	1.2±0.5	HydA	6.9°	7.2
J0919−0623	09h19m42s	−06°23′17″	2.0±0.6	2.9±1.1	2.1±0.8	1.4±0.5	HydA	5.7°	9.8
J0919−1506	09h19m54s	−15°06′06″	2.8±0.9	2.7±1.0	3.0±1.1	2.2±0.8	HydA	3.1°	15.6
J0920−0714	09h20m40s	−07°14′41″	2.0±0.6	2.1±0.8	1.5±0.6	1.8±0.6	HydA	4.9°	10.0
J0920−1402	09h20m49s	−14°02′54″	1.2±0.4	···	1.0±0.4	···	HydA	2.1°	5.1
J0921−3222	09h21m21s	−32°22′13″	5.2±1.7	6.0±2.2	3.3±2.4	8.1±7.5	HydA	20.3°	8.1
J0922−1427	09h22m11s	−14°27′42″	11.2±3.4	9.6±3.4	10.5±3.7	9.6±3.3	HydA	2.6°	62.2
J0922+0826	09h22m17s	+08°26′02″	6.1±2.1	···	5.6±4.0	···	HydA	20.5°	5.5
J0922−2249	09h22m29s	−22°49′22″	2.7±0.9	2.7±1.0	2.4±0.9	2.5±0.9	HydA	10.8°	11.3
J0922−1755	09h22m45s	−17°55′46″	1.1±0.4	0.8±0.4	1.2±0.5	0.9±0.3	HydA	6.0°	5.2
J0922−2135	09h22m49s	−21°35′08″	2.0±0.6	2.3±0.9	2.1±0.8	1.5±0.6	HydA	9.6°	10.6
J0922−0713	09h22m51s	−07°13′50″	9.1±2.7	9.3±3.3	9.6±3.4	6.8±2.4	HydA	5.0°	49.7
J0922−2725	09h22m52s	−27°25′43″	3.1±1.0	3.5±1.3	3.0±1.1	3.6±1.3	HydA	15.4°	9.9
J0923−0429	09h23m03s	−04°29′45″	1.5±0.5	0.8±0.5	2.1±0.8	1.1±0.5	HydA	7.7°	5.1
J0923−0516	09h23m12s	−05°16′16″	1.0±0.4	1.1±0.6	···	0.7±0.3	HydA	6.9°	5.4
J0923−0933	09h23m36s	−09°33′53″	3.8±1.2	3.7±1.3	4.1±1.5	3.1±1.1	HydA	2.8°	22.8
J0924−2907	09h24m01s	−29°07′17″	3.2±1.0	3.5±1.4	3.3±1.2	3.2±1.4	HydA	17.1°	7.2
J0924−0418	09h24m21s	−04°18′17″	1.3±0.5	2.4±1.0	2.3±0.9	0.9±0.4	HydA	7.9°	5.5
J0924+0606	09h24m57s	+06°06′58″	5.1±1.7	5.8±2.2	5.3±3.4	3.7±3.5	HydA	18.3°	6.0
J0925−1244	09h25m18s	−12°44′15″	1.1±0.4	2.2±0.9	1.7±0.6	0.6±0.3	HydA	1.9°	5.9
J0926−2625	09h26m19s	−26°25′30″	2.3±0.8	2.5±1.0	2.4±0.9	2.1±0.8	HydA	14.5°	7.5
J0926−1339	09h26m40s	−13°39′06″	2.7±0.8	1.8±0.7	2.8±1.0	2.2±0.8	HydA	2.6°	18.4
J0927−0644	09h27m11s	−06°44′07″	1.8±0.6	···	1.2±0.5	1.6±0.6	HydA	5.8°	9.4
J0927−0902	09h27m39s	−09°02′27″	1.6±0.5	···	1.0±0.5	1.3±0.5	HydA	3.8°	8.0
J0927−2033	09h27m50s	−20°33′52″	1.4±0.5	1.5±0.6	1.2±0.5	1.2±0.5	HydA	8.8°	5.1
J0927−1828	09h27m58s	−18°28′35″	1.6±0.6	3.1±1.2	1.2±0.5	1.4±0.5	HydA	6.8°	5.4
J0928−1553	09h28m25s	−15°53′04″	1.2±0.4	···	1.5±0.6	1.1±0.4	HydA	4.6°	7.6
J0928−2652	09h28m29s	−26°52′56″	5.4±1.6	5.7±2.0	6.0±2.1	5.3±1.9	HydA	15.0°	16.2

Continued on Next Page...

Table A.1 – Continued

Name	RA	DEC	$S_{\rm avg}$	$S_{123.52}$	$S_{154.24}$	$S_{184.96}$	Field	$r_{\rm FC}$	SNR
J0928−2931	09h28m53s	−29°31′46″	7.9±2.4	8.7±3.1	7.6±2.7	7.7±2.9	HydA	17.6°	15.7
J0929−2415	09h29m24s	−24°15′56″	1.4±0.5	1.3±0.6	1.6±0.6	1.5±0.6	HydA	12.5°	6.0
J0930−1124	09h30m03s	−11°24′54″	1.3±0.4	0.9±0.5	0.8±0.4	1.2±0.5	HydA	3.0°	6.4
J0930+0614	09h30m23s	+06°14′52″	5.5±1.8	6.3±2.4	6.0±4.0	6.5±5.6	HydA	18.6°	6.9
J0930−1808	09h30m48s	−18°08′07″	2.1±0.7	0.5±0.5	2.0±0.7	1.9±0.7	HydA	6.8°	7.5
J0931−0430	09h31m05s	−04°30′34″	1.4±0.5	1.1±0.6	1.1±0.5	1.3±0.5	HydA	8.2°	5.2
J0931−1829	09h31m22s	−18°29′12″	2.0±0.7	1.2±0.6	2.0±0.7	1.8±0.7	HydA	7.2°	5.9
J0931−1237	09h31m36s	−12°37′11″	1.1±0.4	1.7±0.7	1.1±0.4	0.8±0.3	HydA	3.3°	6.4
J0932−2017	09h32m43s	−20°17′19″	8.7±2.6	9.8±3.4	9.8±3.4	6.6±2.3	HydA	8.9°	31.1
J0932−0643	09h32m58s	−06°43′32″	1.2±0.4	1.4±0.7	1.2±0.5	0.9±0.4	HydA	6.5°	5.3
J0934−0734	09h34m16s	−07°34′58″	1.1±0.4	0.5±0.5	1.0±0.5	1.0±0.4	HydA	6.0°	5.5
J0934−2239	09h34m32s	−22°39′32″	1.0±0.4	1.2±0.5	1.2±0.5	0.6±0.3	HydA	11.3°	5.3
J0935−2823	09h35m10s	−28°23′36″	3.6±1.2	4.0±1.5	3.4±1.3	5.1±1.9	HydA	16.8°	7.5
J0935−1859	09h35m36s	−18°59′24″	1.8±0.6	···	2.2±0.8	1.5±0.6	HydA	8.1°	6.2
J0936+0422	09h36m35s	+04°22′28″	15.0±4.5	16.8±5.9	16.3±5.8	13.4±4.8	HydA	17.1°	27.8
J0937−2243	09h37m16s	−22°43′54″	1.2±0.4	1.6±0.6	1.1±0.5	1.2±0.5	HydA	11.6°	5.4
J0937−0420	09h37m25s	−04°20′59″	5.0±1.5	5.7±2.0	4.3±1.6	4.2±1.5	HydA	9.1°	22.0
J0937−1141	09h37m42s	−11°41′08″	2.1±0.7	1.1±0.6	1.0±0.5	1.8±0.7	HydA	4.8°	9.1
J0937−0350	09h37m53s	−03°50′49″	1.5±0.5	1.4±0.7	1.6±0.7	1.5±0.6	HydA	9.6°	5.4
J0937−2816	09h37m57s	−28°16′16″	4.2±1.3	4.2±1.6	5.1±1.9	5.0±1.9	HydA	16.9°	9.4
J0937−2913	09h37m58s	−29°13′25″	11.6±3.5	12.7±4.5	12.4±4.4	12.7±4.5	HydA	17.8°	28.7
J0938−1155	09h38m41s	−11°55′19″	2.3±0.7	4.8±1.7	2.4±0.9	2.1±0.8	HydA	5.0°	9.9
J0938−0419	09h38m42s	−04°19′25″	1.7±0.6	2.0±0.8	1.6±0.7	1.4±0.6	HydA	9.3°	6.0
J0939−2516	09h39m39s	−25°16′01″	2.8±0.9	2.8±1.1	3.1±1.1	2.7±1.0	HydA	14.2°	10.0
J0940−0618	09h40m10s	−06°18′30″	2.0±0.7	···	···	1.9±0.7	HydA	7.9°	7.7
J0940−2047	09h40m48s	−20°47′17″	2.3±0.7	···	···	2.2±0.8	HydA	10.3°	9.4
J0940−3401	09h40m53s	−34°01′03″	4.9±1.7	5.6±2.2	12.0±7.6	···	HydA	22.6°	5.1
J0941−1626	09h41m08s	−16°26′59″	3.6±1.2	3.7±1.4	3.2±1.2	3.2±1.1	HydA	7.1°	7.8
J0941−1205	09h41m13s	−12°05′06″	2.0±0.7	0.5±0.5	0.9±0.5	2.2±0.8	HydA	5.7°	8.5
J0941−0918	09h41m19s	−09°18′03″	1.2±0.4	0.3±0.4	···	1.0±0.4	HydA	6.3°	5.0
J0941−0138	09h41m30s	−01°38′22″	3.3±1.0	3.2±1.2	3.8±1.4	2.8±1.1	HydA	11.9°	9.5
J0941−1432	09h41m37s	−14°32′18″	1.6±0.5	1.9±0.8	···	1.4±0.5	HydA	6.2°	8.1
J0941−1145	09h41m56s	−11°45′25″	4.9±1.5	4.5±1.7	4.4±1.6	4.1±1.5	HydA	5.8°	18.4
J0942−1057	09h42m12s	−10°57′32″	1.3±0.5	0.6±0.6	···	1.1±0.5	HydA	6.0°	6.0
J0942−2902	09h42m21s	−29°02′43″	1.8±0.6	2.1±0.9	1.5±0.8	1.6±1.1	HydA	17.9°	5.2
J0942−1736	09h42m32s	−17°36′15″	1.6±0.6	4.1±1.6	···	1.4±0.5	HydA	8.1°	5.5
J0942−1403	09h42m52s	−14°03′05″	1.4±0.5	···	···	1.2±0.5	HydA	6.4°	6.8
J0942−0947	09h42m56s	−09°47′02″	1.4±0.5	2.5±1.0	1.1±0.5	1.3±0.5	HydA	6.5°	5.3
J0943−0420	09h43m08s	−04°20′28″	1.9±0.6	1.6±0.7	1.8±0.8	1.9±0.7	HydA	9.9°	7.5
J0943+0243	09h43m13s	+02°43′43″	3.2±1.1	3.2±1.3	···	···	EOR2	15.7°	5.8
J0943−0736	09h43m19s	−07°36′49″	5.3±1.6	4.0±1.5	5.6±2.0	4.5±1.6	HydA	7.6°	20.5

Continued on Next Page...

Table A.1 – Continued

Name	RA	DEC	$S_{\rm avg}$	$S_{123.52}$	$S_{154.24}$	$S_{184.96}$	Field	$r_{\rm FC}$	SNR
J0943−0003	09h43m23s	−00°03′43″	3.8±1.2	4.0±1.6	3.7±1.4	3.6±1.3	EOR2	13.5°	10.5
J0943−0919	09h43m28s	−09°19′42″	1.1±0.4	2.6±1.0	1.1±0.5	0.9±0.4	HydA	6.8°	5.4
J0943−0817	09h43m43s	−08°17′04″	1.9±0.6	2.3±0.9	1.3±0.6	1.9±0.7	HydA	7.3°	7.5
J0943−2017	09h43m46s	−20°17′50″	2.0±0.7	3.2±1.2	1.8±0.8	1.6±0.6	HydA	10.3°	6.5
J0944−1326	09h44m16s	−13°26′33″	2.1±0.7	···	···	1.8±0.7	HydA	6.5°	7.9
J0944+0945	09h44m25s	+09°45′17″	24.7±7.5	29.7±10.5	17.6±10.7	17.8±14.6	EOR2	21.6°	24.0
J0945−1808	09h45m10s	−18°08′58″	1.7±0.6	···	···	1.3±0.5	HydA	8.9°	6.4
J0945−1952	09h45m16s	−19°52′41″	6.5±2.0	8.3±2.9	6.0±2.1	5.4±1.9	HydA	10.2°	20.2
J0945−2427	09h45m32s	−24°27′51″	1.8±0.6	2.8±1.1	1.1±0.6	2.0±0.8	HydA	14.0°	5.8
J0945−1110	09h45m39s	−11°10′30″	1.7±0.6	···	0.9±0.5	1.8±0.7	HydA	6.8°	7.1
J0945−2117	09h45m45s	−21°17′08″	1.4±0.5	···	···	1.5±0.6	HydA	11.3°	5.9
J0946−2746	09h46m23s	−27°46′21″	3.3±1.0	3.6±1.3	3.8±1.4	4.1±1.6	HydA	17.0°	9.0
J0946−1327	09h46m42s	−13°27′29″	1.8±0.6	1.4±0.6	1.5±0.6	1.7±0.6	HydA	7.1°	7.6
J0947−0946	09h47m11s	−09°46′09″	1.4±0.5	2.6±1.0	1.8±0.7	1.0±0.4	HydA	7.5°	5.8
J0947−1929	09h47m12s	−19°29′54″	2.5±0.8	···	···	2.0±0.7	HydA	10.2°	7.5
J0947+0543	09h47m14s	+05°43′50″	5.0±1.6	5.8±2.1	5.1±1.9	6.7±2.5	EOR2	17.7°	10.1
J0947−1346	09h47m24s	−13°46′07″	2.9±0.9	2.7±1.0	3.2±1.2	2.5±0.9	HydA	7.3°	13.8
J0947−0538	09h47m30s	−05°38′47″	1.6±0.5	1.7±0.7	1.8±0.7	1.2±0.5	EOR2	9.2°	8.1
J0947+0005	09h47m49s	+00°05′30″	6.9±2.1	8.4±3.0	6.9±2.5	6.2±2.2	EOR2	12.9°	20.4
J0947+0725	09h47m56s	+07°25′19″	67.8±20.4	83.9±29.4	51.2±30.8	40.5±32.5	EOR2	19.2°	92.4
J0948−1119	09h48m05s	−11°19′42″	1.7±0.6	1.5±0.7	···	1.5±0.6	HydA	7.4°	6.2
J0948−1043	09h48m34s	−10°43′08″	2.2±0.7	···	2.5±0.9	1.6±0.6	HydA	7.6°	7.4
J0948−1827	09h48m45s	−18°27′27″	6.5±2.0	8.1±2.9	6.3±2.2	5.2±1.8	HydA	9.8°	29.4
J0949−2631	09h49m01s	−26°31′44″	3.1±1.0	3.1±1.1	4.0±1.5	3.9±1.4	HydA	16.2°	10.7
J0949−3316	09h49m12s	−33°16′27″	4.1±1.4	4.6±1.8	5.6±3.8	7.9±7.7	HydA	22.4°	5.1
J0949+0725	09h49m31s	+07°25′45″	3.0±1.1	2.9±1.4	6.1±3.8	5.2±4.4	EOR2	19.0°	5.1
J0949−2511	09h49m52s	−25°11′46″	15.6±4.7	18.6±6.5	15.1±5.3	11.9±4.2	HydA	15.1°	49.8
J0949−0517	09h49m55s	−05°17′25″	1.2±0.4	1.8±0.7	1.1±0.4	1.0±0.4	EOR2	8.8°	6.6
J0949−2156	09h49m59s	−21°56′13″	1.8±0.6	2.4±0.9	1.8±0.7	1.2±0.5	HydA	12.5°	6.9
J0950−0812	09h50m47s	−08°12′57″	2.3±0.7	2.5±0.9	2.0±0.7	2.1±0.7	EOR2	7.4°	16.8
J0950−0847	09h50m59s	−08°47′41″	1.0±0.3	1.0±0.4	0.9±0.4	1.1±0.4	EOR2	7.3°	6.7
J0951−2050	09h51m29s	−20°50′54″	3.0±0.9	2.8±1.1	3.3±1.2	2.5±0.9	HydA	11.9°	10.8
J0951+0053	09h51m48s	+00°53′50″	2.4±0.8	2.7±1.2	2.5±1.0	2.6±1.0	EOR2	13.0°	5.7
J0951−0559	09h51m59s	−05°59′45″	1.2±0.4	2.2±0.8	1.2±0.4	0.9±0.3	EOR2	8.0°	9.0
J0952−0000	09h52m10s	−00°00′06″	42.8±12.9	56.2±19.7	39.7±13.9	31.7±11.1	EOR2	12.2°	117.6
J0952−1119	09h52m57s	−11°19′13″	1.2±0.4	1.6±0.6	1.1±0.4	1.0±0.4	EOR2	6.8°	7.9
J0953+0002	09h53m12s	+00°02′44″	1.9±0.7	···	2.9±1.1	2.8±1.0	EOR2	12.0°	6.3
J0953−2410	09h53m22s	−24°10′06″	3.2±1.0	4.5±1.6	3.1±1.2	3.1±1.2	HydA	14.7°	9.8
J0953−0050	09h53m27s	−00°50′22″	2.3±0.7	2.3±0.9	2.3±0.9	2.2±0.8	EOR2	11.3°	7.4
J0953−2135	09h53m40s	−21°35′34″	1.8±0.6	1.5±0.7	1.8±0.7	2.0±0.8	HydA	12.8°	5.5
J0953−1947	09h53m43s	−19°47′33″	3.2±1.0	3.2±1.2	3.7±1.3	2.5±0.9	HydA	11.5°	13.5

Continued on Next Page...

Table A.1 – Continued

Name	RA	DEC	$S_{\rm avg}$	$S_{123.52}$	$S_{154.24}$	$S_{184.96}$	Field	$r_{\rm FC}$	SNR
J0954−1235	09h54m03s	−12°35′39″	0.8±0.3	···	1.0±0.4	0.6±0.2	EOR2	6.9°	6.2
J0954−2240	09h54m34s	−22°40′46″	3.1±1.0	···	2.7±1.0	3.3±1.2	HydA	13.7°	10.6
J0954−1634	09h54m50s	−16°34′44″	2.5±0.8	3.2±1.1	2.5±0.9	2.0±0.7	EOR2	9.0°	21.4
J0956−1622	09h56m43s	−16°22′56″	1.1±0.4	2.0±0.7	1.0±0.4	1.0±0.4	EOR2	8.6°	10.4
J0956−1315	09h56m47s	−13°15′35″	1.0±0.3	1.8±0.7	1.1±0.4	0.7±0.3	EOR2	6.6°	8.6
J0956−1343	09h56m58s	−13°43′46″	5.6±1.7	6.9±2.4	5.1±1.8	4.8±1.7	EOR2	6.8°	49.3
J0958−2904	09h58m04s	−29°04′57″	8.9±2.7	9.9±3.6	10.3±6.2	11.5±9.3	HydA	19.4°	14.4
J0958−2556	09h58m14s	−25°56′05″	2.8±0.9	3.6±1.3	2.3±0.9	3.0±1.1	EOR2	16.8°	11.4
J0958+0326	09h58m22s	+03°26′38″	8.5±2.6	10.6±3.7	7.0±2.5	5.3±1.9	EOR2	14.5°	27.0
J0958−1419	09h58m30s	−14°19′54″	1.5±0.5	1.5±0.6	1.3±0.5	1.2±0.4	EOR2	6.8°	13.2
J0958−0138	09h58m31s	−01°38′46″	2.7±0.8	···	2.0±0.7	2.8±1.0	EOR2	9.9°	13.6
J0959−0519	09h59m06s	−05°19′07″	2.2±0.7	2.9±1.0	2.3±0.8	1.7±0.6	EOR2	7.0°	12.4
J0959−0325	09h59m11s	−03°25′08″	1.7±0.5	2.9±1.1	1.5±0.5	1.3±0.5	EOR2	8.4°	11.9
J0959−0559	09h59m36s	−05°59′55″	4.0±1.2	5.8±2.1	4.1±1.5	2.9±1.0	EOR2	6.4°	21.4
J1000+1400	10h00m16s	+14°00′17″	7.5±2.5	9.1±3.5	4.2±3.8	···	EOR2	24.5°	6.3
J1000+0007	10h00m28s	+00°07′37″	6.2±1.9	9.8±3.4	5.4±1.9	3.6±1.3	EOR2	11.2°	27.3
J1000−0820	10h00m34s	−08°20′16″	1.7±0.5	···	1.7±0.6	1.3±0.5	EOR2	5.1°	12.8
J1000−1701	10h00m40s	−17°01′56″	1.0±0.3	···	1.0±0.4	1.0±0.4	EOR2	8.5°	8.6
J1000−0751	10h00m43s	−07°51′27″	0.9±0.3	···	1.0±0.4	0.7±0.3	EOR2	5.2°	5.5
J1000−1929	10h00m44s	−19°29′46″	0.8±0.3	···	0.9±0.4	1.0±0.4	EOR2	10.6°	6.1
J1000−1145	10h00m52s	−11°45′07″	0.8±0.3	···	0.8±0.3	0.7±0.3	EOR2	5.0°	5.7
J1001−2637	10h01m13s	−26°37′51″	2.8±0.9	3.5±1.3	2.5±0.9	2.1±0.8	EOR2	17.2°	9.5
J1001−0024	10h01m29s	−00°24′44″	11.6±3.5	13.8±4.9	12.6±4.4	8.3±2.9	EOR2	10.6°	53.9
J1002−2355	10h02m00s	−23°55′26″	2.2±0.7	2.7±1.0	2.3±0.8	1.8±0.7	EOR2	14.6°	8.3
J1002−2246	10h02m00s	−22°46′55″	1.6±0.5	···	1.7±0.6	2.1±0.8	EOR2	13.5°	5.7
J1003−0437	10h03m52s	−04°37′51″	1.6±0.5	2.5±0.9	1.4±0.5	1.1±0.4	EOR2	6.7°	9.3
J1004−3218	10h04m17s	−32°18′25″	6.3±2.0	7.4±2.8	6.6±4.1	3.7±5.0	EOR2	22.6°	8.1
J1004−1256	10h04m20s	−12°56′49″	0.8±0.3	···	···	0.8±0.3	EOR2	4.9°	5.3
J1004−0236	10h04m21s	−02°36′60″	1.2±0.4	1.8±0.7	1.3±0.5	0.8±0.3	EOR2	8.3°	6.7
J1004−1453	10h04m48s	−14°53′24″	0.8±0.3	0.8±0.4	0.7±0.3	0.6±0.3	EOR2	6.2°	5.2
J1005−1327	10h05m09s	−13°27′32″	1.2±0.4	4.3±1.7	1.8±0.7	0.7±0.3	EOR2	5.1°	6.9
J1005−2145	10h05m10s	−21°45′12″	31.1±9.3	43.7±15.3	28.2±9.9	22.6±7.9	EOR2	12.3°	122.6
J1005−1356	10h05m32s	−13°56′56″	1.6±0.5	···	2.0±0.7	1.2±0.4	EOR2	5.3°	9.0
J1006−1742	10h06m18s	−17°42′04″	2.4±0.7	3.1±1.1	1.8±0.7	2.5±0.9	EOR2	8.4°	14.4
J1006−1112	10h06m49s	−11°12′22″	1.3±0.4	···	1.8±0.7	0.8±0.3	EOR2	3.5°	6.5
J1007+1246	10h07m28s	+12°46′50″	7.5±2.5	8.9±3.4	7.1±4.8	8.4±12.2	EOR2	23.0°	5.6
J1007−1816	10h07m41s	−18°16′06″	0.9±0.3	1.1±0.5	0.9±0.3	1.0±0.4	EOR2	8.8°	5.4
J1008−0452	10h08m01s	−04°52′28″	1.5±0.5	1.3±0.5	0.9±0.4	1.8±0.6	EOR2	5.9°	7.8
J1008−0957	10h08m07s	−09°57′22″	7.2±2.2	10.1±3.6	7.5±2.6	5.4±1.9	EOR2	2.9°	32.2
J1008+0730	10h08m09s	+07°30′01″	36.7±11.1	45.7±16.3	30.5±10.7	25.7±9.1	EOR2	17.7°	22.1
J1008−2723	10h08m20s	−27°23′18″	2.1±0.8	2.5±1.1	2.1±0.8	1.6±0.7	EOR2	17.6°	5.2

Continued on Next Page...

Table A.1 – Continued

Name	RA	DEC	$S_{\rm avg}$	$S_{123.52}$	$S_{154.24}$	$S_{184.96}$	Field	$r_{\rm FC}$	SNR
J1008−2138	10h08m29s	−21°38′40″	2.3±0.7	2.5±0.9	2.5±0.9	2.0±0.7	EOR2	12.0°	10.7
J1008−1351	10h08m56s	−13°51′11″	1.0±0.4	2.7±1.1	1.0±0.4	0.7±0.3	EOR2	4.7°	5.6
J1009−2856	10h09m04s	−28°56′46″	4.6±1.4	5.4±2.0	4.7±2.9	1.5±1.5	EOR2	19.1°	9.9
J1009−3013	10h09m07s	−30°13′29″	3.7±1.2	4.6±1.7	2.8±1.8	2.4±2.6	EOR2	20.4°	9.1
J1009−1207	10h09m19s	−12°07′46″	10.7±3.2	12.3±4.4	10.1±3.5	8.2±2.9	EOR2	3.4°	52.5
J1009−0324	10h09m23s	−03°24′08″	1.0±0.3	1.8±0.7	1.3±0.5	···	EOR2	7.1°	5.2
J1009−1131	10h09m29s	−11°31′17″	1.8±0.6	3.7±1.4	1.5±0.6	1.2±0.5	EOR2	3.0°	9.8
J1009−0132	10h09m45s	−01°32′26″	1.0±0.4	0.9±0.5	1.0±0.4	1.0±0.4	EOR2	8.8°	5.6
J1010−0728	10h10m12s	−07°28′04″	5.2±1.6	6.0±2.1	5.0±1.8	3.9±1.4	EOR2	3.5°	19.8
J1010−0401	10h10m19s	−04°01′38″	4.1±1.3	3.8±1.3	4.9±1.7	3.2±1.1	EOR2	6.4°	26.3
J1010−2336	10h10m43s	−23°36′46″	1.4±0.5	2.4±0.9	0.8±0.4	1.4±0.5	EOR2	13.8°	5.1
J1011−0200	10h11m02s	−02°00′24″	4.2±1.3	5.5±1.9	4.2±1.5	3.1±1.1	EOR2	8.3°	22.7
J1011+0625	10h11m10s	+06°25′20″	29.0±8.8	35.8±12.8	26.6±9.3	15.8±5.6	EOR2	16.5°	21.8
J1011−2612	10h11m52s	−26°12′51″	2.4±0.8	···	3.5±1.3	2.2±0.8	EOR2	16.4°	6.6
J1012−1826	10h12m18s	−18°26′41″	2.2±0.7	2.3±0.9	2.2±0.8	1.9±0.7	EOR2	8.7°	12.5
J1012−2455	10h12m29s	−24°55′09″	1.3±0.5	1.7±0.7	1.0±0.5	1.2±0.5	EOR2	15.1°	5.6
J1012−1153	10h12m50s	−11°53′32″	2.8±0.9	3.6±1.3	2.9±1.0	2.1±0.7	EOR2	2.6°	16.5
J1013−2832	10h13m22s	−28°32′38″	6.0±1.9	7.4±2.7	5.3±3.2	5.6±4.5	EOR2	18.6°	12.8
J1013−3152	10h13m33s	−31°52′09″	7.2±2.2	8.5±3.1	6.7±4.1	8.5±8.2	EOR2	22.0°	11.3
J1013−1350	10h13m41s	−13°50′00″	2.2±0.7	2.0±0.8	2.1±0.8	1.7±0.6	EOR2	4.2°	15.3
J1014−0146	10h14m49s	−01°46′11″	1.0±0.3	0.6±0.5	1.1±0.4	0.8±0.3	EOR2	8.3°	5.0
J1014−0620	10h14m51s	−06°20′36″	0.9±0.3	1.4±0.6	1.4±0.5	0.6±0.3	EOR2	3.9°	6.2
J1015−2357	10h15m02s	−23°57′24″	3.8±1.2	4.9±1.7	3.1±1.1	2.9±1.1	EOR2	14.0°	16.6
J1015−0905	10h15m05s	−09°05′46″	1.7±0.5	1.9±0.8	1.8±0.7	1.4±0.5	EOR2	1.5°	8.8
J1015+0200	10h15m23s	+02°00′30″	3.0±1.0	2.9±1.2	3.5±1.3	2.6±0.9	EOR2	12.0°	9.0
J1016−3047	10h16m43s	−30°47′20″	3.0±1.0	3.6±1.4	3.1±2.0	···	EOR2	20.8°	5.6
J1016−0932	10h16m46s	−09°32′16″	2.8±0.9	3.5±1.3	2.7±1.0	2.2±0.8	EOR2	0.9°	16.1
J1016−2806	10h16m59s	−28°06′03″	3.3±1.1	4.4±1.7	2.7±1.7	3.3±2.8	EOR2	18.1°	7.1
J1017−2016	10h17m08s	−20°16′54″	1.4±0.5	1.6±0.6	1.7±0.6	1.1±0.4	EOR2	10.3°	7.6
J1017−0431	10h17m19s	−04°31′12″	0.8±0.3	0.9±0.4	0.6±0.3	0.8±0.3	EOR2	5.5°	5.9
J1017−1355	10h17m56s	−13°55′07″	0.8±0.3	1.8±0.7	···	0.5±0.2	EOR2	4.0°	6.6
J1018−3145	10h18m00s	−31°45′52″	12.7±3.9	15.2±5.4	11.4±7.0	6.5±7.2	EOR2	21.8°	19.3
J1018−0457	10h18m05s	−04°57′29″	2.1±0.6	2.6±0.9	2.3±0.8	1.6±0.6	EOR2	5.0°	16.8
J1018−1239	10h18m53s	−12°39′53″	0.9±0.3	···	0.5±0.2	0.8±0.3	EOR2	2.7°	7.3
J1019−0758	10h19m03s	−07°58′36″	1.7±0.5	···	1.9±0.7	1.2±0.4	EOR2	2.0°	11.4
J1019−2504	10h19m57s	−25°04′17″	2.1±0.7	2.7±1.0	1.8±0.7	1.5±0.6	EOR2	15.1°	8.8
J1020−3247	10h20m02s	−32°47′37″	9.9±3.1	11.7±4.2	9.8±6.1	···	EOR2	22.8°	11.9
J1020−0248	10h20m16s	−02°48′60″	0.9±0.3	2.5±0.9	1.1±0.4	0.5±0.2	EOR2	7.2°	6.7
J1020−2010	10h20m19s	−20°10′09″	1.0±0.3	···	···	···	EOR2	10.2°	5.9
J1020−0109	10h20m28s	−01°09′22″	1.0±0.4	2.5±1.0	1.4±0.5	0.9±0.4	EOR2	8.8°	5.2
J1020−3212	10h20m39s	−32°12′35″	5.5±1.8	6.5±2.4	5.9±3.8	···	EOR2	22.2°	6.9

Continued on Next Page...

Table A.1 – Continued

Name	RA	DEC	$S_{\rm avg}$	$S_{123.52}$	$S_{154.24}$	$S_{184.96}$	Field	$r_{\rm FC}$	SNR
J1020−1924	10h20m40s	−19°24′14″	1.9±0.6	2.0±0.8	1.8±0.7	1.9±0.7	EOR2	9.4°	11.2
J1020+0352	10h20m43s	+03°52′41″	2.8±0.9	2.9±1.3	3.0±1.1	2.4±1.0	EOR2	13.8°	7.6
J1021−0853	10h21m22s	−08°53′53″	0.7±0.3	···	···	0.6±0.2	EOR2	1.1°	5.0
J1021−2258	10h21m23s	−22°58′43″	1.4±0.5	1.9±0.7	1.0±0.4	0.9±0.4	EOR2	13.0°	5.7
J1021−0532	10h21m26s	−05°32′40″	1.4±0.5	1.8±0.7	1.4±0.5	1.2±0.4	EOR2	4.4°	9.8
J1021−1523	10h21m30s	−15°23′11″	1.4±0.4	1.5±0.6	1.4±0.5	1.1±0.4	EOR2	5.4°	11.5
J1021+0810	10h21m58s	+08°10′38″	3.4±1.1	4.0±1.5	3.4±2.3	1.7±1.8	EOR2	18.2°	7.2
J1022−0108	10h22m05s	−01°08′20″	1.5±0.5	···	1.7±0.6	0.9±0.4	EOR2	8.8°	7.8
J1022−0341	10h22m15s	−03°41′19″	1.2±0.4	1.5±0.6	1.1±0.4	0.9±0.4	EOR2	6.3°	5.9
J1022−2648	10h22m25s	−26°48′11″	2.1±0.7	2.6±1.0	2.1±0.8	2.1±0.9	EOR2	16.8°	6.0
J1022−1036	10h22m38s	−10°36′44″	1.6±0.5	1.5±0.6	···	1.5±0.5	EOR2	0.9°	9.9
J1023−1934	10h23m18s	−19°34′11″	1.2±0.4	···	1.4±0.5	1.1±0.4	EOR2	9.6°	6.2
J1023−1337	10h23m30s	−13°37′24″	0.9±0.3	···	···	0.8±0.3	EOR2	3.8°	6.8
J1023−1359	10h23m45s	−13°59′47″	0.9±0.3	···	0.9±0.3	0.8±0.3	EOR2	4.1°	7.2
J1023−2158	10h23m52s	−21°58′31″	1.6±0.5	1.8±0.7	1.7±0.6	1.3±0.5	EOR2	12.0°	8.3
J1024−0849	10h24m44s	−08°49′43″	1.6±0.5	2.2±0.9	1.6±0.6	1.2±0.4	EOR2	1.6°	7.8
J1024−2008	10h24m48s	−20°08′34″	1.7±0.5	1.9±0.7	2.0±0.7	1.4±0.5	EOR2	10.2°	9.7
J1024−1839	10h24m60s	−18°39′17″	1.7±0.5	3.1±1.1	1.1±0.4	1.1±0.4	EOR2	8.8°	9.5
J1025−1030	10h25m02s	−10°30′34″	2.3±0.7	3.1±1.1	2.3±0.8	2.0±0.7	EOR2	1.3°	12.1
J1025+0624	10h25m06s	+06°24′53″	2.9±0.9	···	2.6±1.1	4.2±1.6	EOR2	16.4°	6.9
J1025−2516	10h25m17s	−25°16′52″	1.7±0.6	2.3±0.9	1.3±0.5	0.9±0.4	EOR2	15.4°	5.7
J1025−2432	10h25m27s	−24°32′60″	2.0±0.6	2.6±1.0	1.9±0.7	1.0±0.5	EOR2	14.6°	6.6
J1025−0216	10h25m39s	−02°16′54″	6.1±1.8	8.4±3.0	6.1±2.2	4.3±1.5	EOR2	7.8°	26.9
J1025−1126	10h25m41s	−11°26′04″	1.2±0.4	2.9±1.0	1.3±0.5	0.7±0.3	EOR2	2.0°	6.1
J1025−1157	10h25m45s	−11°57′09″	1.0±0.3	···	1.0±0.4	0.8±0.3	EOR2	2.4°	5.7
J1025+0519	10h25m46s	+05°19′01″	2.3±0.8	2.3±0.9	2.8±1.1	1.9±0.9	EOR2	15.3°	7.0
J1025−1435	10h25m49s	−14°35′19″	2.3±0.7	2.8±1.0	2.6±0.9	2.0±0.7	EOR2	4.8°	17.9
J1025−0501	10h25m56s	−05°01′17″	1.7±0.5	···	2.6±0.9	1.0±0.4	EOR2	5.2°	9.1
J1026+0627	10h26m40s	+06°27′35″	8.6±2.6	9.9±3.5	9.1±3.3	8.7±3.1	EOR2	16.5°	24.2
J1026+0104	10h26m49s	+01°04′22″	1.4±0.5	1.7±0.8	1.4±0.6	1.0±0.4	EOR2	11.2°	5.1
J1027−0647	10h27m29s	−06°47′52″	1.1±0.4	0.6±0.4	1.2±0.5	1.0±0.4	EOR2	3.7°	5.3
J1027−0717	10h27m38s	−07°17′11″	2.4±0.7	2.1±0.8	2.2±0.8	2.0±0.7	EOR2	3.3°	12.6
J1027−0825	10h27m48s	−08°25′59″	2.0±0.6	2.5±0.9	2.3±0.8	1.4±0.5	EOR2	2.4°	10.3
J1027−2311	10h27m50s	−23°11′17″	2.3±0.7	2.6±1.0	2.7±1.0	1.6±0.6	EOR2	13.4°	9.0
J1027−2940	10h27m55s	−29°40′12″	2.8±0.9	3.4±1.3	2.3±1.5	1.7±2.0	EOR2	19.8°	6.6
J1027−2717	10h27m55s	−27°17′47″	2.2±0.7	2.8±1.0	2.1±0.8	1.3±0.7	EOR2	17.4°	7.9
J1028−3149	10h28m11s	−31°49′34″	3.8±1.3	4.5±1.7	2.7±1.9	···	EOR2	21.9°	5.7
J1028−1659	10h28m11s	−16°59′55″	2.1±0.7	2.5±0.9	2.4±0.9	1.5±0.6	EOR2	7.3°	9.2
J1028−2646	10h28m14s	−26°46′07″	1.6±0.5	2.0±0.8	1.3±0.5	1.9±0.8	EOR2	16.9°	5.5
J1029−2026	10h29m00s	−20°26′50″	3.4±1.0	4.1±1.5	3.6±1.3	2.4±0.9	EOR2	10.7°	17.9
J1029−1244	10h29m33s	−12°44′09″	1.7±0.5	2.0±0.8	1.6±0.6	1.4±0.5	EOR2	3.6°	11.4

Continued on Next Page...

Table A.1 – Continued

Name	RA	DEC	$S_{\rm avg}$	$S_{123.52}$	$S_{154.24}$	$S_{184.96}$	Field	$r_{\rm FC}$	SNR
J1029−0554	10h29m35s	−05°54′29″	2.0±0.6	3.5±1.3	2.3±0.8	1.4±0.5	EOR2	4.7°	9.6
J1029−2246	10h29m35s	−22°46′03″	1.1±0.4	1.8±0.8	1.0±0.4	0.6±0.3	EOR2	13.0°	5.1
J1029−1508	10h29m37s	−15°08′22″	2.1±0.7	2.2±0.9	2.0±0.8	1.8±0.6	EOR2	5.7°	10.7
J1030−0714	10h30m07s	−07°14′43″	0.9±0.4	1.8±0.7	0.9±0.4	0.5±0.3	EOR2	3.7°	5.1
J1030−0309	10h30m17s	−03°09′60″	1.5±0.5	2.5±0.9	1.5±0.6	0.7±0.3	EOR2	7.3°	6.1
J1030+0038	10h30m18s	+00°38′23″	3.3±1.0	3.0±1.2	3.5±1.2	2.5±0.9	EOR2	10.9°	12.4
J1030−1124	10h30m38s	−11°24′14″	2.0±0.7	···	1.6±0.6	1.8±0.6	EOR2	3.0°	8.3
J1030−1324	10h30m42s	−13°24′07″	1.2±0.4	1.5±0.6	1.1±0.4	0.9±0.4	EOR2	4.3°	8.5
J1030−0924	10h30m57s	−09°24′12″	8.6±2.6	9.6±3.4	7.8±2.7	7.2±2.5	EOR2	2.7°	39.5
J1031+0444	10h31m31s	+04°44′39″	5.1±1.6	6.3±2.3	5.0±1.8	3.6±1.3	EOR2	15.0°	16.1
J1031−2338	10h31m31s	−23°38′21″	2.1±0.7	···	2.4±0.9	2.0±0.7	EOR2	13.9°	7.4
J1031−1634	10h31m36s	−16°34′33″	1.2±0.4	···	0.8±0.4	0.8±0.3	EOR2	7.2°	5.1
J1031−1520	10h31m41s	−15°20′24″	3.5±1.1	4.2±1.5	3.8±1.4	2.6±0.9	EOR2	6.1°	15.8
J1032−3421	10h32m60s	−34°21′19″	17.4±5.3	20.7±7.3	14.4±9.4	12.0±9.9	EOR2	24.6°	15.5
J1033−1338	10h33m22s	−13°38′28″	1.2±0.4	0.5±0.4	2.1±0.8	0.9±0.3	EOR2	4.9°	7.5
J1033−1933	10h33m40s	−19°33′16″	4.7±1.4	5.4±2.0	4.4±1.6	3.9±1.4	EOR2	10.1°	17.9
J1033−1209	10h33m42s	−12°09′07″	8.1±2.4	7.1±2.5	7.2±2.5	7.0±2.5	EOR2	4.0°	44.4
J1034−1713	10h34m07s	−17°13′02″	1.9±0.6	2.6±1.0	1.4±0.6	1.5±0.6	EOR2	8.0°	8.6
J1034+1111	10h34m13s	+11°11′23″	5.9±1.9	5.3±2.1	9.6±5.8	···	EOR2	21.4°	8.3
J1034+0006	10h34m27s	+00°06′58″	3.1±1.0	3.5±1.3	2.9±1.1	2.7±1.0	EOR2	10.7°	14.0
J1035−2012	10h35m06s	−20°12′41″	2.0±0.7	1.5±0.8	···	2.0±0.7	EOR2	10.9°	6.6
J1035−2207	10h35m23s	−22°07′52″	1.4±0.5	2.0±0.9	1.5±0.6	1.0±0.4	EOR2	12.7°	5.3
J1035−0224	10h35m48s	−02°24′51″	1.7±0.6	2.2±0.9	2.0±0.8	1.2±0.5	EOR2	8.5°	7.8
J1035−1111	10h35m58s	−11°11′51″	4.8±1.5	5.4±1.9	5.5±1.9	3.5±1.2	EOR2	4.1°	15.5
J1036−1016	10h36m10s	−10°16′55″	2.5±0.8	3.0±1.1	2.6±1.0	1.8±0.7	EOR2	4.0°	6.8
J1036−2524	10h36m17s	−25°24′52″	3.3±1.1	4.2±1.5	2.7±1.0	2.6±1.0	EOR2	15.9°	8.0
J1036+0008	10h36m20s	+00°08′16″	1.7±0.6	2.1±0.8	1.7±0.7	1.3±0.5	EOR2	10.9°	8.3
J1036−1223	10h36m40s	−12°23′56″	1.0±0.4	0.5±0.4	···	1.0±0.4	EOR2	4.7°	5.7
J1036−2731	10h36m43s	−27°31′16″	2.0±0.7	2.6±1.0	1.2±0.6	0.8±0.7	EOR2	18.0°	5.5
J1036−1954	10h36m56s	−19°54′41″	3.4±1.1	3.9±1.5	4.0±1.4	2.4±0.9	EOR2	10.7°	11.5
J1037−2906	10h37m19s	−29°06′52″	3.5±1.2	4.1±1.6	4.0±2.5	···	EOR2	19.6°	6.5
J1037+0226	10h37m24s	+02°26′36″	2.8±0.9	···	2.3±0.9	1.8±0.7	EOR2	13.1°	8.9
J1038−1322	10h38m13s	−13°22′56″	1.0±0.3	2.0±0.8	0.8±0.4	0.7±0.3	EOR2	5.6°	6.0
J1038−0602	10h38m15s	−06°02′53″	2.4±0.8	4.6±1.7	2.5±0.9	1.5±0.6	EOR2	6.0°	9.4
J1038−0429	10h38m55s	−04°29′44″	5.0±1.5	4.7±1.7	5.8±2.0	4.0±1.4	EOR2	7.2°	21.8
J1038+0120	10h38m55s	+01°20′52″	2.1±0.7	2.7±1.1	1.3±0.6	1.7±0.6	EOR2	12.2°	7.8
J1039+0537	10h39m39s	+05°37′17″	3.2±1.1	3.5±1.4	3.9±1.5	3.6±1.4	EOR2	16.3°	6.1
J1039−1145	10h39m45s	−11°45′27″	2.4±0.8	2.4±0.9	2.1±0.8	2.1±0.7	EOR2	5.2°	13.5
J1039−1217	10h39m51s	−12°17′54″	1.1±0.4	2.3±0.9	0.8±0.4	1.0±0.4	EOR2	5.4°	6.7
J1039−0329	10h39m60s	−03°29′16″	1.2±0.5	0.5±0.6	1.0±0.5	1.5±0.6	EOR2	8.1°	5.2
J1040−1923	10h40m55s	−19°23′08″	2.0±0.6	···	2.2±0.8	1.6±0.6	EOR2	10.7°	7.1

Continued on Next Page...

Table A.1 – Continued

Name	RA	DEC	$S_{\rm avg}$	$S_{123.52}$	$S_{154.24}$	$S_{184.96}$	Field	$r_{\rm FC}$	SNR
J1041−1535	10h41m12s	−15°35′46″	1.3±0.4	2.0±0.8	···	1.0±0.4	EOR2	7.6°	7.7
J1041−1457	10h41m21s	−14°57′10″	1.7±0.5	···	1.5±0.6	1.4±0.5	EOR2	7.2°	11.0
J1041−1724	10h41m23s	−17°24′37″	1.8±0.6	1.5±0.6	2.1±0.8	1.9±0.7	EOR2	9.1°	6.8
J1041+0049	10h41m23s	+00°49′16″	1.6±0.5	1.9±0.8	2.0±0.8	0.9±0.4	EOR2	12.0°	6.7
J1041+0208	10h41m25s	+02°08′20″	2.0±0.7	···	3.2±1.2	···	EOR2	13.2°	6.4
J1041+0242	10h41m45s	+02°42′31″	12.6±3.8	14.1±5.0	14.1±4.9	9.2±3.2	EOR2	13.8°	40.6
J1041−1611	10h41m59s	−16°11′51″	1.0±0.4	2.2±0.9	0.6±0.3	1.0±0.4	EOR2	8.2°	5.9
J1042+0317	10h42m05s	+03°17′39″	2.5±0.8	3.1±1.2	2.8±1.1	1.0±0.6	EOR2	14.3°	8.0
J1042−1159	10h42m12s	−11°59′15″	1.9±0.6	2.6±1.0	1.9±0.7	1.8±0.6	EOR2	5.8°	10.9
J1042−2850	10h42m34s	−28°50′15″	3.9±1.3	4.9±1.8	3.6±2.2	2.1±2.0	EOR2	19.6°	8.6
J1042−2013	10h42m39s	−20°13′02″	1.7±0.5	1.7±0.7	2.0±0.8	1.4±0.5	EOR2	11.6°	6.5
J1042+1201	10h42m56s	+12°01′30″	15.5±4.8	18.0±6.4	18.4±11.2	21.7±18.0	EOR2	22.7°	15.1
J1043−2323	10h43m00s	−23°23′35″	1.9±0.6	···	2.3±0.9	1.8±0.7	EOR2	14.5°	7.7
J1043−1352	10h43m08s	−13°52′43″	0.9±0.3	1.4±0.6	1.1±0.5	0.7±0.3	EOR2	6.9°	5.9
J1043−0552	10h43m59s	−05°52′49″	1.1±0.4	1.3±0.6	1.0±0.4	0.7±0.3	EOR2	7.2°	5.2
J1043+0537	10h43m59s	+05°37′43″	3.9±1.3	4.5±1.7	4.6±1.7	3.3±1.3	EOR2	16.7°	7.8
J1044−0854	10h44m10s	−08°54′04″	0.9±0.4	0.8±0.5	0.7±0.3	0.8±0.3	EOR2	6.0°	5.4
J1044−2339	10h44m29s	−23°39′29″	2.0±0.7	1.7±0.7	2.4±0.9	1.5±0.6	EOR2	14.9°	5.6
J1045−2843	10h45m06s	−28°43′16″	3.0±1.0	···	2.7±1.7	···	EOR2	19.7°	6.3
J1045−2153	10h45m28s	−21°53′50″	3.2±1.0	4.1±1.5	3.1±1.1	2.5±0.9	EOR2	13.4°	14.1
J1045−2923	10h45m52s	−29°23′16″	3.5±1.1	4.4±1.7	2.4±1.6	1.3±1.7	EOR2	20.3°	7.1
J1046−2234	10h46m16s	−22°34′57″	2.1±0.7	···	2.4±0.9	1.4±0.6	EOR2	14.1°	7.7
J1046−1717	10h46m51s	−17°17′15″	1.6±0.5	···	1.2±0.5	1.2±0.5	EOR2	9.8°	7.7
J1047−1512	10h47m08s	−15°12′58″	2.2±0.7	3.0±1.1	2.2±0.8	1.8±0.7	EOR2	8.4°	14.0
J1047−0104	10h47m29s	−01°04′53″	4.7±1.4	6.5±2.3	4.3±1.5	2.8±1.0	EOR2	11.2°	19.1
J1048−1932	10h48m04s	−19°32′19″	2.3±0.7	2.5±1.0	2.8±1.0	2.2±0.8	EOR2	11.7°	8.8
J1048−1907	10h48m10s	−19°07′46″	4.3±1.3	5.0±1.8	4.8±1.7	3.2±1.1	EOR2	11.4°	17.6
J1048−1835	10h48m32s	−18°35′55″	2.8±0.9	3.2±1.2	2.9±1.1	2.1±0.7	EOR2	11.0°	11.3
J1048−1734	10h48m39s	−17°34′37″	1.4±0.5	···	2.1±0.8	1.1±0.4	EOR2	10.3°	7.0
J1048−0738	10h48m47s	−07°38′29″	1.2±0.4	2.3±0.9	1.6±0.6	0.6±0.3	EOR2	7.5°	5.9
J1048−1622	10h48m48s	−16°22′15″	1.1±0.4	1.5±0.6	1.3±0.5	0.6±0.3	EOR2	9.5°	5.2
J1049+0100	10h49m12s	+01°00′26″	2.0±0.7	2.6±1.1	1.7±0.7	1.5±0.6	EOR2	13.1°	5.6
J1049−1300	10h49m25s	−13°00′55″	1.3±0.4	2.4±0.9	1.5±0.6	0.8±0.3	EOR2	7.8°	6.6
J1049−0253	10h49m37s	−02°53′06″	4.2±1.3	4.6±1.7	5.7±2.0	3.6±1.3	EOR2	10.2°	20.4
J1050+0809	10h50m13s	+08°09′35″	4.6±1.5	5.3±2.0	5.0±3.1	1.2±1.5	EOR2	19.6°	5.6
J1050−1926	10h50m31s	−19°26′27″	1.8±0.6	1.4±0.7	2.8±1.0	1.1±0.5	EOR2	12.0°	6.1
J1050−1047	10h50m32s	−10°47′50″	1.3±0.5	0.7±0.6	0.8±0.4	1.5±0.6	EOR2	7.5°	6.6
J1050−2731	10h50m35s	−27°31′11″	2.4±0.8	3.1±1.2	1.6±1.0	2.0±1.7	EOR2	19.0°	6.1
J1050−2407	10h50m37s	−24°07′56″	3.6±1.1	4.7±1.7	3.7±1.3	2.4±0.9	EOR2	15.9°	11.4
J1050−1349	10h50m42s	−13°49′06″	1.9±0.6	2.6±1.0	1.6±0.6	1.6±0.6	EOR2	8.4°	10.3
J1050−0002	10h50m48s	−00°02′34″	8.5±2.6	11.0±3.9	9.2±3.2	6.1±2.1	EOR2	12.5°	27.4

Continued on Next Page...

Table A.1 – Continued

Name	RA	DEC	$S_{\rm avg}$	$S_{123.52}$	$S_{154.24}$	$S_{184.96}$	Field	$r_{\rm FC}$	SNR
J1051−2123	10h51m01s	−21°23′05″	2.2±0.7	2.8±1.0	1.9±0.7	1.8±0.7	EOR2	13.6°	10.9
J1051−1520	10h51m04s	−15°20′05″	1.3±0.4	1.7±0.7	1.2±0.5	1.1±0.4	EOR2	9.3°	6.8
J1051−2023	10h51m33s	−20°23′30″	8.3±2.5	9.7±3.4	9.0±3.2	6.6±2.3	EOR2	12.9°	38.7
J1051−0917	10h51m34s	−09°17′23″	19.5±5.9	24.3±8.5	19.3±6.8	15.1±5.3	EOR2	7.8°	84.3
J1052−0025	10h52m02s	−00°25′38″	1.4±0.5	1.2±0.6	1.9±0.8	2.4±0.9	EOR2	12.4°	5.0
J1052−1301	10h52m18s	−13°01′57″	1.6±0.5	2.4±0.9	···	1.5±0.6	EOR2	8.5°	7.9
J1052−1849	10h52m24s	−18°49′16″	3.2±1.0	5.2±1.9	3.4±1.2	2.0±0.7	EOR2	11.8°	13.5
J1053−1342	10h53m19s	−13°42′54″	2.1±0.7	3.7±1.4	1.9±0.7	1.6±0.6	EOR2	9.0°	11.2
J1053−1030	10h53m19s	−10°30′10″	1.1±0.4	···	1.5±0.6	0.8±0.3	EOR2	8.2°	5.0
J1053+0033	10h53m27s	+00°33′13″	2.6±0.8	2.8±1.1	3.4±1.2	2.0±0.8	EOR2	13.4°	7.8
J1054+0314	10h54m32s	+03°14′09″	3.2±1.0	···	2.1±0.8	3.6±1.3	EOR2	15.7°	7.7
J1054−0105	10h54m49s	−01°05′38″	1.4±0.5	2.1±0.8	1.1±0.6	1.2±0.5	EOR2	12.4°	5.4
J1054−0043	10h54m55s	−00°43′18″	1.9±0.6	2.2±0.9	1.9±0.8	2.0±0.8	EOR2	12.7°	6.1
J1055−2413	10h55m10s	−24°13′40″	1.7±0.6	2.0±0.8	2.1±0.8	1.0±0.5	EOR2	16.5°	5.0
J1055−2732	10h55m16s	−27°32′19″	5.6±1.7	7.0±2.5	4.5±2.7	2.8±2.4	EOR2	19.4°	11.4
J1055−2832	10h55m26s	−28°32′34″	5.8±1.8	7.2±2.6	4.8±2.9	2.9±2.5	EOR2	20.4°	10.5
J1055+0205	10h55m31s	+02°05′27″	4.8±1.5	6.4±2.3	4.1±1.5	3.4±1.3	EOR2	14.9°	14.3
J1055+0123	10h55m35s	+01°23′47″	2.8±0.9	3.5±1.4	2.5±0.9	2.4±0.9	EOR2	14.4°	7.8
J1055−1634	10h55m37s	−16°34′50″	2.0±0.6	2.5±1.0	2.2±0.8	1.3±0.5	EOR2	10.9°	8.8
J1055−1557	10h55m52s	−15°57′00″	1.2±0.4	2.1±0.9	1.3±0.5	0.7±0.3	EOR2	10.6°	5.1
J1055−0706	10h55m57s	−07°06′32″	3.2±1.0	3.4±1.3	2.9±1.0	2.7±1.0	EOR2	9.3°	18.9
J1057−1505	10h57m18s	−15°05′04″	1.6±0.5	1.9±0.8	1.5±0.6	1.3±0.5	EOR2	10.4°	6.1
J1057−0806	10h57m20s	−08°06′18″	1.4±0.5	1.8±0.8	1.5±0.6	1.1±0.4	EOR2	9.4°	6.6
J1057−1330	10h57m40s	−13°30′32″	1.3±0.4	2.0±0.8	1.2±0.5	0.9±0.4	EOR2	9.9°	6.4
J1057−2434	10h57m56s	−24°34′07″	2.3±0.7	2.5±1.0	2.7±1.0	2.2±0.9	EOR2	17.2°	6.5
J1058+0134	10h58m33s	+01°34′27″	7.2±2.2	8.3±3.0	7.2±2.6	6.1±2.2	EOR2	15.0°	22.5
J1058−1849	10h58m56s	−18°49′24″	2.8±0.9	3.9±1.4	2.5±0.9	2.1±0.8	EOR2	12.9°	10.2
J1059−1117	10h59m58s	−11°17′14″	1.8±0.6	2.4±0.9	1.9±0.7	1.5±0.6	EOR2	9.9°	9.6
J1101−3143	11h01m19s	−31°43′14″	4.8±1.7	5.6±2.3	4.5±3.4	···	EOR2	23.8°	5.1
J1102−1658	11h02m06s	−16°58′04″	1.3±0.5	1.7±0.7	1.0±0.5	1.1±0.4	EOR2	12.4°	5.1
J1102−0115	11h02m10s	−01°15′39″	32.6±9.8	39.3±13.8	34.4±12.1	23.7±8.3	EOR2	13.6°	98.0
J1102+0251	11h02m14s	+02°51′09″	3.4±1.1	4.3±1.6	2.9±1.1	3.9±1.4	EOR2	16.6°	8.3
J1102−1129	11h02m14s	−11°29′20″	1.2±0.4	1.3±0.6	1.3±0.5	1.0±0.4	EOR2	10.5°	5.3
J1102−1333	11h02m22s	−13°33′15″	1.3±0.5	2.0±0.8	1.4±0.6	0.8±0.3	EOR2	11.0°	5.4
J1102+1027	11h02m23s	+10°27′54″	8.9±3.0	10.4±3.9	9.9±6.2	8.4±7.1	EOR2	23.0°	6.1
J1102−1422	11h02m25s	−14°22′27″	1.8±0.6	2.2±0.9	2.2±0.8	1.3±0.5	EOR2	11.2°	6.2
J1102−0941	11h02m38s	−09°41′08″	6.4±2.0	7.7±2.7	6.5±2.3	5.2±1.8	EOR2	10.5°	25.5
J1102−0237	11h02m42s	−02°37′07″	3.7±1.1	···	3.7±1.3	···	EOR2	12.9°	12.0
J1102−0648	11h02m49s	−06°48′20″	2.4±0.8	2.7±1.0	3.0±1.1	1.6±0.6	EOR2	11.0°	10.7
J1103−3252	11h03m07s	−32°52′29″	5.7±2.0	6.8±2.6	···	9.3±7.8	EOR2	25.0°	5.1
J1103−1514	11h03m29s	−15°14′49″	1.8±0.6	3.5±1.3	1.7±0.7	1.6±0.6	EOR2	11.8°	6.2

Continued on Next Page...

Table A.1 – Continued

Name	RA	DEC	$S_{\rm avg}$	$S_{123.52}$	$S_{154.24}$	$S_{184.96}$	Field	$r_{\rm FC}$	SNR
J1103−1024	11h03m35s	−10°24′52″	1.9±0.6	3.7±1.4	1.7±0.7	0.9±0.4	EOR2	10.7°	6.0
J1103−0510	11h03m38s	−05°10′60″	3.0±0.9	3.6±1.3	3.1±1.2	2.4±0.9	EOR2	11.8°	11.6
J1104−0832	11h04m13s	−08°32′36″	1.9±0.6	2.6±1.0	1.4±0.6	1.5±0.6	EOR2	11.0°	6.6
J1104−1146	11h04m25s	−11°46′46″	2.8±0.9	···	2.9±1.1	2.2±0.8	EOR2	11.0°	12.7
J1105−1853	11h05m25s	−18°53′59″	2.2±0.7	···	2.2±0.8	2.0±0.8	EOR2	14.2°	7.8
J1106−0157	11h06m01s	−01°57′00″	2.9±0.9	2.8±1.1	4.5±1.6	2.0±0.8	EOR2	13.9°	8.8
J1106−0003	11h06m07s	−00°03′30″	3.6±1.2	5.0±1.9	3.4±1.3	2.2±0.9	EOR2	15.1°	8.5
J1106−2445	11h06m11s	−24°45′40″	12.5±3.8	16.2±5.7	9.3±5.6	6.5±5.3	EOR2	18.4°	28.7
J1106−2109	11h06m22s	−21°09′12″	20.7±6.2	26.7±9.4	19.6±6.9	12.7±4.5	EOR2	15.8°	58.8
J1106−0813	11h06m30s	−08°13′08″	1.6±0.5	1.9±0.8	2.2±0.8	1.4±0.6	EOR2	11.6°	6.9
J1106−0051	11h06m38s	−00°51′24″	5.0±1.6	7.9±2.9	4.9±1.8	2.4±0.9	EOR2	14.7°	12.0
J1107+0534	11h07m20s	+05°34′52″	4.8±1.5	5.7±2.2	4.9±3.0	5.0±4.1	EOR2	19.5°	8.2
J1107−0524	11h07m21s	−05°24′55″	3.2±1.0	···	4.5±1.6	1.9±0.7	EOR2	12.6°	10.1
J1107−0308	11h07m49s	−03°08′28″	3.0±0.9	2.7±1.1	4.1±1.5	2.7±1.0	EOR2	13.7°	9.4
J1108+0201	11h08m56s	+02°01′39″	2.9±1.0	3.4±1.3	2.8±1.1	2.2±0.9	EOR2	17.1°	6.3
J1109−0039	11h09m12s	−00°39′05″	2.5±0.9	2.6±1.2	3.1±1.2	2.5±0.9	EOR2	15.3°	5.2
J1109−1921	11h09m21s	−19°21′01″	2.8±0.9	3.7±1.4	2.8±1.1	2.0±0.8	EOR2	15.2°	9.1
J1109−2303	11h09m41s	−23°03′14″	12.5±3.8	16.3±5.7	10.7±3.8	5.8±2.1	EOR2	17.7°	30.1
J1109−1012	11h09m58s	−10°12′08″	4.0±1.2	5.2±1.9	4.1±1.5	2.6±0.9	EOR2	12.3°	12.1
J1110+0416	11h10m25s	+04°16′55″	5.5±1.7	6.4±2.4	5.8±3.6	5.3±4.3	EOR2	19.0°	8.2
J1111+0311	11h11m16s	+03°11′30″	7.1±2.2	8.9±3.2	6.4±3.9	4.9±4.0	EOR2	18.3°	14.4
J1111−1324	11h11m51s	−13°24′26″	1.5±0.5	1.9±0.8	1.4±0.6	1.3±0.5	EOR2	13.1°	5.7
J1112−0232	11h12m04s	−02°32′18″	2.0±0.7	2.2±1.0	2.4±1.0	2.0±0.8	EOR2	14.9°	5.7
J1112−1948	11h12m05s	−19°48′54″	2.3±0.8	2.7±1.1	2.7±1.0	2.1±0.8	EOR2	16.0°	7.8
J1112−2158	11h12m31s	−21°58′41″	3.1±1.0	3.4±1.4	3.9±1.5	2.8±1.1	EOR2	17.4°	6.1
J1112−1219	11h12m59s	−12°19′11″	1.5±0.5	1.8±0.8	1.4±0.6	1.3±0.5	EOR2	13.2°	5.3
J1113−0702	11h13m35s	−07°02′53″	1.9±0.6	2.4±1.0	1.7±0.7	1.5±0.6	EOR2	13.5°	5.5
J1113−0212	11h13m41s	−02°12′33″	10.6±3.2	13.5±4.8	10.0±3.6	7.1±2.5	EOR2	15.4°	28.5
J1114−1934	11h14m18s	−19°34′12″	2.6±0.8	···	2.5±0.9	2.8±1.0	EOR2	16.2°	8.5
J1114−2412	11h14m35s	−24°12′31″	4.3±1.4	5.4±1.9	3.6±2.3	2.3±2.0	EOR2	19.3°	10.7
J1114−0401	11h14m45s	−04°01′33″	2.7±0.9	3.5±1.3	2.4±0.9	2.1±0.8	EOR2	14.8°	8.5
J1115−1026	11h15m12s	−10°26′10″	4.9±1.5	6.2±2.2	4.7±1.7	3.8±1.3	EOR2	13.6°	16.7
J1115−1648	11h15m12s	−16°48′36″	5.4±1.6	7.0±2.5	4.9±1.8	4.1±1.5	EOR2	15.0°	20.1
J1116−1805	11h16m14s	−18°05′33″	2.4±0.8	···	2.1±0.8	1.7±0.7	EOR2	15.9°	7.1
J1117−2211	11h17m06s	−22°11′37″	2.7±0.9	3.1±1.2	3.6±2.3	2.7±2.3	EOR2	18.3°	5.0
J1117−1123	11h17m31s	−11°23′23″	2.1±0.7	2.4±1.0	2.1±0.8	1.6±0.6	EOR2	14.2°	6.4
J1117−0235	11h17m45s	−02°35′44″	4.9±1.5	6.0±2.2	4.7±1.7	3.7±1.4	EOR2	16.1°	12.9
J1118−0741	11h18m00s	−07°41′04″	2.6±0.8	3.3±1.2	2.5±0.9	1.7±0.7	EOR2	14.5°	8.1
J1118−0922	11h18m44s	−09°22′46″	3.2±1.0	3.6±1.4	3.3±1.2	2.6±1.0	EOR2	14.5°	10.2
J1119−0526	11h19m27s	−05°26′54″	5.3±1.6	5.5±2.0	4.6±1.7	4.4±1.6	EOR2	15.4°	15.5
J1119−0303	11h19m28s	−03°03′01″	19.2±5.8	22.4±7.9	19.5±6.8	15.1±5.3	EOR2	16.3°	53.0

Continued on Next Page...

Table A.1 – Continued

Name	RA	DEC	$S_{\rm avg}$	$S_{123.52}$	$S_{154.24}$	$S_{184.96}$	Field	$r_{\rm FC}$	SNR
J1119−1929	11h19m60s	−19°29′59″	2.8±0.9	2.9±1.2	2.7±1.0	3.1±1.2	EOR2	17.3°	8.2
J1121−1530	11h21m02s	−15°30′35″	1.9±0.7	2.7±1.1	1.7±0.7	0.9±0.5	EOR2	15.9°	5.1
J1121−0012	11h21m11s	−00°12′04″	2.2±0.8	2.6±1.0	2.8±1.8	1.3±1.2	EOR2	18.0°	6.0
J1122−1247	11h22m03s	−12°47′45″	2.2±0.7	···	2.9±1.1	2.6±1.0	EOR2	15.4°	5.3
J1123−1832	11h23m09s	−18°32′53″	1.9±0.7	2.1±0.9	2.5±1.0	1.5±0.7	EOR2	17.5°	5.4
J1123+0528	11h23m13s	+05°28′10″	12.2±3.7	14.6±5.2	12.3±7.5	7.8±6.4	EOR2	22.0°	16.2
J1123−2405	11h23m53s	−24°05′53″	3.9±1.2	4.6±1.7	4.4±2.8	2.9±2.5	EOR2	20.8°	8.1
J1123−1217	11h23m54s	−12°17′25″	3.4±1.1	4.1±1.5	3.5±1.3	2.2±0.9	EOR2	15.8°	7.5
J1124+0453	11h24m38s	+04°53′30″	7.9±2.5	9.4±3.4	8.0±5.0	5.4±4.5	EOR2	21.9°	11.6
J1124−0404	11h24m48s	−04°04′09″	2.8±0.9	3.2±1.2	3.2±1.2	2.3±0.9	EOR2	17.1°	7.3
J1124−1705	11h24m50s	−17°05′23″	2.2±0.7	2.4±1.0	3.0±1.2	2.0±0.8	EOR2	17.3°	5.1
J1125−0440	11h25m38s	−04°40′29″	2.6±0.8	3.2±1.2	2.4±1.0	2.6±1.0	EOR2	17.1°	6.8
J1125−2215	11h25m43s	−22°15′22″	2.7±0.9	3.3±1.3	2.8±1.8	1.6±1.5	EOR2	20.0°	5.2
J1126−1913	11h26m09s	−19°13′12″	4.5±1.4	5.6±2.0	4.3±2.6	2.9±2.4	EOR2	18.5°	10.1
J1126−1837	11h26m27s	−18°37′24″	3.3±1.1	4.2±1.6	2.6±1.7	2.6±2.1	EOR2	18.3°	7.4
J1126−0634	11h26m29s	−06°34′24″	3.2±1.1	3.9±1.5	2.8±1.1	3.1±1.2	EOR2	16.8°	6.7
J1129−0704	11h29m17s	−07°04′11″	3.7±1.2	4.6±1.7	3.5±1.4	2.8±1.1	EOR2	17.3°	7.4
J1129−2847	11h29m32s	−28°47′58″	5.7±1.9	6.8±2.6	2.3±2.5	11.5±9.7	EOR2	24.9°	5.9
J1129+0013	11h29m43s	+00°13′55″	4.2±1.4	4.7±1.8	5.4±3.3	4.3±3.6	EOR2	20.1°	6.1
J1129−1450	11h29m60s	−14°50′30″	4.0±1.3	4.5±1.7	4.0±1.5	4.5±1.7	EOR2	17.8°	5.8
J1130−0329	11h30m11s	−03°29′14″	4.6±1.5	5.5±2.0	5.1±3.1	3.2±2.6	EOR2	18.6°	9.6
J1130−1321	11h30m17s	−13°21′03″	8.6±2.6	10.6±3.8	8.2±2.9	6.0±2.2	EOR2	17.5°	15.6
J1133−0402	11h33m16s	−04°02′17″	4.5±1.4	5.4±2.0	4.2±2.6	5.6±4.6	EOR2	19.1°	8.3
J1133−2717	11h33m22s	−27°17′13″	5.2±1.7	6.1±2.3	7.7±4.9	4.0±4.0	EOR2	24.5°	6.1
J1133−1956	11h33m37s	−19°56′51″	12.9±3.9	15.6±5.5	12.2±7.3	6.9±5.6	EOR2	20.4°	23.9
J1134−1728	11h34m28s	−17°28′58″	14.9±4.5	18.6±6.5	11.8±7.1	9.0±7.2	EOR2	19.6°	28.8
J1134−0801	11h34m28s	−08°01′13″	3.4±1.1	···	2.7±1.8	1.5±1.4	EOR2	18.5°	7.0
J1134−2611	11h34m37s	−26°11′50″	4.9±1.6	5.9±2.2	4.1±2.9	3.1±3.5	EOR2	24.0°	5.7
J1135−1825	11h35m17s	−18°25′34″	4.5±1.4	5.2±2.0	4.8±3.0	2.6±2.3	EOR2	20.1°	7.2
J1135−1442	11h35m59s	−14°42′56″	5.2±1.7	6.2±2.3	4.6±2.8	5.9±4.8	EOR2	19.1°	7.6
J1136−0334	11h36m13s	−03°34′15″	3.1±1.1	3.6±1.5	4.0±2.5	1.5±1.5	EOR2	19.9°	5.1
J1137+0113	11h37m44s	+01°13′49″	7.8±2.5	9.1±3.4	8.9±5.5	5.5±4.6	EOR2	22.3°	8.0
J1138−1306	11h38m02s	−13°06′31″	7.2±2.3	8.2±3.0	7.9±4.8	7.2±5.8	EOR2	19.3°	10.7
J1139−1352	11h39m12s	−13°52′11″	33.7±10.1	41.6±14.6	29.2±17.5	21.7±17.4	EOR2	19.7°	44.7
J1140−1038	11h40m24s	−10°38′41″	3.9±1.3	4.5±1.8	4.5±2.9	3.6±3.0	EOR2	19.8°	5.2
J1141+0111	11h41m08s	+01°11′31″	11.5±3.6	13.2±4.8	16.0±9.7	12.8±10.4	EOR2	23.0°	9.9
J1141−1119	11h41m45s	−11°19′48″	4.8±1.6	4.5±1.8	8.9±5.4	7.7±6.2	EOR2	20.1°	5.6
J1141−1911	11h41m46s	−19°11′41″	5.0±1.6	6.0±2.3	3.2±2.1	···	EOR2	21.8°	5.9
J1142−1831	11h42m38s	−18°31′38″	6.0±2.0	7.1±2.7	6.3±3.9	3.4±3.1	EOR2	21.7°	6.8
J1142−1527	11h42m38s	−15°27′41″	3.7±1.2	4.5±1.7	3.6±2.3	2.7±2.5	EOR2	20.9°	6.1
J1142−1144	11h42m40s	−11°44′14″	9.4±2.9	9.7±3.5	13.8±8.3	11.1±8.9	EOR2	20.4°	13.2

Continued on Next Page...

Table A.1 – Continued

Name	RA	DEC	$S_{\rm avg}$	$S_{123.52}$	$S_{154.24}$	$S_{184.96}$	Field	$r_{\rm FC}$	SNR
J1144−1743	11h44m25s	−17°43′56″	5.3±1.8	6.0±2.3	7.5±4.6	4.7±4.1	EOR2	21.9°	6.3
J1144−2057	11h44m56s	−20°57′11″	6.0±1.9	7.2±2.6	5.0±3.2	1.6±3.0	EOR2	23.2°	8.8
J1144−0035	11h44m58s	−00°35′05″	8.9±2.8	10.9±4.0	7.6±4.7	8.0±6.6	EOR2	23.1°	7.8
J1145−2437	11h45m03s	−24°37′01″	4.7±1.6	5.6±2.2	3.3±2.6	···	EOR2	25.0°	5.5
J1145−1441	11h45m39s	−14°41′04″	4.1±1.4	5.0±1.9	4.4±2.8	4.9±4.1	EOR2	21.4°	5.9
J1145−2022	11h45m56s	−20°22′23″	4.0±1.4	4.8±1.9	3.0±2.1	9.0±7.6	EOR2	23.2°	5.6
J1149−1206	11h49m08s	−12°06′49″	12.4±3.8	14.9±5.3	12.7±7.7	7.9±6.4	EOR2	22.0°	14.6
J1152−1029	11h52m48s	−10°29′58″	6.1±2.0	7.4±2.7	···	5.9±4.9	EOR2	22.8°	7.9
J1153−0442	11h53m10s	−04°42′26″	8.1±2.6	9.9±3.7	5.2±3.6	5.6±4.8	EOR2	23.7°	6.7
J1154−1307	11h54m44s	−13°07′52″	5.5±1.9	5.3±2.2	7.8±4.8	5.3±4.6	EOR2	23.4°	5.4
J1155−1804	11h55m35s	−18°04′54″	8.0±2.6	9.3±3.5	9.5±5.9	5.9±5.9	EOR2	24.5°	6.4

Table A.2: Sources Detected With $3 \leq \mathrm{SNR} < 5$

Name	RA	DEC	S_{avg}	$S_{123.52}$	$S_{154.24}$	$S_{184.96}$	Field	r_{FC}	SNR
J0741−1406	07h41m01s	−14°06′20″	6.0±2.1	6.9±2.7	6.1±4.9	1.9±3.6	HydA	23.7°	3.9
J0744−1911	07h44m48s	−19°11′28″	3.9±1.6	4.5±2.0	1.8±3.0	···	HydA	23.5°	3.5
J0747−1146	07h47m55s	−11°46′57″	4.8±1.7	5.5±2.2	5.2±3.7	1.1±2.7	HydA	22.1°	3.8
J0749−0014	07h49m40s	−00°14′44″	6.4±2.3	7.4±2.9	3.9±4.5	9.3±8.6	HydA	24.9°	4.7
J0751−0706	07h51m34s	−07°06′29″	3.9±1.5	4.5±1.9	···	···	HydA	21.9°	3.6
J0753−2134	07h53m46s	−21°34′23″	2.2±0.9	2.5±1.2	1.8±1.6	5.7±5.6	HydA	22.3°	3.0
J0754−2009	07h54m00s	−20°09′44″	3.0±1.1	3.1±1.3	5.1±3.3	3.4±3.9	HydA	21.7°	4.1
J0755−0229	07h55m04s	−02°29′26″	3.5±1.4	4.1±1.7	3.1±2.8	1.7±3.2	HydA	22.7°	3.1
J0755−1946	07h55m06s	−19°46′29″	2.6±1.0	3.0±1.3	2.8±2.0	3.4±3.7	HydA	21.4°	3.7
J0756+0208	07h56m08s	+02°08′48″	6.6±2.4	7.7±3.1	5.4±4.1	6.2±6.8	HydA	24.8°	4.3
J0756−0607	07h56m12s	−06°07′23″	2.3±1.0	2.7±1.2	···	2.0±2.6	HydA	21.1°	3.2
J0757−1721	07h57m18s	−17°21′27″	2.3±0.9	2.7±1.2	2.0±1.5	1.8±2.1	HydA	20.2°	3.3
J0757−1800	07h57m37s	−18°00′19″	3.0±1.1	3.5±1.4	3.0±2.0	2.7±2.7	HydA	20.3°	4.3
J0758−0813	07h58m04s	−08°13′33″	2.1±0.9	2.4±1.2	1.9±1.5	0.9±1.7	HydA	20.1°	3.6
J0759−1009	07h59m41s	−10°09′20″	2.1±0.9	2.7±1.2	···	···	HydA	19.3°	3.0
J0759−1957	07h59m42s	−19°57′37″	1.4±0.6	1.6±0.8	1.2±1.1	1.3±1.9	HydA	20.4°	3.0
J0800−1049	08h00m18s	−10°49′60″	2.1±0.9	2.6±1.2	1.0±1.1	3.6±3.1	HydA	19.1°	3.3
J0801−2230	08h01m57s	−22°30′04″	2.5±1.0	2.8±1.2	3.1±2.1	···	HydA	20.9°	3.1
J0802−1443	08h02m38s	−14°43′29″	1.8±0.7	2.4±1.0	2.8±1.8	···	HydA	18.5°	3.1
J0802−1750	08h02m40s	−17°50′51″	2.6±0.9	2.9±1.2	2.7±1.7	2.3±2.1	HydA	19.1°	3.8
J0803−0334	08h03m06s	−03°34′59″	3.0±1.2	4.1±1.7	3.0±2.2	3.2±3.1	HydA	20.4°	3.1
J0803−1955	08h03m21s	−19°55′18″	1.4±0.6	1.8±0.8	1.2±1.0	···	HydA	19.6°	3.0
J0804−0555	08h04m13s	−05°55′25″	2.6±0.9	2.9±1.2	3.7±2.4	···	HydA	19.2°	3.7
J0804+0440	08h04m24s	+04°40′54″	3.9±1.7	4.1±2.1	7.8±5.6	9.3±8.5	HydA	24.8°	3.1
J0805−1227	08h05m44s	−12°27′37″	2.2±0.8	2.9±1.2	1.8±0.9	0.8±0.9	HydA	17.7°	3.9
J0805−1328	08h05m50s	−13°28′14″	2.2±0.8	2.7±1.1	1.6±0.8	2.3±1.2	HydA	17.7°	4.3
J0806+0124	08h06m16s	+01°24′46″	3.7±1.4	4.9±2.0	···	6.0±5.2	HydA	22.4°	3.2
J0806−2724	08h06m24s	−27°24′53″	3.4±1.2	4.2±1.7	0.6±1.4	···	HydA	22.7°	4.0
J0807−2009	08h07m06s	−20°09′54″	1.4±0.5	1.4±0.7	1.9±1.3	1.7±1.6	HydA	18.8°	3.0
J0807−1205	08h07m35s	−12°05′00″	2.8±1.0	3.2±1.3	2.6±1.1	2.7±1.2	HydA	17.2°	4.7
J0808+0509	08h08m06s	+05°09′23″	4.6±1.9	5.3±2.5	8.2±5.6	14.2±12.3	HydA	24.5°	3.4
J0810−1615	08h10m00s	−16°15′30″	1.7±0.6	2.6±1.1	1.5±0.7	1.2±0.7	HydA	17.0°	4.0
J0810−1952	08h10m48s	−19°52′50″	1.4±0.5	1.7±0.8	1.6±0.7	1.8±1.0	HydA	17.9°	3.9
J0811+0421	08h11m06s	+04°21′51″	5.7±2.0	6.9±2.8	···	6.3±5.9	HydA	23.4°	4.3
J0811−0730	08h11m30s	−07°30′54″	2.4±0.9	2.8±1.1	3.0±1.2	1.4±0.9	HydA	17.0°	4.3
J0812−0657	08h12m02s	−06°57′33″	2.0±0.8	2.4±1.0	2.1±1.0	0.8±0.8	HydA	17.1°	3.0
J0812−2712	08h12m31s	−27°12′19″	2.4±0.9	2.4±1.2	4.4±2.8	···	HydA	21.6°	3.1
J0812−1436	08h12m48s	−14°36′34″	1.4±0.5	2.4±1.0	1.6±0.7	1.6±0.7	HydA	16.1°	3.4
J0812+0222	08h12m50s	+02°22′44″	3.6±1.5	3.0±1.7	8.5±5.3	6.9±5.8	HydA	21.7°	3.5
J0812−2348	08h12m53s	−23°48′03″	2.0±0.7	2.5±1.0	1.5±1.1	1.1±1.5	HydA	19.4°	4.4

Continued on Next Page...

Table A.2 – Continued

Name	RA	DEC	$S_{\rm avg}$	$S_{123.52}$	$S_{154.24}$	$S_{184.96}$	Field	$r_{\rm FC}$	SNR
J0812−0127	08h12m55s	−01°27′10″	2.9±1.1	3.3±1.4	3.1±2.3	1.6±1.7	HydA	19.3°	3.3
J0813−1936	08h13m21s	−19°36′09″	1.4±0.5	1.5±0.7	1.8±0.8	0.7±0.7	HydA	17.3°	4.0
J0813−1131	08h13m44s	−11°31′32″	2.9±1.0	3.3±1.4	2.5±1.0	3.5±1.3	HydA	15.8°	4.3
J0814−2440	08h14m17s	−24°40′27″	1.7±0.6	2.1±1.0	1.4±1.0	1.4±1.7	HydA	19.7°	3.9
J0814−1429	08h14m59s	−14°29′09″	1.4±0.5	2.0±0.9	1.3±0.6	0.9±0.6	HydA	15.5°	4.3
J0814−1914	08h14m60s	−19°14′52″	1.5±0.6	1.8±0.8	1.9±0.8	0.7±0.6	HydA	16.8°	3.7
J0815−0733	08h15m09s	−07°33′58″	2.2±0.8	2.7±1.1	1.9±0.9	1.4±0.8	HydA	16.1°	4.1
J0815−2022	08h15m27s	−20°22′43″	1.1±0.4	1.1±0.6	1.4±0.7	···	HydA	17.2°	3.2
J0816+0428	08h16m19s	+04°28′59″	3.6±1.5	5.0±2.1	···	8.0±6.9	HydA	22.6°	3.2
J0817−0309	08h17m22s	−03°09′02″	1.8±0.8	1.4±0.9	2.2±1.1	3.7±1.5	HydA	17.5°	3.1
J0817−1326	08h17m49s	−13°26′59″	1.1±0.4	2.3±1.0	1.0±0.6	1.1±0.6	HydA	14.8°	3.7
J0817−1613	08h17m55s	−16°13′21″	1.9±0.7	1.9±0.8	1.9±0.8	2.1±0.8	HydA	15.2°	4.6
J0817−1425	08h17m59s	−14°25′33″	1.0±0.4	···	1.3±0.6	1.4±0.6	HydA	14.8°	4.2
J0818−0216	08h18m36s	−02°16′06″	2.8±1.0	···	2.0±1.0	3.0±1.4	HydA	17.7°	4.5
J0818−0526	08h18m57s	−05°26′28″	1.2±0.5	1.4±0.7	1.3±0.7	···	HydA	16.0°	3.0
J0819−2216	08h19m06s	−22°16′38″	1.6±0.6	1.8±0.7	1.6±0.7	1.6±0.9	HydA	17.4°	4.7
J0819−1123	08h19m53s	−11°23′01″	1.8±0.6	1.4±0.7	2.2±0.9	1.8±0.8	HydA	14.3°	4.6
J0820−1321	08h20m02s	−13°21′50″	0.8±0.3	···	1.5±0.7	1.1±0.5	HydA	14.2°	3.1
J0820+0422	08h20m15s	+04°22′05″	3.3±1.3	3.8±1.7	2.8±2.2	···	HydA	21.8°	3.4
J0820−2055	08h20m28s	−20°55′57″	1.3±0.5	···	0.8±0.5	2.0±0.9	HydA	16.4°	3.8
J0820+0451	08h20m43s	+04°51′44″	3.7±1.4	4.1±1.8	4.4±3.1	6.6±5.7	HydA	22.1°	3.3
J0820−0834	08h20m47s	−08°34′53″	1.2±0.5	1.5±0.7	0.9±0.5	1.0±0.5	HydA	14.5°	3.0
J0821−0606	08h21m00s	−06°06′29″	1.4±0.5	1.3±0.7	2.0±0.8	0.8±0.6	HydA	15.3°	3.8
J0821−2458	08h21m07s	−24°58′34″	1.7±0.6	2.4±1.1	1.5±1.0	1.3±1.3	HydA	18.6°	4.0
J0821−2015	08h21m25s	−20°15′22″	1.4±0.5	2.0±0.8	0.8±0.5	1.2±0.6	HydA	15.9°	4.0
J0821−0024	08h21m27s	−00°24′24″	1.9±0.7	2.5±1.0	···	0.5±1.0	HydA	18.3°	3.2
J0821−0949	08h21m33s	−09°49′26″	1.7±0.6	2.3±0.9	1.2±0.6	1.4±0.6	HydA	14.1°	4.7
J0821−0535	08h21m46s	−05°35′52″	1.0±0.4	1.3±0.7	1.0±0.6	0.5±0.5	HydA	15.3°	3.0
J0821+0224	08h21m49s	+02°24′26″	2.6±1.0	3.6±1.5	···	2.5±2.3	HydA	20.1°	3.4
J0822−2718	08h22m38s	−27°18′49″	2.4±0.9	3.2±1.4	1.2±1.0	2.2±2.2	HydA	20.0°	4.0
J0822−2605	08h22m45s	−26°05′05″	2.1±0.8	2.7±1.1	1.4±1.0	2.2±2.0	HydA	19.1°	4.0
J0823−1738	08h23m41s	−17°38′15″	1.2±0.5	2.9±1.1	0.6±0.4	1.7±0.7	HydA	14.3°	3.6
J0824−0117	08h24m10s	−01°17′31″	1.4±0.6	2.1±0.9	···	1.9±1.0	HydA	17.2°	3.3
J0824−0319	08h24m16s	−03°19′54″	1.9±0.7	2.5±1.0	1.6±0.8	···	HydA	15.9°	4.6
J0824−2350	08h24m50s	−23°50′04″	1.2±0.5	1.1±0.8	1.5±0.7	1.2±0.7	HydA	17.3°	3.3
J0824−0439	08h24m52s	−04°39′32″	1.2±0.5	0.6±0.6	1.5±0.7	2.5±1.0	HydA	15.1°	3.4
J0825−2847	08h25m02s	−28°47′55″	3.2±1.1	3.7±1.6	2.8±1.9	1.2±1.8	HydA	20.8°	4.5
J0825−0919	08h25m11s	−09°19′33″	1.1±0.4	1.4±0.6	1.4±0.6	0.6±0.4	HydA	13.3°	3.5
J0825−1413	08h25m15s	−14°13′03″	0.7±0.3	···	1.1±0.5	1.0±0.5	HydA	13.0°	3.3
J0825+0007	08h25m53s	+00°07′59″	1.7±0.7	2.3±1.0	1.3±0.8	1.6±0.9	HydA	17.8°	3.1
J0826−0656	08h26m20s	−06°56′18″	1.3±0.5	2.9±1.2	···	1.6±0.7	HydA	13.8°	4.4

Continued on Next Page...

Table A.2 – Continued

Name	RA	DEC	$S_{\rm avg}$	$S_{123.52}$	$S_{154.24}$	$S_{184.96}$	Field	$r_{\rm FC}$	SNR
J0826−0326	08h26m35s	−03°26′34″	1.3±0.5	1.4±0.7	1.2±0.7	1.3±0.7	HydA	15.4°	3.6
J0827−2345	08h27m09s	−23°45′48″	1.4±0.6	···	1.5±0.7	···	HydA	16.8°	3.2
J0827−1404	08h27m23s	−14°04′26″	1.0±0.4	1.2±0.5	1.1±0.5	0.9±0.4	HydA	12.5°	4.7
J0827−1701	08h27m29s	−17°01′44″	1.4±0.5	1.8±0.8	2.0±0.8	0.9±0.4	HydA	13.2°	3.9
J0827−3322	08h27m30s	−33°22′43″	3.6±1.5	4.1±1.9	4.3±3.5	18.8±15.9	HydA	24.2°	3.4
J0827−2100	08h27m49s	−21°00′18″	1.1±0.4	1.8±0.8	1.1±0.6	···	HydA	15.0°	3.4
J0828−0502	08h28m02s	−05°02′07″	1.4±0.5	1.3±0.7	1.3±0.7	1.3±0.6	HydA	14.2°	4.4
J0828−1450	08h28m02s	−14°50′07″	1.0±0.4	1.8±0.8	0.5±0.4	1.0±0.4	HydA	12.5°	3.7
J0828−2553	08h28m13s	−25°53′47″	2.1±0.7	1.7±0.9	2.7±1.7	2.8±2.4	HydA	18.1°	4.6
J0828−3201	08h28m14s	−32°01′26″	4.7±1.7	5.1±2.1	7.6±5.0	···	HydA	23.0°	4.8
J0828−0655	08h28m50s	−06°55′00″	1.1±0.4	0.8±0.6	0.8±0.5	1.3±0.6	HydA	13.2°	3.5
J0828−1225	08h28m51s	−12°25′12″	0.8±0.3	0.8±0.4	0.6±0.4	0.9±0.4	HydA	12.0°	3.4
J0828−1834	08h28m60s	−18°34′07″	1.1±0.4	···	1.7±0.7	1.4±0.6	HydA	13.5°	3.5
J0829−0750	08h29m03s	−07°50′22″	1.4±0.5	2.2±0.9	1.4±0.7	1.0±0.5	HydA	12.8°	4.7
J0830−1015	08h30m19s	−10°15′23″	1.1±0.4	1.6±0.6	1.0±0.5	0.8±0.4	HydA	11.9°	4.1
J0830+0923	08h30m23s	+09°23′17″	6.8±2.6	7.8±3.4	7.4±6.0	8.5±9.5	HydA	24.5°	3.2
J0830−0142	08h30m46s	−01°42′02″	1.4±0.6	2.0±0.9	1.1±0.7	1.0±0.7	HydA	15.7°	4.2
J0831−0740	08h31m07s	−07°40′03″	1.0±0.4	2.4±1.0	0.4±0.4	1.3±0.5	HydA	12.4°	4.8
J0831−2258	08h31m11s	−22°58′18″	1.2±0.5	0.7±0.6	···	0.6±0.5	HydA	15.6°	4.0
J0831−1709	08h31m18s	−17°09′00″	1.2±0.4	1.3±0.7	1.7±0.7	1.0±0.5	HydA	12.4°	4.3
J0831−0551	08h31m28s	−05°51′46″	1.1±0.4	0.9±0.6	1.1±0.6	1.2±0.5	HydA	13.1°	3.4
J0831−2012	08h31m30s	−20°12′08″	1.7±0.6	1.7±0.7	2.1±0.8	2.0±0.8	HydA	13.8°	4.9
J0831−2438	08h31m53s	−24°38′57″	1.7±0.7	···	1.7±0.8	···	HydA	16.7°	3.4
J0832−3326	08h32m38s	−33°26′00″	5.1±1.8	5.8±2.4	6.3±4.3	9.6±9.1	HydA	23.7°	4.4
J0832−0500	08h32m53s	−05°00′06″	1.5±0.5	0.5±0.5	2.9±1.1	1.9±0.8	HydA	13.2°	4.3
J0833−2608	08h33m21s	−26°08′33″	1.6±0.6	1.9±1.0	1.4±0.7	1.2±0.8	HydA	17.6°	3.4
J0833−0806	08h33m26s	−08°06′54″	1.3±0.5	2.0±0.8	0.6±0.4	1.4±0.5	HydA	11.7°	4.4
J0834−0436	08h34m12s	−04°36′40″	1.4±0.5	2.6±1.0	2.3±0.9	0.9±0.5	HydA	13.2°	3.7
J0834−1251	08h34m25s	−12°51′20″	0.8±0.3	1.3±0.6	1.6±0.7	1.0±0.4	HydA	10.7°	3.2
J0834−1427	08h34m26s	−14°27′32″	1.2±0.4	1.0±0.5	1.0±0.4	1.1±0.5	HydA	10.9°	4.7
J0834−0948	08h34m28s	−09°48′04″	1.1±0.4	1.5±0.6	1.1±0.5	0.8±0.4	HydA	10.9°	5.0
J0834−2642	08h34m29s	−26°42′10″	1.4±0.6	···	1.1±0.6	1.0±0.8	HydA	17.9°	3.1
J0835−1204	08h35m31s	−12°04′50″	0.7±0.3	···	0.3±0.3	1.3±0.5	HydA	10.4°	3.1
J0835−1400	08h35m39s	−14°00′41″	1.2±0.4	1.1±0.5	1.1±0.5	1.2±0.5	HydA	10.5°	4.8
J0835+0406	08h35m45s	+04°06′18″	2.9±1.1	3.2±1.6	2.6±1.9	2.7±2.5	HydA	19.3°	3.0
J0835−2724	08h35m57s	−27°24′15″	1.9±0.7	3.3±1.3	1.3±0.9	1.0±1.0	HydA	18.2°	4.5
J0836−1131	08h36m11s	−11°31′12″	0.9±0.3	···	0.6±0.4	0.8±0.4	HydA	10.3°	3.9
J0836−1512	08h36m23s	−15°12′31″	1.1±0.4	0.8±0.5	1.1±0.5	1.1±0.5	HydA	10.6°	4.1
J0836−1648	08h36m24s	−16°48′12″	0.8±0.3	···	1.0±0.4	···	HydA	11.1°	3.2
J0836−1103	08h36m32s	−11°03′13″	0.9±0.3	···	1.6±0.7	0.7±0.3	HydA	10.2°	3.6
J0836−1033	08h36m44s	−10°33′18″	1.1±0.4	2.3±0.9	···	0.9±0.4	HydA	10.3°	4.6

Continued on Next Page...

Table A.2 – Continued

Name	RA	DEC	$S_{\rm avg}$	$S_{123.52}$	$S_{154.24}$	$S_{184.96}$	Field	$r_{\rm FC}$	SNR
J0837−0448	08h37m21s	−04°48′25″	1.0±0.4	0.7±0.5	1.5±0.7	0.8±0.4	HydA	12.4°	3.2
J0837+0050	08h37m40s	+00°50′51″	1.2±0.5	0.9±0.6	3.7±1.4	1.3±0.8	HydA	16.4°	3.7
J0837−2602	08h37m48s	−26°02′37″	2.0±0.7	3.3±1.4	1.3±0.6	2.0±0.9	HydA	16.9°	3.9
J0837−2948	08h37m49s	−29°48′48″	2.2±0.8	2.5±1.1	···	···	HydA	20.0°	4.3
J0838−2306	08h38m53s	−23°06′29″	1.3±0.5	1.0±0.6	1.5±0.7	1.3±0.6	HydA	14.4°	3.8
J0838−0207	08h38m56s	−02°07′06″	1.7±0.7	1.5±0.7	2.2±0.9	1.7±0.7	HydA	13.9°	3.3
J0839−0749	08h39m00s	−07°49′40″	1.2±0.4	1.4±0.7	0.8±0.4	1.3±0.5	HydA	10.5°	4.7
J0839+0108	08h39m26s	+01°08′19″	1.4±0.6	1.5±0.7	1.8±0.9	1.6±0.9	HydA	16.3°	3.1
J0839−0648	08h39m49s	−06°48′46″	0.8±0.3	1.2±0.6	0.7±0.4	0.6±0.3	HydA	10.8°	3.2
J0840−1019	08h40m15s	−10°19′13″	1.0±0.4	···	1.8±0.7	0.9±0.4	HydA	9.4°	4.4
J0840−0617	08h40m17s	−06°17′09″	0.8±0.3	1.9±0.8	0.3±0.3	···	HydA	11.0°	3.3
J0840−1912	08h40m18s	−19°12′54″	1.1±0.4	1.0±0.5	1.2±0.5	1.0±0.4	HydA	11.6°	4.8
J0840−0314	08h40m37s	−03°14′59″	1.2±0.5	1.7±0.7	0.7±0.4	0.7±0.4	HydA	12.8°	3.6
J0840+1021	08h40m50s	+10°21′18″	5.6±2.4	6.3±2.9	16.7±11.2	···	HydA	24.3°	3.1
J0840−0528	08h40m59s	−05°28′21″	0.8±0.3	1.0±0.5	0.8±0.4	0.7±0.3	HydA	11.3°	3.2
J0841−1344	08h41m03s	−13°44′38″	1.0±0.4	2.1±0.8	1.0±0.5	0.5±0.3	HydA	9.2°	4.8
J0841−0353	08h41m40s	−03°53′11″	1.2±0.4	···	1.2±0.6	1.0±0.5	HydA	12.2°	4.2
J0841−1407	08h41m42s	−14°07′20″	0.8±0.3	0.8±0.5	0.9±0.4	0.6±0.3	HydA	9.1°	3.2
J0841−0640	08h41m58s	−06°40′48″	3.0±1.2	3.6±1.6	···	···	EOR2	24.5°	3.2
J0842−1733	08h42m02s	−17°33′45″	0.9±0.3	1.9±0.7	···	0.8±0.3	HydA	10.3°	4.9
J0842−2747	08h42m27s	−27°47′40″	1.9±0.7	2.2±0.9	1.9±0.8	2.4±1.1	HydA	17.8°	4.3
J0842+0719	08h42m58s	+07°19′34″	5.5±2.2	6.3±2.6	5.8±4.0	8.4±7.3	HydA	21.3°	3.4
J0843+1115	08h43m31s	+11°15′20″	6.3±2.4	7.3±3.1	6.0±6.7	···	HydA	24.9°	3.2
J0843−1653	08h43m38s	−16°53′16″	0.7±0.2	···	···	···	HydA	9.6°	3.6
J0844−0047	08h44m44s	−00°47′52″	1.2±0.5	1.3±0.7	1.7±0.7	1.0±0.5	HydA	14.0°	3.1
J0844−1845	08h44m46s	−18°45′23″	0.7±0.3	0.9±0.4	0.7±0.3	0.5±0.3	HydA	10.4°	3.3
J0844−2140	08h44m49s	−21°40′12″	0.9±0.3	1.0±0.5	0.9±0.4	0.8±0.4	HydA	12.5°	3.8
J0844−2310	08h44m49s	−23°10′48″	1.3±0.5	1.1±0.6	1.3±0.6	2.0±0.8	HydA	13.6°	3.8
J0844+0039	08h44m50s	+00°39′16″	1.5±0.6	···	2.2±0.9	1.7±0.8	HydA	15.2°	4.0
J0844−0936	08h44m54s	−09°36′36″	1.1±0.4	1.2±0.5	1.0±0.5	1.2±0.5	HydA	8.5°	3.9
J0845−1114	08h45m32s	−11°14′15″	0.9±0.3	···	···	1.0±0.4	HydA	8.0°	4.0
J0845+0440	08h45m32s	+04°40′14″	3.4±1.2	3.5±1.6	4.2±2.7	5.8±4.9	HydA	18.6°	4.4
J0845−0716	08h45m53s	−07°16′57″	0.7±0.3	1.1±0.6	0.4±0.3	0.6±0.3	HydA	9.3°	3.5
J0845−1204	08h45m57s	−12°04′19″	0.8±0.3	0.3±0.4	···	0.8±0.3	HydA	7.9°	3.5
J0846+0708	08h46m03s	+07°08′30″	3.1±1.4	3.7±1.7	2.2±2.2	···	HydA	20.8°	3.5
J0846+0156	08h46m20s	+01°56′33″	1.7±0.7	1.7±0.8	2.2±1.0	2.7±1.1	HydA	16.1°	3.3
J0846−3035	08h46m52s	−30°35′13″	2.3±0.9	3.1±1.4	0.5±0.8	···	HydA	19.9°	3.3
J0847−2718	08h47m11s	−27°18′19″	1.7±0.6	2.0±0.9	1.4±0.7	2.5±1.1	HydA	16.9°	3.4
J0847−1545	08h47m27s	−15°45′18″	0.6±0.2	0.3±0.3	1.2±0.5	0.6±0.3	HydA	8.3°	4.3
J0847−1246	08h47m45s	−12°46′07″	0.9±0.3	1.3±0.6	0.5±0.3	1.0±0.4	HydA	7.4°	3.6
J0847−2404	08h47m47s	−24°04′58″	1.1±0.4	0.9±0.5	1.2±0.6	1.3±0.6	HydA	14.0°	3.3

Continued on Next Page...

Table A.2 – Continued

Name	RA	DEC	$S_{\rm avg}$	$S_{123.52}$	$S_{154.24}$	$S_{184.96}$	Field	$r_{\rm FC}$	SNR
J0847−2744	08h47m48s	−27°44′36″	1.7±0.6	2.1±0.9	1.4±0.7	1.4±0.8	HydA	17.2°	3.6
J0847−3119	08h47m54s	−31°19′01″	2.7±1.0	3.5±1.5	0.8±1.0	9.3±8.0	HydA	20.5°	3.7
J0848+0117	08h48m21s	+01°17′41″	1.7±0.6	···	1.0±0.7	2.0±0.9	HydA	15.3°	4.0
J0848−1934	08h48m21s	−19°34′09″	0.7±0.3	1.0±0.4	0.8±0.4	0.5±0.3	HydA	10.4°	4.0
J0848−0043	08h48m51s	−00°43′17″	1.5±0.5	1.1±0.7	1.7±0.8	1.8±0.8	HydA	13.5°	4.2
J0848−0427	08h48m52s	−04°27′09″	1.1±0.4	0.5±0.5	1.0±0.5	1.1±0.5	HydA	10.5°	3.6
J0849+0943	08h49m01s	+09°43′18″	5.1±1.9	5.8±2.5	7.9±5.8	···	HydA	23.0°	3.7
J0849−2457	08h49m05s	−24°57′45″	1.3±0.5	1.9±0.8	0.8±0.5	1.0±0.5	HydA	14.6°	3.6
J0849−1501	08h49m10s	−15°01′24″	0.8±0.3	0.6±0.4	1.0±0.5	0.6±0.3	HydA	7.6°	4.3
J0849−1720	08h49m24s	−17°20′14″	0.6±0.3	0.6±0.3	0.8±0.4	0.4±0.2	HydA	8.7°	3.4
J0850−0119	08h50m13s	−01°19′53″	1.1±0.4	···	1.8±0.8	0.9±0.5	HydA	12.8°	3.1
J0850−2725	08h50m44s	−27°25′27″	1.5±0.5	1.6±0.8	1.7±0.8	3.3±1.3	HydA	16.6°	3.9
J0850−0024	08h50m48s	−00°24′17″	1.3±0.5	2.0±1.0	1.1±0.6	1.2±0.6	HydA	13.5°	3.3
J0851−3317	08h51m06s	−33°17′26″	2.5±1.1	3.2±1.5	4.6±3.1	···	HydA	22.1°	3.4
J0851−1445	08h51m50s	−14°45′59″	0.8±0.3	1.3±0.6	0.5±0.4	0.7±0.3	HydA	6.9°	3.2
J0851+0219	08h51m59s	+02°19′27″	2.2±0.8	3.1±1.3	1.6±0.9	0.9±0.7	HydA	15.8°	3.8
J0852−1032	08h52m21s	−10°32′46″	0.8±0.3	···	1.3±0.5	0.9±0.4	HydA	6.5°	3.5
J0852+0131	08h52m35s	+01°31′32″	2.1±0.8	···	1.0±0.8	1.5±0.8	HydA	15.0°	3.7
J0852−2012	08h52m48s	−20°12′43″	2.0±0.8	2.7±1.1	0.9±0.9	6.9±5.9	EOR2	23.4°	3.1
J0853+0400	08h53m01s	+04°00′11″	1.8±0.8	3.1±1.3	···	0.8±1.2	HydA	17.2°	3.0
J0853−0946	08h53m16s	−09°46′37″	0.7±0.3	···	···	0.8±0.3	HydA	6.5°	3.1
J0853−1446	08h53m20s	−14°46′51″	1.1±0.4	0.7±0.5	1.8±0.7	1.1±0.4	HydA	6.6°	4.5
J0853−0300	08h53m25s	−03°00′07″	0.9±0.4	2.2±0.9	···	0.6±0.4	HydA	10.9°	3.8
J0853−0831	08h53m25s	−08°31′51″	1.3±0.5	1.6±0.8	···	···	EOR2	21.4°	3.7
J0853−3141	08h53m38s	−31°41′14″	2.4±0.9	2.5±1.1	3.4±2.3	···	HydA	20.4°	3.6
J0853−0916	08h53m56s	−09°16′20″	0.7±0.3	0.7±0.4	0.6±0.3	0.6±0.3	HydA	6.6°	3.2
J0854−1658	08h54m06s	−16°58′43″	0.7±0.3	···	1.4±0.6	1.1±0.4	HydA	7.6°	3.2
J0854+0209	08h54m08s	+02°09′30″	3.8±1.4	4.7±1.9	···	···	EOR2	24.6°	3.8
J0854−1831	08h54m10s	−18°31′02″	0.8±0.3	···	0.6±0.3	0.7±0.3	HydA	8.6°	3.8
J0854−1239	08h54m11s	−12°39′32″	0.6±0.3	1.1±0.6	0.7±0.3	0.4±0.2	HydA	5.9°	3.1
J0854−0019	08h54m13s	−00°19′19″	2.1±0.7	···	2.2±0.9	2.3±0.9	HydA	13.2°	4.7
J0854−0800	08h54m31s	−08°00′28″	0.6±0.3	···	0.7±0.4	0.5±0.2	HydA	7.1°	3.1
J0854−1429	08h54m41s	−14°29′46″	0.7±0.3	0.8±0.5	0.9±0.4	0.7±0.3	HydA	6.2°	3.5
J0854−3508	08h54m46s	−35°08′17″	3.6±1.4	4.0±1.8	8.4±5.7	7.4±7.1	HydA	23.7°	3.0
J0855−1131	08h55m07s	−11°31′54″	0.9±0.3	0.8±0.5	0.4±0.3	1.0±0.4	HydA	5.6°	4.1
J0855+0245	08h55m12s	+02°45′24″	2.6±1.0	2.3±1.1	4.2±1.6	4.7±1.8	HydA	15.9°	4.6
J0855−1402	08h55m13s	−14°02′10″	0.9±0.4	1.3±0.6	0.8±0.4	0.8±0.4	HydA	5.9°	4.2
J0855−1707	08h55m49s	−17°07′19″	0.7±0.3	0.7±0.4	0.6±0.3	0.7±0.3	HydA	7.4°	3.9
J0855+0311	08h55m51s	+03°11′33″	2.7±1.0	···	5.1±1.9	5.9±2.2	HydA	16.2°	3.7
J0856−2150	08h56m04s	−21°50′11″	0.9±0.3	0.6±0.5	1.5±0.6	0.7±0.3	HydA	11.1°	3.9
J0856+0337	08h56m55s	+03°37′56″	2.5±0.9	2.3±1.2	3.9±1.6	2.9±1.4	HydA	16.6°	4.6

Continued on Next Page...

Table A.2 – Continued

Name	RA	DEC	$S_{\rm avg}$	$S_{123.52}$	$S_{154.24}$	$S_{184.96}$	Field	$r_{\rm FC}$	SNR
J0857−0436	08h57m16s	−04°36′37″	1.1±0.4	0.5±0.5	1.5±0.6	0.9±0.4	HydA	9.1°	3.7
J0857−0500	08h57m27s	−05°00′28″	1.0±0.4	···	1.0±0.5	1.1±0.5	HydA	8.7°	3.8
J0857−2725	08h57m46s	−27°25′07″	0.9±0.4	0.4±0.5	2.0±0.8	2.5±1.0	HydA	16.1°	3.4
J0857−0408	08h57m54s	−04°08′33″	1.3±0.5	0.7±0.5	2.0±0.8	0.9±0.4	HydA	9.4°	4.8
J0858−1556	08h58m35s	−15°56′45″	0.7±0.3	1.4±0.6	···	0.7±0.3	HydA	6.1°	4.2
J0858−0905	08h58m45s	−09°05′59″	0.6±0.2	···	0.3±0.2	···	HydA	5.6°	3.4
J0859−0251	08h59m54s	−02°51′60″	1.4±0.5	1.3±0.6	1.2±0.5	1.3±0.5	HydA	10.3°	4.5
J0900−2816	09h00m05s	−28°16′54″	1.8±0.6	···	2.9±1.1	2.4±1.1	HydA	16.7°	4.5
J0900+0324	09h00m33s	+03°24′21″	2.0±0.8	···	1.9±1.0	3.6±1.6	HydA	16.1°	3.9
J0900−0430	09h00m38s	−04°30′35″	1.3±0.5	0.5±0.5	1.1±0.5	1.6±0.6	HydA	8.7°	4.4
J0901−2112	09h01m11s	−21°12′06″	0.9±0.3	0.7±0.5	1.1±0.5	0.6±0.3	HydA	10.0°	4.4
J0901−2751	09h01m25s	−27°51′55″	1.1±0.5	···	···	0.6±0.7	HydA	16.3°	3.5
J0901−2555	09h01m39s	−25°55′51″	1.0±0.4	···	···	···	HydA	14.4°	3.3
J0901−0453	09h01m43s	−04°53′05″	1.3±0.5	···	1.9±0.7	2.0±0.8	HydA	8.2°	3.7
J0902−0028	09h02m08s	−00°28′47″	1.4±0.5	0.6±0.5	2.7±1.0	1.4±0.6	HydA	12.3°	3.3
J0902−3426	09h02m09s	−34°26′41″	3.0±1.2	3.4±1.5	3.6±2.9	···	HydA	22.7°	3.3
J0902−0622	09h02m10s	−06°22′39″	1.0±0.4	0.8±0.4	1.2±0.5	0.7±0.4	HydA	6.9°	4.8
J0902−0125	09h02m10s	−01°25′53″	1.6±0.6	2.8±1.1	2.3±0.9	0.6±0.4	HydA	11.4°	3.6
J0902−2250	09h02m11s	−22°50′38″	1.0±0.3	0.6±0.4	1.0±0.4	1.2±0.5	HydA	11.4°	5.0
J0902−2313	09h02m18s	−23°13′14″	0.9±0.3	0.6±0.4	1.0±0.4	1.0±0.4	HydA	11.8°	4.3
J0902−1021	09h02m20s	−10°21′38″	0.7±0.3	0.6±0.4	···	0.7±0.3	HydA	4.2°	3.2
J0903−2043	09h03m17s	−20°43′23″	0.8±0.3	0.8±0.5	0.7±0.4	0.7±0.3	HydA	9.3°	3.4
J0903−0711	09h03m56s	−07°11′26″	0.8±0.3	···	0.8±0.4	0.5±0.3	HydA	6.0°	3.6
J0904−1806	09h04m01s	−18°06′36″	0.6±0.2	···	0.7±0.3	0.8±0.3	HydA	6.9°	3.9
J0904−3252	09h04m17s	−32°52′39″	2.3±0.9	2.4±1.1	4.7±3.1	···	HydA	21.0°	3.3
J0904−3412	09h04m50s	−34°12′22″	3.0±1.2	3.1±1.4	7.6±4.9	24.4±20.2	HydA	22.3°	3.5
J0904+0205	09h04m53s	+02°05′57″	2.3±0.9	2.8±1.1	2.5±1.8	3.5±3.6	EOR2	22.3°	3.1
J0905−1358	09h05m52s	−13°58′09″	0.7±0.3	0.2±0.4	0.4±0.3	0.7±0.3	HydA	3.5°	3.3
J0905−1258	09h05m54s	−12°58′29″	1.1±0.4	0.6±0.5	···	1.0±0.4	HydA	3.1°	4.9
J0906−3336	09h06m07s	−33°36′18″	2.6±1.0	3.1±1.3	3.1±2.4	···	HydA	21.7°	3.3
J0906−0744	09h06m08s	−07°44′52″	1.0±0.4	1.7±0.7	1.0±0.4	0.8±0.3	HydA	5.2°	4.0
J0906−1103	09h06m15s	−11°03′24″	1.2±0.4	···	1.2±0.5	1.0±0.4	HydA	3.1°	4.7
J0906−0658	09h06m44s	−06°58′55″	0.9±0.3	1.1±0.5	0.9±0.4	0.8±0.4	HydA	5.8°	3.5
J0906−1341	09h06m58s	−13°41′47″	0.7±0.3	···	···	0.6±0.3	HydA	3.2°	3.5
J0907−1556	09h07m20s	−15°56′47″	1.0±0.3	···	···	1.1±0.4	HydA	4.7°	4.9
J0907−1816	09h07m46s	−18°16′39″	0.6±0.2	0.6±0.3	0.5±0.2	0.6±0.3	HydA	6.7°	3.4
J0908−2351	09h08m04s	−23°51′04″	0.9±0.3	1.8±0.7	···	1.1±0.4	HydA	12.0°	3.4
J0908−1007	09h08m10s	−10°07′28″	1.5±0.6	···	0.9±0.5	0.6±0.5	EOR2	17.7°	3.2
J0908−0400	09h08m32s	−04°00′51″	1.5±0.5	0.4±0.6	1.9±0.8	1.5±0.6	HydA	8.4°	4.2
J0908+0451	09h08m40s	+04°51′28″	2.8±1.0	3.2±1.4	2.9±1.4	···	HydA	17.1°	4.5
J0908−0937	09h08m41s	−09°37′23″	2.5±1.1	···	2.3±0.9	2.0±0.8	HydA	3.4°	3.8

Continued on Next Page...

Table A.2 – Continued

Name	RA	DEC	$S_{\rm avg}$	$S_{123.52}$	$S_{154.24}$	$S_{184.96}$	Field	$r_{\rm FC}$	SNR
J0909+0326	09h09m31s	+03°26′42″	2.4±1.0	2.7±1.2	2.3±1.0	2.8±1.3	HydA	15.7°	3.2
J0909−2508	09h09m40s	−25°08′15″	0.8±0.3	1.7±0.7	1.1±0.5	0.6±0.3	HydA	13.2°	3.3
J0909+0129	09h09m49s	+01°29′58″	1.8±0.7	2.2±1.0	0.7±0.8	2.4±2.3	EOR2	20.9°	3.8
J0910+0018	09h10m24s	+00°18′44″	1.5±0.6	···	···	1.1±0.6	HydA	12.5°	4.7
J0910+0600	09h10m43s	+06°00′35″	2.8±1.2	3.8±1.7	1.1±1.3	9.9±8.7	EOR2	23.5°	3.1
J0911−2304	09h11m02s	−23°04′51″	0.9±0.3	1.4±0.6	0.8±0.4	0.6±0.3	HydA	11.1°	4.2
J0911+0013	09h11m45s	+00°13′53″	1.7±0.6	2.2±0.9	1.5±0.7	2.2±0.9	HydA	12.4°	4.3
J0911−1625	09h11m51s	−16°25′20″	0.8±0.3	1.1±0.7	1.1±0.5	···	HydA	4.6°	3.3
J0911−1319	09h11m57s	−13°19′16″	1.1±0.4	1.5±0.8	0.8±0.4	0.9±0.4	HydA	2.0°	4.3
J0911−2642	09h11m57s	−26°42′04″	1.4±0.5	1.5±0.7	1.4±0.6	1.9±0.8	HydA	14.7°	4.4
J0912+0808	09h12m29s	+08°08′08″	3.9±1.4	4.7±1.9	2.1±2.3	1.9±5.3	HydA	20.3°	4.3
J0912−2110	09h12m48s	−21°10′41″	1.5±0.6	2.0±0.9	1.4±1.0	0.6±0.6	EOR2	19.7°	3.1
J0913−1353	09h13m04s	−13°53′27″	1.2±0.4	2.4±1.1	0.6±0.4	0.5±0.4	EOR2	16.8°	3.7
J0913−2552	09h13m07s	−25°52′45″	1.6±0.6	2.0±0.9	1.8±1.2	1.6±1.6	EOR2	22.4°	3.4
J0913−2733	09h13m33s	−27°33′22″	2.3±0.8	···	2.0±1.3	···	EOR2	23.5°	4.3
J0914+0508	09h14m03s	+05°08′49″	2.2±0.9	2.8±1.3	1.7±1.1	3.3±1.8	HydA	17.2°	3.3
J0914−2733	09h14m29s	−27°33′22″	1.2±0.5	1.4±0.6	1.3±0.6	1.7±0.7	HydA	15.5°	3.4
J0914+1012	09h14m44s	+10°12′27″	5.5±2.1	6.6±2.8	3.0±3.7	···	HydA	22.3°	3.7
J0915−1458	09h15m00s	−14°58′54″	0.6±0.3	1.1±0.5	0.6±0.4	0.4±0.2	HydA	3.0°	3.7
J0915+0713	09h15m03s	+07°13′24″	2.8±1.0	3.2±1.3	3.8±2.7	···	HydA	19.3°	3.6
J0915+0227	09h15m05s	+02°27′48″	1.9±0.7	2.0±0.9	2.2±1.0	2.4±1.0	HydA	14.6°	4.6
J0915−2311	09h15m17s	−23°11′17″	0.8±0.3	0.6±0.4	···	0.8±0.4	HydA	11.1°	3.8
J0915−2038	09h15m42s	−20°38′30″	1.1±0.4	···	1.7±0.7	1.5±0.6	HydA	8.6°	4.5
J0916−0015	09h16m38s	−00°15′45″	1.5±0.6	2.6±1.2	1.3±0.9	···	EOR2	18.5°	3.2
J0916−1406	09h16m58s	−14°06′04″	0.9±0.3	···	0.8±0.4	0.8±0.3	HydA	2.1°	4.0
J0916−0938	09h16m60s	−09°38′36″	1.0±0.4	1.4±0.7	···	0.5±0.3	EOR2	15.5°	3.1
J0917−1858	09h17m08s	−18°58′45″	0.6±0.2	0.6±0.3	0.2±0.3	0.7±0.3	HydA	6.9°	3.4
J0917−2130	09h17m25s	−21°30′06″	1.3±0.4	0.3±0.5	···	1.6±0.6	HydA	9.4°	5.0
J0917−0838	09h17m29s	−08°38′08″	1.0±0.4	3.1±1.2	0.7±0.4	0.7±0.4	HydA	3.4°	4.4
J0917−1633	09h17m29s	−16°33′28″	0.6±0.3	···	0.6±0.4	0.5±0.2	HydA	4.5°	4.1
J0917−3012	09h17m59s	−30°12′12″	1.8±0.7	2.2±0.9	1.1±0.9	0.6±1.3	HydA	18.1°	3.2
J0918−1301	09h18m04s	−13°01′08″	1.1±0.4	···	1.4±0.6	0.9±0.4	HydA	0.9°	4.1
J0918−3050	09h18m15s	−30°50′37″	2.7±0.9	3.5±1.4	1.1±1.0	2.0±2.3	HydA	18.8°	4.5
J0918−0201	09h18m32s	−02°01′36″	1.0±0.4	2.1±0.9	0.6±0.6	0.8±0.4	HydA	10.0°	3.1
J0918+1114	09h18m34s	+11°14′45″	5.4±2.2	6.1±2.8	7.8±6.9	···	HydA	23.3°	3.0
J0918+1226	09h18m48s	+12°26′31″	5.7±2.3	6.5±2.9	···	···	HydA	24.5°	3.3
J0919−2037	09h19m33s	−20°37′03″	0.8±0.3	0.3±0.4	0.6±0.4	0.8±0.4	HydA	8.6°	3.6
J0919+0220	09h19m35s	+02°20′05″	1.5±0.6	2.4±1.0	0.9±0.8	0.6±0.5	HydA	14.4°	3.5
J0919−0929	09h19m37s	−09°29′45″	0.8±0.3	0.8±0.5	0.8±0.4	0.6±0.3	HydA	2.6°	3.2
J0919−1846	09h19m51s	−18°46′52″	0.8±0.3	1.3±0.5	···	0.8±0.3	HydA	6.7°	4.6
J0920+0136	09h20m40s	+01°36′42″	1.4±0.6	1.6±0.8	1.3±1.0	2.0±1.7	EOR2	18.8°	3.3

Continued on Next Page...

Table A.2 – Continued

Name	RA	DEC	$S_{\rm avg}$	$S_{123.52}$	$S_{154.24}$	$S_{184.96}$	Field	$r_{\rm FC}$	SNR
J0920+0028	09h20m53s	+00°28′38″	1.4±0.6	···	1.6±0.9	1.9±0.8	HydA	12.6°	3.3
J0921+0913	09h21m07s	+09°13′07″	5.0±2.0	5.1±2.3	11.4±7.3	···	HydA	21.3°	3.4
J0921−2615	09h21m09s	−26°15′33″	1.0±0.4	1.2±0.6	···	1.0±0.5	HydA	14.2°	3.2
J0921−2010	09h21m24s	−20°10′19″	0.6±0.3	0.8±0.4	1.0±0.4	0.3±0.2	HydA	8.1°	3.1
J0921−1116	09h21m35s	−11°16′53″	0.7±0.3	···	1.2±0.5	0.4±0.2	HydA	1.2°	3.3
J0921−2358	09h21m40s	−23°58′10″	1.1±0.4	1.6±0.7	0.5±0.6	1.9±1.6	EOR2	19.7°	3.1
J0921−3606	09h21m52s	−36°06′48″	5.7±2.0	6.5±2.6	10.9±7.8	6.5±6.0	HydA	24.1°	4.5
J0921−1725	09h21m56s	−17°25′46″	0.8±0.3	0.6±0.3	0.7±0.4	0.8±0.3	HydA	5.4°	4.3
J0922−0643	09h22m10s	−06°43′15″	1.0±0.4	···	1.3±0.5	0.7±0.5	EOR2	14.7°	3.2
J0922−2500	09h22m48s	−25°00′39″	1.4±0.5	1.6±0.7	···	···	EOR2	20.3°	3.7
J0922−1640	09h22m50s	−16°40′08″	0.5±0.2	0.7±0.4	0.8±0.4	0.4±0.2	HydA	4.7°	3.1
J0923−0806	09h23m21s	−08°06′32″	0.9±0.3	1.1±0.5	0.9±0.4	0.8±0.3	HydA	4.2°	4.7
J0923−2604	09h23m33s	−26°04′55″	1.6±0.6	1.9±0.8	1.8±1.2	0.5±0.8	EOR2	20.9°	3.9
J0923−2835	09h23m55s	−28°35′29″	1.6±0.6	···	1.7±0.7	1.3±0.8	HydA	16.6°	3.5
J0923−2531	09h23m59s	−25°31′33″	1.0±0.4	1.1±0.5	1.1±0.6	0.9±0.5	HydA	13.5°	3.1
J0924−2202	09h24m07s	−22°02′59″	0.8±0.3	1.4±0.6	1.1±0.5	0.8±0.3	HydA	10.1°	3.3
J0925−1425	09h25m17s	−14°25′15″	0.7±0.3	0.9±0.4	0.7±0.3	0.6±0.3	HydA	2.9°	4.1
J0925−2043	09h25m18s	−20°43′06″	0.9±0.3	0.8±0.5	1.0±0.4	0.7±0.3	HydA	8.8°	3.9
J0925+0023	09h25m20s	+00°23′34″	1.1±0.4	1.4±0.7	1.2±0.5	0.6±0.5	EOR2	17.1°	3.3
J0925−0828	09h25m40s	−08°28′56″	0.8±0.3	0.7±0.4	···	0.7±0.3	HydA	4.0°	4.6
J0926−1129	09h26m03s	−11°29′33″	0.9±0.3	1.9±0.8	0.5±0.3	0.8±0.3	HydA	2.0°	4.9
J0926−2321	09h26m19s	−23°21′44″	1.0±0.4	0.9±0.5	1.0±0.5	1.1±0.4	HydA	11.5°	3.9
J0926−2207	09h26m27s	−22°07′05″	0.6±0.2	···	0.6±0.3	0.4±0.2	HydA	10.2°	3.0
J0926−2529	09h26m42s	−25°29′03″	1.2±0.4	1.3±0.6	1.4±0.6	1.0±0.5	HydA	13.6°	3.5
J0927−0554	09h27m33s	−05°54′25″	0.9±0.3	0.6±0.4	0.9±0.4	0.8±0.3	HydA	6.6°	4.4
J0927−1122	09h27m36s	−11°22′02″	0.9±0.3	···	0.9±0.4	0.8±0.3	HydA	2.4°	4.7
J0927−1423	09h27m37s	−14°23′59″	0.5±0.2	0.4±0.3	0.7±0.3	0.4±0.2	HydA	3.3°	3.6
J0928+0750	09h28m05s	+07°50′02″	2.7±1.1	3.3±1.5	1.9±1.7	8.8±7.5	EOR2	22.0°	3.6
J0928+0230	09h28m06s	+02°30′31″	1.8±0.7	2.3±1.1	2.0±1.0	1.0±0.6	HydA	14.8°	3.3
J0928−3454	09h28m10s	−34°54′23″	3.3±1.3	3.8±1.6	5.0±4.0	···	HydA	23.0°	3.4
J0928−1212	09h28m54s	−12°12′59″	0.6±0.2	0.3±0.3	0.3±0.3	0.6±0.2	HydA	2.6°	3.0
J0928−3008	09h28m55s	−30°08′15″	1.9±0.8	···	···	2.3±2.2	HydA	18.2°	3.6
J0929−1531	09h29m06s	−15°31′13″	0.8±0.3	1.7±0.7	···	0.8±0.3	HydA	4.4°	4.9
J0929+0115	09h29m11s	+01°15′55″	1.8±0.6	2.3±1.0	2.0±0.8	1.4±0.7	EOR2	16.9°	4.5
J0929+1133	09h29m20s	+11°33′39″	5.7±2.1	6.6±2.7	1.7±6.5	···	HydA	23.8°	3.1
J0929−1256	09h29m35s	−12°56′46″	0.7±0.3	1.5±0.6	0.3±0.2	0.7±0.3	HydA	2.9°	4.3
J0929−3534	09h29m44s	−35°34′16″	3.9±1.5	4.5±1.9	···	1.5±4.0	HydA	23.7°	3.2
J0929+0155	09h29m45s	+01°55′04″	2.1±0.8	2.7±1.3	2.3±1.0	0.8±0.6	HydA	14.3°	3.9
J0930+0529	09h30m01s	+05°29′34″	2.1±0.8	3.4±1.4	···	···	EOR2	19.9°	3.8
J0930−1501	09h30m09s	−15°01′01″	0.6±0.2	0.8±0.5	0.5±0.2	···	EOR2	13.2°	3.6
J0930−3134	09h30m22s	−31°34′48″	2.3±0.9	2.8±1.2	···	···	EOR2	24.5°	3.0

Continued on Next Page...

Table A.2 – Continued

Name	RA	DEC	$S_{\rm avg}$	$S_{123.52}$	$S_{154.24}$	$S_{184.96}$	Field	$r_{\rm FC}$	SNR
J0930−2206	09h30m53s	−22°06′06″	0.9±0.3	0.9±0.4	0.9±0.4	0.7±0.3	HydA	10.5°	4.0
J0931+0826	09h31m01s	+08°26′13″	3.4±1.3	4.0±1.8	4.0±2.7	···	EOR2	22.1°	3.1
J0931−0951	09h31m13s	−09°51′24″	0.7±0.2	0.9±0.5	0.6±0.3	0.4±0.2	EOR2	12.0°	3.8
J0931+0954	09h31m20s	+09°54′14″	5.4±2.0	6.4±2.7	···	23.4±22.5	HydA	22.2°	3.5
J0931−3434	09h31m36s	−34°34′18″	3.4±1.2	3.9±1.6	2.4±2.8	5.1±6.7	HydA	22.7°	4.1
J0931−0405	09h31m51s	−04°05′07″	1.4±0.5	0.9±0.5	1.5±0.6	1.3±0.5	HydA	8.7°	4.8
J0931−0244	09h31m55s	−02°44′58″	1.2±0.4	1.4±0.7	0.9±0.4	1.2±0.5	HydA	9.9°	3.9
J0932−1444	09h32m02s	−14°44′20″	0.6±0.2	1.7±0.7	0.2±0.2	···	HydA	4.3°	4.5
J0932−0838	09h32m25s	−08°38′00″	0.8±0.3	0.8±0.6	0.7±0.3	0.8±0.3	EOR2	11.8°	3.0
J0932−2139	09h32m42s	−21°39′24″	1.1±0.4	1.4±0.6	1.1±0.5	0.7±0.3	HydA	10.2°	4.5
J0932−1802	09h32m45s	−18°02′07″	1.1±0.4	1.1±0.6	1.1±0.5	0.8±0.3	HydA	6.9°	3.3
J0932−3002	09h32m55s	−30°02′16″	2.0±0.8	2.1±1.0	2.3±1.5	2.3±2.2	HydA	18.3°	3.4
J0933−1702	09h33m00s	−17°02′04″	1.1±0.4	···	···	1.1±0.4	HydA	6.1°	4.4
J0933−3032	09h33m35s	−30°32′27″	2.0±0.8	2.0±0.9	3.1±2.0	1.3±1.7	HydA	18.8°	3.1
J0933−2753	09h33m36s	−27°53′20″	2.0±0.7	2.1±0.9	2.1±0.9	1.7±0.8	HydA	16.2°	4.6
J0933−2325	09h33m44s	−23°25′53″	0.8±0.3	0.2±0.4	1.0±0.4	1.2±0.5	HydA	12.0°	3.9
J0934−1642	09h34m26s	−16°42′23″	0.6±0.2	0.5±0.5	0.6±0.3	0.7±0.3	EOR2	13.0°	3.4
J0934−0839	09h34m45s	−08°39′55″	0.9±0.3	1.1±0.6	1.0±0.5	0.6±0.3	HydA	5.3°	4.0
J0934−0026	09h34m59s	−00°26′07″	0.9±0.4	···	0.6±0.4	0.9±0.4	EOR2	14.7°	3.2
J0935+0838	09h35m23s	+08°38′51″	4.7±1.8	5.5±2.3	3.6±3.4	12.1±12.1	HydA	21.2°	3.2
J0935−0715	09h35m27s	−07°15′19″	0.8±0.3	0.8±0.6	1.1±0.4	0.8±0.3	EOR2	11.4°	3.1
J0935+0204	09h35m29s	+02°04′19″	4.4±1.5	4.8±1.8	4.6±1.8	3.9±1.5	HydA	14.8°	4.7
J0935−3233	09h35m46s	−32°33′08″	3.3±1.2	3.9±1.5	2.9±2.1	···	HydA	20.9°	4.4
J0935−1404	09h35m48s	−14°04′58″	0.7±0.3	1.2±0.5	···	0.7±0.3	HydA	4.8°	3.8
J0935−3126	09h35m53s	−31°26′24″	2.5±0.9	2.8±1.1	3.1±2.0	···	HydA	19.8°	4.3
J0936−0243	09h36m10s	−02°43′11″	0.9±0.4	0.8±0.5	0.8±0.4	1.0±0.4	HydA	10.4°	3.3
J0936−0420	09h36m11s	−04°20′45″	0.9±0.4	1.5±0.7	1.5±0.7	0.5±0.3	HydA	8.9°	3.2
J0936−0453	09h36m29s	−04°53′07″	0.9±0.3	1.6±0.8	1.0±0.4	0.4±0.2	EOR2	11.9°	3.8
J0936−2647	09h36m35s	−26°47′19″	1.1±0.4	1.6±0.7	0.9±0.5	0.8±0.5	HydA	15.4°	3.5
J0936−1107	09h36m51s	−11°07′49″	1.2±0.5	···	1.7±0.6	0.9±0.4	HydA	4.7°	4.3
J0936+0458	09h36m58s	+04°58′22″	2.7±1.0	2.9±1.3	3.9±1.9	1.7±1.4	HydA	17.7°	4.3
J0937−2616	09h37m02s	−26°16′06″	1.0±0.4	1.3±0.6	0.8±0.6	···	EOR2	19.2°	4.0
J0937−1542	09h37m17s	−15°42′46″	0.8±0.3	···	0.6±0.3	0.7±0.3	EOR2	11.9°	3.3
J0937−3640	09h37m20s	−36°40′32″	3.5±1.4	3.9±1.8	···	···	HydA	25.0°	3.5
J0937−0949	09h37m36s	−09°49′17″	0.8±0.3	···	···	1.1±0.4	HydA	5.3°	3.0
J0937−2434	09h37m39s	−24°34′08″	0.9±0.3	1.8±0.7	0.5±0.3	···	EOR2	17.7°	3.5
J0938−0837	09h38m01s	−08°37′59″	0.8±0.3	···	0.6±0.4	0.8±0.3	HydA	6.0°	3.3
J0938−2557	09h38m23s	−25°57′01″	1.0±0.4	1.5±0.7	0.7±0.4	1.1±0.5	HydA	14.7°	3.3
J0938−1926	09h38m44s	−19°26′51″	0.8±0.3	1.7±0.7	0.8±0.4	0.8±0.4	EOR2	13.8°	3.2
J0938−3238	09h38m52s	−32°38′08″	4.1±1.4	4.5±1.8	6.8±4.2	···	HydA	21.1°	5.0
J0938−1100	09h38m59s	−11°00′04″	1.0±0.4	···	0.6±0.4	1.0±0.4	HydA	5.2°	3.4

Continued on Next Page...

Table A.2 – Continued

Name	RA	DEC	$S_{\rm avg}$	$S_{123.52}$	$S_{154.24}$	$S_{184.96}$	Field	$r_{\rm FC}$	SNR
J0939+0200	09h39m28s	+02°00′32″	4.9±2.0	5.7±2.1	4.7±1.9	5.3±2.0	HydA	15.0°	3.3
J0939−0742	09h39m44s	−07°42′27″	0.7±0.3	0.5±0.4	0.6±0.3	1.3±0.5	EOR2	10.2°	3.1
J0939−2425	09h39m48s	−24°25′07″	0.9±0.4	1.3±0.6	0.7±0.4	0.6±0.4	EOR2	17.3°	3.5
J0940−0553	09h40m14s	−05°53′28″	0.9±0.4	0.4±0.5	1.4±0.6	0.7±0.3	HydA	8.2°	3.1
J0940−3312	09h40m30s	−33°12′53″	3.8±1.4	4.4±1.8	6.4±4.2	···	HydA	21.8°	4.3
J0940−2610	09h40m51s	−26°10′41″	1.3±0.5	1.3±0.6	1.9±0.8	1.3±0.6	HydA	15.1°	4.5
J0940−3110	09h40m55s	−31°10′37″	1.8±0.7	2.2±1.0	1.1±1.0	1.6±2.3	HydA	19.8°	3.4
J0941−0648	09h41m21s	−06°48′53″	0.7±0.3	···	1.0±0.4	0.2±0.2	EOR2	10.1°	3.7
J0941−1117	09h41m39s	−11°17′26″	0.8±0.4	···	1.2±0.5	0.7±0.3	EOR2	9.5°	3.7
J0941−2324	09h41m40s	−23°24′18″	1.3±0.5	1.3±0.6	2.0±0.8	1.2±0.5	HydA	12.6°	4.9
J0941−2742	09h41m45s	−27°42′06″	2.1±0.7	2.5±1.0	1.9±0.8	2.1±1.0	HydA	16.6°	5.0
J0941−0319	09h41m45s	−03°19′52″	1.1±0.4	1.5±0.7	0.9±0.4	0.9±0.4	EOR2	11.6°	4.0
J0942−1310	09h42m01s	−13°10′51″	0.7±0.3	0.9±0.5	0.5±0.3	0.6±0.3	EOR2	9.9°	3.6
J0942−0816	09h42m08s	−08°16′49″	0.7±0.3	1.9±0.7	0.7±0.3	0.8±0.3	EOR2	9.5°	3.5
J0942+0627	09h42m08s	+06°27′58″	2.6±0.9	3.1±1.3	2.7±1.8	1.5±1.6	EOR2	19.0°	4.4
J0942−1513	09h42m18s	−15°13′60″	1.0±0.4	0.9±0.5	0.7±0.3	1.0±0.4	HydA	6.7°	3.2
J0942−0323	09h42m26s	−03°23′18″	1.3±0.5	1.1±0.6	1.5±0.7	1.2±0.5	HydA	10.6°	4.5
J0942+0028	09h42m26s	+00°28′37″	1.4±0.6	1.7±0.9	1.8±0.7	···	EOR2	14.0°	3.1
J0942−2240	09h42m40s	−22°40′16″	0.6±0.3	0.4±0.3	0.8±0.5	1.1±0.4	HydA	12.1°	3.3
J0942−2937	09h42m54s	−29°37′29″	1.4±0.6	1.6±0.7	···	···	HydA	18.5°	3.3
J0943+0104	09h43m02s	+01°04′28″	1.8±0.7	2.7±1.2	1.6±0.7	0.9±0.6	EOR2	14.4°	4.4
J0943−0506	09h43m21s	−05°06′15″	0.8±0.4	0.8±0.5	0.7±0.5	0.7±0.3	HydA	9.3°	3.4
J0943+0551	09h43m32s	+05°51′46″	2.8±1.1	3.2±1.4	3.2±2.5	4.3±3.9	HydA	19.0°	3.2
J0943−1235	09h43m41s	−12°35′34″	1.3±0.5	···	1.0±0.5	1.2±0.5	HydA	6.3°	4.8
J0943−1924	09h43m43s	−19°24′48″	1.5±0.5	···	1.9±0.7	1.0±0.4	HydA	9.6°	5.0
J0943−2354	09h43m55s	−23°54′51″	1.4±0.5	1.8±0.8	1.5±0.6	1.0±0.4	HydA	13.3°	4.9
J0944−0258	09h44m22s	−02°58′39″	1.4±0.5	1.1±0.6	1.3±0.6	1.5±0.6	HydA	11.2°	4.2
J0944−3055	09h44m22s	−30°55′36″	2.4±0.9	2.9±1.2	2.1±1.5	···	HydA	19.8°	4.4
J0944−0930	09h44m48s	−09°30′12″	1.0±0.4	0.6±0.4	···	0.9±0.4	HydA	7.0°	4.0
J0944−1145	09h44m52s	−11°45′55″	1.1±0.4	1.1±0.6	0.7±0.4	1.0±0.4	HydA	6.6°	3.9
J0945+0855	09h45m02s	+08°55′45″	3.6±1.4	4.8±2.0	0.7±1.4	···	EOR2	20.8°	4.9
J0945−3016	09h45m05s	−30°16′45″	1.6±0.7	2.1±1.0	0.9±0.9	1.2±1.8	EOR2	21.9°	3.3
J0945−0702	09h45m56s	−07°02′50″	0.6±0.3	0.7±0.4	···	0.5±0.2	EOR2	8.9°	3.2
J0946−0418	09h46m15s	−04°18′60″	1.1±0.4	2.2±0.9	···	0.9±0.4	EOR2	10.1°	3.6
J0946−1051	09h46m26s	−10°51′12″	0.9±0.4	···	1.8±0.7	0.9±0.4	HydA	7.0°	3.6
J0947−0039	09h47m13s	−00°39′40″	1.4±0.6	···	0.7±0.6	2.7±1.1	HydA	13.5°	3.7
J0947+0422	09h47m17s	+04°22′48″	1.5±0.6	1.9±0.8	1.2±0.7	0.9±0.7	EOR2	16.5°	3.4
J0947−0447	09h47m36s	−04°47′59″	0.9±0.4	0.5±0.5	···	1.3±0.5	HydA	10.3°	3.3
J0948−0339	09h48m03s	−03°39′47″	1.1±0.4	1.6±0.7	0.9±0.4	0.6±0.3	EOR2	10.2°	4.6
J0948−2706	09h48m20s	−27°06′08″	1.2±0.5	1.4±0.6	1.1±0.7	···	HydA	16.6°	3.2
J0948−2355	09h48m29s	−23°55′55″	1.6±0.6	1.4±0.6	1.8±0.8	2.0±0.8	HydA	13.9°	4.6

Continued on Next Page...

Table A.2 – Continued

Name	RA	DEC	$S_{\rm avg}$	$S_{123.52}$	$S_{154.24}$	$S_{184.96}$	Field	$r_{\rm FC}$	SNR
J0949−1955	09h49m04s	−19°55′17″	1.5±0.5	···	1.3±0.5	1.6±0.6	HydA	10.8°	4.7
J0949−2545	09h49m32s	−25°45′33″	0.7±0.3	1.3±0.6	0.3±0.4	···	EOR2	17.4°	3.5
J0949−1532	09h49m32s	−15°32′41″	0.7±0.3	0.8±0.4	0.6±0.3	0.6±0.3	HydA	8.4°	3.4
J0949−0227	09h49m37s	−02°27′51″	1.1±0.4	2.9±1.1	1.3±0.6	···	HydA	12.4°	3.1
J0950−3344	09h50m27s	−33°44′38″	3.2±1.2	3.7±1.5	···	6.2±6.9	HydA	22.9°	3.5
J0950−2845	09h50m41s	−28°45′42″	1.3±0.5	1.6±0.7	0.8±0.7	0.8±1.1	EOR2	20.0°	3.1
J0950−1722	09h50m42s	−17°22′33″	0.6±0.2	1.0±0.4	0.5±0.2	0.6±0.3	EOR2	10.3°	3.9
J0950−2805	09h50m44s	−28°05′07″	1.2±0.4	1.4±0.7	1.0±0.7	1.2±1.2	EOR2	19.4°	3.5
J0950−2658	09h50m49s	−26°58′02″	1.0±0.4	0.9±0.5	2.2±1.4	1.9±1.6	EOR2	18.3°	3.1
J0950−1027	09h50m60s	−10°27′17″	0.7±0.3	0.4±0.3	0.8±0.3	0.8±0.3	EOR2	7.2°	3.5
J0951−1944	09h51m09s	−19°44′51″	0.9±0.4	0.3±0.4	0.8±0.4	1.4±0.5	HydA	11.1°	3.2
J0951−3031	09h51m21s	−30°31′48″	2.2±0.8	2.7±1.1	1.3±1.1	···	EOR2	21.6°	4.0
J0951−2126	09h51m30s	−21°26′23″	1.1±0.4	1.1±0.6	0.9±0.4	1.3±0.6	HydA	12.3°	3.4
J0952−1537	09h52m05s	−15°37′44″	0.8±0.3	1.8±0.7	···	0.6±0.2	EOR2	8.9°	4.3
J0952−0224	09h52m21s	−02°24′21″	0.8±0.3	1.5±0.6	0.4±0.3	0.7±0.3	EOR2	10.2°	4.2
J0952−1410	09h52m22s	−14°10′35″	0.6±0.2	0.6±0.4	0.7±0.3	0.3±0.2	EOR2	8.0°	3.6
J0952−0934	09h52m41s	−09°34′15″	0.5±0.2	···	0.4±0.2	0.5±0.2	EOR2	6.8°	3.2
J0952−3413	09h52m59s	−34°13′33″	2.6±1.1	3.0±1.4	2.3±3.0	5.8±6.7	HydA	23.5°	3.2
J0953−2445	09h53m23s	−24°45′48″	1.1±0.5	2.0±0.8	0.9±0.6	···	HydA	15.2°	3.2
J0954+0616	09h54m09s	+06°16′20″	1.7±0.7	1.7±0.9	3.6±1.4	0.8±0.8	EOR2	17.5°	3.2
J0954+0042	09h54m27s	+00°42′05″	1.7±0.6	···	1.5±0.6	1.0±0.5	EOR2	12.4°	4.1
J0954−0356	09h54m28s	−03°56′01″	0.4±0.2	0.6±0.3	0.5±0.3	···	EOR2	8.8°	3.5
J0954−0230	09h54m47s	−02°30′55″	0.9±0.3	0.6±0.4	0.8±0.3	1.2±0.5	EOR2	9.8°	4.3
J0954−3054	09h54m48s	−30°54′40″	3.5±1.3	4.0±1.7	3.7±2.4	3.2±3.2	HydA	20.7°	3.5
J0954−2422	09h54m55s	−24°22′34″	1.4±0.5	1.6±0.7	1.7±0.8	1.7±0.7	HydA	15.1°	3.9
J0955+0755	09h55m10s	+07°55′46″	2.7±1.0	3.5±1.4	1.1±1.1	1.7±1.9	EOR2	18.9°	4.7
J0955+0935	09h55m11s	+09°35′04″	2.8±1.1	3.7±1.6	0.4±1.2	···	EOR2	20.5°	4.1
J0955−0155	09h55m54s	−01°55′57″	0.6±0.3	···	0.3±0.3	0.7±0.3	EOR2	10.0°	3.1
J0956−1459	09h56m07s	−14°59′13″	0.6±0.2	0.9±0.4	0.8±0.3	0.3±0.2	EOR2	7.7°	4.8
J0956−1948	09h56m08s	−19°48′24″	0.5±0.2	0.7±0.4	0.5±0.2	0.4±0.2	EOR2	11.4°	3.3
J0956−1141	09h56m24s	−11°41′11″	0.4±0.2	···	0.5±0.2	0.6±0.2	EOR2	6.1°	3.3
J0956−1849	09h56m32s	−18°49′08″	0.4±0.2	1.3±0.5	···	0.6±0.3	EOR2	10.5°	3.3
J0956−1738	09h56m32s	−17°38′40″	0.4±0.2	0.4±0.3	0.6±0.2	0.2±0.1	EOR2	9.6°	3.8
J0956−0722	09h56m36s	−07°22′48″	0.6±0.2	1.0±0.5	0.5±0.2	0.4±0.2	EOR2	6.4°	4.3
J0957−0641	09h57m03s	−06°41′53″	0.7±0.3	···	···	0.6±0.3	EOR2	6.6°	4.5
J0957−1706	09h57m13s	−17°06′47″	0.5±0.2	0.6±0.3	0.4±0.2	0.4±0.2	EOR2	9.0°	3.8
J0957−2836	09h57m57s	−28°36′53″	2.9±1.0	3.1±1.3	4.8±3.0	3.3±2.8	HydA	19.0°	4.6
J0958−2935	09h58m04s	−29°35′07″	2.5±1.0	2.5±1.2	4.4±2.8	1.9±2.0	HydA	19.8°	3.3
J0958−3408	09h58m16s	−34°08′52″	2.5±1.1	2.8±1.3	···	···	HydA	23.9°	3.4
J0958+0543	09h58m23s	+05°43′58″	1.9±0.7	1.7±0.8	3.3±1.3	2.9±1.2	EOR2	16.6°	4.6
J0958−1448	09h58m27s	−14°48′28″	0.4±0.2	0.9±0.4	0.6±0.2	0.2±0.1	EOR2	7.2°	3.4

Continued on Next Page...

Table A.2 – Continued

Name	RA	DEC	$S_{\rm avg}$	$S_{123.52}$	$S_{154.24}$	$S_{184.96}$	Field	$r_{\rm FC}$	SNR
J0958−2208	09h58m29s	−22°08′35″	1.1±0.4	···	1.5±0.6	0.9±0.4	EOR2	13.2°	4.0
J0958−1101	09h58m34s	−11°01′38″	0.5±0.2	0.5±0.3	0.2±0.2	0.8±0.3	EOR2	5.4°	3.3
J0959−1728	09h59m03s	−17°28′48″	0.5±0.2	0.6±0.3	0.3±0.2	0.3±0.2	EOR2	9.1°	3.9
J0959−0236	09h59m08s	−02°36′36″	0.9±0.3	0.7±0.4	···	1.1±0.4	EOR2	9.0°	4.6
J0959−3011	09h59m17s	−30°11′41″	2.8±1.1	3.8±1.6	···	···	HydA	20.5°	3.1
J0959+0120	09h59m24s	+01°20′07″	1.1±0.4	1.2±0.6	1.2±0.5	1.3±0.5	EOR2	12.4°	4.2
J0959−2147	09h59m48s	−21°47′30″	1.2±0.4	1.4±0.7	1.4±0.5	1.0±0.4	EOR2	12.8°	4.4
J0959−2016	09h59m54s	−20°16′24″	0.5±0.2	1.0±0.5	0.3±0.2	0.2±0.2	EOR2	11.4°	3.4
J1000−3409	10h00m17s	−34°09′07″	2.4±1.0	2.9±1.3	···	3.7±4.6	EOR2	24.6°	3.8
J1001+1108	10h01m01s	+11°08′19″	4.0±1.4	4.9±1.9	1.8±1.7	4.5±5.5	EOR2	21.6°	4.6
J1001+0728	10h01m04s	+07°28′53″	1.5±0.6	1.9±0.8	0.9±0.9	1.3±1.5	EOR2	18.1°	3.1
J1001−2428	10h01m34s	−24°28′14″	1.0±0.4	···	0.7±0.3	···	EOR2	15.2°	4.2
J1001−3057	10h01m44s	−30°57′54″	3.5±1.3	4.2±1.7	1.8±1.6	4.6±4.4	HydA	21.4°	4.4
J1001−1831	10h01m53s	−18°31′21″	0.6±0.2	0.7±0.3	0.4±0.2	0.6±0.2	EOR2	9.6°	4.2
J1002−1207	10h02m11s	−12°07′13″	0.7±0.3	0.9±0.7	0.9±0.4	0.5±0.2	EOR2	4.9°	4.7
J1002−1913	10h02m11s	−19°13′53″	0.5±0.2	···	0.9±0.4	0.6±0.3	EOR2	10.2°	3.1
J1002−2732	10h02m19s	−27°32′32″	1.5±0.6	1.9±0.8	···	1.8±1.5	EOR2	18.1°	4.1
J1002−0907	10h02m25s	−09°07′58″	1.0±0.4	1.4±0.7	1.5±0.6	1.1±0.5	HydA	11.3°	3.1
J1002−0717	10h02m32s	−07°17′30″	0.6±0.3	···	0.7±0.3	0.6±0.3	EOR2	5.1°	3.9
J1002+0839	10h02m43s	+08°39′54″	2.3±0.8	3.0±1.2	2.0±1.5	···	EOR2	19.1°	4.5
J1002−2700	10h02m51s	−27°00′30″	1.2±0.5	1.4±0.7	1.5±0.6	0.8±0.5	EOR2	17.5°	3.4
J1003+0123	10h03m12s	+01°23′09″	1.2±0.4	1.4±0.6	0.8±0.4	1.3±0.5	EOR2	12.1°	3.8
J1003−1320	10h03m21s	−13°20′45″	0.6±0.2	···	···	0.4±0.2	EOR2	5.3°	3.4
J1003−1144	10h03m46s	−11°44′04″	0.8±0.3	···	1.3±0.5	0.6±0.3	EOR2	4.4°	4.7
J1004−0545	10h04m01s	−05°45′02″	1.4±0.5	2.8±1.1	0.7±0.5	0.9±0.5	HydA	13.0°	4.4
J1004−1049	10h04m10s	−10°49′53″	1.1±0.4	1.2±0.6	1.6±0.7	0.9±0.4	HydA	11.4°	4.0
J1004−0902	10h04m20s	−09°02′25″	0.9±0.3	···	0.7±0.3	1.0±0.4	EOR2	4.0°	3.4
J1004−0716	10h04m23s	−07°16′30″	1.0±0.4	0.6±0.4	1.3±0.6	1.0±0.5	HydA	12.4°	4.1
J1004+1017	10h04m26s	+10°17′24″	2.3±0.9	2.9±1.3	1.8±1.6	4.5±4.6	EOR2	20.6°	3.4
J1004−2143	10h04m55s	−21°43′10″	0.8±0.4	···	0.9±0.4	0.7±0.3	EOR2	12.3°	3.5
J1005−1523	10h05m16s	−15°23′23″	0.6±0.3	0.5±0.3	0.8±0.3	0.5±0.2	EOR2	6.5°	3.2
J1005−1719	10h05m27s	−17°19′27″	0.7±0.3	···	0.6±0.3	0.9±0.4	EOR2	8.2°	4.1
J1005−0135	10h05m58s	−01°35′60″	0.7±0.3	···	0.4±0.3	0.9±0.4	EOR2	9.1°	4.1
J1005−2220	10h05m59s	−22°20′03″	1.4±0.6	2.3±1.0	0.8±0.6	1.4±0.6	HydA	15.4°	3.0
J1006−2149	10h06m02s	−21°49′05″	0.8±0.3	0.6±0.5	···	···	EOR2	12.3°	4.6
J1006−2522	10h06m06s	−25°22′39″	1.5±0.5	1.6±0.7	1.7±0.8	1.3±0.8	HydA	17.5°	3.6
J1006−0246	10h06m09s	−02°46′22″	0.7±0.3	···	0.6±0.3	0.6±0.3	EOR2	8.0°	3.4
J1006−2913	10h06m28s	−29°13′13″	2.0±0.7	2.3±1.0	2.5±1.6	2.7±2.4	EOR2	19.5°	4.0
J1006−2003	10h06m29s	−20°03′52″	0.9±0.3	1.3±0.5	0.7±0.3	0.5±0.2	EOR2	10.6°	4.6
J1006−0620	10h06m44s	−06°20′22″	1.2±0.5	0.7±0.4	1.3±0.6	1.9±0.8	HydA	13.3°	3.8
J1006−0949	10h06m55s	−09°49′17″	1.2±0.5	1.9±0.8	0.5±0.6	0.9±0.5	HydA	12.2°	3.7

Continued on Next Page...

Table A.2 – Continued

Name	RA	DEC	$S_{\rm avg}$	$S_{123.52}$	$S_{154.24}$	$S_{184.96}$	Field	$r_{\rm FC}$	SNR
J1007−0642	10h07m23s	−06°42′01″	1.0±0.4	···	1.1±0.5	1.0±0.4	EOR2	4.5°	4.9
J1008+1201	10h08m11s	+12°01′07″	4.5±1.6	5.5±2.2	1.5±1.9	19.8±17.3	EOR2	22.2°	4.2
J1008+0031	10h08m16s	+00°31′41″	1.6±0.6	2.5±0.9	1.7±0.7	1.0±0.5	EOR2	10.9°	4.7
J1008−0427	10h08m39s	−04°27′41″	1.0±0.3	0.7±0.4	0.9±0.4	1.1±0.4	EOR2	6.2°	4.8
J1008+0811	10h08m48s	+08°11′58″	4.9±1.8	6.2±2.6	6.5±4.0	···	EOR2	18.4°	3.6
J1008−2458	10h08m48s	−24°58′12″	0.9±0.4	1.1±0.6	0.7±0.4	1.2±0.5	EOR2	15.2°	3.5
J1009−0625	10h09m15s	−06°25′18″	1.0±0.4	0.7±0.4	···	1.0±0.4	EOR2	4.4°	4.9
J1010−1503	10h10m01s	−15°03′27″	0.9±0.3	1.3±0.6	0.8±0.4	0.8±0.3	EOR2	5.6°	4.6
J1010−1708	10h10m07s	−17°08′13″	0.7±0.3	···	0.7±0.3	0.5±0.2	EOR2	7.6°	3.1
J1010−1236	10h10m12s	−12°36′51″	1.1±0.5	···	1.2±0.6	0.9±0.4	HydA	12.7°	3.1
J1010−0753	10h10m28s	−07°53′41″	1.2±0.5	···	1.3±0.5	1.2±0.5	EOR2	3.2°	4.9
J1010−2441	10h10m52s	−24°41′31″	1.7±0.6	2.2±0.9	0.4±0.6	2.6±1.2	HydA	17.8°	4.6
J1010−0427	10h10m59s	−04°27′15″	0.8±0.3	1.2±0.5	1.2±0.5	0.7±0.3	EOR2	6.0°	4.2
J1011−2523	10h11m19s	−25°23′10″	1.5±0.6	1.4±0.7	2.8±1.8	···	HydA	18.3°	3.4
J1011−0821	10h11m30s	−08°21′39″	0.8±0.3	1.1±0.6	0.7±0.4	0.8±0.3	EOR2	2.7°	3.8
J1011+0418	10h11m42s	+04°18′21″	1.7±0.7	2.8±1.2	···	1.1±0.7	EOR2	14.4°	3.8
J1011−3015	10h11m44s	−30°15′43″	1.4±0.6	1.7±0.8	0.9±0.8	3.3±3.3	EOR2	20.4°	3.3
J1011−1444	10h11m55s	−14°44′17″	1.0±0.3	1.6±0.7	0.9±0.4	0.7±0.3	EOR2	5.2°	5.0
J1011−0454	10h11m59s	−04°54′00″	0.8±0.3	0.8±0.4	1.0±0.4	0.5±0.2	EOR2	5.5°	4.8
J1012−3351	10h12m00s	−33°51′46″	3.4±1.3	4.1±1.7	5.6±3.8	13.4±11.5	EOR2	24.0°	4.1
J1012−1731	10h12m05s	−17°31′10″	1.3±0.5	···	1.5±0.7	1.5±0.6	HydA	14.1°	3.6
J1012−1758	10h12m18s	−17°58′24″	1.3±0.5	0.7±0.7	2.1±0.9	1.3±0.5	HydA	14.4°	3.4
J1012−2726	10h12m25s	−27°26′16″	2.5±0.9	···	2.1±0.9	···	EOR2	17.6°	4.3
J1012+0503	10h12m40s	+05°03′30″	1.9±0.8	3.1±1.4	0.7±0.7	0.8±0.6	EOR2	15.1°	3.1
J1012−1858	10h12m45s	−18°58′00″	0.8±0.3	0.3±0.4	1.2±0.4	0.6±0.3	EOR2	9.2°	4.3
J1013−2458	10h13m12s	−24°58′38″	1.6±0.6	1.7±0.8	···	3.1±2.6	HydA	18.3°	3.7
J1013−0930	10h13m28s	−09°30′42″	1.4±0.5	2.7±1.1	1.4±0.7	1.9±0.8	HydA	13.8°	3.6
J1013−3224	10h13m38s	−32°24′55″	3.6±1.3	4.2±1.7	3.7±2.5	···	EOR2	22.5°	4.9
J1013+1044	10h13m46s	+10°44′33″	2.9±1.2	3.5±1.6	2.6±1.9	···	EOR2	20.8°	4.1
J1014+0122	10h14m23s	+01°22′18″	1.2±0.5	1.7±0.8	1.7±0.7	···	EOR2	11.4°	3.6
J1014−1213	10h14m34s	−12°13′59″	1.1±0.4	0.8±0.6	1.3±0.6	1.4±0.6	HydA	13.8°	3.1
J1014−1725	10h14m45s	−17°25′60″	1.0±0.4	1.5±0.8	0.8±0.5	0.8±0.5	HydA	14.7°	3.2
J1014−0006	10h14m46s	−00°06′58″	0.7±0.3	···	0.7±0.4	0.9±0.4	EOR2	9.9°	3.4
J1014−2944	10h14m56s	−29°44′54″	2.2±0.8	2.7±1.1	1.5±1.0	···	EOR2	19.8°	4.9
J1015+0319	10h15m16s	+03°19′55″	1.6±0.6	···	1.8±0.8	1.7±0.7	EOR2	13.4°	3.6
J1015+1141	10h15m39s	+11°41′05″	3.2±1.3	···	1.7±1.7	4.9±6.9	EOR2	21.7°	3.2
J1015−0800	10h15m39s	−08°00′59″	0.9±0.3	0.7±0.5	0.8±0.4	0.8±0.3	EOR2	2.2°	3.9
J1015−0512	10h15m40s	−05°12′57″	0.5±0.2	0.5±0.3	0.5±0.2	0.4±0.2	EOR2	4.9°	3.6
J1015+0242	10h15m48s	+02°42′59″	4.0±1.5	5.1±2.1	1.0±1.6	···	HydA	20.6°	4.2
J1015−0817	10h15m54s	−08°17′35″	0.8±0.3	1.7±0.7	0.8±0.4	0.5±0.2	EOR2	2.0°	4.3
J1015−1949	10h15m55s	−19°49′52″	1.4±0.5	1.5±0.7	1.7±0.8	0.9±0.6	HydA	15.9°	4.3

Continued on Next Page...

Table A.2 – Continued

Name	RA	DEC	$S_{\rm avg}$	$S_{123.52}$	$S_{154.24}$	$S_{184.96}$	Field	$r_{\rm FC}$	SNR
J1016−2219	10h16m06s	−22°19′57″	0.9±0.3	···	0.8±0.4	0.9±0.4	EOR2	12.4°	3.4
J1016+0744	10h16m21s	+07°44′57″	6.0±2.4	6.5±2.9	9.0±6.2	···	HydA	24.5°	3.6
J1016−0621	10h16m28s	−06°21′35″	0.6±0.2	1.0±0.4	0.6±0.3	0.6±0.2	EOR2	3.7°	4.3
J1016−2731	10h16m31s	−27°31′56″	1.9±0.7	2.6±1.1	1.8±0.8	0.8±0.7	EOR2	17.6°	3.4
J1016+0943	10h16m39s	+09°43′04″	2.6±1.0	2.7±1.3	4.4±2.8	4.7±4.4	EOR2	19.7°	3.9
J1016+0450	10h16m40s	+04°50′46″	4.3±1.7	5.8±2.5	3.9±3.1	3.9±5.0	HydA	22.3°	3.1
J1016+0138	10h16m45s	+01°38′13″	1.2±0.5	0.7±0.6	···	2.0±0.7	EOR2	11.6°	4.1
J1016+0418	10h16m48s	+04°18′41″	2.0±0.8	5.3±2.1	1.4±0.7	···	EOR2	14.3°	3.3
J1017−1222	10h17m21s	−12°22′24″	0.5±0.2	1.7±0.7	···	0.3±0.2	EOR2	2.5°	3.4
J1017−1847	10h17m26s	−18°47′38″	0.6±0.2	1.6±0.7	0.5±0.2	0.5±0.2	EOR2	8.8°	3.2
J1017+0032	10h17m36s	+00°32′22″	1.0±0.4	1.1±0.6	0.9±0.4	0.9±0.4	EOR2	10.5°	4.1
J1017−0651	10h17m52s	−06°51′08″	0.6±0.2	0.4±0.3	0.7±0.3	0.6±0.2	EOR2	3.2°	4.7
J1018−0601	10h18m03s	−06°01′03″	0.5±0.2	0.1±0.2	0.6±0.3	0.6±0.2	EOR2	4.0°	3.7
J1018−0929	10h18m28s	−09°29′30″	0.6±0.3	···	0.6±0.3	···	EOR2	0.6°	3.2
J1018−1755	10h18m35s	−17°55′38″	0.6±0.3	0.6±0.4	···	0.6±0.3	EOR2	8.0°	4.4
J1019−0128	10h19m03s	−01°28′50″	0.6±0.3	0.8±0.6	0.7±0.3	0.6±0.3	EOR2	8.5°	3.3
J1019−0403	10h19m23s	−04°03′08″	0.6±0.2	0.8±0.4	0.8±0.3	0.5±0.2	EOR2	5.9°	3.5
J1019−0235	10h19m24s	−02°35′18″	0.7±0.3	0.2±0.3	0.7±0.3	0.7±0.3	EOR2	7.4°	4.1
J1019+0535	10h19m40s	+05°35′47″	2.0±0.7	2.7±1.2	1.3±0.7	1.6±0.8	EOR2	15.6°	4.3
J1019+1405	10h19m53s	+14°05′41″	3.7±1.5	4.4±1.9	···	···	EOR2	24.1°	3.1
J1020+1037	10h20m03s	+10°37′45″	2.7±1.0	3.7±1.5	1.2±1.4	4.9±4.9	EOR2	20.6°	4.0
J1020−3418	10h20m17s	−34°18′51″	3.4±1.3	4.1±1.8	1.9±3.0	4.9±4.9	EOR2	24.3°	3.6
J1020−2950	10h20m27s	−29°50′15″	1.4±0.6	1.9±0.9	1.1±0.9	3.1±3.1	EOR2	19.9°	3.2
J1020−1655	10h20m33s	−16°55′21″	0.5±0.2	···	0.7±0.3	0.5±0.2	EOR2	7.0°	3.3
J1020+0526	10h20m52s	+05°26′26″	4.5±1.8	5.7±2.6	1.6±2.6	···	HydA	23.4°	3.0
J1021+1133	10h21m08s	+11°33′05″	3.1±1.2	3.8±1.6	2.8±2.1	···	EOR2	21.5°	3.6
J1021−1556	10h21m14s	−15°56′19″	0.5±0.2	0.5±0.4	0.7±0.3	0.3±0.1	EOR2	6.0°	3.4
J1021−2401	10h21m31s	−24°01′19″	0.8±0.3	1.1±0.5	0.8±0.4	0.6±0.3	EOR2	14.1°	3.0
J1021+1303	10h21m34s	+13°03′55″	3.8±1.5	4.6±2.0	···	···	EOR2	23.0°	3.7
J1022−0725	10h22m00s	−07°25′45″	0.5±0.2	···	0.3±0.2	···	EOR2	2.6°	3.2
J1022+0014	10h22m38s	+00°14′47″	0.7±0.3	···	0.5±0.3	0.8±0.4	EOR2	10.2°	3.5
J1022−0415	10h22m47s	−04°15′35″	0.7±0.3	0.8±0.4	0.7±0.3	···	EOR2	5.7°	3.4
J1022−2032	10h22m50s	−20°32′05″	0.7±0.2	0.7±0.4	0.7±0.3	···	EOR2	10.6°	3.8
J1023−1712	10h23m10s	−17°12′23″	0.6±0.3	···	1.0±0.4	0.6±0.2	EOR2	7.3°	3.4
J1023−1126	10h23m11s	−11°26′01″	0.8±0.3	0.9±0.4	1.1±0.4	0.6±0.3	EOR2	1.7°	4.8
J1023+0237	10h23m12s	+02°37′04″	3.0±1.3	3.3±1.7	6.2±4.0	···	HydA	21.8°	3.8
J1023−2750	10h23m26s	−27°50′35″	1.4±0.5	1.9±0.8	1.0±0.5	1.1±0.8	EOR2	17.9°	3.7
J1023+0229	10h23m45s	+02°29′51″	0.8±0.3	···	0.6±0.4	0.6±0.4	EOR2	12.5°	4.2
J1024−0035	10h24m08s	−00°35′22″	0.9±0.3	0.4±0.5	0.8±0.4	1.1±0.4	EOR2	9.4°	3.2
J1024−0759	10h24m19s	−07°59′04″	0.5±0.2	···	···	0.4±0.2	EOR2	2.2°	3.1
J1024−3014	10h24m20s	−30°14′46″	2.5±0.9	3.0±1.2	2.0±1.4	1.6±2.6	EOR2	20.3°	4.7

Continued on Next Page...

Table A.2 – Continued

Name	RA	DEC	$S_{\rm avg}$	$S_{123.52}$	$S_{154.24}$	$S_{184.96}$	Field	$r_{\rm FC}$	SNR
J1024−3157	10h24m56s	−31°57′24″	2.6±1.0	3.0±1.4	2.1±1.6	13.3±11.8	EOR2	22.0°	3.3
J1025−2248	10h25m18s	−22°48′34″	1.0±0.4	1.2±0.5	1.3±0.5	0.6±0.3	EOR2	12.9°	4.4
J1025−1558	10h25m24s	−15°58′34″	0.7±0.3	0.7±0.4	0.7±0.3	0.7±0.3	EOR2	6.1°	4.1
J1025−0327	10h25m24s	−03°27′27″	0.7±0.3	1.1±0.5	0.5±0.3	0.5±0.3	EOR2	6.6°	3.4
J1025−0430	10h25m36s	−04°30′21″	0.7±0.3	···	0.9±0.4	0.3±0.2	EOR2	5.6°	3.3
J1025−2905	10h25m57s	−29°05′23″	2.0±0.7	2.6±1.0	0.9±0.7	2.4±2.3	EOR2	19.2°	4.4
J1026−1642	10h26m03s	−16°42′01″	1.0±0.3	···	1.1±0.4	1.0±0.4	EOR2	6.9°	4.2
J1026−2115	10h26m19s	−21°15′44″	0.6±0.2	···	0.6±0.3	0.6±0.3	EOR2	11.4°	3.3
J1026−1251	10h26m49s	−12°51′13″	0.6±0.2	···	0.7±0.3	0.7±0.3	EOR2	3.3°	3.7
J1026+1431	10h26m53s	+14°31′09″	4.0±1.7	4.8±2.2	···	···	EOR2	24.5°	3.0
J1026−0227	10h26m58s	−02°27′00″	0.8±0.3	1.6±0.6	0.7±0.3	0.7±0.4	EOR2	7.7°	3.9
J1026−1216	10h26m60s	−12°16′21″	0.5±0.2	···	0.9±0.3	0.5±0.2	EOR2	2.9°	3.6
J1027+0734	10h27m02s	+07°34′09″	2.1±0.8	2.2±1.0	3.1±1.4	1.3±1.0	EOR2	17.6°	3.7
J1027+1347	10h27m10s	+13°47′25″	3.9±1.5	4.7±2.0	···	···	EOR2	23.8°	3.3
J1027−3111	10h27m36s	−31°11′21″	2.7±1.0	3.3±1.3	1.6±1.2	6.5±6.3	EOR2	21.3°	4.2
J1027−1912	10h27m49s	−19°12′20″	1.1±0.4	1.0±0.5	1.1±0.4	0.9±0.3	EOR2	9.4°	4.5
J1028+0344	10h28m10s	+03°44′55″	1.3±0.5	1.5±0.7	1.1±0.6	1.5±0.7	EOR2	13.9°	3.7
J1028−1129	10h28m11s	−11°29′58″	0.8±0.3	0.5±0.4	0.8±0.4	0.6±0.3	EOR2	2.5°	3.4
J1028+1158	10h28m32s	+11°58′58″	3.6±1.3	4.4±1.8	3.0±2.5	···	EOR2	22.0°	4.1
J1029+0305	10h29m20s	+03°05′19″	1.2±0.4	2.0±0.9	0.8±0.4	···	EOR2	13.3°	3.3
J1029−3039	10h29m31s	−30°39′25″	2.4±0.9	2.9±1.2	0.8±0.9	···	EOR2	20.8°	4.7
J1029−0514	10h29m51s	−05°14′14″	1.0±0.4	1.5±0.7	0.9±0.4	0.6±0.3	EOR2	5.3°	4.5
J1030−3445	10h30m19s	−34°45′45″	5.0±1.8	5.4±2.3	10.8±7.6	9.4±7.8	EOR2	24.9°	3.7
J1030−0429	10h30m25s	−04°29′31″	0.8±0.3	···	0.6±0.3	0.8±0.3	EOR2	6.0°	4.0
J1030−1735	10h30m49s	−17°35′15″	1.0±0.4	1.3±0.5	1.1±0.5	0.7±0.3	EOR2	8.1°	3.6
J1031−0612	10h31m06s	−06°12′49″	1.1±0.4	···	···	1.0±0.4	EOR2	4.6°	4.9
J1031−3329	10h31m09s	−33°29′22″	4.2±1.5	5.0±2.0	1.8±2.5	4.2±4.7	EOR2	23.7°	4.2
J1031−1450	10h31m17s	−14°50′43″	0.7±0.3	···	···	0.7±0.3	EOR2	5.6°	3.6
J1032+0402	10h32m09s	+04°02′46″	1.5±0.5	1.9±0.9	1.6±0.7	1.0±0.6	EOR2	14.3°	4.3
J1032−2407	10h32m36s	−24°07′01″	1.2±0.5	1.0±0.7	1.4±0.6	1.5±0.6	EOR2	14.5°	3.0
J1033−2537	10h33m39s	−25°37′40″	1.6±0.6	1.7±0.8	1.8±0.7	1.2±0.6	EOR2	16.0°	3.7
J1034−0503	10h34m00s	−05°03′03″	0.7±0.3	···	0.6±0.3	0.6±0.3	EOR2	6.0°	3.5
J1034−2103	10h34m15s	−21°03′39″	0.8±0.3	2.8±1.1	0.9±0.4	0.6±0.3	EOR2	11.6°	3.7
J1034−1533	10h34m17s	−15°33′09″	0.7±0.3	1.6±0.7	1.5±0.6	0.7±0.3	EOR2	6.6°	3.4
J1034+1428	10h34m18s	+14°28′48″	4.7±1.9	5.5±2.4	···	···	EOR2	24.7°	3.5
J1034−2132	10h34m20s	−21°32′56″	1.0±0.4	0.6±0.6	···	0.9±0.4	EOR2	12.1°	3.5
J1034−1320	10h34m48s	−13°20′17″	0.6±0.2	···	···	0.8±0.3	EOR2	4.9°	3.8
J1034−1813	10h34m49s	−18°13′24″	1.2±0.5	1.1±0.6	2.0±0.7	0.9±0.4	EOR2	9.0°	3.4
J1035+0039	10h35m05s	+00°39′25″	0.8±0.3	0.9±0.5	1.5±0.6	0.9±0.4	EOR2	11.3°	3.3
J1035−2404	10h35m13s	−24°04′01″	1.3±0.5	1.3±0.7	1.5±0.6	1.1±0.5	EOR2	14.6°	3.3
J1035−0332	10h35m22s	−03°32′24″	0.8±0.3	2.0±0.8	···	0.8±0.3	EOR2	7.5°	3.4

Continued on Next Page...

Table A.2 – Continued

Name	RA	DEC	$S_{\rm avg}$	$S_{123.52}$	$S_{154.24}$	$S_{184.96}$	Field	$r_{\rm FC}$	SNR
J1035−1250	10h35m23s	−12°50′37″	0.9±0.3	···	1.0±0.4	0.8±0.3	EOR2	4.7°	4.8
J1035−1421	10h35m28s	−14°21′19″	0.6±0.2	0.5±0.3	0.7±0.3	0.5±0.2	EOR2	5.8°	3.3
J1035+0338	10h35m53s	+03°38′57″	1.5±0.5	1.3±0.7	1.2±0.6	2.7±1.0	EOR2	14.2°	4.0
J1036−1529	10h36m22s	−15°29′31″	0.9±0.3	···	1.2±0.5	1.0±0.4	EOR2	6.8°	3.7
J1036−0707	10h36m36s	−07°07′34″	0.7±0.3	2.1±0.8	0.7±0.4	0.7±0.3	EOR2	5.0°	3.7
J1036−1850	10h36m44s	−18°50′49″	2.7±1.0	3.2±1.3	4.5±2.9	···	HydA	20.1°	3.1
J1036−3344	10h36m47s	−33°44′55″	3.4±1.3	4.0±1.7	5.7±4.5	···	EOR2	24.1°	4.1
J1036−2937	10h36m53s	−29°37′59″	2.5±0.9	3.0±1.2	1.9±1.3	···	EOR2	20.1°	4.6
J1036−3112	10h36m60s	−31°12′16″	1.9±0.7	2.3±1.0	···	···	EOR2	21.6°	3.1
J1037−2649	10h37m01s	−26°49′06″	1.6±0.6	2.2±0.9	1.2±0.5	1.1±0.6	EOR2	17.3°	4.3
J1037−2559	10h37m04s	−25°59′04″	1.5±0.6	1.9±0.8	1.3±0.6	0.6±0.5	EOR2	16.5°	4.4
J1037−1858	10h37m13s	−18°58′54″	1.1±0.5	1.0±0.6	2.0±0.8	0.6±0.3	EOR2	9.9°	3.5
J1037−1702	10h37m41s	−17°02′19″	1.1±0.4	1.3±0.6	1.1±0.5	1.0±0.4	EOR2	8.3°	4.1
J1037−1925	10h37m52s	−19°25′42″	1.3±0.5	···	2.0±0.8	0.9±0.4	EOR2	10.4°	4.0
J1037−0314	10h37m54s	−03°14′06″	0.9±0.4	1.1±0.6	0.9±0.4	0.7±0.3	EOR2	8.0°	4.4
J1037−3150	10h37m57s	−31°50′04″	2.0±0.8	2.4±1.0	1.3±1.3	5.0±5.8	EOR2	22.3°	3.8
J1038−1549	10h38m03s	−15°49′34″	0.7±0.3	···	1.2±0.5	0.9±0.3	EOR2	7.3°	4.3
J1038−2502	10h38m48s	−25°02′35″	1.6±0.6	2.3±0.9	0.9±0.5	1.0±0.5	EOR2	15.7°	4.4
J1038−2150	10h38m56s	−21°50′47″	1.3±0.5	···	···	1.0±0.4	EOR2	12.7°	4.6
J1038+0435	10h38m58s	+04°35′24″	1.6±0.6	1.8±0.8	1.8±0.8	2.1±0.9	EOR2	15.3°	3.8
J1039−2008	10h39m28s	−20°08′31″	0.9±0.4	0.4±0.6	0.9±0.5	1.1±0.4	EOR2	11.2°	3.6
J1039−1536	10h39m40s	−15°36′60″	0.8±0.3	1.4±0.6	···	0.9±0.3	EOR2	7.4°	4.2
J1040−0634	10h40m09s	−06°34′41″	0.9±0.4	1.0±0.5	0.6±0.4	0.9±0.4	EOR2	6.0°	3.4
J1040−2223	10h40m18s	−22°23′26″	1.3±0.5	1.4±0.7	1.7±0.7	···	EOR2	13.3°	3.7
J1040+0626	10h40m19s	+06°26′13″	2.2±0.8	3.1±1.3	···	2.2±1.0	EOR2	17.2°	3.9
J1040−2915	10h40m37s	−29°15′55″	2.5±0.9	3.0±1.3	2.6±1.7	···	EOR2	19.9°	4.3
J1040−1442	10h40m37s	−14°42′06″	0.7±0.3	···	0.5±0.4	0.8±0.3	EOR2	6.9°	3.1
J1041−1139	10h41m16s	−11°39′44″	0.6±0.3	···	1.4±0.5	0.6±0.2	EOR2	5.5°	3.6
J1041−3020	10h41m48s	−30°20′50″	1.8±0.7	2.2±1.0	1.5±1.3	2.4±2.7	EOR2	21.0°	3.2
J1041−2725	10h41m52s	−27°25′56″	1.1±0.4	1.3±0.6	1.0±0.7	···	EOR2	18.2°	3.4
J1042−0741	10h42m00s	−07°41′17″	0.8±0.3	···	0.9±0.4	0.7±0.3	EOR2	5.9°	4.3
J1042+0604	10h42m17s	+06°04′22″	1.9±0.8	2.4±1.1	1.9±1.0	1.2±0.8	EOR2	17.0°	3.0
J1042−1413	10h42m25s	−14°13′13″	0.9±0.3	···	0.7±0.4	1.0±0.4	EOR2	6.9°	5.0
J1042−0128	10h42m37s	−01°28′39″	3.6±1.5	4.3±1.9	···	7.4±9.3	HydA	23.5°	3.0
J1042−3222	10h42m47s	−32°22′42″	2.1±0.8	2.6±1.1	···	···	EOR2	23.0°	3.8
J1043−1436	10h43m04s	−14°36′48″	0.7±0.3	0.4±0.5	0.4±0.3	0.7±0.3	EOR2	7.3°	3.8
J1043−0020	10h43m11s	−00°20′43″	1.0±0.4	1.3±0.6	0.6±0.4	1.2±0.5	EOR2	11.2°	5.0
J1043−0520	10h43m15s	−05°20′37″	0.6±0.3	0.5±0.5	1.6±0.6	0.4±0.2	EOR2	7.4°	3.3
J1043−1716	10h43m28s	−17°16′23″	1.0±0.4	···	1.8±0.7	0.6±0.3	EOR2	9.3°	3.7
J1043−2533	10h43m32s	−25°33′03″	1.2±0.5	1.6±0.7	1.1±0.5	0.7±0.5	EOR2	16.6°	4.3
J1043−2334	10h43m39s	−23°34′07″	2.9±1.2	3.3±1.5	1.9±2.4	2.6±4.7	HydA	23.3°	4.9

Continued on Next Page...

Table A.2 – Continued

Name	RA	DEC	$S_{\rm avg}$	$S_{123.52}$	$S_{154.24}$	$S_{184.96}$	Field	$r_{\rm FC}$	SNR
J1043−0934	10h43m43s	−09°34′29″	0.6±0.3	2.4±0.9	···	0.4±0.2	EOR2	5.8°	3.2
J1043−2212	10h43m57s	−22°12′07″	0.9±0.4	···	1.8±0.7	0.9±0.4	EOR2	13.5°	3.3
J1044−0112	10h44m32s	−01°12′17″	0.9±0.3	0.8±0.5	0.9±0.4	1.0±0.4	EOR2	10.7°	3.7
J1044−3013	10h44m33s	−30°13′19″	2.0±0.7	2.5±1.0	4.3±2.8	2.4±2.6	EOR2	21.0°	4.5
J1044−0245	10h44m35s	−02°45′56″	1.2±0.4	1.4±0.7	1.1±0.5	0.9±0.4	EOR2	9.4°	4.5
J1044−1914	10h44m46s	−19°14′29″	1.0±0.4	1.0±0.5	1.8±0.7	1.0±0.4	EOR2	11.0°	4.4
J1045+0106	10h45m25s	+01°06′57″	1.1±0.5	1.0±0.6	1.2±0.5	1.3±0.5	EOR2	12.7°	3.2
J1046−0459	10h46m09s	−04°59′23″	0.7±0.3	0.8±0.5	0.7±0.3	0.6±0.3	EOR2	8.1°	3.3
J1046−2002	10h46m16s	−20°02′13″	1.2±0.4	1.2±0.6	1.3±0.5	1.1±0.4	EOR2	11.9°	4.7
J1046−2539	10h46m36s	−25°39′35″	1.3±0.5	1.8±0.8	0.7±0.4	1.5±0.7	EOR2	16.9°	3.7
J1047−1708	10h47m13s	−17°08′40″	3.0±1.2	3.4±1.5	5.8±4.0	7.4±6.8	HydA	22.1°	3.2
J1047−1657	10h47m24s	−16°57′09″	1.0±0.4	0.6±0.4	1.0±0.4	1.1±0.4	EOR2	9.6°	4.7
J1047−0631	10h47m26s	−06°31′30″	1.0±0.4	1.6±0.7	0.9±0.4	0.7±0.3	EOR2	7.6°	4.8
J1048−2457	10h48m46s	−24°57′59″	1.4±0.5	0.9±0.6	1.6±0.7	1.5±0.6	EOR2	16.5°	3.6
J1049−2807	10h49m22s	−28°07′23″	1.5±0.6	1.7±0.8	2.0±1.3	···	EOR2	19.4°	3.2
J1049−0941	10h49m24s	−09°41′41″	1.0±0.4	···	0.9±0.4	0.9±0.3	EOR2	7.2°	3.7
J1049−2528	10h49m29s	−25°28′26″	1.2±0.5	1.1±0.6	1.9±0.8	1.9±0.8	EOR2	17.0°	3.7
J1049−1216	10h49m53s	−12°16′07″	2.9±1.1	3.3±1.4	3.8±3.4	8.9±8.7	HydA	22.4°	3.4
J1049−0438	10h49m56s	−04°38′41″	0.9±0.3	0.9±0.6	0.7±0.4	0.9±0.4	EOR2	9.1°	4.7
J1049−1857	10h49m57s	−18°57′15″	1.1±0.4	0.7±0.6	1.3±0.6	1.0±0.4	EOR2	11.5°	3.7
J1050−1030	10h50m06s	−10°30′10″	1.2±0.4	4.2±1.6	···	1.0±0.4	EOR2	7.4°	4.4
J1050−0041	10h50m08s	−00°41′33″	1.3±0.5	1.8±0.8	1.3±0.6	1.4±0.6	EOR2	11.9°	4.1
J1050−0629	10h50m17s	−06°29′41″	0.6±0.3	1.9±0.8	···	0.6±0.3	EOR2	8.2°	3.1
J1050−2151	10h50m41s	−21°51′28″	0.9±0.3	1.1±0.5	1.1±0.5	0.5±0.3	EOR2	14.0°	4.1
J1050−0659	10h50m48s	−06°59′09″	0.7±0.3	2.5±1.0	···	0.6±0.3	EOR2	8.2°	3.9
J1050−2049	10h50m49s	−20°49′51″	1.1±0.4	1.2±0.6	1.6±0.6	0.9±0.4	EOR2	13.1°	4.7
J1050−0250	10h50m50s	−02°50′10″	1.0±0.4	2.3±1.0	0.5±0.4	0.7±0.3	EOR2	10.4°	4.0
J1051−2340	10h51m43s	−23°40′25″	1.2±0.4	1.5±0.7	1.3±0.5	0.7±0.4	EOR2	15.7°	4.2
J1051−0346	10h51m58s	−03°46′30″	1.0±0.4	0.7±0.7	1.1±0.5	1.0±0.4	EOR2	10.0°	4.0
J1052+0345	10h52m18s	+03°45′28″	1.6±0.6	···	···	···	EOR2	15.9°	3.1
J1052−0709	10h52m29s	−07°09′20″	0.8±0.3	0.4±0.4	0.8±0.3	0.6±0.3	EOR2	8.5°	3.8
J1052−2439	10h52m30s	−24°39′33″	1.4±0.5	···	1.4±0.6	1.0±0.5	EOR2	16.6°	4.1
J1052−1452	10h52m43s	−14°52′55″	1.0±0.3	1.2±0.6	1.2±0.5	0.7±0.3	EOR2	9.4°	4.7
J1052+0802	10h52m51s	+08°02′38″	3.5±1.4	4.5±1.9	2.4±1.6	···	EOR2	19.8°	3.3
J1053−1138	10h53m36s	−11°38′07″	0.8±0.3	···	0.8±0.3	0.9±0.3	EOR2	8.4°	3.8
J1053−1516	10h53m52s	−15°16′27″	0.7±0.3	0.5±0.4	0.9±0.4	0.6±0.3	EOR2	9.8°	3.1
J1053+0229	10h53m58s	+02°29′44″	1.5±0.6	2.0±0.9	2.0±0.8	0.4±0.5	EOR2	15.0°	4.1
J1054−0205	10h54m13s	−02°05′11″	1.0±0.4	1.0±0.5	1.4±0.6	1.0±0.4	EOR2	11.6°	4.8
J1054−0530	10h54m43s	−05°30′44″	0.8±0.3	1.0±0.6	0.8±0.4	0.5±0.3	EOR2	9.7°	3.7
J1055−0734	10h55m02s	−07°34′46″	0.8±0.3	···	1.4±0.5	0.5±0.2	EOR2	9.0°	3.7
J1055−2200	10h55m16s	−22°00′53″	0.8±0.3	0.9±0.4	1.0±0.4	0.3±0.2	EOR2	14.7°	3.2

Continued on Next Page...

Table A.2 – Continued

Name	RA	DEC	$S_{\rm avg}$	$S_{123.52}$	$S_{154.24}$	$S_{184.96}$	Field	$r_{\rm FC}$	SNR
J1056−0451	10h56m21s	−04°51′27″	0.8±0.3	1.4±0.8	0.9±0.4	0.4±0.3	EOR2	10.3°	3.1
J1056−2540	10h56m23s	−25°40′01″	1.3±0.5	1.8±0.8	···	0.8±0.6	EOR2	17.9°	3.2
J1056−1530	10h56m41s	−15°30′04″	0.9±0.4	1.7±0.7	1.0±0.5	1.0±0.4	EOR2	10.5°	3.1
J1057+0014	10h57m20s	+00°14′23″	0.9±0.4	1.0±0.5	1.2±0.6	1.0±0.5	EOR2	13.8°	3.1
J1057−0929	10h57m33s	−09°29′24″	0.6±0.3	0.6±0.4	0.5±0.3	0.6±0.3	EOR2	9.2°	3.2
J1057−2512	10h57m43s	−25°12′38″	1.5±0.6	2.3±0.9	0.3±0.4	0.6±0.5	EOR2	17.7°	4.0
J1057−0601	10h57m56s	−06°01′00″	0.8±0.3	0.7±0.5	1.7±0.7	0.4±0.2	EOR2	10.2°	3.7
J1058−1625	10h58m15s	−16°25′27″	0.9±0.4	···	1.0±0.5	1.1±0.4	EOR2	11.3°	3.3
J1058−1933	10h58m25s	−19°33′32″	1.4±0.5	1.6±0.7	1.3±0.6	1.5±0.6	EOR2	13.3°	4.6
J1058−2731	10h58m36s	−27°31′06″	2.2±0.9	3.8±1.5	0.8±0.7	1.9±1.7	EOR2	19.8°	3.3
J1059−0900	10h59m16s	−09°00′11″	0.9±0.3	1.9±0.8	0.8±0.4	0.7±0.3	EOR2	9.7°	3.3
J1059−0443	10h59m23s	−04°43′25″	0.9±0.4	1.4±0.7	1.1±0.5	0.5±0.3	EOR2	11.1°	3.2
J1059−1711	10h59m43s	−17°11′22″	1.0±0.4	1.2±0.6	1.0±0.5	0.8±0.3	EOR2	12.0°	3.6
J1100−2056	11h00m06s	−20°56′52″	1.1±0.4	1.7±0.7	0.8±0.5	0.7±0.3	EOR2	14.6°	3.6
J1100−1013	11h00m07s	−10°13′13″	1.0±0.4	1.0±0.5	0.9±0.4	1.0±0.4	EOR2	9.9°	4.6
J1100+0444	11h00m23s	+04°44′35″	2.4±0.9	3.1±1.4	2.7±1.1	2.0±0.9	EOR2	17.8°	4.7
J1100−0123	11h00m24s	−01°23′15″	1.3±0.5	1.3±0.7	1.7±0.7	0.9±0.5	EOR2	13.2°	3.1
J1100−0744	11h00m27s	−07°44′41″	0.9±0.3	0.8±0.5	0.7±0.4	0.8±0.4	EOR2	10.2°	3.5
J1100−1919	11h00m47s	−19°19′25″	1.5±0.5	2.0±0.8	1.4±0.6	0.9±0.4	EOR2	13.6°	4.5
J1101−2729	11h01m06s	−27°29′40″	2.3±0.9	···	3.8±2.4	···	EOR2	20.0°	4.5
J1101−0338	11h01m27s	−03°38′45″	1.4±0.5	1.9±0.7	1.0±0.5	1.0±0.4	EOR2	12.0°	4.2
J1101−2317	11h01m35s	−23°17′28″	1.0±0.4	1.2±0.6	2.2±0.9	0.7±0.4	EOR2	16.6°	3.2
J1101+0014	11h01m45s	+00°14′10″	1.4±0.5	1.8±0.8	0.8±0.6	0.7±0.4	EOR2	14.5°	3.2
J1101−3112	11h01m47s	−31°12′28″	4.4±1.6	5.2±2.1	6.8±4.4	1.0±2.9	EOR2	23.4°	4.1
J1101−3037	11h01m55s	−30°37′28″	3.3±1.4	4.0±1.8	3.3±2.3	2.6±3.3	EOR2	22.8°	3.2
J1101−0721	11h01m60s	−07°21′36″	1.0±0.4	1.7±0.7	1.0±0.5	0.8±0.3	EOR2	10.7°	3.6
J1102−2015	11h02m13s	−20°15′49″	1.3±0.5	2.2±0.9	0.8±0.5	0.8±0.4	EOR2	14.5°	4.1
J1102−0618	11h02m15s	−06°18′34″	1.0±0.4	1.6±0.7	1.3±0.6	0.5±0.3	EOR2	11.1°	4.0
J1102−1456	11h02m27s	−14°56′39″	1.4±0.5	1.2±0.7	1.5±0.6	1.1±0.4	EOR2	11.5°	4.3
J1102+0100	11h02m31s	+01°00′05″	1.1±0.5	2.9±1.1	2.5±1.0	0.9±0.5	EOR2	15.2°	3.3
J1102+0457	11h02m51s	+04°57′47″	2.1±0.8	1.7±1.1	3.7±2.3	1.7±1.5	EOR2	18.3°	3.2
J1103−1833	11h03m32s	−18°33′46″	1.3±0.5	1.6±0.7	0.8±0.4	1.4±0.5	EOR2	13.6°	4.4
J1103−1100	11h03m38s	−11°00′47″	1.0±0.4	1.5±0.7	0.8±0.4	0.7±0.3	EOR2	10.8°	3.3
J1104−2331	11h04m01s	−23°31′29″	1.0±0.4	1.6±0.7	0.3±0.4	1.0±0.5	EOR2	17.1°	3.8
J1104−2714	11h04m05s	−27°14′59″	2.0±0.7	2.2±0.9	3.4±2.1	1.0±1.2	EOR2	20.2°	3.6
J1104+1103	11h04m21s	+11°03′31″	5.4±2.0	6.5±2.7	4.3±3.3	···	EOR2	23.7°	3.4
J1104−1241	11h04m58s	−12°41′46″	1.0±0.4	···	···	1.3±0.5	EOR2	11.3°	3.9
J1105−1637	11h05m11s	−16°37′54″	1.3±0.5	1.1±0.6	1.6±0.6	1.2±0.5	EOR2	12.8°	3.7
J1105−2411	11h05m12s	−24°11′42″	1.4±0.6	1.5±0.8	2.1±0.9	2.3±0.9	EOR2	17.8°	3.1
J1105−1354	11h05m18s	−13°54′33″	1.1±0.4	···	0.9±0.4	1.2±0.5	EOR2	11.7°	3.8
J1105−2205	11h05m24s	−22°05′24″	1.8±0.6	2.6±1.0	2.0±0.8	1.0±0.5	EOR2	16.3°	4.9

Continued on Next Page...

Table A.2 – Continued

Name	RA	DEC	$S_{\rm avg}$	$S_{123.52}$	$S_{154.24}$	$S_{184.96}$	Field	$r_{\rm FC}$	SNR
J1105−1332	11h05m57s	−13°32′36″	0.9±0.4	···	0.8±0.4	1.6±0.6	EOR2	11.8°	4.3
J1106−2315	11h06m31s	−23°15′59″	1.5±0.6	2.1±0.9	1.3±0.6	1.6±0.7	EOR2	17.3°	3.8
J1106−1442	11h06m53s	−14°42′52″	1.1±0.4	1.9±0.8	0.7±0.4	1.2±0.5	EOR2	12.4°	3.9
J1107−0420	11h07m11s	−04°20′23″	1.5±0.5	2.0±0.9	1.3±0.6	1.2±0.5	EOR2	13.0°	4.5
J1107−1228	11h07m16s	−12°28′09″	0.9±0.4	1.2±0.6	1.2±0.5	0.6±0.3	EOR2	11.8°	3.1
J1107+0842	11h07m37s	+08°42′25″	3.7±1.4	4.7±1.9	2.5±1.9	1.9±2.1	EOR2	22.1°	3.8
J1108−1016	11h08m10s	−10°16′40″	1.5±0.5	2.0±0.8	1.6±0.7	1.1±0.5	EOR2	11.8°	4.2
J1108−2607	11h08m19s	−26°07′58″	2.4±0.9	2.8±1.1	3.7±2.3	1.3±1.3	EOR2	19.8°	4.9
J1108−1519	11h08m23s	−15°19′50″	1.4±0.5	1.7±0.7	1.6±0.6	1.0±0.4	EOR2	12.9°	4.4
J1108−1844	11h08m39s	−18°44′54″	1.5±0.5	3.4±1.3	0.7±0.4	0.7±0.4	EOR2	14.7°	4.2
J1108−0657	11h08m58s	−06°57′60″	1.2±0.5	2.3±0.9	2.2±0.8	0.6±0.4	EOR2	12.4°	3.6
J1109−0841	11h09m15s	−08°41′25″	1.1±0.4	1.2±0.6	1.3±0.6	0.9±0.4	EOR2	12.2°	3.9
J1109−0435	11h09m17s	−04°35′22″	1.3±0.5	1.5±0.8	1.3±0.6	1.1±0.5	EOR2	13.3°	3.3
J1109−1629	11h09m23s	−16°29′29″	1.2±0.4	1.9±0.8	0.6±0.4	0.9±0.4	EOR2	13.7°	3.8
J1109−0524	11h09m30s	−05°24′11″	1.9±0.7	2.1±1.0	2.1±0.8	1.7±0.7	EOR2	13.1°	4.7
J1110−1738	11h10m04s	−17°38′38″	1.3±0.5	1.3±0.7	2.1±0.8	1.1±0.5	EOR2	14.4°	3.7
J1110−2205	11h10m08s	−22°05′47″	2.3±0.8	2.7±1.1	2.6±1.0	1.5±0.7	EOR2	17.1°	4.4
J1110−1131	11h10m31s	−11°31′07″	0.9±0.4	···	1.7±0.6	0.4±0.3	EOR2	12.5°	3.8
J1110−2734	11h10m39s	−27°34′13″	1.6±0.7	1.9±0.9	2.6±1.7	···	EOR2	21.3°	3.4
J1111−1801	11h11m04s	−18°01′27″	1.5±0.5	0.7±0.8	2.6±1.0	1.7±0.7	EOR2	14.8°	5.0
J1111−0108	11h11m06s	−01°08′24″	1.4±0.6	2.2±1.0	1.3±0.7	0.5±0.4	EOR2	15.4°	3.1
J1111−2129	11h11m10s	−21°29′59″	1.9±0.7	1.6±0.9	2.6±1.0	1.7±0.8	EOR2	16.8°	3.6
J1111+0110	11h11m35s	+01°10′04″	1.9±0.7	2.0±1.0	3.4±1.3	0.5±0.5	EOR2	17.0°	4.9
J1111−2336	11h11m43s	−23°36′20″	2.1±0.8	3.1±1.2	···	0.8±0.8	EOR2	18.4°	4.2
J1112−2308	11h12m41s	−23°08′39″	2.1±0.7	2.4±1.0	2.3±1.5	2.0±1.7	EOR2	18.2°	4.9
J1112−1910	11h12m44s	−19°10′44″	1.3±0.5	1.6±1.1	1.4±0.6	1.0±0.5	EOR2	15.7°	3.7
J1112+1112	11h12m45s	+11°12′45″	4.9±1.9	6.3±2.7	···	···	EOR2	24.9°	3.8
J1112−1434	11h12m50s	−14°34′39″	0.9±0.4	1.3±0.6	1.1±0.5	0.2±0.2	EOR2	13.7°	3.8
J1113−1822	11h13m03s	−18°22′32″	1.4±0.5	···	1.5±0.6	1.6±0.6	EOR2	15.3°	3.9
J1113−1357	11h13m09s	−13°57′54″	1.2±0.4	1.6±0.7	1.0±0.5	0.7±0.3	EOR2	13.6°	4.2
J1113−0758	11h13m11s	−07°58′04″	1.2±0.4	1.2±0.6	1.1±0.5	1.2±0.5	EOR2	13.3°	3.9
J1113−1148	11h13m23s	−11°48′11″	1.3±0.5	0.8±0.5	2.1±0.8	1.0±0.4	EOR2	13.2°	4.2
J1114+1048	11h14m39s	+10°48′59″	4.3±1.7	5.1±2.2	3.8±2.8	8.5±7.5	EOR2	24.8°	3.2
J1114−2739	11h14m42s	−27°39′14″	2.4±0.9	2.5±1.1	3.5±2.2	2.0±2.0	EOR2	21.9°	3.3
J1115−1209	11h15m00s	−12°09′42″	1.2±0.5	1.1±0.6	1.4±0.6	1.0±0.4	EOR2	13.7°	4.4
J1115−0504	11h15m00s	−05°04′06″	1.6±0.6	2.0±0.9	2.0±0.8	1.5±0.6	EOR2	14.5°	4.0
J1115+0751	11h15m08s	+07°51′22″	2.8±1.2	3.1±1.5	3.5±2.4	3.2±3.0	EOR2	22.5°	3.2
J1115−0532	11h15m12s	−05°32′45″	1.8±0.6	1.7±0.8	2.1±0.9	2.1±0.8	EOR2	14.3°	4.9
J1115−1330	11h15m48s	−13°30′40″	0.8±0.3	1.1±0.5	0.8±0.4	0.4±0.3	EOR2	14.1°	3.1
J1116−0943	11h16m18s	−09°43′51″	1.3±0.5	1.5±0.7	1.5±0.6	1.2±0.5	EOR2	13.8°	3.7
J1116−0207	11h16m21s	−02°07′02″	1.4±0.6	1.4±0.9	2.0±0.9	1.2±0.6	EOR2	16.0°	3.1

Continued on Next Page...

Table A.2 – Continued

Name	RA	DEC	$S_{\rm avg}$	$S_{123.52}$	$S_{154.24}$	$S_{184.96}$	Field	$r_{\rm FC}$	SNR
J1116−3045	11h16m47s	−30°45′21″	4.1±1.5	4.9±2.0	···	···	EOR2	24.6°	4.0
J1116−2755	11h16m47s	−27°55′28″	2.6±0.9	3.2±1.3	1.6±1.3	···	EOR2	22.4°	4.0
J1116−1154	11h16m50s	−11°54′13″	1.2±0.5	1.8±0.8	0.8±0.4	1.0±0.4	EOR2	14.1°	3.6
J1116−0847	11h16m55s	−08°47′18″	1.5±0.5	···	1.3±0.6	1.2±0.5	EOR2	14.1°	4.5
J1117−0705	11h17m03s	−07°05′25″	1.2±0.5	···	0.3±0.4	0.9±0.4	EOR2	14.4°	3.0
J1117−1626	11h17m51s	−16°26′35″	1.0±0.4	1.2±0.6	1.5±0.6	0.9±0.4	EOR2	15.5°	3.1
J1118+0407	11h18m03s	+04°07′59″	2.5±0.9	2.9±1.3	2.5±1.7	···	EOR2	20.2°	3.5
J1118−2130	11h18m05s	−21°30′11″	1.7±0.7	2.1±1.0	1.8±1.2	1.0±1.0	EOR2	18.1°	3.4
J1118−2615	11h18m36s	−26°15′53″	2.4±0.9	3.0±1.2	2.0±1.4	···	EOR2	21.4°	3.3
J1118+0302	11h18m47s	+03°02′38″	1.7±0.7	2.1±1.0	2.5±1.7	2.6±2.2	EOR2	19.6°	3.3
J1119−0449	11h19m09s	−04°49′37″	1.2±0.5	1.9±0.8	0.4±0.4	···	EOR2	15.5°	3.1
J1119+0336	11h19m11s	+03°36′60″	2.0±0.8	2.5±1.1	2.7±1.8	2.4±2.1	EOR2	20.0°	3.6
J1119−1446	11h19m14s	−14°46′14″	1.1±0.4	1.5±0.7	0.7±0.4	0.5±0.3	EOR2	15.2°	4.3
J1119−3029	11h19m51s	−30°29′03″	4.9±1.7	5.7±2.3	11.7±7.4	···	EOR2	24.8°	4.9
J1119−2100	11h19m52s	−21°00′18″	1.7±0.6	2.1±0.9	1.8±1.2	0.9±0.9	EOR2	18.1°	3.7
J1119−2504	11h19m55s	−25°04′30″	2.5±0.9	3.0±1.2	···	···	EOR2	20.8°	4.7
J1120−2159	11h20m11s	−21°59′40″	2.2±0.8	2.8±1.1	2.1±1.4	1.6±1.4	EOR2	18.8°	4.1
J1120−1737	11h20m21s	−17°37′46″	1.0±0.4	2.9±1.2	1.2±0.5	1.1±0.5	EOR2	16.5°	3.3
J1121−0711	11h21m01s	−07°11′53″	1.3±0.5	1.9±0.8	1.1±0.5	1.0±0.5	EOR2	15.3°	3.3
J1122+0244	11h22m08s	+02°44′58″	1.7±0.7	2.3±1.1	1.6±1.3	1.7±1.6	EOR2	20.0°	3.3
J1122−0129	11h22m25s	−01°29′36″	1.2±0.5	3.1±1.2	0.3±0.5	1.9±0.8	EOR2	17.6°	3.4
J1122−1428	11h22m60s	−14°28′41″	2.1±0.7	2.9±1.2	1.7±0.7	1.9±0.7	EOR2	16.0°	5.0
J1123−2730	11h23m06s	−27°30′30″	2.6±1.0	3.3±1.4	1.0±1.2	2.2±2.4	EOR2	23.0°	3.9
J1123+0108	11h23m18s	+01°08′59″	1.7±0.6	2.1±0.9	1.3±1.1	2.4±2.0	EOR2	19.2°	3.3
J1123−2221	11h23m28s	−22°21′16″	2.1±0.8	2.5±1.0	1.9±1.3	2.9±2.4	EOR2	19.6°	3.5
J1123+0016	11h23m32s	+00°16′09″	1.9±0.7	2.3±0.9	2.1±1.4	1.5±1.4	EOR2	18.8°	4.2
J1123−0332	11h23m34s	−03°32′00″	1.2±0.5	1.6±0.7	1.0±0.6	1.8±0.8	EOR2	17.0°	3.6
J1124−1505	11h24m15s	−15°05′52″	2.2±0.8	3.3±1.3	1.3±0.6	1.6±0.7	EOR2	16.5°	3.8
J1124−2140	11h24m17s	−21°40′53″	1.8±0.7	2.1±0.9	1.9±1.3	1.1±1.1	EOR2	19.4°	3.6
J1124+0412	11h24m49s	+04°12′35″	2.6±1.0	3.4±1.4	1.9±1.7	···	EOR2	21.5°	3.7
J1124+0234	11h24m49s	+02°34′34″	2.3±0.9	2.7±1.3	2.3±1.9	1.5±1.6	EOR2	20.4°	3.1
J1125−1139	11h25m18s	−11°39′14″	2.3±0.8	2.9±1.2	2.3±0.9	1.4±0.6	EOR2	16.1°	4.6
J1125−1806	11h25m40s	−18°06′18″	1.8±0.6	2.4±1.0	1.8±0.8	0.4±0.5	EOR2	17.9°	4.0
J1126−0731	11h26m01s	−07°31′28″	2.5±0.9	2.4±1.0	3.2±1.2	3.2±1.2	EOR2	16.5°	4.8
J1126−2431	11h26m10s	−24°31′43″	1.7±0.7	2.1±1.0	1.4±1.1	···	EOR2	21.4°	3.1
J1126−1530	11h26m24s	−15°30′19″	2.6±1.0	3.5±1.4	2.3±1.0	1.6±0.7	EOR2	17.1°	3.9
J1127−1605	11h27m30s	−16°05′05″	2.0±0.8	2.7±1.1	2.1±1.0	0.8±0.5	EOR2	17.5°	3.2
J1127−0107	11h27m46s	−01°07′01″	1.8±0.7	2.2±1.0	1.9±1.3	···	EOR2	19.0°	3.3
J1128−1749	11h28m25s	−17°49′53″	2.1±0.8	1.7±0.8	3.5±2.2	2.8±2.3	EOR2	18.3°	4.2
J1128−2054	11h28m32s	−20°54′41″	2.0±0.7	2.6±1.0	2.3±1.5	···	EOR2	19.8°	4.3
J1128−1639	11h28m44s	−16°39′26″	1.8±0.7	1.7±0.9	···	2.6±1.0	EOR2	18.0°	3.3

Continued on Next Page...

Table A.2 – Continued

Name	RA	DEC	$S_{\rm avg}$	$S_{123.52}$	$S_{154.24}$	$S_{184.96}$	Field	$r_{\rm FC}$	SNR
J1128−2611	11h28m57s	−26°11′41″	2.8±1.1	3.4±1.5	1.6±1.5	···	EOR2	23.0°	3.1
J1129−2456	11h29m12s	−24°56′54″	3.1±1.1	3.6±1.5	3.5±2.3	2.0±2.0	EOR2	22.2°	4.7
J1129−0121	11h29m51s	−01°21′02″	1.7±0.7	2.3±1.0	2.5±1.6	0.9±0.9	EOR2	19.4°	3.2
J1130+0056	11h30m22s	+00°56′26″	3.5±1.2	4.3±1.7	2.8±1.9	1.8±1.8	EOR2	20.6°	4.4
J1130−0533	11h30m38s	−05°33′59″	1.5±0.6	1.7±0.8	2.0±1.3	1.5±1.3	EOR2	18.0°	3.8
J1130−0742	11h30m41s	−07°42′30″	2.2±0.8	2.6±1.1	4.0±1.5	···	EOR2	17.6°	4.1
J1130−1906	11h30m51s	−19°06′49″	2.9±1.0	3.5±1.4	3.3±2.1	2.4±2.0	EOR2	19.4°	4.8
J1130−2003	11h30m56s	−20°03′43″	2.0±0.8	2.3±1.0	2.5±1.6	1.2±1.3	EOR2	19.8°	3.1
J1130−2707	11h30m59s	−27°07′40″	3.5±1.3	4.2±1.7	5.9±3.9	2.8±3.1	EOR2	24.0°	3.7
J1131−2523	11h31m36s	−25°23′42″	2.7±1.0	3.1±1.3	3.5±2.3	2.3±2.5	EOR2	22.9°	3.2
J1132−2033	11h32m09s	−20°33′43″	3.0±1.0	3.7±1.4	2.6±1.7	1.6±1.6	EOR2	20.3°	4.6
J1133−2309	11h33m05s	−23°09′32″	2.7±0.9	3.1±1.3	3.4±2.2	···	EOR2	21.9°	4.6
J1133−0941	11h33m33s	−09°41′02″	1.3±0.6	1.4±0.7	···	···	EOR2	18.1°	3.1
J1134−0859	11h34m17s	−08°59′25″	2.6±0.9	3.2±1.3	2.2±1.5	2.5±2.1	EOR2	18.3°	4.8
J1134+0501	11h34m32s	+05°01′22″	3.5±1.3	4.6±1.9	0.9±1.4	···	EOR2	23.8°	3.6
J1134+0355	11h34m46s	+03°55′28″	3.2±1.2	3.5±1.5	4.4±2.9	2.5±2.6	EOR2	23.2°	3.9
J1135−0139	11h35m03s	−01°39′39″	2.4±0.9	2.7±1.2	3.4±2.1	2.5±2.2	EOR2	20.4°	4.2
J1135−2020	11h35m14s	−20°20′22″	2.8±1.0	3.2±1.3	3.1±2.0	3.4±3.0	EOR2	20.9°	4.1
J1135−1206	11h35m25s	−12°06′44″	2.0±0.8	2.1±1.0	2.8±1.8	1.5±1.5	EOR2	18.6°	3.3
J1136−1734	11h36m26s	−17°34′57″	2.9±1.0	3.4±1.4	2.4±1.6	2.8±2.4	EOR2	20.0°	4.7
J1136−1139	11h36m43s	−11°39′16″	2.0±0.8	2.0±1.0	3.4±2.2	2.4±2.1	EOR2	18.9°	3.2
J1137−0053	11h37m33s	−00°53′30″	3.5±1.2	4.4±1.8	2.8±1.9	0.4±1.1	EOR2	21.3°	4.4
J1138−0223	11h38m41s	−02°23′45″	2.5±1.0	2.7±1.3	···	3.4±2.8	EOR2	20.9°	3.8
J1139−2123	11h39m12s	−21°23′32″	2.9±1.1	3.5±1.4	2.6±1.8	···	EOR2	22.2°	4.3
J1139−0958	11h39m16s	−09°58′41″	3.2±1.2	3.7±1.5	4.2±2.7	2.8±2.4	EOR2	19.5°	4.5
J1140−2501	11h40m52s	−25°01′37″	3.5±1.3	4.3±1.8	1.7±1.9	3.4±4.5	EOR2	24.4°	3.5
J1141−1406	11h41m18s	−14°06′02″	3.1±1.2	3.5±1.5	2.6±1.8	4.4±3.7	EOR2	20.3°	3.3
J1141−0809	11h41m38s	−08°09′51″	2.7±1.0	3.2±1.3	3.1±2.0	2.6±2.3	EOR2	20.2°	4.3
J1141−0727	11h41m54s	−07°27′31″	2.5±0.9	3.1±1.3	1.8±1.3	···	EOR2	20.4°	3.6
J1141−0456	11h41m57s	−04°56′47″	2.4±0.9	2.9±1.2	2.8±1.9	···	EOR2	20.9°	3.4
J1142−0252	11h42m20s	−02°52′39″	3.7±1.3	4.3±1.7	4.2±2.7	···	EOR2	21.6°	4.5
J1142+0152	11h42m50s	+01°52′02″	5.4±2.0	6.5±2.7	6.2±4.0	4.4±3.9	EOR2	23.7°	4.0
J1143−0530	11h43m56s	−05°30′37″	2.7±1.0	3.2±1.4	2.6±1.8	2.5±2.3	EOR2	21.2°	3.6
J1144−1705	11h44m43s	−17°05′31″	2.7±1.0	3.2±1.4	3.3±2.2	···	EOR2	21.8°	3.3
J1145+0041	11h45m04s	+00°41′07″	4.4±1.7	4.9±2.1	6.7±4.3	5.3±4.5	EOR2	23.7°	3.4
J1146−0850	11h46m20s	−08°50′38″	3.4±1.3	4.0±1.7	4.9±3.1	3.4±2.9	EOR2	21.3°	4.4
J1146+0016	11h46m30s	+00°16′27″	4.0±1.5	4.7±2.0	5.1±3.4	···	EOR2	23.8°	3.5
J1146−0805	11h46m35s	−08°05′38″	4.4±1.6	5.6±2.2	5.2±3.3	3.0±2.6	EOR2	21.4°	4.5
J1148−0622	11h48m35s	−06°22′58″	3.3±1.3	4.2±1.8	1.9±1.6	···	EOR2	22.2°	3.1
J1149−0405	11h49m02s	−04°05′53″	4.6±1.6	5.6±2.2	5.5±3.6	···	EOR2	22.8°	4.9
J1149−0902	11h49m12s	−09°02′02″	2.6±1.1	3.2±1.5	2.2±1.7	···	EOR2	22.0°	3.2

Continued on Next Page...

Table A.2 – Continued

Name	RA	DEC	$S_{\rm avg}$	$S_{123.52}$	$S_{154.24}$	$S_{184.96}$	Field	$r_{\rm FC}$	SNR
J1149−1131	11h49m13s	−11°31′43″	3.1±1.2	3.9±1.8	2.9±2.1	2.2±2.2	EOR2	21.9°	3.4
J1149−0455	11h49m30s	−04°55′59″	4.3±1.5	5.4±2.1	3.8±2.6	···	EOR2	22.7°	4.8
J1150−1942	11h50m04s	−19°42′24″	4.5±1.6	5.4±2.1	3.9±2.6	···	EOR2	23.8°	4.5
J1150−1057	11h50m14s	−10°57′43″	3.0±1.1	3.6±1.6	3.4±2.4	2.1±2.0	EOR2	22.2°	3.1
J1150−1236	11h50m26s	−12°36′57″	3.7±1.4	4.3±1.8	4.0±2.7	5.2±4.4	EOR2	22.3°	4.1
J1151−2111	11h51m24s	−21°11′16″	3.4±1.3	4.1±1.7	1.7±2.1	···	EOR2	24.7°	3.3
J1153−1109	11h53m13s	−11°09′21″	2.7±1.1	3.9±1.6	1.8±1.7	···	EOR2	22.9°	3.2
J1157−1542	11h57m16s	−15°42′47″	4.0±1.6	4.7±2.1	5.2±3.4	4.3±4.0	EOR2	24.4°	3.3
J1159−0942	11h59m10s	−09°42′42″	6.0±2.0	7.1±2.8	6.2±4.1	1.5±2.2	EOR2	24.4°	4.5
J1159−1125	11h59m29s	−11°25′16″	4.1±1.5	5.1±2.1	2.5±2.3	4.3±3.9	EOR2	24.5°	3.4

THIS PAGE INTENTIONALLY LEFT BLANK

Bibliography

Argüeso, F., González-Nuevo, J., & Toffolatti, L. 2003, ApJ, 598, 86

Baldwin, J. E., Boysen, R. C., Hales, S. E. G., et al. 1985, MNRAS, 217, 717

Barkana, R. 2006, MNRAS, 372, 259

Barkana, R., & Loeb, A. 2005, ApJ, 624, L65

Beardsley, A. P., Hazelton, B. J., Morales, M. F., et al. 2012, ArXiv e-prints

Bernardi, G., Mitchell, D. A., Ord, S. M., et al. 2011, MNRAS, 413, 411

Bernardi, G., de Bruyn, A. G., Brentjens, M. A., et al. 2009, A&A, 500, 965

Bharadwaj, S., & Ali, S. S. 2004, MNRAS, 352, 142

Blake, C., & Wall, J. 2002, MNRAS, 329, L37

Bock, D. C.-J., Large, M. I., & Sadler, E. M. 1999, AJ, 117, 1578

Bouwens, R. J., Illingworth, G. D., Labbe, I., et al. 2011, Nature, 469, 504

Bowman, J. D., Morales, M. F., & Hewitt, J. N. 2007, ApJ, 661, 1

—. 2009, ApJ, 695, 183

Bowman, J. D., & Rogers, A. E. E. 2010, Nature, 468, 796

Broderick, J. W., Bryant, J. J., Hunstead, R. W., Sadler, E. M., & Murphy, T. 2007, MNRAS, 381, 341

Burke, G. J., & Poggio, A. J. 1981, Lawrence Livermore Laboratory

Chippendale, A. P. 2009, PhD thesis, The University of Sydney

Cohen, A. S., Lane, W. M., Cotton, W. D., et al. 2007, AJ, 134, 1245

Condon, J. J. 1974, ApJ, 188, 279

—. 1997, PASP, 109, 166

Condon, J. J., Cotton, W. D., Greisen, E. W., et al. 1998, AJ, 115, 1693

Condon, J. J., Griffith, M. R., & Wright, A. E. 1993, AJ, 106, 1095

Cornwell, T. J., Golap, K., & Bhatnagar, S. 2008, IEEE Journal of Selected Topics in Signal Processing, 2, 647

Dagkesamanskiĭ, R. D., Samodurov, V. A., & Lapaev, K. A. 2000, Astronomy Reports, 44, 18

Datta, A., Bowman, J. D., & Carilli, C. L. 2010, ApJ, 724, 526

De Breuck, C., van Breugel, W., Röttgering, H. J. A., & Miley, G. 2000, A&AS, 143, 303

De Breuck, C., van Breugel, W., Stanford, S. A., et al. 2002, AJ, 123, 637

de Oliveira-Costa, A., Bernardi, G., & Gonzalez-Nuevo, J. in prep.

de Oliveira-Costa, A., & Capodilupo, J. 2010, MNRAS, 404, 1962

de Oliveira-Costa, A., & Lazio, J. 2010, arXiv:1004.3167

de Oliveira-Costa, A., Tegmark, M., Gaensler, B. M., et al. 2008, MNRAS, 388, 247

Di Matteo, T., Ciardi, B., & Miniati, F. 2004, MNRAS, 355, 1053

Di Matteo, T., Perna, R., Abel, T., & Rees, M. J. 2002, ApJ, 564, 576

Dillon et al., J. in prep.

Douglas, J. N., Bash, F. N., Bozyan, F. A., Torrence, G. W., & Wolfe, C. 1996, AJ, 111, 1945

Fan, X. 2006, New A Rev., 50, 665

Furlanetto, S. R., & Briggs, F. H. 2004, New A Rev., 48, 1039

Furlanetto, S. R., Oh, S. P., & Briggs, F. H. 2006, Phys. Rep., 433, 181

Geil, P. M., Gaensler, B. M., & Wyithe, J. S. B. 2011, MNRAS, 418, 516

Gnedin, N. Y., & Shaver, P. A. 2004, ApJ, 608, 611

González-Nuevo, J., Toffolatti, L., & Argüeso, F. 2005, ApJ, 621, 1

Griffith, M. R., & Wright, A. E. 1993, AJ, 105, 1666

Griffith, M. R., Wright, A. E., Burke, B. F., & Ekers, R. D. 1994, ApJS, 90, 179

—. 1995, ApJS, 97, 347

Hales, S. E. G., Baldwin, J. E., & Warner, P. J. 1988, MNRAS, 234, 919

—. 1993a, MNRAS, 263, 25

Hales, S. E. G., Masson, C. R., Warner, P. J., & Baldwin, J. E. 1990, MNRAS, 246, 256

Hales, S. E. G., Masson, C. R., Warner, P. J., Baldwin, J. E., & Green, D. A. 1993b, MNRAS, 262, 1057

Hales, S. E. G., Mayer, C. J., Warner, P. J., & Baldwin, J. E. 1991, MNRAS, 251, 46

Hales, S. E. G., Riley, J. M., Waldram, E. M., Warner, P. J., & Baldwin, J. E. 2007, MNRAS, 382, 1639

Hamaker, J. P., Bregman, J. D., & Sault, R. J. 1996, A&AS, 117, 137

Hamilton, A. J. S. 1993, ApJ, 417, 19

Hancock, P. J., Murphy, T., Gaensler, B. M., Hopkins, A., & Curran, J. R. 2012, arXiv:1202.4500

Harker, G., Zaroubi, S., Bernardi, G., et al. 2009, MNRAS, 397, 1138

Harrington, R. F. 1993, Field Computation by Moment Methods (Wiley-IEEE Press)

Hinshaw, G., Spergel, D. N., Verde, L., et al. 2003, ApJS, 148, 135

Hogan, C. J., & Rees, M. J. 1979, MNRAS, 188, 791

Högbom, J. A. 1974, A&AS, 15, 417

Hogg, D. W. 1999, ArXiv Astrophysics e-prints

Iliev, I. T., Mellema, G., Pen, U.-L., Bond, J. R., & Shapiro, P. R. 2008, MNRAS, 384, 863

Intema, H. T., van der Tol, S., Cotton, W. D., et al. 2009, A&A, 501, 1185

Intema, H. T., van Weeren, R. J., Röttgering, H. J. A., & Lal, D. V. 2011, A&A, 535, A38

Ishwara-Chandra, C. H., Sirothia, S. K., Wadadekar, Y., Pal, S., & Windhorst, R. 2010, MNRAS, 405, 436

Jackson, C. 2005, PASA, 22, 36

Jacobs, D. C. 2011, private communication

Jacobs, D. C., Aguirre, J. E., Parsons, A. R., et al. 2011, ApJ, 734, L34

Kassim, N. E., Lazio, T. J. W., Erickson, W. C., et al. 2007, ApJS, 172, 686

Komatsu, E., Smith, K. M., Dunkley, J., et al. 2011, ApJS, 192, 18

Kratzenberg, E. 2010, private communication

Kumar, A., Padmanabhan, T., & Subramanian, K. 1995, MNRAS, 272, 544

Lane, W. M., Clarke, T. E., Taylor, G. B., Perley, R. A., & Kassim, N. E. 2004, AJ, 127, 48

Large, M. I., Mills, B. Y., Little, A. G., Crawford, D. F., & Sutton, J. M. 1981, MNRAS, 194, 693

Lidz, A., Zahn, O., McQuinn, M., Zaldarriaga, M., & Hernquist, L. 2008, ApJ, 680, 962

Liu, A., & Tegmark, M. 2011, Phys. Rev. D, 83, 103006

—. 2012, MNRAS, 419, 3491

Liu, A., Tegmark, M., Bowman, J., Hewitt, J., & Zaldarriaga, M. 2009, MNRAS, 398, 401

Lonsdale, C. J., Cappallo, R. J., Morales, M. F., et al. 2009, IEEE Proceedings, 97, 1497

Madau, P., Meiksin, A., & Rees, M. J. 1997, ApJ, 475, 429

Mao, Y., Tegmark, M., McQuinn, M., Zaldarriaga, M., & Zahn, O. 2008, Phys. Rev. D, 78, 023529

McQuinn, M., Zahn, O., Zaldarriaga, M., Hernquist, L., & Furlanetto, S. R. 2006, ApJ, 653, 815

Mesinger, A., Furlanetto, S., & Cen, R. 2011, MNRAS, 411, 955

Mitchell, D. A., Greenhill, L. J., Wayth, R. B., et al. 2008, IEEE Journal of Selected Topics in Signal Processing, 2, 707

Morales, M. F., Hazelton, B., Sullivan, I., & Beardsley, A. 2012, ArXiv e-prints

Morales, M. F., & Hewitt, J. 2004, ApJ, 615, 7

Morales, M. F., & Wyithe, J. S. B. 2010, ARA&A, 48, 127

National Research Council, C. f. a. D. S. o. A. a. A. 2010, New Worlds, New Horizons in Astronomy and Astrophysics (The National Academies Press)

Nayak, A., Daiboo, S., & Shankar, N. U. 2010, MNRAS, 408, 1061

Noordam, J. E. 2004, in Society of Photo-Optical Instrumentation Engineers (SPIE) Conference Series, Vol. 5489, Society of Photo-Optical Instrumentation Engineers (SPIE) Conference Series, ed. J. M. Oschmann Jr., 817–825

Nusser, A. 2005, MNRAS, 364, 743

Oberoi, D., Matthews, L. D., Cairns, I. H., et al. 2011, ApJ, 728, L27

Ord, S. M., Mitchell, D. A., Wayth, R. B., et al. 2010, PASP, 122, 1353

Paciga, G., Chang, T.-C., Gupta, Y., et al. 2011, MNRAS, 413, 1174

Pandey, V. N. 2006, PhD thesis, Raman Research Institute

Parsons, A., McQuinn, M., Jacobs, D., Aguirre, J., & Pober, J. 2011, ArXiv e-prints

Parsons, A. R., Backer, D. C., Foster, G. S., et al. 2010, AJ, 139, 1468

Peacock, J. A. 1999, Cosmological Physics (Cambridge University Press)

Pedani, M. 2003, New A, 8, 805

Pen, U.-L., Chang, T.-C., Hirata, C. M., et al. 2009, MNRAS, 399, 181

Pindor, B., Wyithe, J. S. B., Mitchell, D. A., et al. 2011, PASA, 28, 46

Press, W. H., Teukolsky, S. A., Vetterling, W. T., & Flannery, B. P. 1992, Numerical recipes in C. The art of scientific computing (Cambridge University Press)

Pritchard, J., & Loeb, A. 2010, Nature, 468, 772

Pritchard, J. R., & Loeb, A. 2011, Prog. Rep. Phys., submitted (arXiv:1109.6012)

Rengelink, R. B., Tang, Y., de Bruyn, A. G., et al. 1997, A&AS, 124, 259

Rogers, A. E. E. 2007, edges Memo 37

Rogers, A. E. E., & Williams, C. L. 2008, mWA Memo 4-September-2008

Rottgering, H. J. A., Braun, R., Barthel, P. D., et al. 2006, 'Cosmology, Galaxy Formation and Astroparticle Physics on the Pathway to the SKA' eds. H. R. Klockner, S. Rawlings, M. Jarvis, A. Taylor (ASTRON: Dwingeloo), p169

Santos, M. G., Cooray, A., & Knox, L. 2005, ApJ, 625, 575

Schwab, F. R. 1984, AJ, 89, 1076

Scott, D., & Rees, M. J. 1990, MNRAS, 247, 510

Shaver, P. A., Windhorst, R. A., Madau, P., & de Bruyn, A. G. 1999, A&A, 345, 380

Sirothia, S. K., Kantharia, N. G., Ishwara-Chandra, C. H., & Gopal-Krishna. 2011, The GMRT Sky Survey, `http://tgss.ncra.tifr.res.in/`

Slee, O. B. 1977, Australian Journal of Physics Astrophysical Supplement, 43, 1

—. 1995, Australian Journal of Physics, 48, 143

Swarup, G., Ananthakrishnan, S., Kapahi, V. K., et al. 1991, Current Science, Vol. 60, NO.2/JAN25, P. 95, 1991, 60, 95

Tasker, N. J., Condon, J. J., Wright, A. E., & Griffith, M. R. 1994, AJ, 107, 2115

Taylor, G. B., Carilli, C. L., & Perley, R. A., eds. 1999, Astronomical Society of the Pacific Conference Series, Vol. 180, Synthesis Imaging in Radio Astronomy II

Tegmark, M. 1997, Physical Review Letters, 79, 3806

Tegmark, M., Hamilton, A. J. S., Strauss, M. A., Vogeley, M. S., & Szalay, A. S. 1998, ApJ, 499, 555

Tegmark, M., Blanton, M. R., Strauss, M. A., et al. 2004, ApJ, 606, 702

Thompson, A. R., Moran, J. M., & Swenson, Jr., G. W. 2001, Interferometry and Synthesis in Radio Astronomy, 2nd Edition (Wiley-Interscience)

Tingay et al., S. J. in prep.

van der Tol, S. ., Jeffs, B. D., & van der Veen, A.-J. . 2007, IEEE Transactions on Signal Processing, 55, 4497

Vedantham, H., Udaya Shankar, N., & Subrahmanyan, R. 2011, ArXiv e-prints

Wang, X., Tegmark, M., Santos, M. G., & Knox, L. 2006, ApJ, 650, 529

Williams, C. L., Bowman, J. D., Hewitt, J. N., et al. 2007, mWA Antenna Memo

Williams, C. L., Hewitt, J. N., Levine, A. M., et al. 2012, ArXiv e-prints

Wilman, R. J., Miller, L., Jarvis, M. J., et al. 2008, MNRAS, 388, 1335

Wright, A. E., Griffith, M. R., Burke, B. F., & Ekers, R. D. 1994, ApJS, 91, 111

Wright, A. E., Griffith, M. R., Hunt, A. J., et al. 1996, ApJS, 103, 145

Yan, H.-J., Windhorst, R. A., Hathi, N. P., et al. 2010, Research in Astronomy and Astrophysics, 10, 867

Zaldarriaga, M., Furlanetto, S. R., & Hernquist, L. 2004, ApJ, 608, 622

Zhang, X., Zheng, Y., Chen, H., et al. 1997, A&AS, 121, 59

Zheng, W., Postman, M., Zitrin, A., et al. 2012, ArXiv e-prints